CYRIC

ANNUAL REPORT

2016-2017

(January 2016 - December 2017)

CYCLOTRON AND RADIOISOTOPE CENTER
TOHOKU UNIVERSITY

CYRIC

ANNUAL REPORT

2016-2017

(January 2016 - December 2017)

CYCLOTRON AND RADIOISOTOPE CENTER
TOHOKU UNIVERSITY
http://www.cyric.tohoku.ac.jp/

PREFACE

CYRIC was established in 1977 as an institution for carrying out multidisciplinary research with the cyclotron and radioisotopes, and for training researchers of Tohoku University for safe treatment of radioisotopes and radiations. The cyclotron of CYRIC was manufactured by Sumitomo Heavy Industry Inc., Japan, form the design of CGR-Mev, France. The first beam was extracted at the end of December 1977. The scheduled operation of the cyclotron for research studies started in July 1979. We usually operate the cyclotron four whole days a week for research studies. The Great East Japan Earthquake occurred on March 11, 2011, the accelerator facilities were severely damaged because of strong shaking that continued for a few minutes. We have made great efforts on the recovery of our daily research activities until now. Fortunately, the scheduled operation of the cyclotron for collaborative research studies has re-started since October, 2012 from the one year and half interruption of our services. CYRIC consists of four buildings: cyclotron building (5400 m^2), radioisotope building (2000 m^2), molecular imaging research building (1000 m^2), and CYRIC Collaboration building (250 m^2). As the example of medical and pharmaceutical fields, our CYRIC demonstrated the usefulness of FDG-PET scans in patients with cancer for the first time in early 1980's. Other highly respected achievement of CYRIC is the application of molecular imaging to drug development including the imaging of neurotransmitter receptors and amyloid and tau proteins in Alzheimer disease. Fully functioning CYRIC facilities can ensure the further development of molecular imaging in near future.

In conformity with the aim of establishment of CYRIC, the cyclotron has been used for studies in various fields of research, such as nuclear physics, nuclear chemistry, solid-state physics and element analysis by PIXE and activation, and for radioisotope production for use in engineering, biology, pharmaceutical science and medicine. Six divisions (Division of Accelerator, Division of Instrumentations, Division of Radio-pharmaceutical Chemistry, Division of Cyclotron Nuclear Medicine, Division of Radiation Protection and Safety Control, and Division of Geriatric Behavioral Neurology) work for maintenance, development of facilities, and for studies of their individual research fields. The divisions belong to the graduate schools of Tohoku University.

Both the K=110 MeV AVF cyclotron and the K=12 MeV AVF cyclotron have been

steady operated in the last two years. Total beam-times during the 2016 and 2017 fiscal years were 2055 and 2042 hours, respectively. In order to elucidate a role of an extra neutron in the multi-α cluster structure, the measurement of decay-α particles has been performed using the $^{12}C(^{13}C,3\alpha)$ reaction. The study of the $^{24}Mg + \alpha$ cluster structure in ^{28}Si has been started toward the search for the multi-α cluster structure. Heavy ion irradiation experiments using the cocktail beam have increased by the collaboration between the industry and CYRIC. The OPERA-QiSS program which is a consortium of many research institutes and industrial companies to develop quantum technologies for the safe and smart society has been launched. In this program, we will standardize the evaluation of the neutron-induced soft error rate and develop a high-resolution Compton camera to visualize the gamma-ray. The RI production system using the fast neutron beam has been developed with JAEA, QST, and Kyushu University groups.

The development of the laser cooled RI beam line constructed at TOF trough TR5 has been continued. This new beam line is used to study the fundamental physics using heavy elements such as an electric dipole moment (EDM) of francium atoms, and will be extended for the research on atomic physics and radiation chemistry. The thermal ionizer, neutralizer and optical trapping system are ready, and the first observation of laser trapped Fr atoms was done in 2018. The improvement of beam transportation and neutralization of Fr ions to realize the high trapping efficiency is in progress. The development of the cold-atom co-magnetometer to measure the EDM was also performed, and Dr. A. Uchiyama received the Kuroda Chika Award for this work.

In the research program on proton therapy, experimental studies on proton computed-tomography (pCT) has been performed to obtain water-equivalent length (WEL) in proton-therapy treatment planning because pCT potentially provides more accurate WEL data than XCT. The experimental results have shown that pCT significantly reduces the uncertainties in range simulation based on XCT, and has clinical benefits in taking full advantage of proton therapy.

Radiopharmaceuticals for clinical positron emission tomography (PET) is one of the important work for the Division of Radio-pharmaceutical Chemistry. During the reporting period, total number of clinical supply of PET tracers increased but there was no translation of new PET tracer for clinical research. PET tracers relating to dementia imaging were mainly supplied for clinical studies. Although both [^{11}C]BF-227 and [^{11}C]PiB had been used for amyloid imaging of Alzherimer's disease (AD) patients previously, in-house preparation and supply of [^{11}C]BF-227 was terminated due to the reason that PET image quality of [^{11}C]PiB

is superior to that of [^{11}C]BF-227. [^{11}C]PiB is now recognized as the gold standard tracer for amyloid imaging and used most frequently all over the world. PET tracers prepared and supplied for clinical studies in the two years were [^{18}F]THK-5351 (22 preparations), [^{11}C]doxepin (21), [^{11}C]raclopride (40), [^{11}C]PiB (68), and [^{15}O]water (7).

Regarding basic research on radiopharmaceuticals, we further advanced the development of various types of PET tracers and related technologies. One of the main theme was characterization and optimization of the THK tracers to reduce off-target binding of 2-arylquinoline type structure. Several compounds of the new chemical scaffolds were designed, synthesized, and biologically evaluated. Another main theme was development of ^{18}F-labeled phosphonium compounds for mitochondria imaging by PET. Using the convenient and effective method we developed, we could optimize the structure of ^{18}F-labeled phosphonium compounds. In addition to the above themes, we continued the research on radiosynthesis of a positron emitter labeled protein using cell-free protein synthesis system and succeeded to prepare a ^{11}C-labeled tra-scFv antibody for imaging of HER2. Furthermore, research on micro-scale nucleophilic radiofluorination had started and are yielding some promising results applicable for radiosynthesis of many types of ^{18}F-labeled tracers.

Various clinical PET studies were conducted, focusing on brain physiology and pathophysiology. Neurological disorders such as progressive supranuclear palsy and corticobasal syndrome were new targets for clinical tau PET imaging. THK-5351 binding has been demonstrated to be a mixture of bindings to tau proteins as well as monoamine oxidase inhibitor B (MAO-B), collectively interpreted as a sign of astrogliosis in the brain. For more accurate and reliable quantification in these PET studies, basic examinations have been done regarding partial volume correction and determination of SUVR values. Technically, they have been so important. In addition, a breakthrough has been made in terms of pathophysiology of a stress disorder such as irritable bowel syndrome, using radioactive water PET study combined with the effects of therapeutic drugs. Brain glucose metabolic change was measured in various subjects. A cases report on cervical dystonia may be very interesting. A clinical study on patients with mild pain demonstrated the effects of chiropractic intervention. A healthy volunteer study was conducted during cognitive tasks. This cognitive study was done in a multimodal setting including FDG PET and near infrared spectroscopy (NIRS). This multimodal study resulted in a new discovery in the physiological mechanism of sedation due to antihistamines.

We conducted the beginners training for safe handling of radiation and radioisotopes twice a year in 2016 and 2017 for staffs and students of Tohoku University. The courses included 1) Radiositopes and radiation generators (501 trainees in 2016 and 530 trainees in

2017), 2) X-ray machines and electron microscope (373 trainees in 2016 and 344 trainees in 2017). The total numbers of trainees in English classes for foreign students and scientists were 90 in 2016 and 87 in 2017, respectively.

The four most frequent used radioisotopes in CYRIC in 2016 and 2017 were C-11, O-15, F-18, and P-32. There were 330 individuals in 2016 and 319 individuals in 2017 who were registered as radiation workers in CYRIC.

The aim of Division of Geriatric Behavioral Neurology is to study the neuroscience of dementia and contribute to the welfare of elderly people. Our work in the northern area of Miyagi prefecture has always been our priority. Since 1988, our research group and the town of Tajiri (now the city of Osaki) have been performed the community-based stroke and dementia prevention (the Osaki-Tajiri Project), followed by the similar projects in the cities of Kurihara, Tome, and Wakuya. We have reported the prevalence and incidence of dementia, and clinical validity of drug treatment and/or psychosocial intervention with reference to PET examinations using the following tracers: [^{15}O]oxygen, [^{11}C]CO, [^{18}F]fluorodeoxy glucose, [^{18}F]fluorodopa, [^{11}C]YM-09151-2, and [^{11}C]donepezil. Unfortunately, dementia patients in a community do not always receive an adequate medical and welfare management based on a scientific evidence including diagnosis of dementing diseases, psychosocial intervention, and caregiver education. Therefore, the Division of Geriatric Behavioral Neurology aims the followings: 1) to establish a method for assessing cognitive functions of older adults and database; 2) to develop a comprehensive model for dementia including medical and welfare management based on the neurological basis; and 3) to improve the level of medical and welfare for dementia and education. In addition, the Division of Geriatric Behavioral Neurology has collaborated with the New Industry Creation Hatchery Center (NICHe) on the study of the development of the driving simulator for early detection of dementia.

We are most grateful to Tohoku University and to the Ministry of Education, Sports, Culture, Science and Technology for continuous support.

December 2018

Hiroshi WATABE, Director
Masatoshi ITOH
Atsuki TERAKAWA
Shozo FURUMOTO
Manabu TASHIRO
Shigeo MATSUYAMA
Kenichi MEGURO

CONTENTS

I. NUCLEAR PHYSICS

II. NUCLEAR INSTRUMENTATION

IV. NUCLEAR MEDICAL ENGINEERING

V. RADIOCHEMISRTY AND NUCLEAR CHEMISTRY

VI. RADIOPHARMACEUTICAL CHEMISTRY AND BIOLOGY

VII. NUCLEAR MEDICINE

I. NUCLEAR PHYSICS

I. 1. Measurement of ^{3}He Analyzing Power for Proton-^{3}He Scattering at 70 MeV with Polarized ^{3}He Target

Watanabe A.[1], Wada Y.[1], Sekiguchi K.[1], Akieda T.[1], Eto D.[1], Ino T.[2], Itoh M.[3], Kawahara K.[1], Kon H.[1], Miki K.[1], Mukai T.[1], Nakai S.[1], Sakai D. [1], Shibuya S.[1], Shiokawa Y.[1], Taguchi T.[1], Uesaka T.[4], Wakui T.[5], and Watanabe M.[1]

[1]*Department of Physics, Tohoku University*
[2]*KEK*
[3]*Cyclotron and Radioisotope Center, Tohoku University*
[4]*RIKEN Nishina Center*
[5]*National Institute of Radiological Science*

Study of three-nucleon forces (3NFs) is essentially important in clarifying nuclear phenomena, e.g. discrete states of nuclei and equation of state of nuclear matter. Few-nucleon scattering offers good opportunities to investigate dynamical aspects of these forces, such as momentum, spin, and iso-spin dependencies. The nucleon-deuteron scattering has provided a solid basis to nail down detailed properties of 3NFs[1)], however, the total isospin channel of the 3NFs is limited to T=1/2. Recently importance of the iso-spin dependence study of 3NFs have been pronounced for understanding of nuclear system with larger-isospin asymmetry, e.g. neutron-rich nuclei, neutron matter, and neutron stars[2)]. The p+^{3}He scattering is an attractive probe since this system is the simplest one where the 3NFs in the channels of total isospin T=3/2 can be studied. In order to explore the properties of three-nucleon forces via proton-^{3}He scattering we have performed the measurements of ^{3}He analyzing powers at 70 MeV by using the newly developed polarized ^{3}He target.

In the polarized ^{3}He target system alkali-hybrid spin-exchange optical pumping method is adopted for polarizing ^{3}He nucleus[3)]. The Rb atoms are optically pumped and polarized and they in turn transfer their polarization to the K atoms. Spin exchange collisions among Rb, K, and ^{3}He atoms transfer the polarization to ^{3}He through hyper-fine interactions[4)]. The target cell consists of double chamber which includes the target chamber and the optical pumping one. Both are connected by a thin transfer tube. This is designed to separate the

target chamber from the optical pumping one which needs external oven to produce Rb/K vapor. The target cell contains the ^{3}He gas with pressure of 3 atm at room temperature together with a small amount of N_2 gas and Rb/K vapor. The pumping chamber is heated to about 493 K to provide high Rb/K vapor density and maintain the polarization of ^{3}He nucleus. Circularly polarized photons with power of 50 W are used to optically pump Rb atoms. Polarized ^{3}He nuclei are allowed to diffuse into the target chamber. The target cell is made of GE180 glass which is known to have a very long relaxation time for the polarization of ^{3}He. The polarizations are monitored by the adiabatic fast passage (AFP) NMR method. The NMR signals give relative values of the polarization. The absolute values of the target polarization are calibrated by using frequency shift of the electron spin resonance of Rb atoms. Typical values of polarizations are 50%.

Experiments with 70 MeV proton beams in conjunction with the polarized ^{3}He target were performed at the room TR4. Proton beams bombarded the polarized ^{3}He target and they were stopped in the faraday cup. Beam intensities were about 10 nA during the experiment. Scattered protons were detected by the *dE-E* scintillation counters. They consisted of a plastic scintillator with thickness of 0.2-1 mm and a NaI(Tl) scintillator with thickness of 55 mm. The measured angles were 35-125 degrees in the laboratory system which are equivalent to 46-141 degrees in the center of mass system. In the measurement we successfully obtained asymmetry of the events from proton-^{3}He scattering.

The preliminary results of the ^{3}He analyzing power for p-^{3}He scattering at 70 MeV are shown in Fig. 1. The statistical errors together with the systematic ones are also shown. The data are compared with the rigorous numerical calculation of the four-nucleon scattering based on the modern nucleon-nucleon potentials[5]. Here the INOY[6] and CDBonn[7] potentials are taken into account. Clear differences are found at the angles 70-100 degrees and 130-140 degrees in the center of mass system. The results of comparison indicate that 3NFs are needed in the calculations in order to describe the experimental data.

References

1) Sekiguchi K, et al., *Phys Rev.* C **65** (2002) 034003; *ibid*, **89** (2014) 064007.
2) For example, Pieper SC, et al., *Phys Rev* C **64** (2001) 014001; Demorest PB, et al., *Nature* **467** (2010) 1081; Gandolfi S, et al., *Phys Rev* C **85** (2012) 032801.
3) E. Babcock, et al., *Phys Rev. Lett.* **91** (2003) 123003.
4) Happer W, et al., *Rev. Mod. Phys.* **44** (1972) 169.

5) Deltuva, A., private communications.
6) Doleschall, P., *Phys Rev.* C **69** (2004) 054001.
7) Machleidt, R., *Phys Rev.* C **63** (2001) 024001.

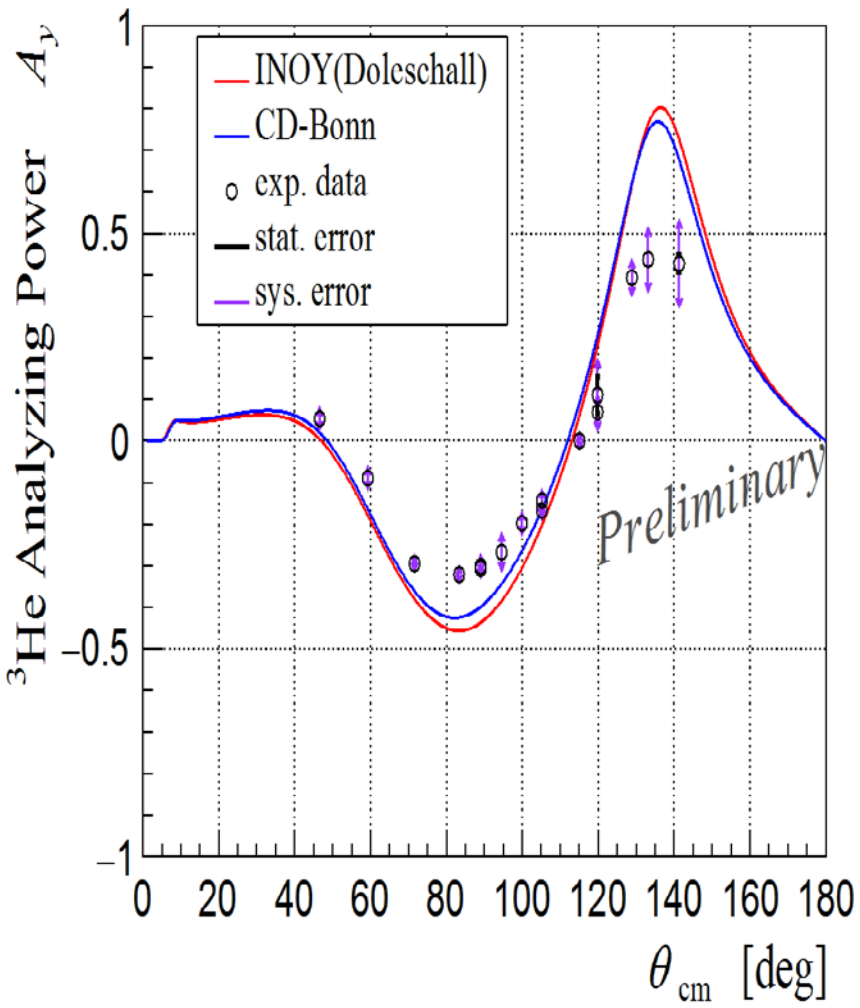

Figure 1. Preliminary results of ^{3}He analyzing power for p-^{3}He elastic scattering at 70 MeV. The rigorous numerical four-body calculations based on the INOY (CDBonn) potentials are shown in the red (blue) curve.

I. 2. Performance Evaluation of Newly Developed Recoil Proton Detection System "CATCH" with pp Scattering at 80 MeV

Akazawa Y.[1], Miwa K.[1], Ikeda M.[1], Ozawa S.[1], Fujioka. N.[1], Tamura H.[1], Koike T.[1], Sekiguchi K.[1], Miki K.[1], Umetsu H.[1], Honda R.[2], Nakada Y.[2], and Kobayashi K.[2]

[1]Department of Physics, Tohoku University,
[2]Department of Physics, Osaka University

A scattering experiment between a Σ hyperon and a proton is planned at J-PARC K1.8 beam line (J-PARC E40 experiment[1)]) in order to investigate the baryon-baryon interaction and to confirm the repulsive force due to the Pauli effect in quark level, which is considered as one of the origins of the repulsive core in the nuclear force. The quark Pauli effect has not been confirmed experimentally. In order to compare the measured cross section with predicted ones from theoretical models with and without this effect, the accuracy of the measured differential cross section of the Σ^+p elastic scattering reaction is required to be better than ±10% at 3 mb/sr. We also derive Σ-nucleon interaction systematically from the cross section of the Σ^+p and Σ^-p elastic scatterings and the Σ^-p→Λn reaction.

In order to identify the Σp scattering event kinematically, we need to measure the momentum vector of the Σ beam and the scattering angle (trajectory of recoil proton) and the kinetic energy of the recoil proton. We will use two spectrometer systems installed at the upstream and at the downstream of a liquid hydrogen target. The momentum of Σ particle produced in the target by a $\pi p \rightarrow \Sigma K^+$ reaction is reconstructed by the momenta of the incident π beam and scattered K^+ measured by each spectrometer. In addition to the spectrometer system, a detector system for a recoil proton is necessary and required to measure the trajectory and the energy of the recoil proton. Since a high intensity π beam of 20 MHz is used in this experiment for the Σ production, a sufficient time response is also required for the detector. For this reason, we developed a new detector system, so called "CATCH" (Cylindrical Active Tracker and Calorimeter system for Hyperon-proton scattering).

CATCH is designed to have a large acceptance by covering 300 mm thickness of the

liquid hydrogen target cylindrically with a long sensitive area of 400 mm in the beam direction. CATCH consists of a Cylindrical Fiber Tracker (CFT) and a bismuth germanate (BGO) calorimeter as shown in Fig. 1.

CFT is a tracking detector with a fast time response made of 5,000 scintillation fibers with a diameter of 0.75 mm. In order to reconstruct trajectories three dimensionally, we fabricated two types of cylindrical layers where fibers are placed with the straight and spiral configurations on the surface of the cylindrical layer, respectively. As for the BGO calorimeter, 24 BGO crystals are placed for surrounding CFT and are used to measure the kinetic energy of the recoil proton. The size of one crystal piece is $30\times25\times400$ mm^3.

After each detector was fabricated, CFT and the BGO calorimeter were combined together as CATCH. We developed such a new detector system by taking a long time. Especially, since CFT uses a large number of scintillation fibers and has a special shape, it required a lot of R&D. In these development periods including the development of the BGO calorimeter, we also performed test experiments at CYRIC to evaluate the performance of the prototype[2)]. Reflecting these feedbacks, we completed the construction of the actual type of CATCH at the end of 2016.

In order to evaluate the performance of CATCH system for the first time, we performed a pp and pC scattering experiment at CYRIC (Tohoku University) in January 2017. A Polyethylene (CH_2) target of 800 μm thickness installed inside CATCH was irradiated by an 80 MeV proton beam, and scattered protons were measured by CATCH. The measurement accuracy of the differential cross section was evaluated by deriving it from the scattered protons measured by CATCH. Also, we examined energy and fiber position calibration methods and aimed to establish analysis method.

The angular resolution of CFT and the energy resolution of BGO calorimeter are required to be better than 2 degrees (σ_θ) and 3 MeV (σ), respectively for the identification of the scattering reactions. The angular resolution was evaluated to be 1.6 degrees (σ_θ) from the opening angle between two protons emitted from pp scattering. The energy calibrations of CFT and the BGO calorimeter were performed by using the relation between the energy of the scattered protons and the scattering angle θ measured by CFT. The energy resolution of the BGO calorimeter was obtained to be 1.5 MeV (σ) for 80 MeV proton, and that of CFT was obtained to be better than 20% for the energy deposit of a proton in CFT (8 MeV ~ 20 MeV). These performances satisfy our requirements for the Σp scattering experiment. As a result of the energy calibration, the correlation between the scattered proton's energy

and the scattering angle θ was consistent with the kinematic calculation as shown in Fig. 2.

The differential cross sections of pp and pC scatterings were derived by the number of the identified event by CATCH system. Data were taken with three different target positions to investigate the position dependence of the CATCH performance which has a long active region. We could only derive the relative cross sections due to a problem in the measurement of the absolute beam intensity. However, we found that the angular distributions of the obtained relative differential cross sections were consistent with the reference results as shown in Fig. 3. The difference between the measured result and the reference data is regarded as a systematic error in the cross section, which was found to be within ±10%. It satisfies the requirement for the Σp scattering experiment of ±10%. The almost same result was obtained for the pC scattering reaction. These results suggested that we have established an analysis method for deriving the cross section for the newly developed CATCH system.

In conclusion we fabricated the CATCH system and performed the test experiment for the first time. As the results of the performance evaluation, the systematic error in the cross section is within ±10%. We have confirmed that the CATCH system has sufficient performances for the Σp scattering experiment at J-PARC. Although we also took a proton-deuteron scattering data with a Deuteron gas target for study of the three-nucleon forces, it is currently under analysis.

References

1) K. Miwa et al.: Proposal for an experiment at J-PARC, http://jparc.jp/NuclPart/pac_1101/pdf/KEK_ J-PARCPAC2010-12.pdf.
2) Akazawa Y., Master thesis, Tohoku University (2014).

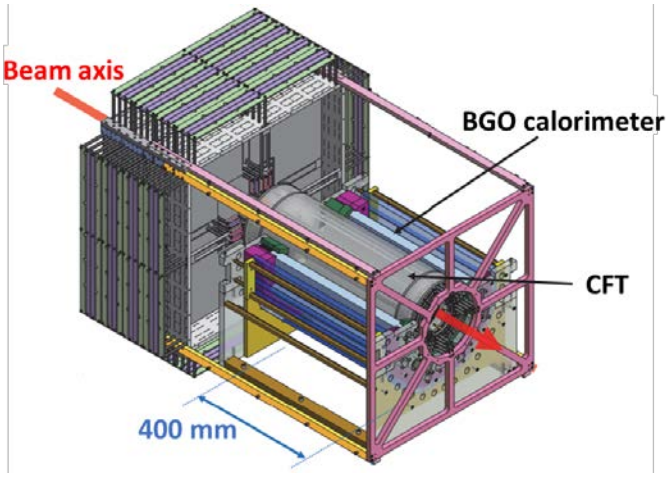

Figure 1. CATCH consists of a Cylindrical Fiber Tracker (CFT) and a BGO calorimeter. It surrounds the target cylindrically in order to measure the recoil proton with a large acceptance.

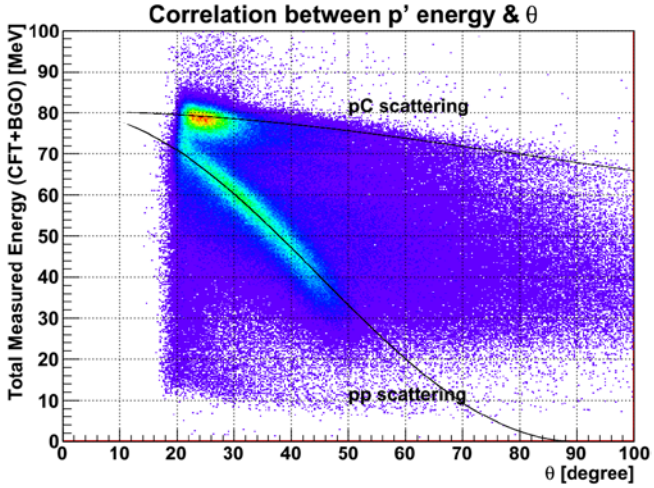

Figure 2. The correlation between the energy and the scattering angle θ of the scattered proton measued by CATCH. It was consistent with the kinematical lines of pp and pC scatterings.

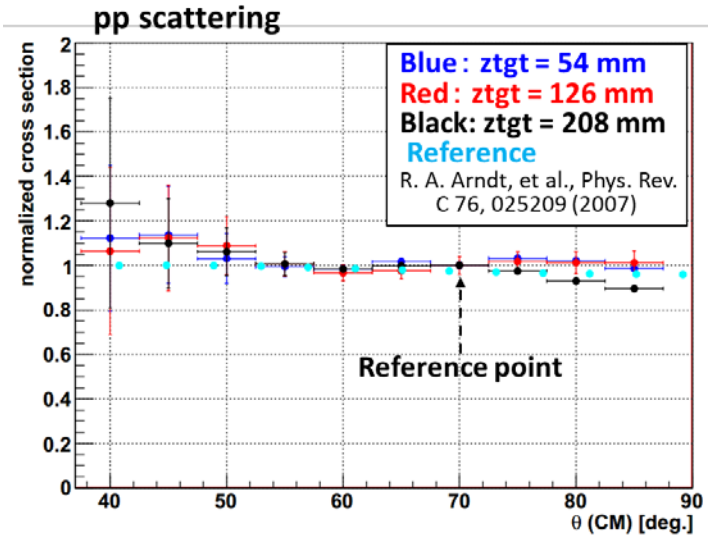

Figure 3. The angular distributions of the obtained relative differential cross sections for three target position. They are consistent with the reference results within ±10% of a systematic error.

I. 3. Search for the Alpha Gas-like State in ^{13}C

Itoh M.[1], Nasu Y.[1], Ishibashi Y.[1], Karasudani K.[1], Matsuda Y.[1], Okamoto J.[1], Akimune H.[2], Heguri K.[2], Tanaka J.[2], and Hirakawa K.[3]

[1]Cyclotron and Radioisotope Center, Tohoku University
[2]Department of Physics, Konan University
[3]Research Center for Nuclear Physics, Osaka University

The α cluster structure appears in excited states in A = 4N nuclei which have equal numbers of protons and neutrons. The Hoyle state, which is the second 0^+ (0_2^+) state at E_x = 7.65 MeV in ^{12}C, is typical one and is considered to have a dilute gas-like structure in which three α clusters are loosely bound[1)]. This structure is called an α gas-like structure.

Recently, the α gas-like structure is considered to appear in A≠4N nuclei in which constituent clusters occupy mainly the lowest orbit of the cluster mean-field potential. In this experiment, we focus on the α gas-like structure in ^{13}C in order to study the role of an excess neutron in the 3α gas-like structure. In the orthogonality condition model (OCM) calculation, the fifth $1/2^+$ ($1/2_5^+$) state at E_x = 14.9 MeV in ^{13}C is considered to have the 3α + *n* gas-like structure in which all constituent clusters including an excess neutron enter into the s orbit[2)]. In this $1/2^+$ state, the weak repulsive even-parity α-*n* force is considered to make the excitation energy higher than the 3α + *n* threshold.

In order to search for the $1/2_5^+$ state at Ex = 14.9 MeV, we carried out the measurement of decay α particles from the ^{12}C(^{13}C,3α*n*)^{12}C reaction. The 129.2 MeV $^{13}C^{4+}$ beam accelerated by the 930 AVF cyclotron bombarded the self-supported natural carbon foil with a thickness of 50 μg/cm^2. The picture of the experimental set-up is shown in Fig. 1. Three double-sided silicon strip detectors (DSSDs) were used. The right DSSD (DSSD1) and the two left-upper DSSDs (DSSD2, DSSD3) in Fig. 1 were for detections of recoil ^{12}C particles and decay 3α particles, respectively. DSSD1 has horizontally 40 channels and vertically 40 channels with a size of 40 × 40 mm^2 and a thickness of 1000 μm. To reduce numbers of readout channels, two or three strips were connected into a channel. The total readout channels were reduced into 32 channels. DSSD2 and DSSD3 have horizontally and vertically

16 channels with a size of 50 × 50 mm^2 and a thickness of 1500 μm, respectively. The DSSDs were set so as to detect decay 3α particles with the efficiency of 95 % or more in the excitation energy from 12.3 MeV to 15.6 MeV. The energy and scattering angle of the decay neutron were kinematically calculated from those of the detected recoil ^{12}C and decay 3α particles.

The identification of the state which has the 3α gas-like structure has been done as follows. The state of the 3α gas-like structure is considered to decay through the $^{12}C(0_2^+)$ + *n* channel, mainly. Therefore, we searched the state which mainly decay through the $^{12}C(0_2^+)$ + *n* channel in the 3α + *n* decay channels. Figure 2 shows the total energy distribution of the 3α particles in the 3α system obtained by using the invariant mass method. It is clear that events around the peak at 7.65 MeV which correspond to those of the $^{12}C(0_2^+)$ + *n* decay channel can be separated completely. Figure 3 shows the excitation energy spectra of ^{13}C obtained from the four momentum of the recoil ^{12}C using the missing mass method. The blue histogram shows that of all events in coincidence with three α particles detected in the DSSD2 and DSSD3. The red histogram shows that of the events which decay through the $^{12}C(0_2^+)$ + *n* channel among them. Owing to the energy dependence of the detection efficiency of the 3α particles emitted from the $^{12}C(0_2^+)$ state, the energy spectrum of the $^{12}C(0_2^+)$ + *n* channel becomes a little flat. However, the peak at around E_x = 13.2 MeV is still large compared with the other excitation energy region. Therefore, we tentatively conclude that the ratio of the decay through the $^{12}C(0_2^+)$ + *n* channel in the excited state at around 13.2 MeV in ^{13}C is high compared with the surrounding excitation energy region. However, it is mentioned that the excitation energy obtained from the energy of the recoil ^{12}C has large errors, at least 300 keV, due to the target thickness and some troubles of DSSD. Other details of the experiment and analysis are written in Ref. 3), thoroughly.

In summary, we measured the ratio of the decay branch of the $^{12}C(0_2^+)$ + *n* channel among 3α decay channels in the $^{12}C(^{13}C, 3\alpha n)^{12}C$ reaction using the 129.2 MeV $^{13}C^{4+}$ beam. It was found that the decay ratio of the $^{12}C(0_2^+)$ + *n* channel to other 3α decay channels in the excited state at around 13.2 MeV in ^{13}C was higher than those in the other excitation energy region. In order to obtain the clear conclusion, we have a plan to measure the excitation energy of ^{13}C more precisely.

References

1) Tohsaki A, et al., *Phys. Rev. Lett.* **87** (2001) 192501.
2) Yamada T, and Funaki Y, Phys. Rev. C 92 (2015) 034326.
3) Nasu Y, Master's thesis, Tohoku University (2016).

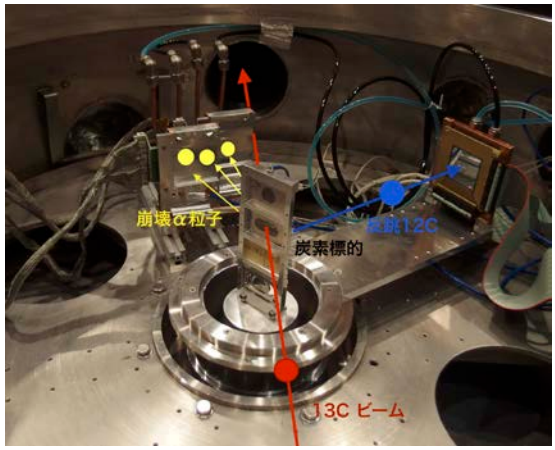

Figure 1. Experimental set-up. The ^{13}C beam comes from the lower side of the picture. The recoil ^{12}C particle was detected in the right side of the DSSD in the picture. Decay-alpha particles were caught in two left-upper DSSDs.

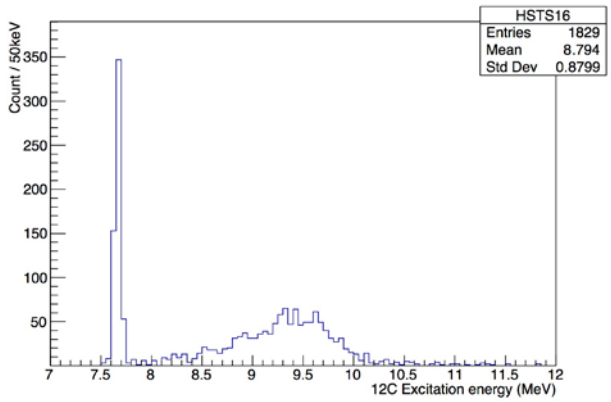

Figure 2. The total energy distribution in the c.m. frame of the 3α system is shown. The energy is added to the 3α threshold energy of 7.27 MeV in ^{12}C.

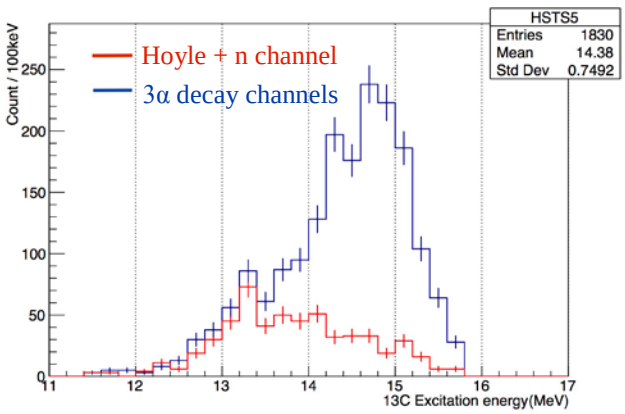

Figure 3. The energy spectra of ^{13}C are shown. The blue histogram shows that obtained from the recoil ^{12}C energy in coincidence with 3α particles. The red histogram show that gated in the Hoyle state + *n* channel.

I. 4. Study of the Alpha Cluster State in ^{28}Si by the Inversed Kinematic Method

Itoh M., Okamoto J., Matsuda Y., Ishibashi Y., Karasudani K., Kasamatsu K., and Ishida S.

Cyclotron and Radioisotope Center, Tohoku University

The clustering phenomena is one of the common features in many-body systems. In the nuclear clustering, the alpha cluster structure often appears in various light nuclei due to the high binding energy of the alpha particle. The alpha cluster states also affect the nucleosynthesis in the stellar evolution. For example, the process of the carbon creation strongly depends on the structure of the second excited state in ^{12}C, which is considered to be a dilute 3-α gas-like structure and called the Hoyle state. The ^{12}C nucleus is produced by the two-step process via the Hoyle state as $\alpha + \alpha \rightarrow {}^{8}\mathrm{Be}$, ${}^{8}\mathrm{Be} + \alpha \rightarrow {}^{12}\mathrm{C}^{*}(\mathrm{Hoyle}) \rightarrow {}^{12}\mathrm{C} + 2\gamma$. In this study, we aimed to investigate the ^{24}Mg + α structure in ^{28}Si. The ^{28}Si has various cluster structures such as ^{24}Mg + α, ^{12}C + ^{16}O, and ^{20}Ne + ^{8}Be. Among them, the ^{24}Mg + α cluster has two types of configurations. One is the configuration of the prolate shape, in which an α cluster is located to the position along the major axis of the prolate ^{24}Mg cluster. The other is that of the oblate shape, in which an α cluster is placed to the position along the minor axis of the ^{24}Mg cluster. The ground state of ^{28}Si is considered to have the duality of the oblate deformed mean-field structure and cluster structures as the ^{24}Mg + α and ^{20}Ne + ^{8}Be configuration[1]. Therefore, states excited by inelastic scattering are mainly the oblate type of ^{24}Mg + α cluster states. In this experiment, we try to determine J^{π} values of ^{24}Mg + α cluster states by measuring the angular correlation function for the α decay in the ^{12}C(^{28}Si, α^{12}C)^{24}Mg reaction.

The experiment was performed at the 41 course in CYRIC using the large scattering chamber. The $^{28}Si^{9+}$ ions were produced by the 10 GHz ECR ion source using a quartz (SiO_2) rod[2] and accelerated up to 280 MeV by the 930 AVF cyclotron. The ^{28}Si beam bombarded to a natural carbon foil with a thickness of 50 μg/cm^2 in the scattering chamber. Figure 1 shows the experimental set-up in the scattering chamber. The recoiling ^{12}C and decay α particles

were detected in double-sided silicon detectors with a size of 40 × 40 mm^2 and a thickness of 1000 μm (DSSD1) and with a size of 50×50 mm^2 and a thickness of 1500 μm (DSSD2, DSSD3), respectively. DSSD1 has horizontally and vertically 40 channel strips in each side. To reduce numbers of readout channels, two or three strips were connected into a channel. Total readout channels of DSSD1 were 32 channels. ^{12}C particles were identified using the time of flight method (TOF). In front of DSSD2, DSSD3, aluminum plates with a thickness of 125 μm and plastic scintillators with a thickness of 30 μm were installed in order to stop scattered ^{28}Si and ^{24}Mg particles and to identify the α particle, respectively. Figure 2 shows the typical two-dimensional histogram of the plastic scintillator and DSSD2. α particles are clearly identified in Fig. 2. The accidental coincidence events were neglected, since they were less than 1% compared to the true events extracted using TDC information as shown in Fig. 3. The true region in Fig. 3 was used in the analysis. The angle and energy of the decay ^{24}Mg particle were obtained by the calculation of the kinematics, assuming the detected α particle came from the $^{28}Si^* \rightarrow {}^{24}Mg + \alpha$ decay channel.

Figure 4 shows the excitation energy spectrum of ^{28}Si in coincidence with an α particle in DSSD2 or DSSD3 obtained by the missing mass method calculated from the recoiling ^{12}C energy and angle. The excitation energy over 14 MeV was not covered in this experimental setting. The tail below the $^{24}Mg + \alpha$ breakup threshold energy of 9.9 MeV might come from accidental coincidence events. In order to extract the excitation energy of the $^{24}Mg + \alpha$ cluster state, the excitation energy region was divided into four 1 MeV bins as 10-11, 11-12, 12-13, and 13-14 MeV. To determine the J^π value of the state, the angular correlation of the decay α with respect to the momentum transfer direction will be obtained. The analysis is in progress.

References

1) Y. Chiba, Y. Taniguchi, and M. Kimura, Phys. Rev. C **95** (2017) 044328.
2) J. Okamoto et al, *CYRIC Annual Report 2014-2015* (2016) 23.

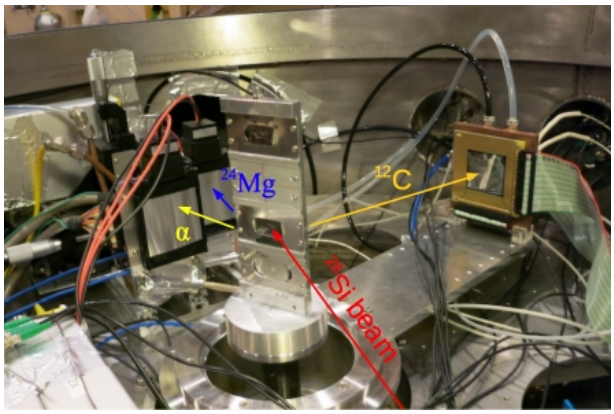

Figure 1. Experimental set-up.

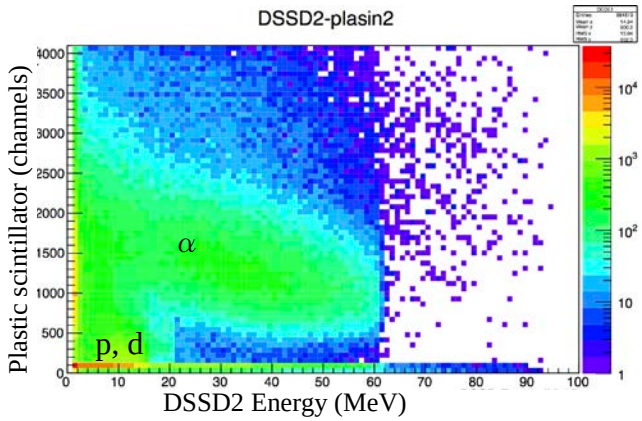

Figure 2. Two-dimensional histogram of ADC channels of the plastic scintillator and energy obtained by DSSD2.

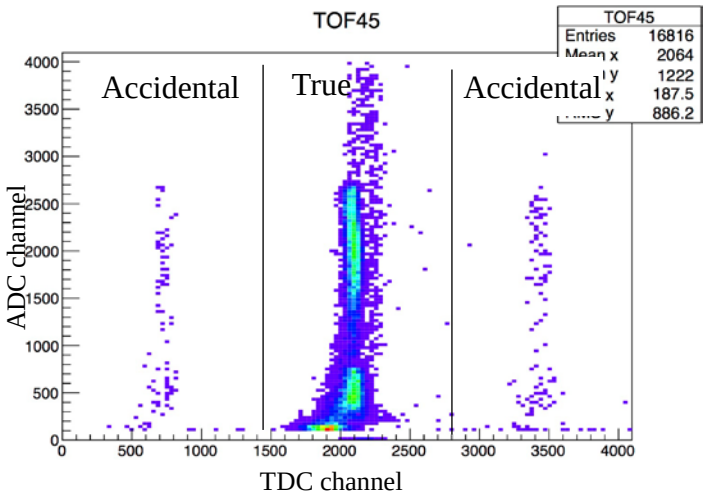

Figure 3. The TOF spectrum for DSSD2

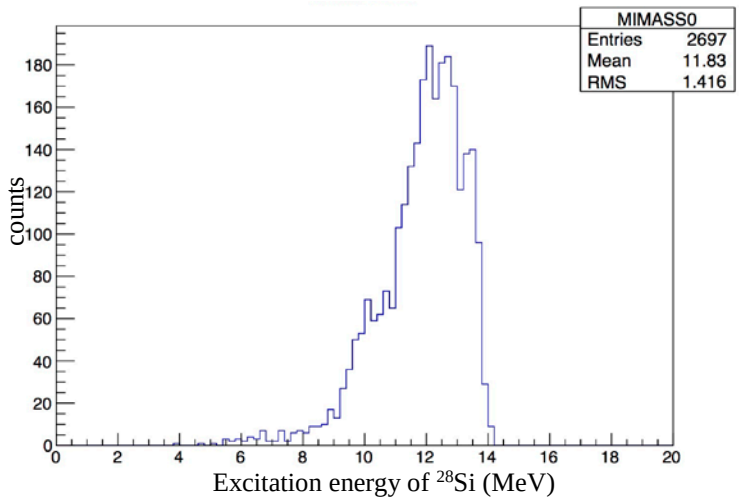

Figure 4. Excitation energy spectrum of ^{28}Si

I. 5. Extraction Time of Francium Ion Produced via a Nuclear Fusion Reaction from a Gold Surface

Kawamura H.[1,2], Ito S.[2], Dammalapati U.[2], Harada K.[2], Inoue T.[1,2], Itoh M.[2], Sakamoto K.[2], Tanaka K. S.[2], Uchiyama A.[2], Yoshioka R.[2], and Sakemi Y.[3]

[1]Frontier Research Institute for Interdisciplinary Sciences (FRIS), Tohoku University
[2]Cyclotron and Radioisotope Center, Tohoku University
[3]Center for Nuclear Study, The University of Tokyo

Experimental research is ongoing toward tests of fundamental symmetries in physics. Francium (Fr) is produced via a nuclear fusion evaporation reaction between oxygen and gold, and Fr ion can be produced through a thermal ionization on the surface of a hot gold target. Since it is empirically known that Fr ion yield depends on the temperature of the gold target, our apparatus includes a heater to heat the target. In 2011, Sakemi et al. reported that the Fr ion yield drastically increased a hundredfold after the melting of the gold target[1)]. In 2012, Hayamizu reported that the degree of increase by melting the target was about threefold, and the ion yield was different in rising or falling temperature even though the temperature was the same[2,3)]. In 2015, Arikawa reported that the drastic increase from the target melting was not observed, and the ion yield was maximized when the temperature was falling from high temperatures[4)]. In this method, the production process of Fr ion relates closely to the property of the gold surface. It is considered that such conflicting results occurred because the surface condition of the surface is easily varied by various causes. The extraction time of ion from the target was investigated as it might affect an increase or decrease of Fr ion yield[5)]. The extraction time of radioactive isotopes was often reported as a diffusion time in a metal target[6,7)].

Fr ion is produced in the following process. First, an oxygen beam ($^{18}O^{5+}$) with 100 MeV of total energy enters into the gold target (^{197}Au), and gradually loses its energy. ^{210}Fr and ^{211}Fr are produced when the oxygen beam energy is around 80–100 MeV[8,9)]. At about 8 μm of depth below the surface, the oxygen energy is less than 75 MeV and Fr is not produced. At about 30 micron of the depth, the oxygen beam stops. Since the oxygen beam irradiates the gold target at a 45-degree angle, the effective depth for Fr is $1/\sqrt{2}$ times deeper.

Therefore, the produced Fr is found in approximately Gaussian distribution at a mean depth of 3 μm from the target surface with a standard deviation of 1 μm. Next, the Fr diffuses in the gold target, arrives at the surface, and finally desorbs to vacuum. When Fr desorbs, Fr becomes a positive ion because the ionization potential of Fr is smaller than the work function of the gold surface. The ionized Fr is accelerated and shaped as a beam by applying electrostatic fields. Thus, it takes the produced Fr a finite extraction time to become an ion beam. Since Fr is a radioactive element, Fr will decay before the desorption if the extraction time is too long. If the temperature of the gold target is higher, the diffusion speed gets higher, the extraction time gets shorter, and the ion yield might increase. The extraction time was measured at different target temperatures.

The ion extraction time was measured as follows. Before the fact, the oxygen beam was stopped by a beam shutter. Then, at time $t = 0$, the shutter opened and the beam irradiation of the target started. Now, a Fr beam was produced and arrived at a beam monitor. This beam monitor was a silicon semiconductor detector to monitor the Fr ion beam by counting α particles emitted from Fr. The time evolution of the α counting by the monitor is shown in Fig. 1. As can be seen from Fig. 1, the significant counts started at $t = t_{\mathrm{A}}$. This time t_{A} includes the time of Fr production by the nuclear fusion reaction and the time of the flight of the oxygen beam and the francium beam, but they are negligibly short. Hence, t_{A} was dominated by the time that the produced Fr diffused and desorbed. The following equation was fitted to the time evolution $N(t)$ of the α counting, and t_{A} was derived:

$$N(t) \propto \begin{cases} R(t) & \text{for } t < t_A \\ R(t) + f(1 - e^{-\lambda(t - t_A)}) & \text{for } t \geq t_A \end{cases}$$

Here, $R(t)$ indicates residual components of Fr previously supplied, f indicates the Fr beam intensity, and λ indicates the decay constant of Fr. Fitting parameters are not only t_{A} but also f and λ. It was confirmed that λ was constant as it did not depend on the target temperature and roughly corresponded to literature data. The temperature of the gold target increased from the oxygen beam irradiation, but it needed a finite time to saturate the temperature rising. During the time t_{A}, the rising range was less than $50^{\mathrm{o}}\mathrm{C}$ which was sufficiently small compared to the temperature range of the measurement.

The measurement results of the ion extraction time are shown in Figs. 2 and 3. Figure 2 shows data for ^{210}Fr and ^{211}Fr, and Fig. 3 shows data for ^{209}Fr. The ^{210}Fr and ^{211}Fr were not able to be separated because of the detector's resolution. The extraction time is clearly small when the target temperature is higher. It seems that there is hysteresis between the situations

in rising temperature and falling temperature. This result suggests the probability that the temperature change affects the property of bulk as well as the surface of the gold target. The result of ^{209}Fr differs from the result of ^{210}Fr and ^{211}Fr in the context of the value of the extraction time and the behavior to the temperature change. Compared to ^{210}Fr and ^{211}Fr, ^{209}Fr is produced with a higher energy of the oxygen beam and at a shallower production depth. The production depth will affect the extraction time. In addition, the half-life of ^{209}Fr ($t_{1/2} = 50.0$ s) is different from that of ^{210}Fr ($t_{1/2} = 190.8$ s) and ^{211}Fr ($t_{1/2} = 186$ s). There is a possibility that the effect of the different lifetimes was not considered in the data analysis. Besides, the error tends to be large for shorter extraction times because of the properties of the measurement and analysis method. The statistical error of ^{209}Fr was larger because its ion yield was lower than that of ^{210}Fr. The measured extraction time is smaller than the lifetime of the Fr isotopes and should not affect the ion yield very much. The experimental results implied that the length of the extraction time is not an essential factor in increasing and decreasing the Fr ion yield.

The yield of Fr ion is an essential parameter to perform the test experiments of fundamental symmetries with higher precision. Subsequent development is required for increasing the ion yield.

References

1) Sakemi Y, Harada K, Hayamizu T, et al., *J. Phys.: Conf. Ser.* **302** (2011) 012051.
2) Hayamizu T, "Development of a slow francium beam for a search for the electron EDM" (in Japanese), Master's thesis, Tohoku University (2012).
3) Kawamura H, Aoki T, Arikawa H, et al., *Hyperfine Interact* **214** (2013) 133.
4) Arikawa H., "The development of the high purity francium beam toward the search for the violation of the fundamental symmetry" (in Japanese), Master's thesis, Tohoku University (2015).
5) Ito S, "Production of francium beam through the surface ionization toward a search for the permanent electric dipole moment of the electron" (in Japanese), Master's thesis, Tohoku University (2018).
6) Melconian D, Trinczek M, Gorelov A, et al., *Nucl. Instrum. Meth. A* **538** (2005) 93.
7) de Mauro C, Calabrese R, Corradi L, et al., *Phys. Rev. A* **78** (2008) 063415.
8) Corradi L, Behera BR, Fioretto E, et al., *Phys. Rev. C* **71** (2005) 014609.
9) Stancari G, Veronesi S, Corradi L, et al., *Nucl. Instrum. Meth. A* **557** (2006) 390.

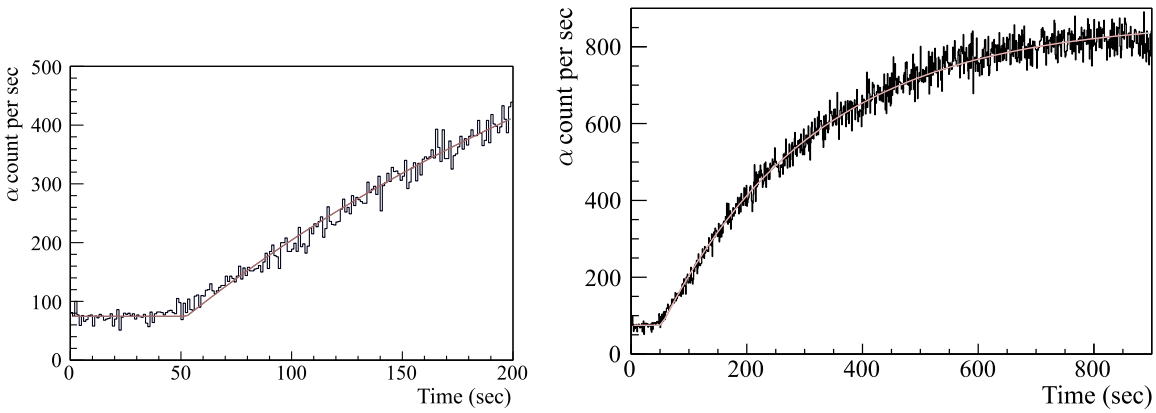

Figure 1. Typical result of the time evolution of the α counting. (Left) Time $t = 0$ to 200 sec. The counts are significantly rising up at around $t = 50$ sec. (Right) Time $t = 0$ to 900 sec for the same data.

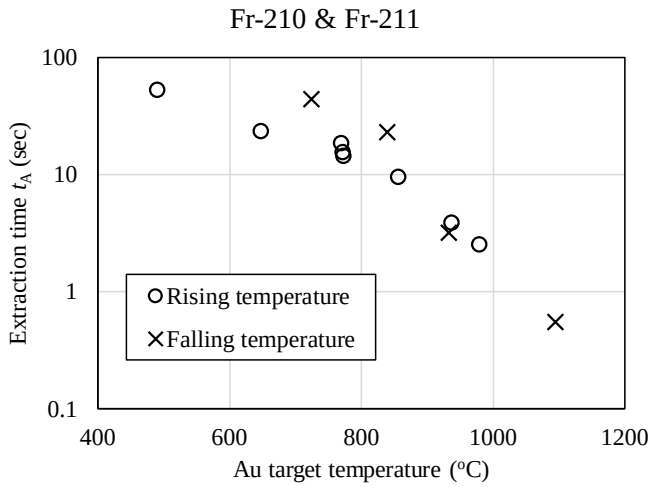

Figure 2. Preliminary result of the extraction time for the system of ^{210}Fr and ^{211}Fr.

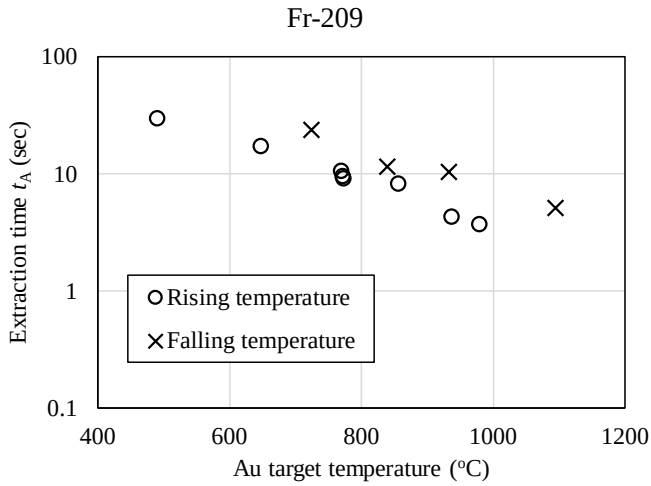

Figure 3. Preliminary result of the extraction time of the system of ^{209}Fr.

I. 6. New Student Experiment: Observation of Isobaric Analog States via the (*p*,*n*) Reactions at 30 MeV

Miki K.[1], Shibuya S.[1], Watanabe M.[1], Sakai D.[1], Matsuda Y.[2], Tanaka K. S.[2], Itoh M.[2], Kawahara K.[1], Maeda K.[1], Mukai T.[1], Nakai S.[1], Sekiguchi K.[1], and Watanabe A.[1]

[1]Department of Physics, School of Science, Tohoku University
[2]Cyclotron and Radioisotope Center, Tohoku University

Overview — We have developed a new student experiment program for the undergraduate 3rd grade in the department of physics, school of science, Tohoku university. The title of the program is "Nuclear radius and charge-symmetry studied with the charge-exchange nuclear reaction". In this program, the students run the measurements of the (*p*,*n*) reaction at the incident proton energy of 30 MeV and observe the peak of the isobaric analog state (IAS). From its excitation energy, the students can discuss the basic nuclear properties, such as the radius of the target nuclei and the charge-symmetry of the nuclear structure. This program provides the students with a full experience of nuclear physics experiment including the planning, the conducting of the accelerator experiment, the data analysis, and the presenting of their achievements.

Experiment — The experiment was performed at the 32 course in the CYRIC (Fig. 1). The proton beam was accelerated up to 30 MeV by the 930 cyclotron and impinged on the targets. The unreacted beam was bent away by the sweeper dipole magnet and transported to the beam dump, where the beam charge was integrated by the Faraday cup. The neutrons scattered at the 0 degrees from the target were detected by a pair of NE213 liquid scintillation detectors installed at 7.5 m away from the target. Each detector covered the solid angle of 5 msr. The background gamma-ray signals were distinguished from neutron signals and rejected by the pulse-shape discrimination capability of the NE213 scintillator. The energy of the neutron was determined from its time of flight, and the excitation energy of the target nucleus was obtained by means of the missing-mass method. The excitation energy spectra of the (*p*,*n*) reactions were obtained for the four kinds of targets: ^{27}Al (27 mg/cm^2), ^{nat}Cu (27 mg/cm^2), ^{nat}Ag (31 mg/cm^2), and ^{197}Au (39 mg/cm^2). For each target, a

strong peak was found in the neutron spectrum, which was attributed to the IAS.

Discussion — From the obtained spectra, the students determined the excitation energies of the IAS (E_{IAS}) for each target nuclei. The E_{IAS} corresponds to the difference of the Coulomb energy between the mother and daughter nuclei and it is related to the nuclear radius. The students determined the radius of target nuclei and investigated its mass-number dependence. They also discussed the reasons of the difference in the strengths of the IAS peaks for various targets, considering the isospin structure of the target nuclei.

Response from students — This program was conducted for two times in October and November in 2017, and accepted 6 students for each time. Although 12 students in total could be accepted in this program, the number of students who applied for this program was 23. This implies that this program sounded very attractive to many young students. It is also emphasized that about a half of students who took this program applied for experimental nuclear physics groups for their laboratory assignment in the 4th grade. This indicates that this program successfully motivate the students to join the nuclear science region.

Acknowledgments — The authors appreciate the efforts of the CYRIC staffs for providing high quality stable beam and also for cooperating on this educational project very willingly. They also thank the staffs in the ELPH facility for lending them the liquid scintillation detectors.

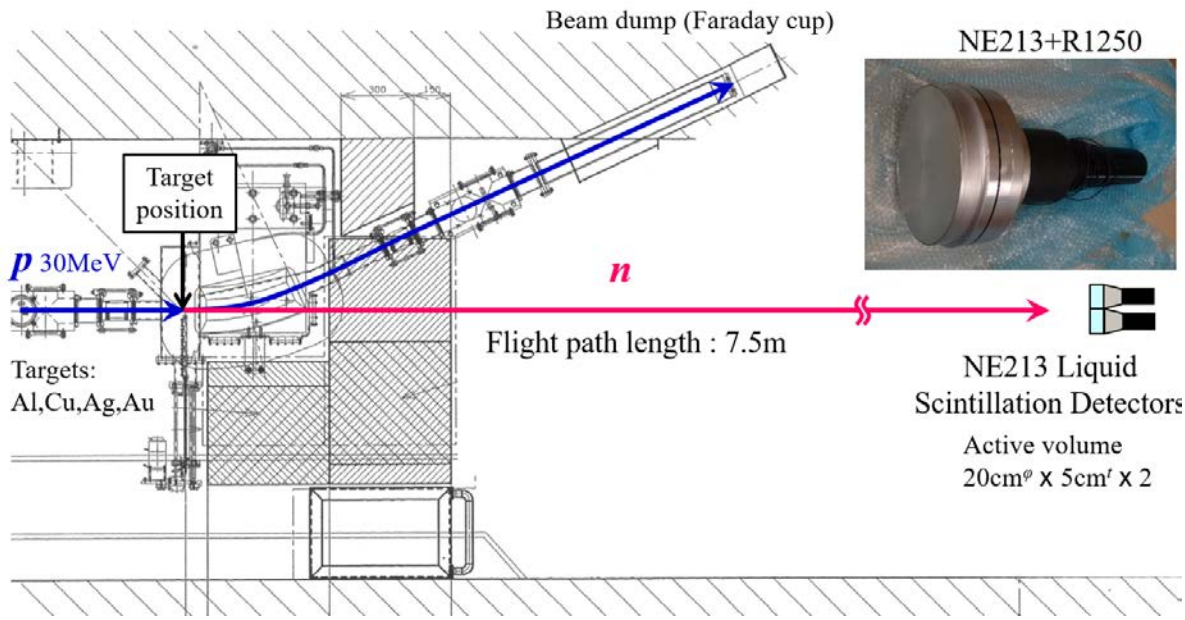

Figure 1. Layout of the experimental setup at the 32 course. The proton beam impinged on the target, and the scattered neutrons were detected by a pair of liquid scintillation detectors installed at 7.5 m away from the target.

I. 7. Fifth Training School on Nuclear and Particle Physics Experiments Using Accelerator Beams

Kawamura H.[1,2], Tanaka S. K.[2], Ishikawa T.[3], Muto T.[3], Tamura H.[4], and CYRIC Physics Group[2]

[1]Frontier Research Institute for Interdisciplinary Sciences (FRIS), Tohoku University
[2]Cyclotron and Radioisotope Center, Tohoku University
[3]Research Center for Electron Photon Science, Tohoku University
[4]Department of Physics, Tohoku University

Under the support program of KEK (High Energy Accelerator Research Organization)[1)], the fifth training school was held on nuclear and particle physics experiments using accelerator beams[2)] at Tohoku University in February 2017. The purpose of this school was to foster human resources to support Japanese accelerator sciences, which are preeminent in the world. The target was to let undergraduates in Japan consider accelerator sciences as a career path, by experiencing accelerator experiments and by deepening the understanding of sciences such as nuclear and particle physics, beam physics, and accelerator physics. Ten undergraduate students from eight universities (Fukuoka University, Kitasato University, Saitama University, Shizuoka University of Science and Technology, Tokyo University of Science, University of Toyama, Ochanomizu University, and Rikkyo University) participated in the school. The implementation period lasted six days. The first part and the last part of the school were organized at CYRIC and ELPH (Research Center for Electron Photon Science), respectively.

The experimental theme in CYRIC was “Experiments in a low-velocity electrostatic beam line” and included four practice themes: (1) Production of radioactive francium isotopes through a nuclear fusion evaporation reaction, with a gold target and oxygen beam supplied from 930-AVF cyclotron. (2) Transportation of an ion beam produced with a surface ionizer. (3) Alpha-ray spectroscopy of checking source ^{241}Am with silicon semiconductor detector. (4) Simulation evaluation of the nuclear fusion evaporation reaction with PACE4 fusion-evaporation code. These practice works were mainly performed using a francium-dedicated experimental apparatuses group[3)], which are

developed by the Fr EDM collaboration at CYRIC. The students were split into three teams, and rotated each theme. Each theme had typically one academic staff and one teaching assistant.

In ELPH, the students performed two experimental themes: “Beam of an electron accelerator”; and “Measurement of the momentum and time of flight of positrons”, with the electron synchrotron accelerator.

According to the results of a questionnaire handed out after the school ended, the practical experiments were received well by the students, and motivated them to consider the career path. Some of the students, especially science-conscious ones, said that they would participate in the school even if there was no financial support for the travel costs (although the organizer subsidized a large part of the travel costs required for participation). These opinions show the ability of the practical experiments to amuse while treating the real accelerators.

The results of this and past schools are beginning to show a fostering of human resources to support Japanese accelerator sciences[4)]. Some of the students participating in earlier schools entered the doctoral course. Most of the participating students hope to continue at the school. In the future, this school, or the same workshop, will continue to be required for supporting the accelerator sciences.

References

1) KEK Support Program, https://www.kek.jp/en/ForResearcher/SupportProgram/
2) Official website of the 5th training school on nuclear and particle physics experiments using accelerator beams, http://inst.cyric.tohoku.ac.jp/~sakemi/cyric2016.html
3) Kawamura H, Ando S, Aoki T, et al., *Review of Scientific Instruments* **87** (2016) 02B921.
4) Kawamura H, Inoue T, *Daigaku no Butsuri Kyouiku* **23** (2017) 167.

II. NUCLEAR INSTRUMENTATION

II. 1. Upgrade of an Extraction System for Highly Intense Beams from 10 GHz ECR Ion Source

Matsuda Y.[1], Kasamatsu K.[1], Itoh M.[1], Ishibashi Y.[1], Okamoto J.[1], Karasudani K.[1], Ishida S.[1], Takahashi N.[2], Takahashi K.[2], Suzuki J.[2], Honma T.[2], and Akashige Y.[2]

[1]Cyclotron and Radioisotope center, Tohoku University
[2]SHI Accelerator Service

The 930 AVF cyclotron accelerator provides various ion beams with three external ion sources in CYRIC. ECR1 and another ion source supply light ions. ECR10 supplies heavy ions up to Xe[1)]. In addition to the variety, it is also important to provide the beam over a wide range of the beam intensity. For this purpose, we utilize a biased disk method[2)] and a support gas method[3)] for ECR10. For further increase of the beam intensity, a previous research attempted to upgrade an extraction system of ECR10[4)]. The original extraction system consists of two electrodes: a plasma electrode and a ground electrode. The simple configuration is stable and easy to extract the ions but is difficult to increase the number of ions without an increase of the emittance. Therefore, the previous research added two electrodes between the existing electrodes; one works as an extraction electrode, and the other works as a focusing electrode. These electrodes were connected by ceramic rods. Unfortunately, the extraction system could not work continuously because the extracted ions and the secondary particles collided the ceramic rods directly and the insulation resistance immediately decreased. Here we report a modification of the extraction system.

Figure 1 shows the modified extraction system. The ceramic rods are placed away from the beam axis. The electrodes are made of SUS316. The extraction electrode, the focusing electrode, and the ground electrode are designed to block the path of particles toward the ceramic rods. The details and the layout were determined with IGUN[5)], which can simulate extraction of positive ions from ion sources. After installing the system, we confirmed that we could apply about ±5 kV and +5 kV to the extraction electrode and the focusing electrode with respective to the ground electrode, respectively. A higher voltage than the above value triggered discharge or fluctuation of the voltage.

In order to demonstrate the practicality of the extraction system, we extracted ^{16}O ions. Figure 2 shows the experimental setup. The extracted ions are analyzed by a bending magnet and a slit. The current is measured with a Faraday cup. Because the distance between ECR10 and the glazer magnet is more than 1 m and focusing elements are not enough, the emittance of the beam becomes large due to its space charge. Therefore, we will evaluate the effect of the extraction system after an upgrade of the beam line in the future. The test was done for a few days. During the test, a decrease of the insulation resistance was not observed. Figure 3 shows the measured beam current as a function of the mass number to charge ratio. The maximum beam current of $^{16}O^{5+}$ was about 80 μA, which is the almost same as the maximum current with the original extraction system (about 90 μA).

After the demonstration, ECR10 has supplied various ions ($^{12}C^{4+}$, $^{15}N^{3+}$, $^{16}O^{5+}$, $^{18}O^{5+}$, $^{20}Ne^{4+}$, $^{40}Ar^{8+}$, $^{84}Kr^{17+}$, and $^{129}Xe^{25+}$) with the extraction system. These beam currents were the same as those with the original extraction system. During the operation, no maintenance has been performed since it is very difficult to uninstall the extraction system. Therefore, the electrodes have been shaved gradually and substances have attached to the ceramic rods. Finally, the insulation resistance between the focusing electrode and the ground electrode decreased by one order of magnitude. Now the extraction system is under maintenance. The total operating time was more than 500 hours.

In summary, in order to increase the beam intensity from the 930 AVF cyclotron accelerator, we are upgrading an extraction system of ECR10. We solved a problem of insulation resistance of ceramic rods by modifying shape of three electrodes. By using the extraction system, we have supplied various ions to CYRIC users. The currents were the same as those with the original extraction system. In the future, we will evaluate the effect of the extraction system by upgrading the beam line. In addition, we will improve a method to uninstall the extraction system for maintenance.

References

1) Nakagawa T., Jpn. J. Appl. Phys., **30** (1991) L930; Wakui T., et al., *CYRIC Annual Report* **2010-2011** 31.
2) Melin G. et al., *Proc. 10th Int. Workshop on ECR Ion Sources,* (1990) 1; Nakagawa T., Jpn. J. Appl. Phys., **30** (1991) L1588.
3) A. G. Drentje, *Nucl. Instrum. Methods Phys. Res. B* **9** (1985) 526; Wakui T., et al., *CYRIC Annual Report* **2012-2013** 45.
4) Shimbara Y., et al., *CYRIC Annual Report* **2012-2013** 51.
5) Becker R., Herrmannsfeldt WB., *Rev. Sci. Instrum.* **63 (1992)** 2756.

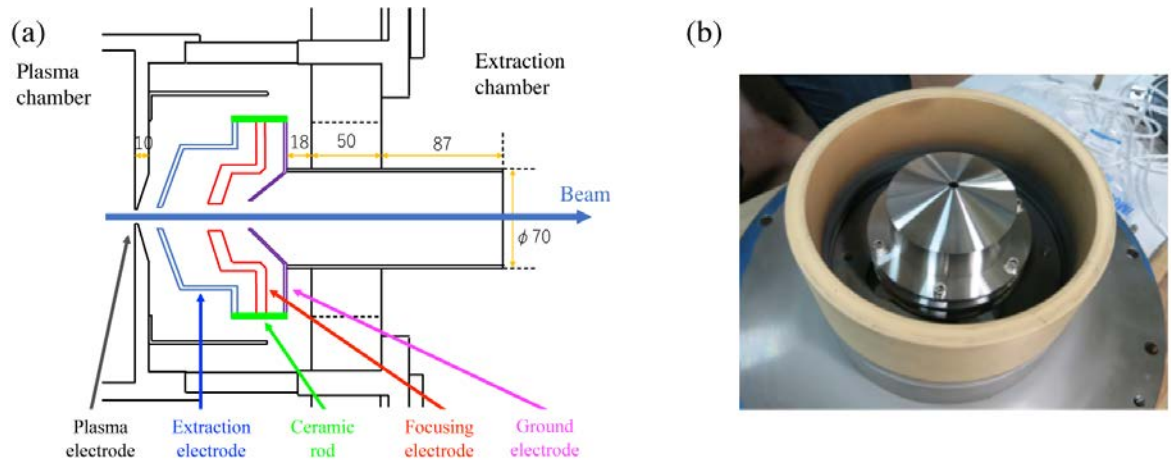

Figure 1. Schematic view (a) and picture (b) of the modified extraction system.

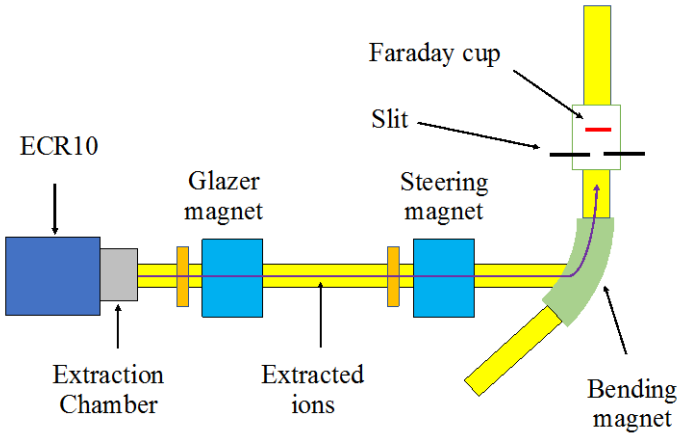

Figure 2. Experimental setup.

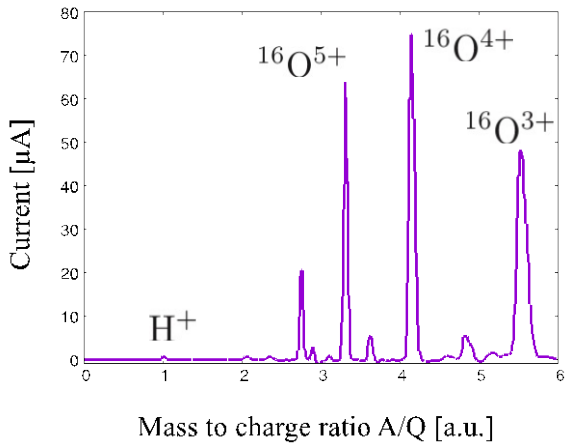

Figure 3. Beam current as a function of the mass number to charge ratio.

II. 2. Development of a Gas Scintillation Counter for RI Beams

Ishida S.[1], Matsuda Y.[1], Itoh M.[1], Ishibashi Y.[1], Okamoto J.[1], Karasudani K.[1], Kasamatsu K.[1], Zenihiro J.[2], Harada T.[3], Sakaguchi H.[4], Terashima S.[5], Ota S.[6], and Dozono M.[6]

[1]Cyclotron and Radioisotope Center, Tohoku University
[2]RIKEN Nishina Center
[3]Toho University
[4]Reserch Center for Nuclear Physics, Osaka University
[5]Beihang University
[6]Center for Nuclear Study, Tokyo University

In many experiments with RI beams, the identification of the beam particles should be performed. A plastic scintillator is often used as a time of flight (TOF) counter. The required specification is constant timing of the signal, constant intrinsic time resolution, fast decay time to identify the particles in highly intense RI beams and 100% detection efficiency. However, due to the radiation damages, the number of photons from the plastic scintillator gradually decreases. In order to solve the problem, we have developed a gas scintillation counter. The gas scintillation counter can ignore the radiation damage by flowing the gas continuously. Since outgas from the counter decreases the number of photons, it is important to flow the gas in this sense. As a counter gas, pure rare gas such as Xe gas is the best since the energy to produce a scintillation photon is lower than that of the plastic scintillator and the decay time is as fast as that of the plastic scintillator. However, the cost of pure Xe gas is high and the gas handling is difficult. Therefore, we investigated another candidate which is cheap and easy to handle the gas.

We can identify the heavy ions by measuring the TOF, the energy loss, and the magnetic rigidity. The resolution of the mass number is written as,

$$\left(\frac{\sigma A}{A}\right)^2 = \left(\gamma^2 \frac{\sigma\beta}{\beta}\right)^2 + \left(\frac{\sigma B\rho}{B\rho}\right)^2 + \left(\frac{\sigma Z}{Z}\right)^2,$$

where A is the mass number, γ is the Lorentz factor, Z is the atomic number, β is the velocity, and $B\rho$ is the magnetic rigidity. In case of experiments with Big-RIPS in RIKEN-RIBF, the TOF resolution has to be less than 225 ps in order to identify 300 MeV/u ^{132}Sn.

The experiment was performed at the 33 course in CYRIC. The picture of the experimental

setup is shown in Fig. 1. Two gas scintillation counters (Gas1, Gas2) and two plastic scintillators (*ΔE*, *E*) were irradiated with a 19.3 MeV/u ^{14}N beam accelerated by the 930 AVF cyclotron. Energy loses in each detector are shown in Table 1. The size of the gas volume is 50 mm (H) × 65 mm (V) × 55 mm (D). The thicknesses of *ΔE* and *E* are 30 μm and 1.0 mm, respectively. In this experiment, we flew pure Xe gas, pure Ar gas, pure Kr gas and pure N_2 gas at a pressure of 1 atm in the gas volume. In addition, N_2 gas was also mixed with Xe gas to reduce the purity of Xe gas. Two PMTs were directly attached to the left and right sides of the gas volume. For Gas1 and Gas2, R6041-406 and R6041-506 were used, respectively. The anode signals from the PMTs are shown in Fig. 2. Since the number of dynodes in left R6041-406 was less than that in right side, the timing between the left side and the right side was different. For Xe-N_2 gas as well as 100% Xe gas and 100% Kr gas, the decay time is less than 20 ns and the signal separates from the noise level completely. The decay time of 100% N_2 gas is also fast even though the pulse height is not enough for 19.3 MeV/u ^{14}N. N_2 gas also seems to be candidate since the energy loss of 300 MeV/*u* ^{132}Sn in the gas volume is about 50 MeV. The distribution of the time difference between Gas1 and *dE* for 99.6% Xe gas is shown in Fig.3. The spread of each time difference is written as,

$$\sigma T_{dE-Gas1}^2 = \sigma T_{dE}^2 + \sigma T_{Gas1}^2,$$
$$\sigma T_{dE-Gas2}^2 = \sigma T_{dE}^2 + \sigma T_{Gas2,}^2$$
$$\sigma T_{Gas1-Gas2}^2 = \sigma T_{Gas1}^2 + \sigma T_{Gas2}^2 .$$

Threfore, the intrinsic time resolutions are,

$$\sigma T_{Gas1}^2 = \frac{(\sigma T_{dE-Gas1}^2 + \sigma T_{dE-Gas2}^2 + \sigma T_{Gas1-Gas2}^2)}{2} - \sigma T_{dE-Gas2}^2,$$
$$\sigma T_{Gas2}^2 = \frac{(\sigma T_{dE-Gas1}^2 + \sigma T_{dE-Gas2}^2 + \sigma T_{Gas1-Gas2}^2)}{2} - \sigma T_{dE-Gas1}^2.$$

The intrinsic time resolutions are shown in Table 2. Here, we ignore the time jitter of the PMT since the intrinsic time resolution is considered to be larger than the time jitter.

Figure 4 shows the resolution of mass number as a function of TOF resolution. The TOF resolution for 99.6% Xe gas is less than 225 ps, which corresponds to 5σ resolution for 300 MeV/*u* ^{132}Sn. The difference of the resolution between 100% Xe gas and 99.6% Xe gas is about 0.03. This result shows that it is possible to identify the particle around A~100 with Xe-N_2 gas.

In summary, we measured number of photons, decay time of scintillation lights, and intrinsic time resolution for 100% Xe gas, 100% Kr gas, 100% Ar gas, 100% N_2 gas and Xe-N_2 gas.

These quantities of Xe-N_2 gas as well as 100% Xe gas and 100% Kr gas are enough to identify 300 MeV/u ^{132}Sn in highly intense RI beams. N_2 gas also seems to be candidate even though the pulse height is smaller than that of 100% Xe gas.

Table 1. Energy loss in each detector.

Detector	pla(30 μm)	gas					pla(1.0 mm)
		Xe 100%	Kr 100%	Ar 100%	N_2 100%	Xe 99.6%	
Energy loss	15.0 MeV	29.4 MeV	24.0 MeV	18.3 MeV	14.0 MeV	29.3 MeV	9.72 MeV

Table 2. Intrinsic time resolution.

Resolution[ps]	Xe 99.6%	Kr 100%	Xe 100%
dE	70 ± 100	50 ± 200	90 ± 60
Gas1	200 ± 40	270 ± 40	170 ± 30
Gas2	230 ± 30	360 ± 30	170 ± 30

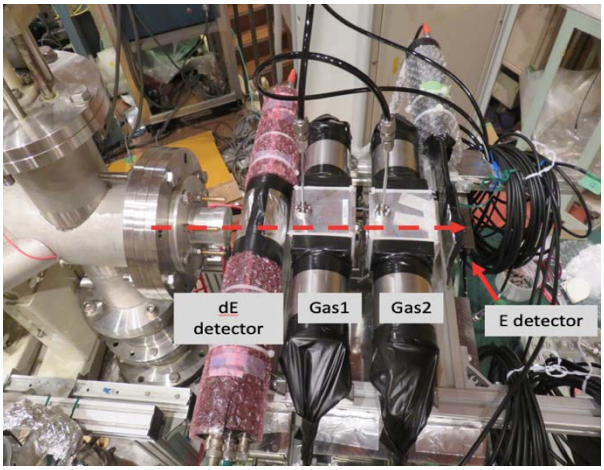

Figure 1. Experimental setup.

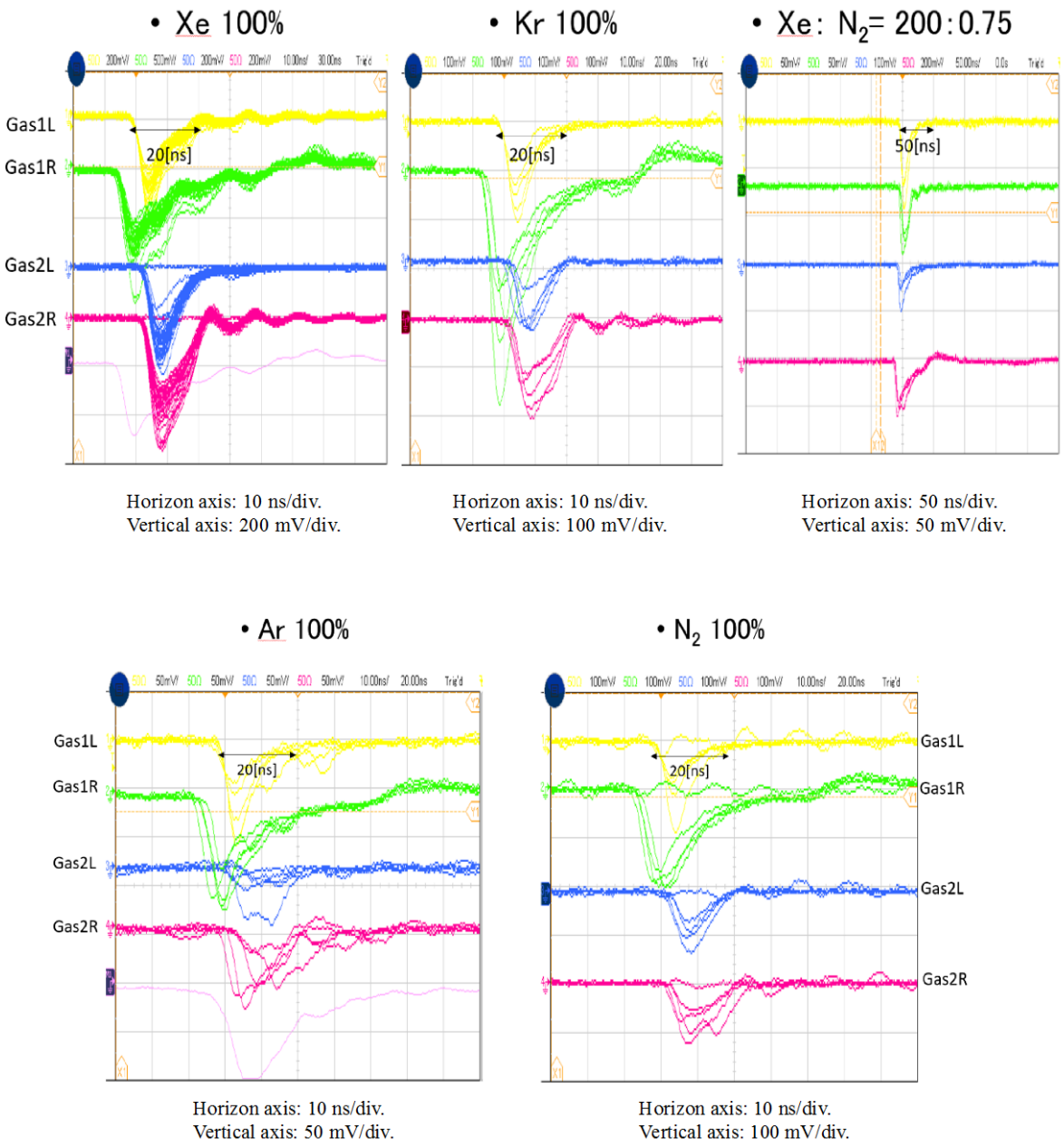

Figure 2. Output signals from PMTs.

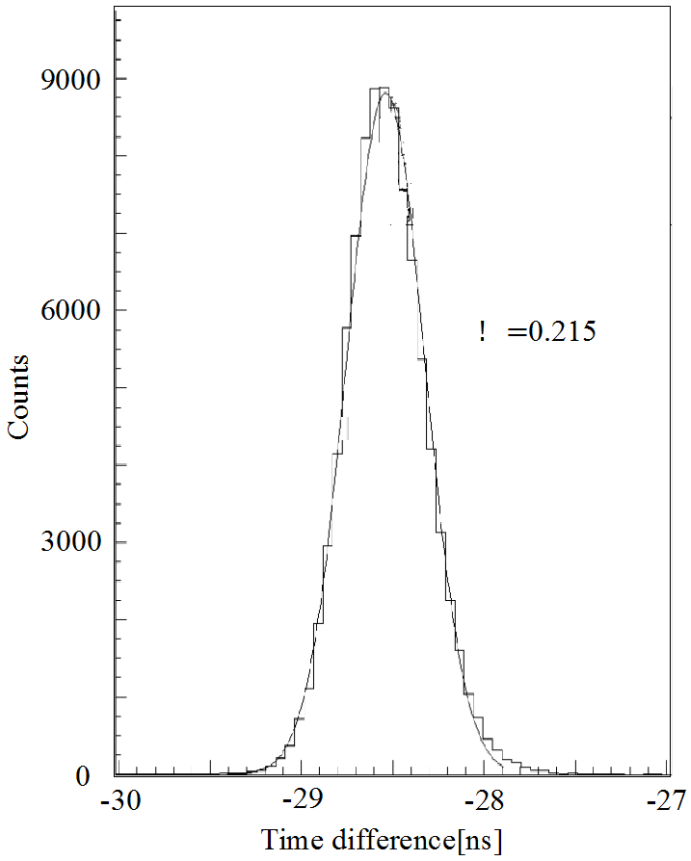

Figure 3. Time difference between Gas1 and dE for 99.6% Xe gas.

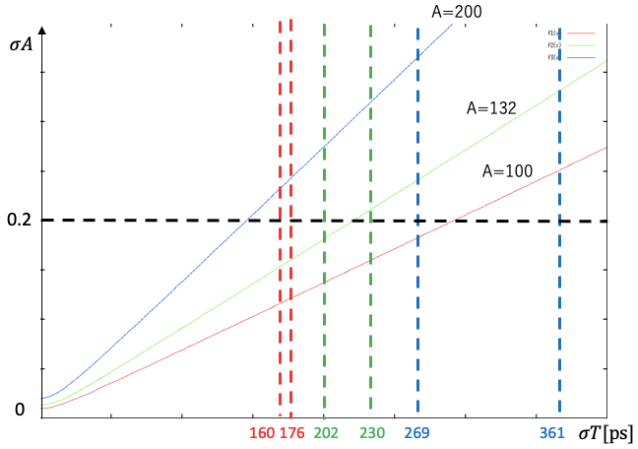

Figure 4. Relation between resolution of mass number and resolution of TOF. Red line:*A*=100, green line: *A* =132, blue line: *A* =200, red broken lines: intrinsic time resolutions of gas1 and gas2 for Xe 100%, green broken line: intrinsic time resolutions of gas1 & gas2 in Xe 99.6%, blue broken line: intrinsic time resolutions of gas1 & gas2 in Kr 100%, black broken line: 5σ resolution of mass number.

II. 3. Performance Test of Low-pressure MWDC with 1/3-Cell Staggered Layers

Nishi T.[1], Matsumoto S.Y.[1,2], Fujioka H.[2], Itahashi K.[1], Kawabata T.[1], Matsuda Y.[3], Miki K.[4], Miwa M.[1,5], Takaki M.[6], Tanaka Y.K.[7], Uesaka T.[1], Watanabe Y.N.[8], Yako K.[6], and Zenihiro J.[1]

[1]*Nishina Center, RIKEN*
[2]*Department of Physics, Kyoto University*
[3]*Cyclotoron and Radioisotope Center, Tohoku University*
[4]*Department of Physics, Tohoku University*
[5]*Department of Physics, Toho University*
[6]*Center for Nuclear Study, University of Tokyo*
[7]*GSI Helmholtzzentrum für Schwerionenforschung GmbH*
[8]*Department of Physics, The University of Tokyo*

In December 2017, we conducted a performance test for a new low-pressure multi-wire drift chamber (MWDC) using proton beams to evaluate tracking resolution and efficiency, as well as their stability under a high-rate beam condition. In this paper, we report the current status of the analysis.

The MWDC is developed as a tracking detector mainly for two experiments of missing mass spectroscopy: a precise measurement of deeply bound pionic atoms via the (d, ^{3}He) reaction (piAF)[1)] and a search for double Gamow-Teller giant resonance via the (^{12}C, ^{12}Be) reaction (DGTGR)[2)]. In these experiments, the tracking detector is required (1) to detect light ions under a high-rate background condition (an order of MHz triton in the DGTGR experiment and proton in the piAF experiment) and (2) to achieve high resolution for the precise spectroscopy.

For these purposes, we designed and constructed new MWDCs with two features, use of low-pressure gas and plane configuration of 1/3-cell staggered layers. First, the new MWDCs are operated with low-pressure (~0.1 atm) gas to set in vacuum[3)]. In the preceding experiment of pionic atom spectroscopy[4)], MWDCs with a gas pressure of 1 atm were operated in air. A vacuum window (50-μm-thick stainless) located up-stream caused multiple scattering. While the intrinsic tracking resolution was found to be ~0.1 mm (FWHM), the effect of multiple scattering resulted in the deterioration of the position

resolution up to 4.1 mm (FWHM) at maximum. This deterioration is suppressed by using the low-pressure MWDC. Another point is a new configuration of planes with sets of 1/3-cell staggered three-layer structures (XX'X"(0°), UU'U"(+30°), VV'V"(-30°)), to obtain a homogeneous position spectrum. A typical MWDC has a set of two layer structures shifted by 1/2 cells and shows a non-negligible inhomogeneity in the spectra originating in an analytic bias in the proximity of both the sense and potential wires. This effect is expected to be exhibited even with an exactly known drift-time to length conversion with a finite resolution, as demonstrated by a simple Monte Carlo simulation[5)] and becomes prominent in extremely high-statistics data. For each set of 1/3-cell staggered layers in the new MWDCs, we use the drift length information of two of the three layers by neglecting the data of the layer where the trajectory is closest to a wire, to avoid the bias in the proximity of wires.

The test experiment was conducted in 1.5 days at the room TR4 in CYRIC, by using primary proton beams of 30 MeV/u. The beam energy was selected to simulate the energy loss of the signal ^{3}He of 120 MeV/u in the pionic atom experiment. The beam was detected and identified by two plastic scintillators at the upstream and downstream of the MWDCs as shown in Fig. 1. MWDC is operated with pure isobutane gas at 13.3 kPa.

Figure 2 shows the evaluated detection efficiency as a function of the voltage applied to cathode planes and potential wires. The red, blue and magenta color corresponds to the single, double, and more than three hits per plane in one event, respectively. As shown in the figure, the single-plane efficiency is greater than 98% with a voltage of higher than -1300 V. The plane resolution and stability under the high-rate condition are also evaluated with voltage of -1350 V. The plane resolutions are evaluated to be 0.27 ~ 0.35 mm (FWHM), which satisfy the experimental requirement. The stability test of the MWDC was performed with ~100 kHz proton beams. The condition is comparable with the expected high-rate background in terms of the space charge effect. Under this severe condition, we confirmed that the detection efficiency and resolution does not change by more than a few percent. A new tracking method using 1/3-cell staggered layers is also analyzed. Though the analysis is still in progress, the preliminary spectrum obtained with 2 of 3 layers shows better homogeneity compared with that with all layers.

From the above results, we found that the new MWDC shows satisfactory performance for our experiments. The precise analysis is ongoing.

References

1) K. Itahashi *et al.*, RIBF Proposal **No.135** (2015).
2) T. Uesaka *et al.*, RIBF Proposal **No.141** (2015).
3) H. Miya *et al.*, Nucl. Instr. Meth. **B 317** (2013) 701.
4) T. Nishi *et al.*, Phys. Rev. Lett. **120** (2018) 152505.
5) Y. K. Tanaka, Ph. D. thesis, Univ. Tokyo (2016) Appendix B.

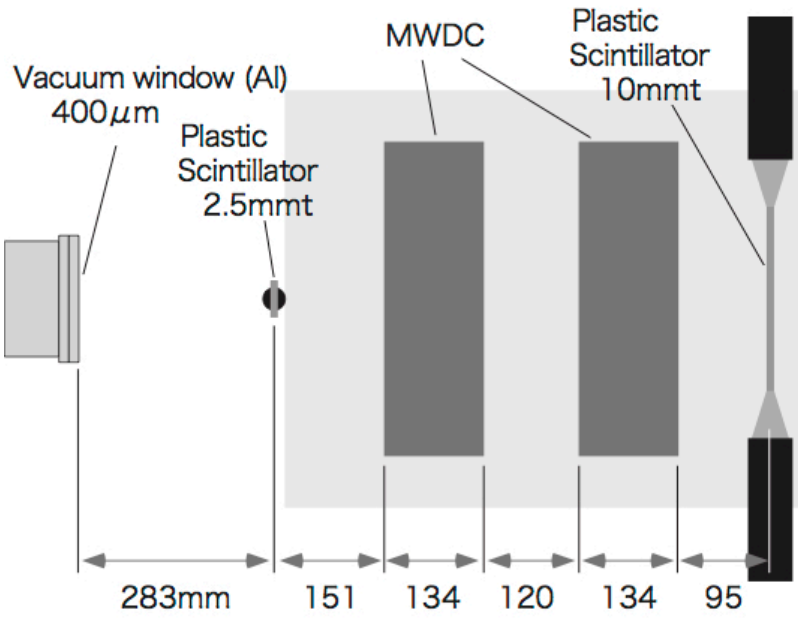

Figure 1. Detector setup on the beam line at room TR4.

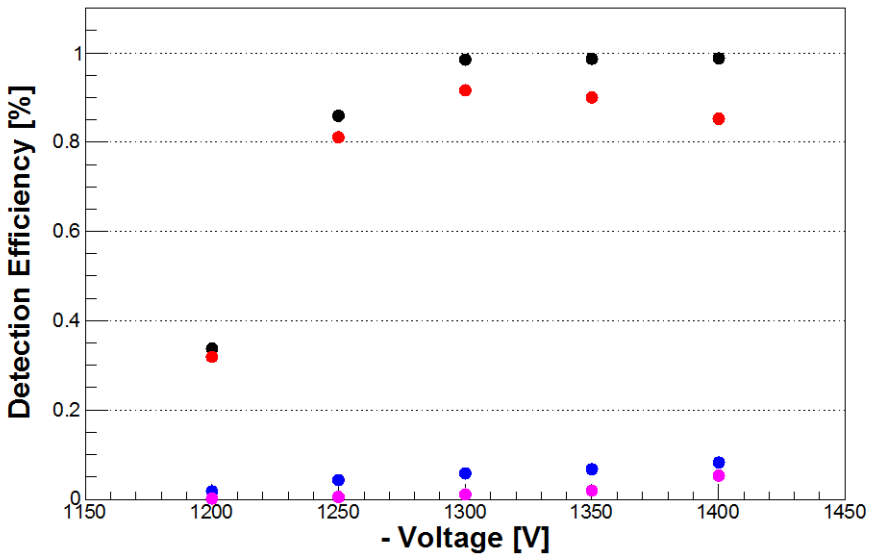

Figure 2. Evaluated detection efficiency of the single plane as a function of voltage for cathode planes and potential wires. The red, blue, and magenta colors correspond to the multiplicity (= number of fired wires par plane) is one, two, and more than three in one event. The black points show the overall efficiency of the plane.

II. 4. Measurement of Liquid Scintillator Properties Using the 70 MeV Quasi-monochromatic Neutron Beam

Furuta H.[1], Hino Y.[1], Bezerra T.J.C.[1], Chauveau E.[1], Kiryu S.[1], Narazaki T.[1], Sharankova R.[2], and Suekane F.[1]

[1]Research Center for Neutrino Science, Tohoku University
[2]Graduate School of Science, Tokyo Institute of Technology

This group is preparing a sterile neutrino experiment, JSNS^2 at J-PARC Materials and Life Science Experimental Facility (MLF)[1)]. The MLF beam line produces $\bar{\nu}_\mu$ in the decay of stopping muon (μ^+). The energy of $\bar{\nu}_\mu$ is E~40 MeV. The JSNS^2 experiment detects $\bar{\nu}_e$ produced by $\bar{\nu}_\mu$ oscillation at a baseline L=24 m.

$$\mu^+ \xrightarrow{\text{Decay at rest}} \bar{\nu}_\mu \xrightarrow{\text{Oscillation(4th neutrino)}} \bar{\nu}_e \qquad (1)$$

Neutrino oscillation at this E/L can not be explained by the standard 3 neutrino flavor oscillations and if it is observed, it indicates that 4th neutrino, called sterile neutrino, exists.

The $\bar{\nu}_e$ is detected in liquid scintillator (LS) using the inverse beta decay interaction, followed by the neutron capture γ's.

$$\bar{\nu}_e + p \rightarrow e^+ + n: \quad n + {}^{A}\mathrm{Gd} \rightarrow {}^{A+1}\mathrm{Gd}^* \rightarrow {}^{A+1}\mathrm{Gd} + \gamma s \left(\Sigma E_\gamma \sim 8\mathrm{MeV}\right) \qquad (2)$$

The $\bar{\nu}_e$ turns to positron in the inverse beta decay interaction and the positron emits scintillation light whose amount is approximately proportional to the energy of the incident neutrino. The proton turns to neutron in the interaction. The neutron quickly thermalizes in the liquid scintillator and, typically 30 μs after, is captured by gadolinium and produces γ-rays whose total energy is 8 MeV. By taking the delayed coincidence between the positron signal and the neutron capture signal, $\bar{\nu}_e$ is identified.

The main background for this process is fast neutrons produced in interactions of cosmic-ray muons and surrounding materials. Since the mass of the neutron and proton is almost the same, when the fast neutron collides with a free proton in the liquid scintillator,

it transfers its energy efficiently to the proton and loses its energy quickly and finally be captured by the gadolinium.

$$n + p \rightarrow p + n: \quad n + {}^{A}\mathrm{Gd} \rightarrow {}^{A+1}\mathrm{Gd}^{*} \rightarrow {}^{A+1}\mathrm{Gd} + \gamma s \left(\Sigma E_{\gamma} \sim 8\mathrm{MeV}\right) \qquad (3)$$

This event pattern is very similar to that of $\bar{\nu}_e$ signal, (2), and if the recoiled proton emits scintillation light equivalent to that of e^+, the fast neutron signal mimics the $\bar{\nu}_e$ signal. A possible method to remove the fast neutron background is to use, so called, pulse shape discrimination (PSD) technique. Since the proton mass is much larger than it's kinetic energy, the *dE/dx* is much larger than that of positron signal. In this case, the ratio of the slow component and fast component of the scintillation signal becomes larger than that from light particles such as electron, positron or γ-ray. By measuring this property, the fast neutron signal can be removed from the neutrino signal.

The PSD capability may depend on the energy. However, PSD data for JSJS[2] neutrino energy range are scarce. Therefore, we performed the direct measurement of the PSD capability of our own liquid scintillator candidate using the 70 MeV quasi-monochromatic neutron beam at CYRIC. In addition to the measurement of the PSD capability, the scintillation quenching properties of the proton and the corresponding Birks constant at the neutrino energy range was also measured.

Figure 1 shows the conceptual layout of the experiment. The quasi-monochromatic neutron beam is produced by hitting lithium target with 70 MeV CYRIC proton beam. The energy of the neutron beam is measured by the Time of Flight (ToF1). Figure 2a shows the energy spectrum of the neutron beam measured by ToF1. A clear peak is observed at around 60 MeV.

Scattered-off neutrons from the Target LS are detected by Tagging LS. The energy of the scattered-off neutron is measured by ToF2. For elastic scattering with proton, the energy of the scattered proton is uniquely determined from the scattering angle. Figure 2b shows an example of the correlation between the visible energy of the Target LS (detailed energy calibration was not performed yet at this stage) and the energy of the neutron escaped from the Target LS measured by ToF2. The neutron selection in the Tagging LS using its PSD data was performed to further reduce the γ-ray background. A clear proton elastic scattering peak is seen in Fig. 2b. We performed the measurements at three different angles and used the neutrons with monotonously decreasing energy distribution to cover wide energy range.

After detailed energy calibration of the liquid scintillator, the quenching factor of the

proton was measured. There are a lot of measurements of quenching properties of scintillation light from liquid scintillators but most of them were performed at lower energies. Therefore, it is important for us to measure the quenching factor of protons for energy range of ~40MeV. Figure 3 shows relation between the energy deposit in the target LS measured by the ToF1 and ToF2 and the visible energy. The visible energy is smaller than the energy deposit and the energy shift is parametrized as the Birks formula as shown below.

$$\frac{dL}{dx} = \frac{S(dE/dx)}{1 + k_B(dE/dx)} \tag{4}$$

where dL/dx is the scintillation light emission per unit path length. k_B is called the Birks constant which represents the quenching value. S is the conversion factor between dL/dx and dE/dx. For example, if there is no quenching (k_B=0), S=(dL/dx)/(dE/dx). dE/dx is obtained from Monte Carlo simulation. From this experiment, the Birks constant is measured as

$$k_B = 0.012\text{mm/MeV}.$$

This value is consistent with the values measured at low energy experiments. This result will be implemented in the Monte Carlo simulation for JSNS^2 experiment.

Next, the PSD capability of our liquid scintillator was measured. Figure 4a shows the energy dependence of the PSD parameter (ratio of the tail charge and total charge of signals). The ratio does not change much for energies up to 50 MeV. The width becomes narrower due to larger photoelectron statistics. This data indicates the PSD technique is still useful for this energy range. Figure 4b shows expected PSD parameter distribution in real detector calculated by Monte Carlo simulation using the PSD information obtained in this experiment. The Figure 4b shows that the separation of neutron and neutrino is very good and that the reduction of the fast neutron background using the PSD is satisfactory for the JSNS^2 experiment. The JSNS^2 experiment can go forward safely based on these results.

References

1) JSNS^2 group, arXiv:1310.1437, arXive:1502.02255, PTEP 2015(2015) no.6, 063C01, arXive:1507.07076, arXive:1601.01046, arXive:1610.08186, arXive:1705.08629
2) JSNS^2 group, ArXiv:1705.08629, Section 4.1, p67 (Submitted to PTEP)

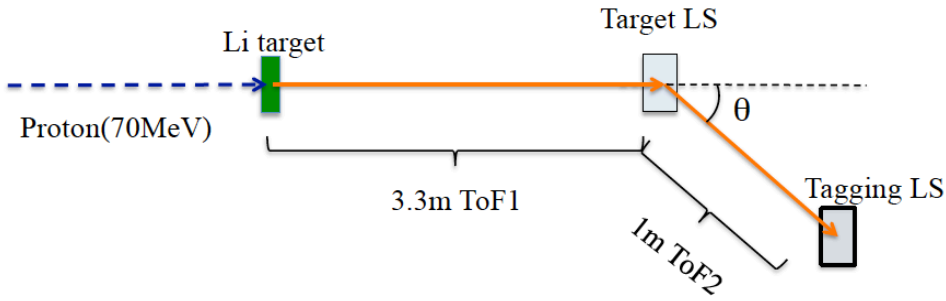

Figure 1. Set up of the experiment. The Target and Tagging LS is contained in a 100cc glass vial. The angle of the tagging LS was changed to cover a wide energy range in the target LS.

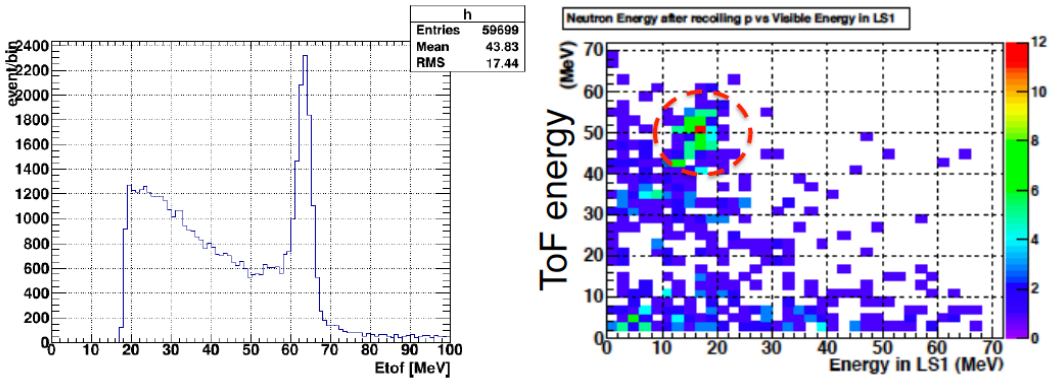

(*a*) (*b*)

Figure 2. (a) The neutron beam energy measured by the ToF1. (b) The relation between the visible energy of the Target LS and the energy of the escaped neutron measured by the ToF2 (vertical axis).

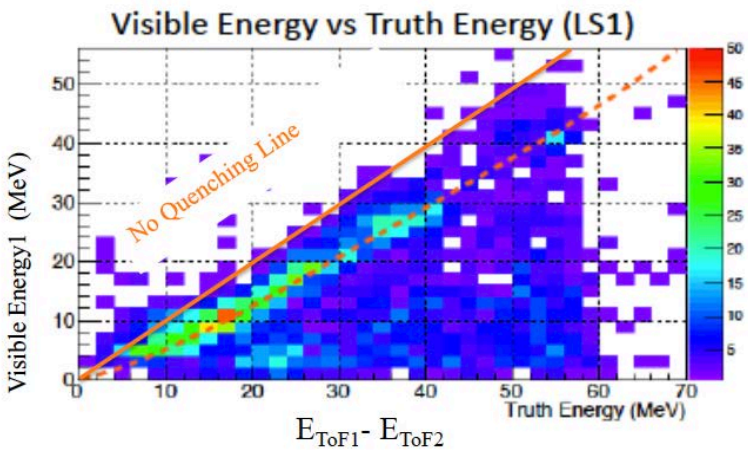

Figure 3. Quenching of scintillation light of proton. The horizontal axis is the deposited energy and the vertical axis is the visible energy for recoiled proton.

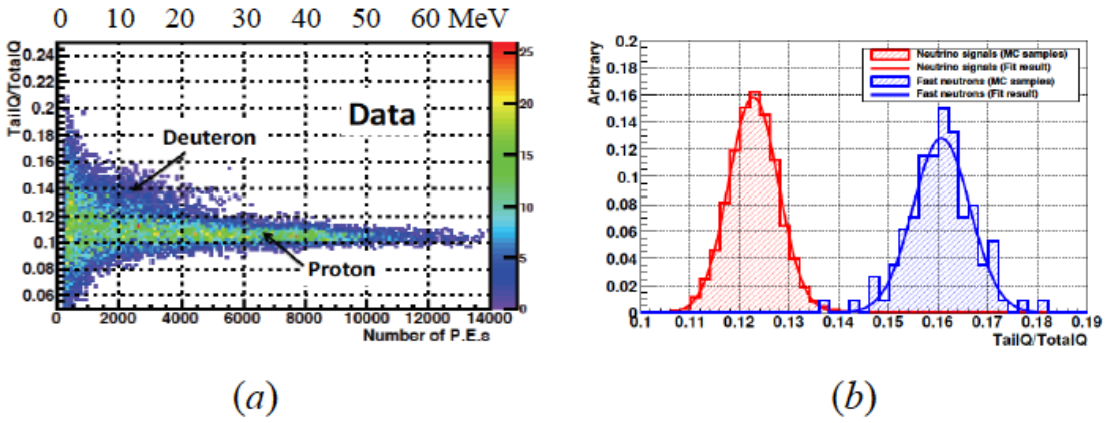

Figure 4. (*a*) Energy dependence of the PSD parameter (Tail and Total Charge ratio). 10,000 p.e. corresponds to roughly 50MeV. (*b*) Comparison of the PSD parameter distribution for neutrino like events (red) and neutron like events (blue).

II. 5. Two-dimensional Beam Profile Monitor for Alpha Emitter

Tanaka S. K.[1], Dammalapati U.[1], Harada K.[1], Itoh M.[1], Ito S.[1], Inoue T.[1], Kawamura H.[1], Sakamoto K.[1], Uchiyama A.[1], Yoshioka R.[1], and Sakemi Y.[1]

[1]*Cyclotron and Radioisotope Center, Tohoku University*
[2]*RIKEN Nishina Center*
[3]*Center for Nuclear Study, the University of Tokyo*

Search of the permanent electric dipole moment (EDM) using various kinds of atom and molecules has been carried out in recent years. The infinite value of electron EDM would imply of a new physics beyond the standard model of particle physics. We are preparing the precise measurement of the electron electric dipole moment (EDM) using a francium in CYRIC. Francium is one of a suitable atom to search the electron EDM. It is the heaviest alkaline metal so that it has a large enhancement factor of EDM and can be applied laser cooling technique.

Francium is produced by nuclear fusion reaction between an oxygen beam (^{18}O) provided from CYRIC and gold target. The intensity of the Fr production is limited such as 10^6 /s by the the intensity of the oxygen beam[1)]. Fr is ionized by surface ionization on the gold target, and transport 12 m length to the measurement area which is free from background noise of the cyclotron acceralator. Then the Fr ions are neutralized and load to the trapping area by heating the foil. The size of the yttrium foil is only 10 mm × 10 mm, so that the control and focus of the Fr^+ beam to this small area is important to the efficiency of the number of the Fr loaded to the trapping area. Also, we need to care about the other ions along with the Fr ions which cause atomic collisions in the trapping area. Typically, the intensity of francium beam is 10^6 /s and that of other ions (K^+, Ca^+, Au^+ ...) is 10^{10} /s. We removed light ions from Fr^+ with Wien Filter[2)]. Two-dimensional beam profiles of both Fr beam and other ions beam are valuable information to optimize the purity of the Fr beam. However, Au^+ is not removeable with the specification of mass filter, and we couldn't observe the Fr beam profile hidden from the dominant other ion beam profiles. Therefore, we developed new two-dimensional beam profile monitor for alpha emitter ion beam separated from the

other ion beam by using a micro channel plate (MCP) and phosphor screen.

Two beam profile monitors (BPM1 and BPM2) are installed on the Fr beamline (Figs. 1 and 2). BPM1 is loaded on the downstream end of the beamline. Beamline downstream of the neutralizer is free from electromagnetic field so that beam profile on the neutralizer can be reconstructed geometrically from BPM1. The BPM2 is used to make a diagnosis of the production distribution of Fr ions and other dominant number of ions on the target, since production distribution of these ions are different from that of Fr ions.

Two BPMs are consisted of a chevron micro channel plate (MCP) which has a diameter of 40 mm, and a phosphor screen. The MCP is a chevron MCP (two plates mounted) which has a diameter of 40 mm, and the phosphor screen is RHEED screen (SG63-2). The impacts of the ion beams on the MCP produce cascade of electrons that propagate through the one of the small channels by applying a strong electric field across the MCP. The electron clouds are converted to the visible light by the phosphor screen and observe it by CCD camera (Basler acA2500-14um for BPM1 and acA1300-60gm for BPM2).

Since intensity of the Fr beam is relatively small compared to the other ion beams, we could not observe the Fr beam by using this method. Fr beam profile is observable from produce cascade of electrons by decay alpha of ^{210}Fr instead. So, the measurement sequence is as follows:

- Inject the ion beam to the BPM. Dominant part of the ion beam is observable.
- Keep injection for 10 minutes which is enough to accumulate the Fr atoms on the surface of the MCP
- Stop injection to the BPM. Just after that, we can observe the Fr beam profile.

In case of BPM2, SSD detector is installed nearby the MCP to observe the decay alpha particles from ^{210}Fr to measure the absolute Fr beam intensity.

We test these two BPMs by produced Fr ion beams. Figure 3 shows a typical result of this test measurement. The total brightness on the monitor is increased by the number of the Fr atoms on the MCP. After the stop beam injection, we can observe only the decay alpha particle from Fr atoms. Therefore, we can obtain both beam profile of Fr and the others simultaneously.

As described above, we developed the two-dimensional beam profile monitor for alpha emitter especially francium. Also, we used it for the improvement of the Fr beam by using the Wien Filter and achieve the purity of 1 instead 10^{-6} without the filter.

References

1) H. Kawamura, et al., *JPS Conf. Proc.* **6** (2015) 030068.
2) Arikawa H, "The development of the high purity francium beam toward the search for the violation of the fundamental symmetry (in Japanese)", Master thesis, Tohoku University (2015).

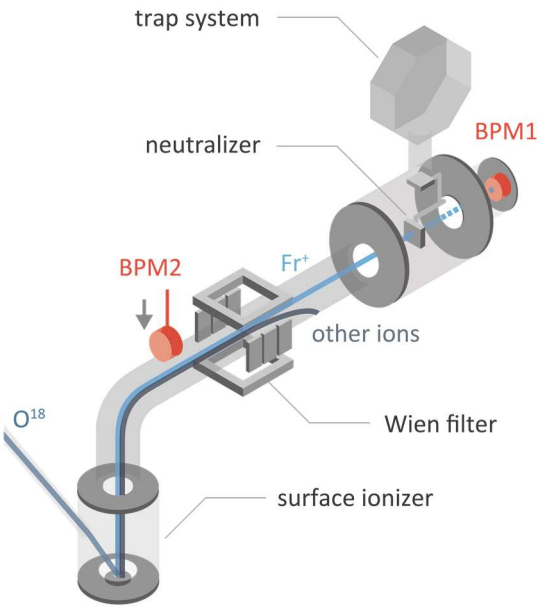

Figure 1. Fr beamline

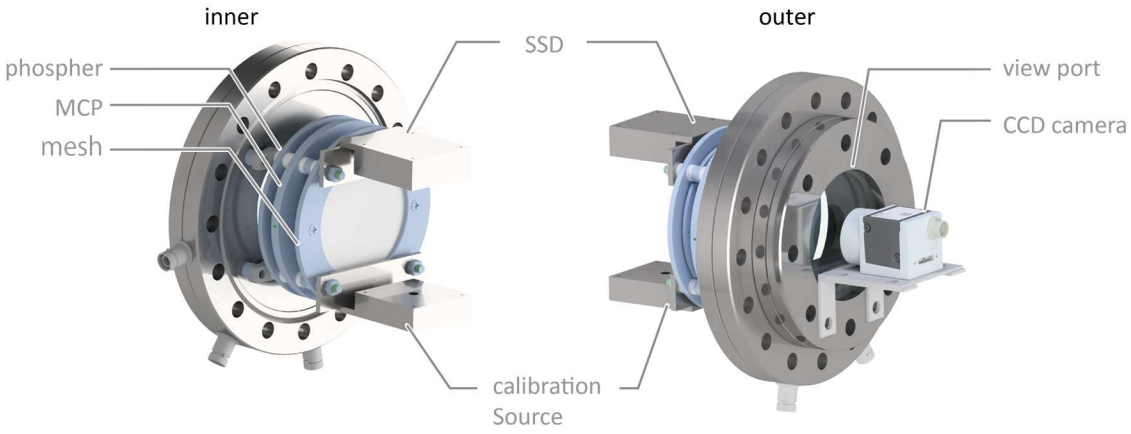

Figure 2. The schematic view of the BPM1

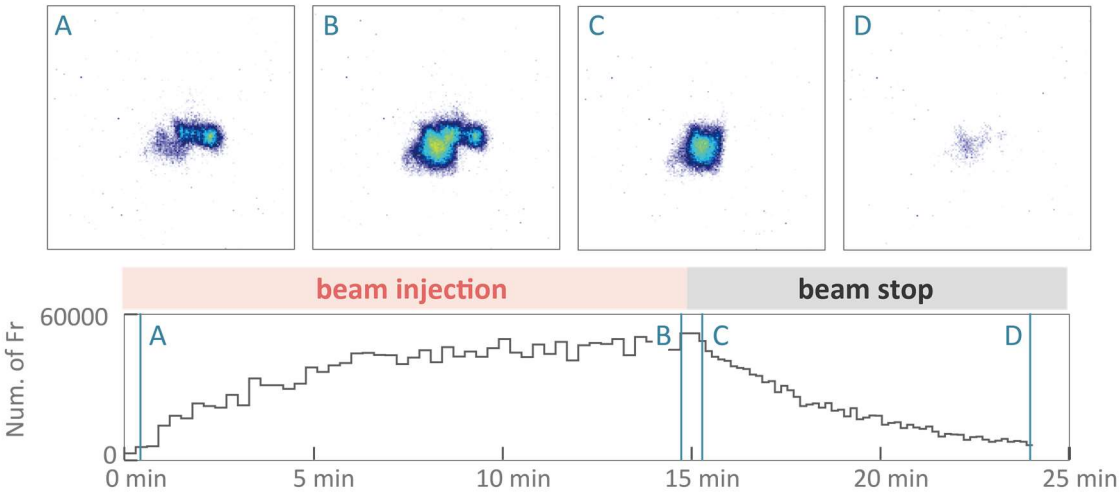

Figure 3. Typical measurement sequence of beam profile monitor

II. 6. Development of an Optical Dipole Force Trap System for the Search of an Electron Electric Dipole Moment

Harada K.[1], Sakamoto K.[1], Dammalapati U.[1], Uchiyama A.[1], Kawamura H.[2,1], Inoue T.[2,1], Tanaka K.[1], Ito S.[1], Yoshioka R.[1], Itoh M.[1], Aoki T.[3], Hatakeyama A.[4], and Sakemi Y.[5]

[1]Cyclotron and Radioisotope Center, Tohoku University
[2]Frontier Research Institute for Interdisciplinary Sciences, Tohoku University
[3]Graduate School of Arts and Sciences, University of Tokyo
[4]Department of Applied Physics, Tokyo University of Agriculture and Technology
[5]Center for Nuclear Study, University of Tokyo

In its present state, the universe is mostly occupied by matter, and it is thought that there are few antiparticles having the same mass and spin but with a different electric charge. It is a significant mystery why matter and antimatter, which are considered to have existed in equal number in the early universe, presently show such a large difference in their amounts. The violation of the combined operator of Charge conjugation (C) and parity (P) is thought to be necessary to explain the matter-anti-matter asymmetry, and it is provided by the finite value of an electric dipole moment (EDM) as the combined operator of C, P and time-reversal (T) is expected to be invariance. The EDM is a physical quantity that breaks the T and P symmetry. However, the value of the EDM predicted in the framework of the standard model is quite small, and is difficult to measure. However, if the EDM is measured as a finite value whose value is larger than that predicted, it will lead to a new physics beyond the standard model.

The upper limit of an electron EDM obtained from a thorium monoxide (ThO) experiment was shown to be 8.7×10^{-29} ecm[1)]. A ThO molecule has a large effective internal electric field, and is an advantageous material for an EDM search. However, in atomic or molecular beam experiments, a significant systematic effect is caused by the moving magnetic field effect. Owing to the geometric phase shift generated by the field gradient, these systematic errors mimic the true EDM signal and limit the measurement accuracy of the EDM.

Francium (Fr) atom, which has a large enhancement factor, are very useful for the

search of an electron EDM. Because Fr is an alkali atom, it is possible to slow down the atomic velocity, greatly extending the interaction time, and to localize the atoms within a small space using laser cooling and a trapping technique. This technique can also reduce the influence of non-uniformity of the applied electric and magnetic fields in an EDM search experiment. Moreover, a longer interaction between the atoms and applied electric field increases the sensitivity of an EDM signal as compared with an EDM search experiment using atomic and molecular beams.

The development of an optical dipole force trap (ODT) and optical lattice systems for an electron EDM search using Fr and rubidium (Rb) atoms is progressing at the Cyclotron and Radioisotope Center (CYRIC) of Tohoku University. Because Rb atoms have chemical properties similar to those of Fr atoms, Rb atoms have been mainly used in the development of ODT systems. The use of an ODT is a variegated technique for the trapping of neutral atoms within a region with high electric field strength, and is useful for EDM measurements. A magneto-optical trap (MOT) is widely used as a precooling method before atoms are loaded into an ODT. Details regarding the development of a MOT system for the trapping of Rb and Fr atoms have been reported[2,3]. The typical density and number of Rb atoms in the magneto-magnetic trap were estimated through absorption imaging to be approximately 10^{10} atoms/cm^3 and 10^9 atoms. For a transfer from an MOT to an ODT, it is important that the temperature of the atomic cloud be sufficiently lower than the potential produced by the ODT light. In a previous study, it was shown that the temperature of the atomic cloud was higher than the potential of the ODT light, and the efficiency of the transfer to the ODT was poor. Therefore, we investigated whether an atomic cloud is cooled to below the Doppler cooling limit temperature through polarization gradient cooling (PGC) using the time of flight (TOF). To allow PGC to work well, a precise adjustment of the ambient magnetic field is needed. The results are shown in Fig. 1, where the vertical axis indicates the radius of the atomic cloud, and the horizontal axis indicates the time after turning off the MOT light. The spread of the atom cloud is observed through absorption imaging using a camera with a cooled charge-coupled device (CCD). The estimated temperatures of the atoms were 800 (red circle) and 20 (blue rectangle) μK, respectively, which indicates that the temperature decreases when PGC is added, and the value is also lower than the Doppler cooling limit temperature, as compared with the MOT.

We introduced a new light source for the optical dipole force trapping of atoms trapped using an MOT with PGC. The light source consists of a seed light and a fiber amplifier. The wavelength of the light was 1,064 nm. The output power was approximately

50 W after passing through the fiber amplifier when inputting a seed light power of 120 mW. After passing through the isolator for the prevention of a return light, the light enters an acousto-optic modulator (AOM) for switching. First-order light diffracted by the AOM is extracted based on the aperture, and magnified using f = 50 and f = 300 lenses. Thereafter, the light passes through a f = 250 lens installed in front of the port of the vacuum chamber, and becomes incident inside the chamber. The ODT light passing through the chamber is blocked using a beam dumper to prevent scattering into the surroundings. The atomic cloud trapped in the ODT is observed from a photograph taken using the cooled CCD camera. To prevent the ODT light from entering the camera as stray light, a filter for blocking light with a wavelength of 1,064 nm is attached to the camera. When the light intensity reached 35 W, the number of atoms captured by the ODT was confirmed, as shown in Fig. 2, which is an image taken after 35 ms of holding only ODT light. The number of atoms was evaluated by taking the sum of the optical density around the image of the ODT, the estimated number of which was approximately 10^6.

This work was supported by JSPS KAKENHI, grant numbers JP26220705, JP16K17676, JP21104005, and JP18K03663; the SEI Group CSR Foundation; the Shimadzu Science Foundation; and the Futaba Electronics Memorial Foundation.

References

1) The ACME Collaboration, Baron J et al., Science 343 (2014) 269.
2) Hayamizu T et al., JPS Conf. Proc. 1 (2014) 013065.
3) Harada K et al., J. Phys.: Conf. Ser. 691 (2016) 012017.

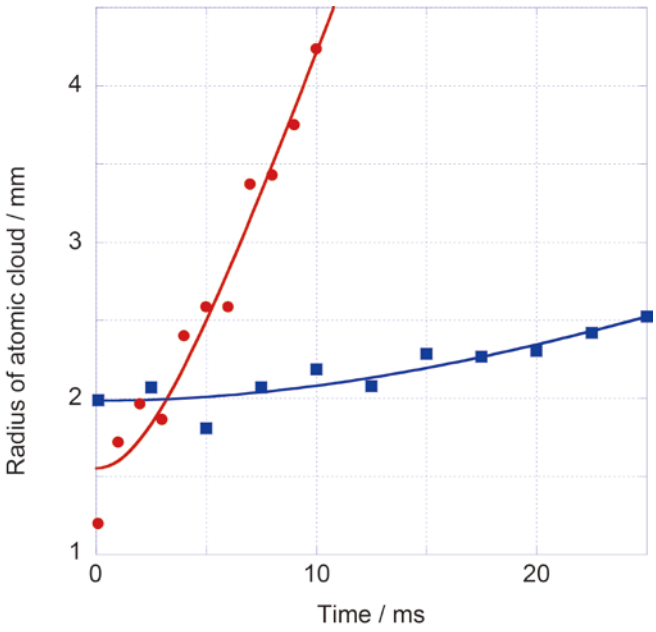

Figure 1. Time of flight. The blue rectangle and red circle indicate the results with and without PGC, respectively. The lines are the fitting curves.

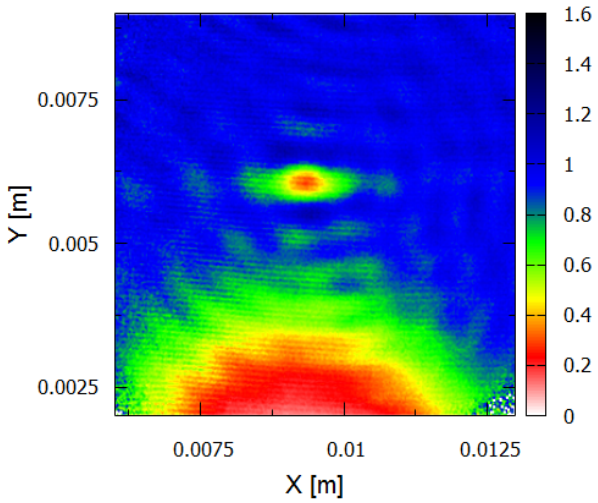

Figure 2. Absorption imaging of atoms after being captured by an ODT for 35 ms. The large absorption shown at the bottom of the image is an atomic cloud under a free-fall without being captured by the ODT.

II. 7. Atomic Magnetometer toward the Fr EDM Experiment

Inoue T.[1,2], Dammalapati U.[2], Harada K.[2], Itoh M.[2], Ito S.[2], Kawamura H.[1,2], Sakamoto K.[2], Tanaka K.[2], Uchiyama A.[2], Yoshioka R.[2], Asahi K.[3], Yoshimi A.[4], and Sakemi Y.[5]

[1]*Frontier Research Institute for Interdisciplinary Science, Tohoku University*
[2]*Cyclotron and Radioisotope Center, Tohoku University*
[3]*RIKEN Nishina center*
[4]*Research Institute for Interdisciplinary Science, Okayama University*
[5]*Center for Nuclear Study, University of TOKYO*

A permanent electric dipole moment (EDM) of an elementary particle, which is associated with the spin, is a good observable to probe the physics beyond the standard model (SM) of elementary particles, since the EDM violates the CP symmetry and is sensitive to CP violation in the physics in the SM[1)]. The electron EDM is enhanced in the heavy atom due to the relativistic effect[2)]. The francium (Fr) atom has the largest enhancement factor of the electron EDM in the alkali atom[3)]. We plan to search for the electron EDM by using laser cooled Fr atoms[4)].

Since the EDM couples with the electric field, it is deduced from a measurement of the energy splitting of the spin with a static electric field. In the actual EDM experiment, we need a static magnetic field in addition to the static electric field due to a tiny energy shift of the EDM. Then, the monitor of the magnetic field, which is applied to the Fr atom, is an important issue. In order to monitor the magnetic field, we are developing a rubidium (Rb) atomic magnetometer based on a nonlinear magneto-optical rotation (NMOR) effect with frequency modulated light[5)].

The principle of the NMOR effect of the Rb atom is as follows. A laser light with a wavelength tuned to the Rb D1 transition produces the spin alignment state of the Rb atom. The time evolution of the spin alignment under the applied magnetic field occurs and the spin alignment rotates around the magnetic field. Then, the laser light interacts with the rotated spin alignment. As a result, the polarization plane of the laser light is rotated, which has the dispersive shape as a function of the magnetic field. This effect occurs around the zero magnetic field due to the relaxation of the spin alignment in the high field. By using

the frequency-modulated (FM) light, the NMOR effect in the finite field can be observed due to a match between the modulation frequency of the laser light and the spin precession frequency of the Rb atom. Thus, we can monitor the magnetic field by measuring the rotation angle of the laser light.

The magnetometer apparatus is shown in Fig. 1. The light source is the DFB laser. The frequency of the laser light is modulated by the modulation of the laser current. The Rb atom is confined to the Paraffin coated glass cell. Paraffin is an anti-relaxation material[6]. The glass cell is placed inside the magnetic shield which is introduced in order to suppress the effect of the stray magnetic field. The magnetic field is produced by the 3 axis Helmholtz-like coil inside the shield. The laser light transmitted to the cell is divided by using a polarized beam splitter to measure the rotation angle of the polarization plane. The intensities of the divided lights are detected by the balanced photo-detector and its output is sensed in a lock-in amplifier for phase sensitive detection. The output of the lock-in amplifier is monitored by an oscilloscope.

Figure 2 shows the FM-NMOR spectrum. The field sensitivity of the magnetometer is limited by the linewidth and the signal-to-noise ratio of the spectrum. By optimizing the experimental conditions (such as power, frequency or modulation depth of the laser light), the present sensitivity reaches about 20 $pT/Hz^{1/2}$. Then, we performed the actual filed measurement. The result of the measurement is shown in Fig. 3. The rectangle magnetic field is applied along to the incident direction of the laser light by using the 3 axis Helmholtz-like coil. The strength of the applied field is about 300 pT, which is estimated by the interpolation of the calibration using the flux gate magnetometer. The magnetometer responds to the changes in the applied magnetic field as shown in Fig. 3. Frequency component noise of about 50 Hz, which can be derived from the power supply, is also observed. We need to suppress this noise in order to improve the sensitivity of the magnetometer.

This work was supported by MEXT/JSPS KAKENHI Grant Number 26220705.

References

1) Kriplovich I.B., Lamoreaux S.K., CP Violation Without Strangeness, Springer, Heidelberg (1997).
2) Ginges J. S. M. and Flambaum V. V., *Phys. Rep* **397** (2004) 63.
3) Mukherjee D., Sahoo B. K., Nataraj H. S. and Das B. P., J. *Phys. Chem A* **113** (2009) 12549.
4) Inoue T., Ando S., Aoki T., Arikawa H., Ezure S., Harada K., Hayamizu T., Ishikawa T., et al., *Hyperne Interact* **231** (2015) 157.
5) Kimball D. F. J., Jacome L. R., Guttikonda S., Bahr E. J. and Chan L. F. J., *Appl. Phys* **106** (2009)

063113.
6) Alexandrov E. B., Balabas M. V., Pazgalev A. S., Vershovskii A. K., Yakobson N. N., *Laser Phys* **6** (1996) 244.

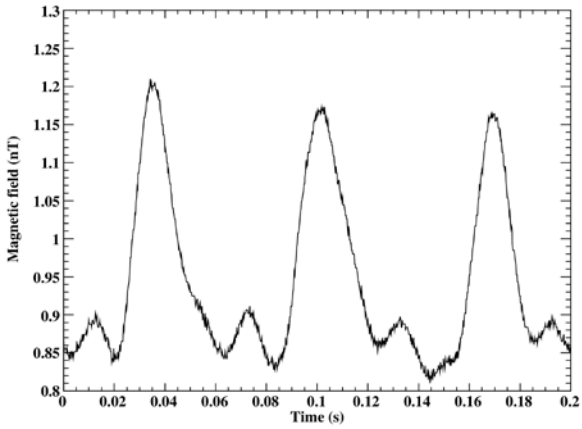

Figure 1. Experimental setup.

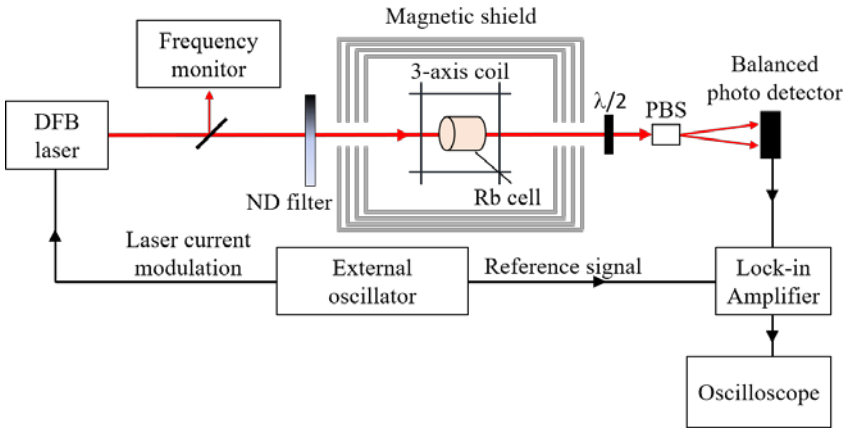

Figure 2. FM-NMOR spectrum.

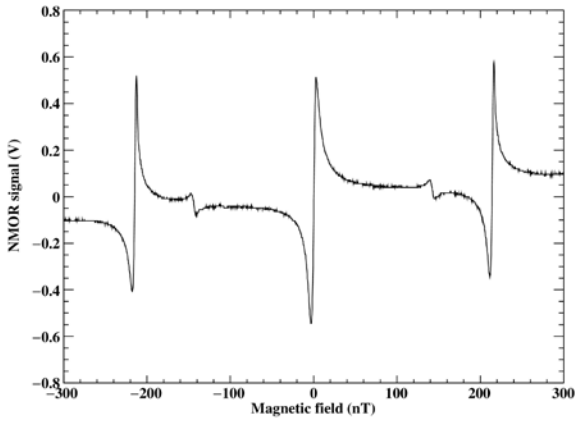

Figure 3. Magnetic field measurement.

II. 8. Prompt Gamma-Ray Detection with TlBr Detectors for Proton Radiation Therapy

Hitomi K.[1], Higuma T.[1], Hosokawa H.[1], Nogami M.[1], and Terakawa A.[2]

[1]Department of Quantum Science and Energy Engineering, Tohoku University
[2]Cyclotoron and Radioisotope Center, Tohoku University

Monitoring in vivo beam rage in the patient during proton radiation therapy is important for improving the accuracy of the treatment dose. The nuclei in the patient tissue interacting with protons during the therapy emit prompt gamma rays. It is possible to determine the in vivo beam rage in the patient by measuring the prompt gamma rays during proton therapy. Detection of prompt gamma rays for proton therapy has been studied by various researchers[1-3]. In this study, prompt gamma-ray detection for proton therapy was performed with thallium bromide (TlBr) semiconductor detectors. Gamma-ray detectors fabricated from TlBr crystals exhibit a high detection efficiency for gamma rays because of the high atomic numbers (81 and 35) and high density (7.56 g/cm^3) of the material. The high detection efficiency and good energy resolutions[4] make the TlBr detector a promising candidate for constructing prompt gamma-ray imagers.

Gamma-ray detectors were fabricated from TlBr crystals grown by the traveling molten zone method in this study. The starting materials for the crystal growth were commercially available TlBr materials. The zone refining method was employed for purifying the starting materials. The grown crystals were cut into wafers with a diamond wire saw. The surfaces of the wafers were polished mechanically. Thallium electrodes were deposited on the wafers by the vacuum evaporation method. The detectors had a planar cathode and a pixel anode surrounded by a guard electrode. Charge sensitive preamplifiers were connected to the cathode and the anode. The output waveforms were recorded with a digitizer. The pulse waveforms were analyzed with a PC for obtaining the pulse height spectra.

Prompt gamma-ray detection experiments were performed using a proton therapy system[5] at Cyclotron and Radioisotope Center (CYRIC), Tohoku University. Schematic drawing of the experiments for the prompt gamma-ray detection is shown in Fig. 1. The water

phantom was irradiated with 80-MeV protons. A lead collimator (slit size: 0.4 cm and thickness: 10 cm) was placed between the water phantom and the TlBr detector. By changing the proton range using the range shifter, prompt gamma rays from the water phantom was measured with the TlBr detector to obtain position dependency of prompt gamma-ray emissions along with the proton path. The dose distribution in the water phantom for the proton irradiation was measured with a thimble chamber. The prompt gamma-ray distribution for the experimental setup was simulated with PHITS.

Figures 3 and 4 show position dependency of prompt gamma-ray counts obtained from the simulation and the TlBr detector, respectively, superimposed with the dose distribution obtained from the thimble chamber. The experimental data was well consistent with the simulation data. The prompt gamma-ray counts decreased around the Bragg peak of the dose distribution. The experimental data demonstrated that TlBr detectors were useful for determining the proton beam range.

References

1) Polf JC, et al., *Phys Med Biol* **54** (2009) N519.
2) Smeets J, et al., *Phys Med Biol* **57** (2012) 3371.
3) McCleskey M, et al., *Nucl Instr Meth A* **785** (2015) 163.
4) Hitomi K, et al., *Nucl Instr Meth A* **747** (2014) 7.
5) Terakawa A, et al., The proceedings of the 16th Pacific Basin nuclear Conference (16PBNC), Aomori, Japan, Oct. 13-18, 2008 paper ID : P161378.

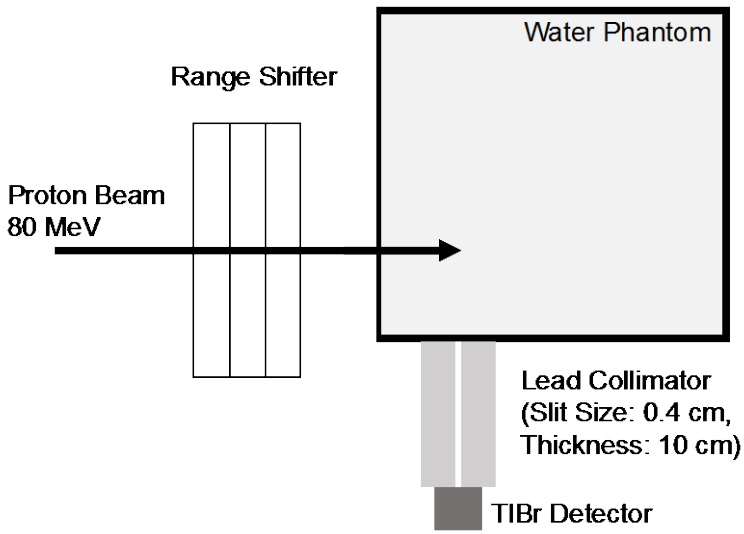

Figure 1. Schematic drawing of the experiments for the prompt gamma-ray detection.

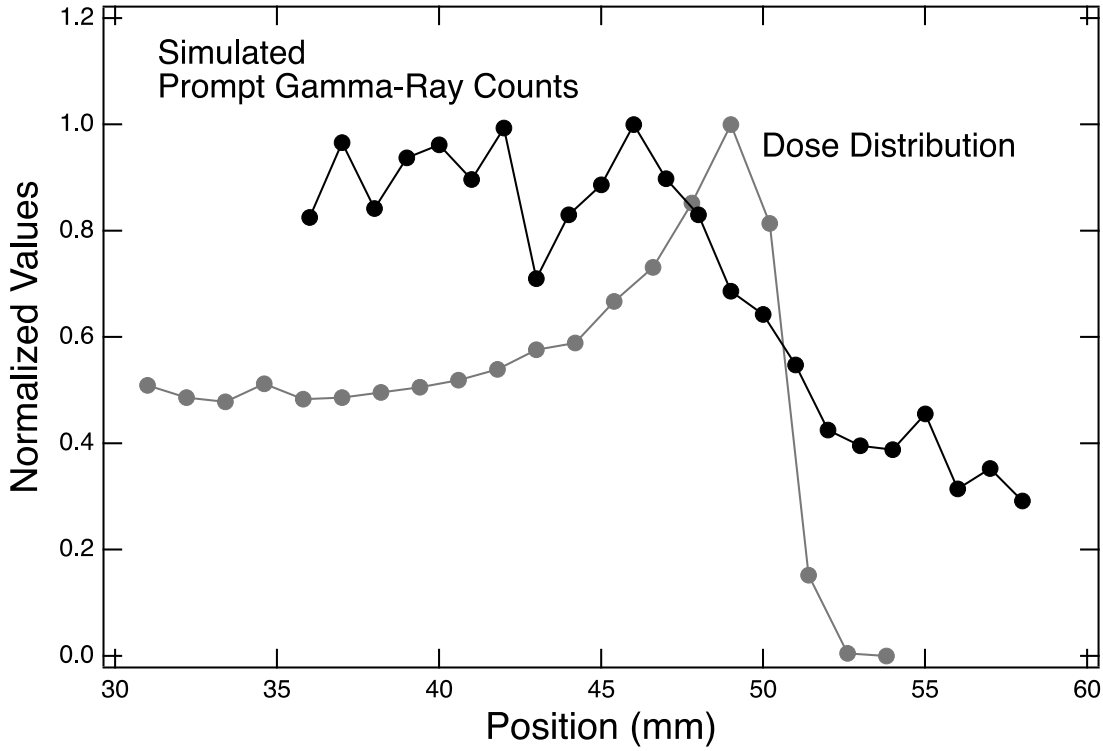

Figure 2. Position dependency of prompt gamma-ray counts obtained from the simulation, superimposed with the dose distribution obtained from the thimble chamber.

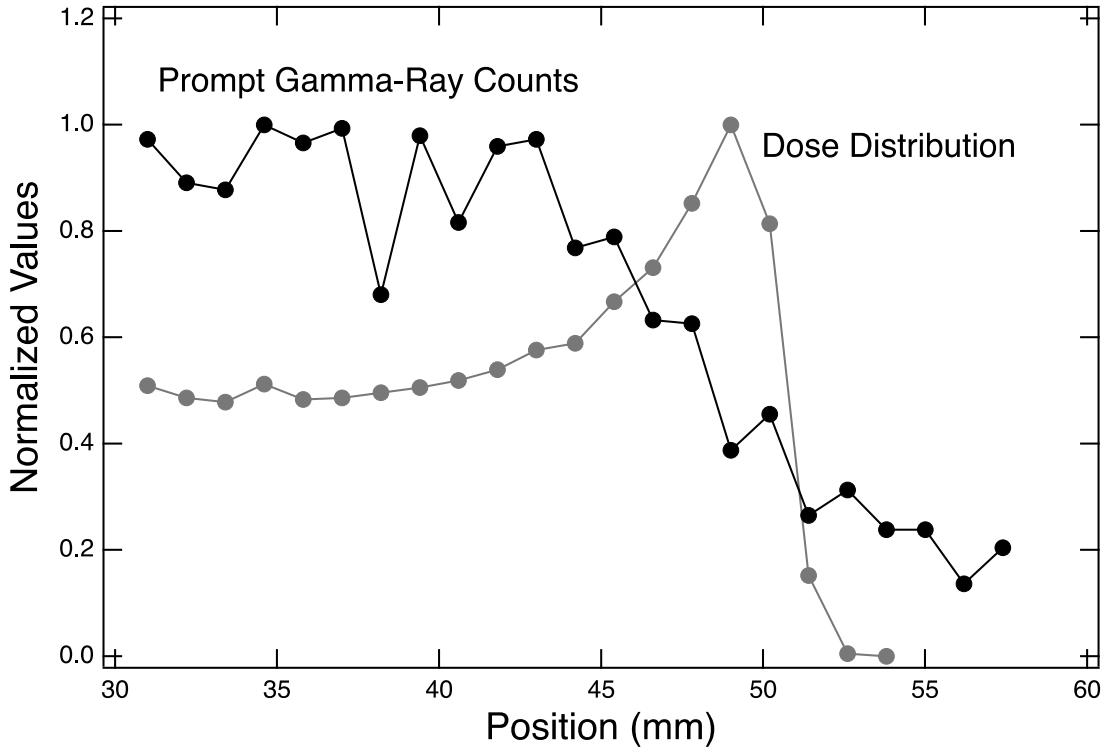

Figure 3. Position dependency of prompt gamma-ray counts obtained from the TlBr detector, superimposed with the dose distribution obtained from the thimble chamber.

II. 9. Development of a New Measurement System for Primary Knock-on Atoms (PKA)

Tsai P.E.[1,], Iwamoto Y.[1], Hagiwara M.[2], Sato T.[1], Satoh D.[1], Abe S.[1], Itoh M.[3], and Watabe H.[3]*

[1]*Nuclear Science and Engineering Center, Japan Atomic Energy Agency*
[2]*Radiation Science Center, High Energy Accelerator Research Organization*
[3]*Cyclotron and Radioisotope Center, Tohoku University*

Introduction

Primary knock-on atoms (PKAs) created in spallation reactions are critical for various applications, particularly for radiation damage assessment in accelerator facilities and in space environment. PKAs have a continuous mass distribution from target nuclide down to one atomic mass unit (amu) and a wide energy distribution from a few tens of MeV down to sub-MeV. The PKA energy spectra and its yields are one of the fundamental parameters for radiation damage calculation models[1]. Yet the experimental data up to date are still limited, due to the high measurement thresholds and the insufficient mass resolutions to identify PKA species in the conventional experimental setups using solid state detectors[2].

To provide the important experimental PKA data, we proposed a new measurement system consisting of two fast timing detectors for time of flight (ToF) measurement, and one dE-E gas ionization chamber (GIC) for stopping power (dE) and total kinetic energy (E) measurement.

Detectors and experimental setup

Each fast timing detector, as shown in Fig. 1, consists of (i) an ultrathin carbon foil (3-6 μg/cm^2) for creating secondary electrons (SE) when PKAs pass through it with minimal energy losses, (ii) an accelerating grid for SE, (iii) an electrostatic mirror for reflecting the SE traveling direction, and (iv) a microchannel plate (MCP) detector for collecting the reflected SE and creating fast signals with ~600-ps full width at half maximum (FWHM).

[*]*Present address: 2-4, Shirakata, Tokai, Ibaraki 319-1195, Japan*

The dE-E energy detector is a customized gas ionization chamber (Fig. 2) filled with isobutane gas at pressures between 15 and 50 mbar. The low-noise preamplifiers are placed inside the gas chamber to reduce the noise level. This customized gas ionization chamber features (i) a 50-nm thick silicon nitride window to minimize the PKA energy losses, and (ii) two segments of anodes and cathodes with the lengths of 2 cm and 10 cm, respectively, to measure the stopping powers and the total kinetic energies of PKAs in a single detector chamber. The gas pressure can be regulated by the gas flow system to fit different PKA species and different initial kinetic energies of PKA.

The first timing detector is located right behind the thin target foil, and the second one is 15 cm apart from it, followed by the dE-E GIC. The whole measurement system is placed inside the scattering chamber in vacuum.

Feasibility study and tests

The expected performance of the new PKA measurement system regarding the measurement thresholds, energy resolutions, and mass resolutions was simulated and evaluated by the general-purpose Monte Carlo radiation transport code, PHITS[3] version 2.85, with the implemented INCL-4.6 model for proton-induced nuclear reactions, and ATIMA for stopping power and energy loss calculations of charged particles.

Figure 3 shows an example of the PHITS simulation results of the ToF vs E relationship (on the left) and the dE vs E relationship (on the right) from a thin carbon foil bombarded by 70-MeV protons. By combining these two relationships, the PKA isotopes can be identified, and the PKA energies can then be determined by ToF given the known distance and the measured flight time. From the PHITS simulations for carbon targets, it is found that the PKA masses can be separated above ~1.5-2 MeV (~0.15 MeV/nucleon) for all isotopes heavier than alpha.

In the first prototype test of the ToF detector performed at CYRIC in July 2017, we substituted the GIC with a 250-μm silicon strip detector (SSD), as the experimental setup shown in Figure 1, to focus on the test of the timing detectors only. However, the triple coincidence rate of the three detectors were lower than expected, possibly due to poor alignment of the three detectors, the non-uniform electric fields created by the electrostatic mirror that lower the timing detector efficiency, and/or the high noise contribution to the timing detectors. The measurement system is hence under modification based on the feasibility test results.

Acknowledgments

This study was supported by JSPS KEKENHI Grant Number JP17K14918.

References

1) Lu W, Gallmeier F, Geoghegan P, Ferguson P, and Wechsler M, *J Nucl Mater* **431**, (2012) 33.
2) Westfall G, Sextro R, Poskanzer A, Zebelman A, Butler G, and Hyde E, *Phys Rev C* **17** (1978) 1368.
3) Sato T, Iwamoto Y, Hashimoto S, Ogawa T, Furuta T, Abe S, Kai T, Tsai P, Matsuda N, Iwase H, Shigyo N, Sihver L and Niita K, *J Nucl Sci Technol* **55** (2018) 684.

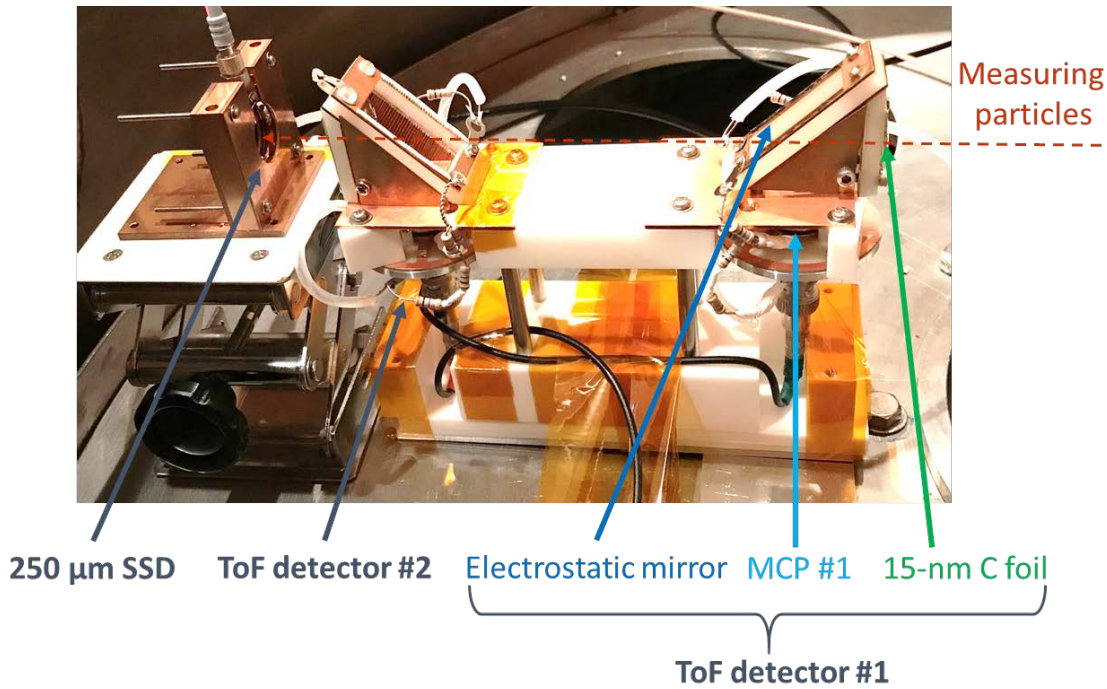

Figure 1. The experimental setup at CYRIC for the feasibility test of the new PKA measurement system.

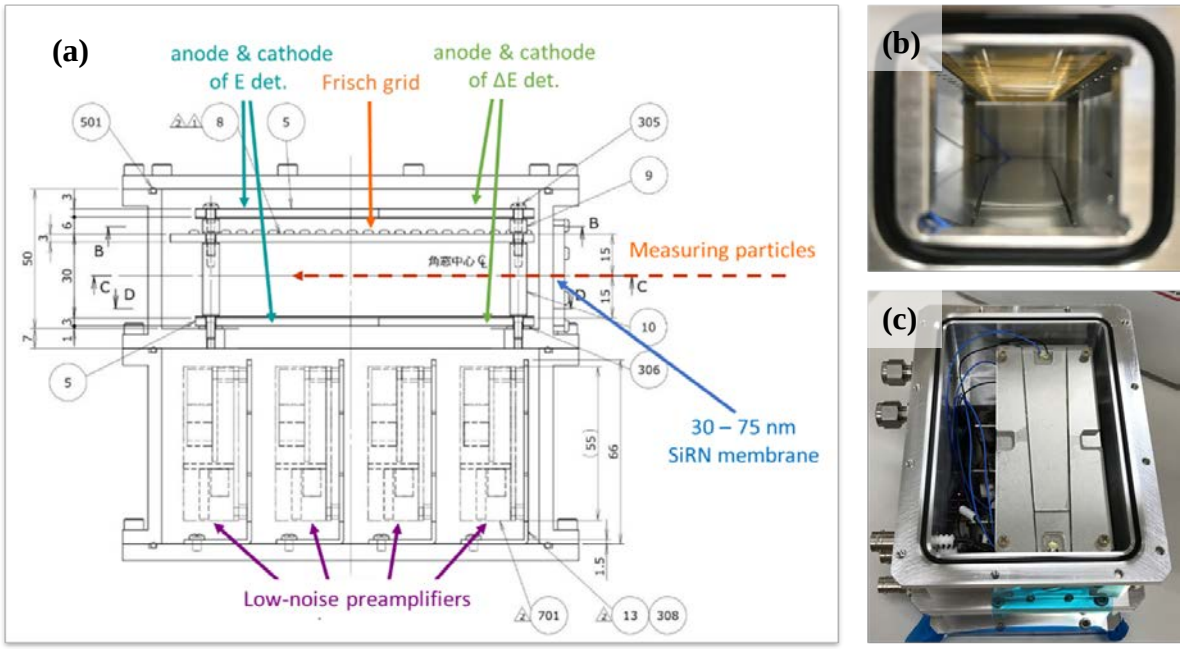

Figure 2. (a) Design of the gas ionization chamber (GIC). (b) View from the GIC window showing the Frisch grid on the top and the cathodes on the bottom. (c) Top view of the two anodes.

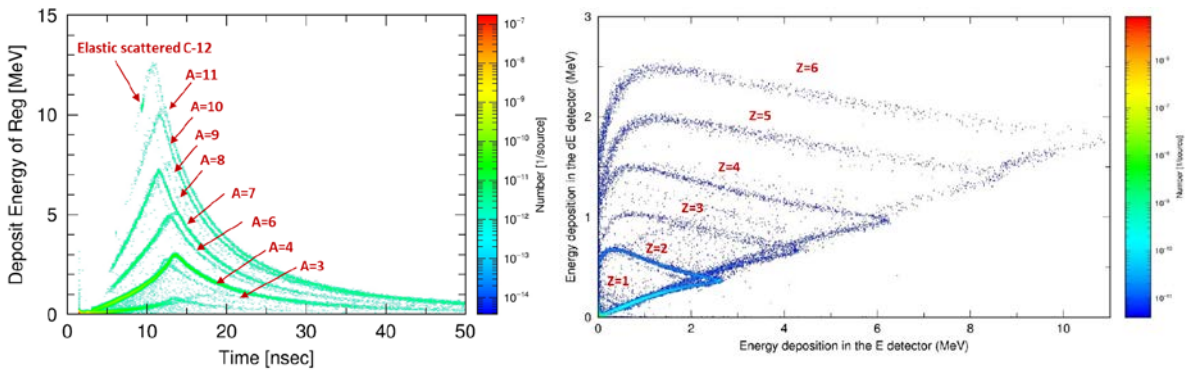

Figure 3. The ToF-E relationship (left) and the dE-E relationship (right) simulated by PHITS for 70-MeV protons bombarding a thin ^{12}C target.

II. 10. Development of Neutron/Ion Irradiation System

Ishibashi Y., Itoh M., Matsuda Y., Tanaka K., Nasu Y., Okamoto J., Karasudani K., Yoshioka R., Ishida S., and Kasamatsu K.

Cyclotron and Radioisotope Center, Tohoku University

*

New fundamental technologies which control quantum particles such as neutron, muon, radioactive nuclei, etc., are developed to provide the safety infrastructure for the super smart society (Society 5.0). Neutron/ion irradiation experiments are performed using the 930AVF cyclotron in CYRIC to evaluate soft errors of semiconductor devices which are used for Internet of Things (IoT).

Table 1 shows the operation time of the AVF cyclotron by the beam, and the ratio is shown in Fig. 1. Table 2 lists the ion nuclides which can be supplied by the cocktail beam acceleration technique in CYRIC. These beams can be switched without changing the magnetic field of the AVF cyclotron. Cocktail beam irradiation experiments occupied about half of the irradiation beam time. In cocktail beam experiments, many users apply several ion beams to change the LET. In order for users to take a longer irradiation time in the limited beam time, we need to switch the beam quickly. In the present status, flux measurements take long time to adjust the flux to the required one.

Previously, for the flux measurements, we have used a Si detector located at the irradiation position (downstream of the vacuum window). In this method, it was necessary to enter the experimental room several times for installing a Si detector and removing it after the flux adjustment. In order to reduce these times, we installed a Si detector in the beam line and attached it to a remotely controllable ladder which can be inserted and removed from the beam line. Because this detector was located upstream of beam irradiation position, it was necessary to calibrate the actual flux by comparing with the flux of the beam at the irradiation position. Then, the detector once calibrated, flux adjustment was possible without entering the experimental room unless the beam nuclide changes. However, the Si detector deteriorated rapidly due to the radiation damage. In addition, in the case of a high intensity beam (more than 10^3 particles/s/cm^2) irradiation, it was

necessary to attach a collimator in order to reduce the number of beam particles which hit the detector to less than 10^3 particles/s.

In order to solve the problem, we installed plastic scintillation detectors instead of the Si detectors. The plastic scintillators are more resistant to the radiation damage than the Si detector. These improvements shortened the time of the flux measurement, and increase the irradiation time in the limited beam time.

Table 1. Irradiation time for each beam nuclide.

	Proton	Neutron	Cocktail beam
FY2016 (2016/05 ~ 2017/03)	91 h	148 h	273 h
FY2017 (2017/05 ~ 2018/03)	0 h	185 h	182 h
Total	91 h	333 h	455 h

Table 2. Ion nuclides of cocktail beams that can be supplied in CYRIC.

Ion nuclides	Energy [MeV]	LET(Si)[MeV/mg/cm^2]
$^{15}N^{3+}$	56.3	3.3
$^{20}Ne^{4+}$	75	6.3
$^{40}Ar^{8+}$	150	15.3
$^{84}Kr^{17+}$	322.5	39.9
$^{129}Xe^{25+}$	454.2	69.2

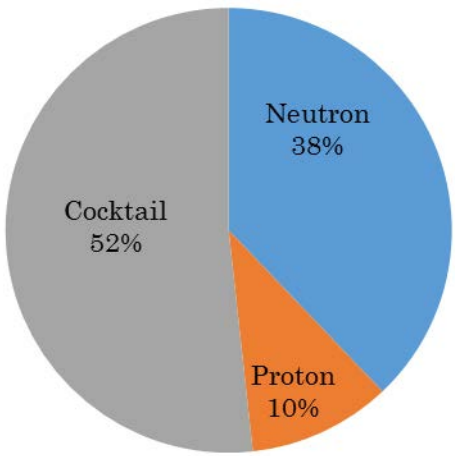

Figure 1. Ratio of the beam time of irradiation nuclides.

III. NUCLEAR ENJINEERING

III. 1. Tensile Properties of Helium Implanted Pure Tungsten

Miyazawa T.[1,], Niki K.[1], Hwang T.[1], Tsuchida K.[1], Hattori T.[1], Fukuda M.[2], Nogami S.[1], and Hasegawa A.[1]*

[1]Graduate School of Engineering, Tohoku University
[2]National Institutes for Quantum and Radiological Science and Technology

Introduction

Tungsten (W) is the most promising material for use as the divertor material for fusion reactors because of its high melting temperature, high resistance for sputtering and low tritium inventory. During fusion reactor operation, the divertor will be exposed to high-flux neutron irradiation, which results in displacement damage and nuclear transmutation elements in the component materials of the divertor. Solid elements such as rhenium (Re) and osmium (Os), and gaseous elements such as helium (He) and hydrogen (H) will be produced in the W matrix by nuclear transmutation reactions. The effects of Re and Os on material properties have been studied for several years[1)]. Helium-induced hardening effect in W has been studied[2)], while fracture behavior on He-implanted W have not yet been studied.

Helium is insoluble in all metals and is easily precipitated on defects or interfaces in materials such as point defect clusters, dislocations, precipitates and grain boundaries[3)]. It is well known that He precipitation on the grain boundary of metals causes grain-boundary embrittlement[4)]. Helium production in W by the transmutation reaction is estimated to be approximately 20 appm for the operation of DEMO for 5 years[5)]. In the case of austenitic stainless steels, it is known that just 5 appm He causes grain-boundary embrittlement at high temperatures[6,7)]. The grain-boundary embrittlement caused by He strongly depends on the He concentration, test temperature, and material. In contrast, low-temperature embrittlement is a well-known characteristic property of W. The low ductile-brittle transition temperature of the matrix and the weak grain-boundary bonding strength of W are

[*]Present address: Japan Atomic Energy Agency

considered the main reasons for the embrittlement, but the effects of He on the mechanical properties of W at a lower temperature and at the temperature of reactor operation have not yet been clarified. The present study aimed to clarify the effects of He on mechanical properties of pure W using tensile tests.

Experimental

Examined material of this work is a powder metallurgical processed pure W followed by hot rolling and stress relieved at 900ºC for 20 min. Detailed material data such as the fabrication process and chemical composition are described in the literature[8]. A small tensile specimen (SS-J) with a thickness of 0.23 mm was fabricated by electric discharge machining (EDM). The gauge section of the tensile specimens was 5 mm long and 1.2 mm wide.

Helium implantation was performed using the 50 MeV α-particle (He^{2+}-ion) beam of the cyclotron accelerator at Tohoku University. A tandem-type energy degrader system was used to obtain a uniform He distribution along the implanted direction. The specimen temperature during the implantation process was kept below 100ºC. Figure 1 shows the distribution of He and displacement damage in W calculated using the SRIM code[9] with a displacement threshold energy of 90 eV[10], when the He concentration at the uniformly implanted region was 100 appm. A calculated projected range of the 50 MeV He-ions in W was 0.26 mm. A uniform depth distribution of He was obtained along the specimen thickness direction. Three levels of He implantation (20, 100, and 200 appm) were conducted using the same irradiation conditions. Displacement damage by the He implantation were approximately 0.002, 0.01, and 0.02 dpa. After the He implantation, the tensile specimens were heat treated at 1100ºC for 100 hours in a vacuum-sealed quartz tube with zirconium foils in order to recrystallize pure W[11].

Vickers microhardness testing was performed on the tab of the tensile specimens at room temperature, with an indentation load of 1.96 N and a dwell time of 15 sec. Tensile tests were conducted in vacuum at 400 and 700ºC at a strain rate of 1.0×10^{-3}/sec. After the tensile test, fracture surfaces of the ruptured specimens were observed by a scanning electron microscope (SEM).

Results

Figure 2 shows the dependence of Vickers hardness on the He concentration before

and after the post-implantation annealing. Softening occurred for unimplanted specimens by the annealing because of recrystallization, while slight decreases of hardness were observed for He-implanted specimens after the post-implantation annealing. Post-implantation annealed specimens showed almost the same hardness as as-received unimplanted specimens.

Figures 3 and 4 show tensile stress-strain curves obtained at 400 and 700ºC, respectively. In the case of unimplanted specimens, the tensile strength decreased and total elongation increased after the annealing, which are typical changes of tensile properties for recrystallized materials. However, the tensile stress-strain curves for He-implanted specimens have almost the same shape as as-received specimens. The changes of tensile properties for post-implantation annealed specimens with respect to He concentration are not significant.

Figures 5 and 6 show SEM images of the fracture surfaces after the tensile tests. The reduction in area at 400 and 700ºC is also shown in Figs. 5 and 6, respectively. Large reduction in area with dimples were formed and ductile fracture was observed on the surface of all the ruptured specimens. No grain-boundary fracture surface was observed under the experimental conditions. Overall, the reduction in area at 700ºC was higher than that at 400ºC. The amount of plastic deformation in areas other than the necked region of specimens tested at 400ºC would be larger than that of specimens tested at 700ºC[12]. The delamination of the layered structure, which was typically observed in rolled W plates[12,13], was observed in the fracture surfaces except for unimplanted specimens tested at 400ºC.

Discussion

In thermal treatment conditions (1100ºC x 100 hours) in this study, it is considered that the mobility of He in W was low level to form He bubbles from the results of TDS. Post-implantation annealing was expected to the scavenging effect to sweep He on the dislocations and sub-grain boundary into the grain boundary due to the recovery and the recrystallization by the annealing of 1100ºC. It was confirmed to the recovery and the recrystallization in the unimplanted specimens after this annealing, while it was confirmed the moderate recovery in the He-implanted specimens. It is considered that implantation He arrests the dislocations and decreases the mobility of dislocations, and then suppress the recovery. He bubbles with size of 1 nm were finally observed in hot-rolled W with He concentration of 600 appm after the annealing of 1250ºC[14]. Therefore, large size He bubbles also might not form in He-implanted pure W after the annealing of 1100ºC x 100

hours in this study. Recovery of hardness caused by the annealing was almost constant with He concentration (20, 100, and 200 appm). This result indicates that extremely small amount of He can suppress the dislocation movement.

The deformation behavior by tensile tests at 400 and 700ºC for He-implanted specimens after the annealing of 1100ºC x 100 hours showed almost the same shape as as-received specimens. This means that implanted He form a new cluster and then hardly influence the dislocation slip at these temperatures. Fracture modes in these experimental conditions showed almost the same mode as as-received pure W. Fracture surfaces of as-received pure W were observed delamination of the layered structure caused by rolled-structure. It is considered that the recovery of dislocation structure by the annealing of 1100ºC x 100 hours is suppressed. Therefore, it is indicated that the recovery of dislocations in the matrix by the annealing or the accumulation of He into the grain-boundary by the dislocation movement during the plastic deformation at 400 and 700ºC is not occurred.

It is reported that the recrystallization of hot-rolled W with 600 appm He implantation did not occur for annealing temperatures below 1827ºC[14)]. He bubbles would suppress the recrystallization of hot-rolled pure W because He clusters might form on dislocations in low angle grain boundaries and cell walls in the matrix. Because of the suppression of recrystallization by the He clusters, the tensile properties of He-implanted specimens after post-implantation annealing show almost the same trend as those of as-received specimens under the experimental conditions. The results indicate that 20 appm of He implantation is level enough to suppress the recrystallization of pure W. Microstructure observation will be needed to explain clearly the experimental results, especially suppression effect of recrystallization by He implantation, for future works.

Summary

The effects of He on the mechanical properties of pure W were investigated using tensile tests. The obtained results are summarized as follows:

- The tensile properties of He-implanted specimens after post-implantation annealing show almost the same trend as those of specimens under these experimental conditions.
- Dimples were formed and ductile fracture was observed on the surface of all specimens. No grain-boundary fracture surface was observed under these experimental conditions.
- He bubbles would suppress the recrystallization of rolled pure W plates because He bubbles decorated to dislocations in low-angle grain boundaries.

・ 20 appm of He implantation is level enough to suppress the recrystallization of pure W.

References

1) Hasegawa A, Fukuda M, Yabuuchi K, Nogami S, *J. Nucl. Mater.* **471** (2016) 175-183.
2) Kong F, Qu M, Yan S, Zhang A, Peng S, Xue J, Wang Y, *Nuclear Instruments and Methods in Physics Research B* **406** (2017) 643-647.
3) Trinkaus H, Singh B, *J. Nucl. Mater.* **323** (2003) 229-242.
4) Braski D, Schroeder H, Ullmaier H, *J. Nucl. Mater.* **83** (1979) 265-277.
5) Bolt H, Barabash V, Federici G, Linke J, Loarte A, Roth J, Sato K, *J. Nucl. Mater*. **307-311** (2002) 43-52.
6) Kramer D, Brager H, Rhodes C, Pard A, *J. Nucl. Mater.* **25** (1968) 121-131.
7) Hasegawa A, Masuda N, Satou M, Abe K, Effects of helium on grain boundary fracture of austenitic stainless steel: 10th International Conference on Environmental Degradation of Materials in Nuclear Power Systems – Water Reactors-, Lake Tahoe, NV, USA, 2002.
8) Fukuda M, Nogami S, Yabuuchi K, Hasegawa A, Muroga T, *Fusion Sci. Technol*. **68** (2015) 690-693.
9) <http://www.srim.org/>.
10) Standard Practice for Neutron Radiation Damages Simulation by Charge-Particle Irradiation, E521-96, Annual Book of ASTM Standards, 12.02, 1996.
11) Tsuchida K, Miyazawa T, Hasegawa A, Nogami S, Fukuda M, *Nucl. Mater. Energy* **15** (2018) 158-163.
12) Sasaki K, Yabuuchi K, Nogami S, Hasegawa A, *J. Nucl. Mater*. **461** (2015) 357-364.
13) Fukuda M, Nogami S, Hasegawa A, Usami H, Yabuuchi K, Muroga T, *Fusion Eng. Des.* **89** (2014) 1033-1036.
14) Chernikov V, Lakhotkin J, Ullmaier H, Trinkaus H, Jung P, Bierfeld H, *J. Nucl. Mater.* **212-215** (1994) 375-381.

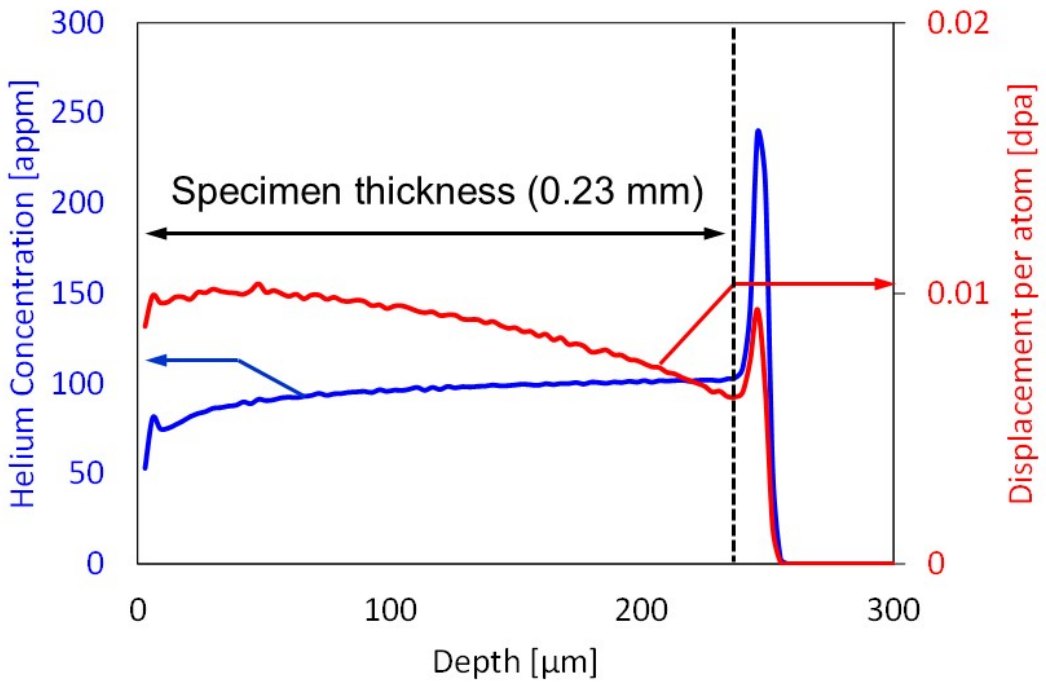

Figure 1. Distribution of He and displacement damage in W calculated using the SRIM code [9] when the He concentration at the uniformly implanted region was 100 appm.

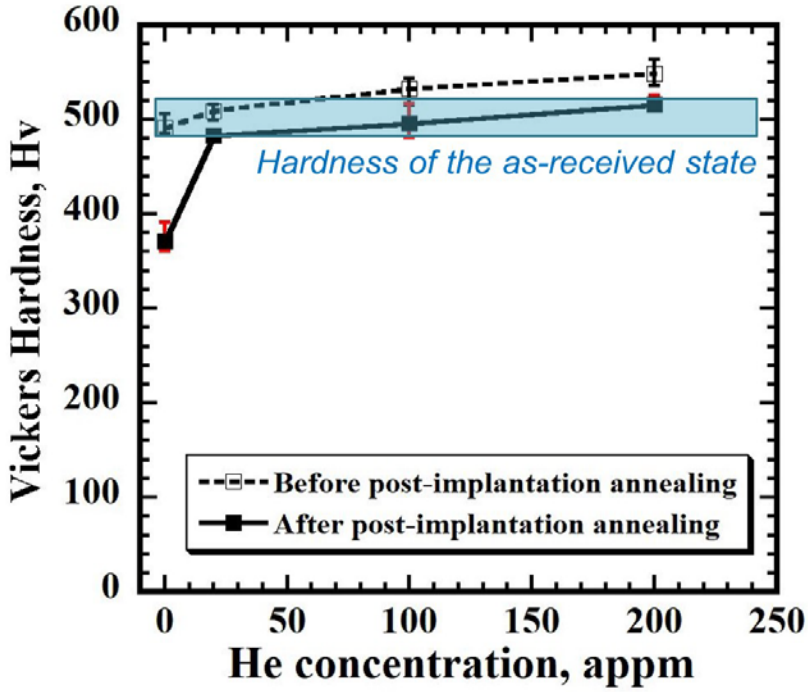

Figure 2. Dependence of Vickers hardness on He concentration before and after post-implantation annealing.

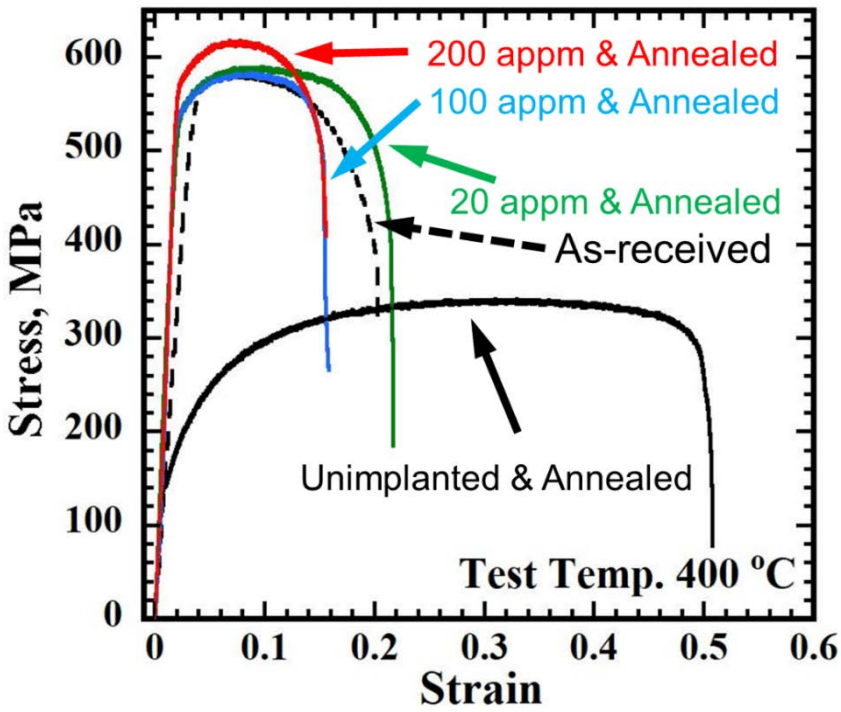

Figure 3. T ensile stress-strain curves at 400ºC.

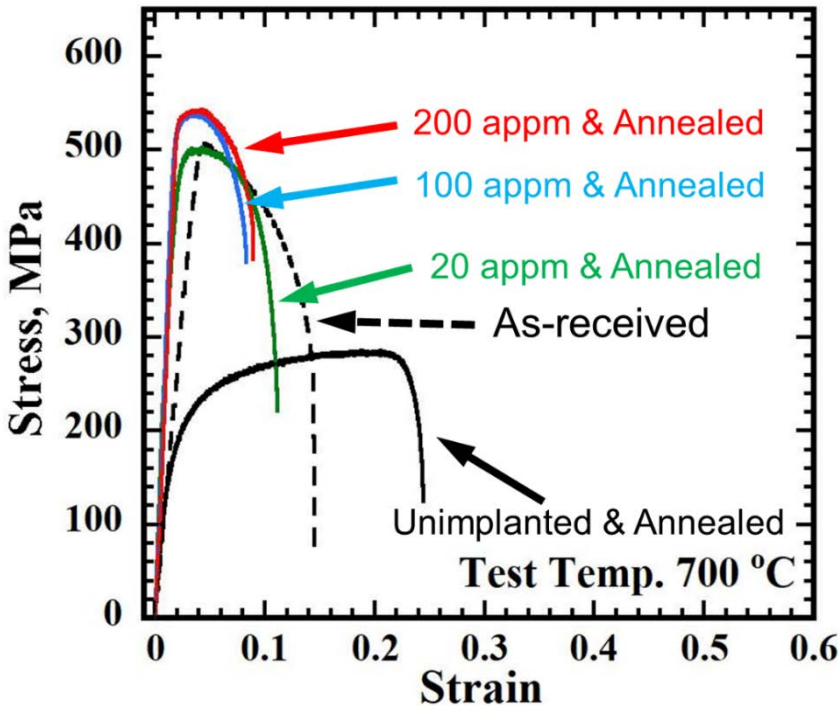

Figure 4. Tensile stress-strain curves at 700ºC.

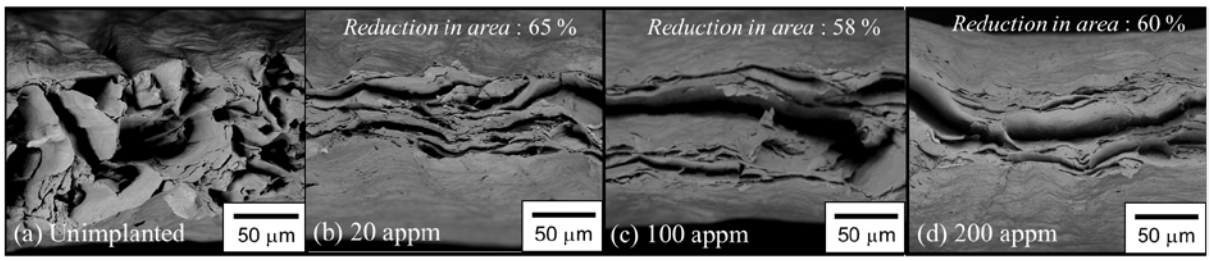

Figure 5. SEM images of the fracture surface tested at 400ºC for (a) unimplanted, (b) 20 appm He implanted, (c) 100 appm He implanted, and (d) 200 appm He implanted specimens.

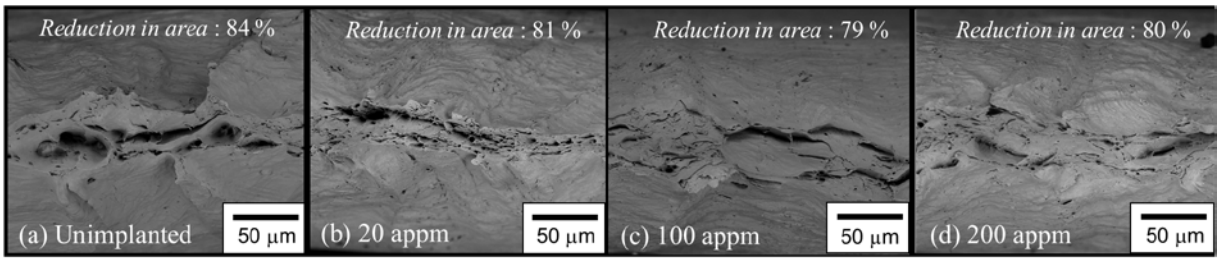

Figure 6. SEM images of the fracture surface tested at 700ºC for (a) unimplanted, (b) 20 appm He-implanted, (c) 100 appm He-implanted, and (d) 200 appm He-implanted specimens.

III. 2. The Irradiation Resistance of Zr-1.8Nb Alloy under the 140 MeV-C^{4+} Irradiation

Kano S.[1], Yang H.[1], Zhao Z.[1], McGrady J.P.[1], Itoh M.[2], Tanaka K.S.[2], and Abe H.[1]

[1]Department of Nuclear Engineering, The University of Tokyo
[2]Cyclotron and Radioisotope Center, Tohoku University

The material examined in the present study was a Zr–1.8Nb (wt.%) alloy recently developed as the fuel cladding tubes of pressurized water reactors. Such kind of Zr-based alloys are widely reported to exhibit remarkable hardening/strengthening due to the irradiation, typically ~100 MPa increase in the yield strength (YS) at room temperature[1,2]. The irradiation defects in Zr-based alloys (i.e. dislocation loops) are divided into two groups: the <a>-type loop formed on the prismatic planes and the <c>-type loop on the basal plane. The <a>-type loop is either vacancy or interstitial nature; in both cases the Burgers vector (*b*) is 1/3 $\langle 11\bar{2}0 \rangle$. This type of dislocation loop is produced with low doses less than 5×10^{25} n/m^2 [3]. The size is typically 5–20 nm and the number density is 10^{21}–10^{22} /m^3 primarily depending on the irradiation temperature. At high doses greater than ~5×10^{25} n/m^2 the <c>-type dislocation loops start to appear. They are mainly vacancy-type in nature and the Burgers vector is either 1⁄2 $\langle 0001 \rangle$ or 1⁄6 $\langle 20\bar{2}3 \rangle$[4-6]. The <c>-type loop is in many cases larger than the <a>-type loop in terms of size and lower in number density. The <c>-type dislocation loops are extensively believed to be closely related to performance degradations such as irradiation growth and the ductility loss induced by irradiation[7-10]. Therefore, the aim of the present study is to examine the irradiation resistance in the new developed Zr-1.8Nb alloy in terms of mechanical property change and irradiation defects evolution.

The tube shaped Zr-1.8 Nb (wt.%) alloy was used as the start materials. The tube was firstly cut in half, and the half piece was subsequently cold-rolled into a flat sheet. The thickness was reduced from 0.55 to 0.38 mm. The rolling direction was parallel to the axial direction of the tube. Finally, the cold-rolled sheets were annealed at 853 K for 24 h in vacuum (<5×10^{-4} Pa) and followed by cooling, so as to recrystallize the Zr matrix.

The small size tensile specimens (gauge section: 5 mm in length and 1.2 mm in width)

were punched out from the cold-rolled and annealed sheets with the length direction being perpendicular to the rolling direction. Both sides of tensile specimens were mechanically grinded and finished with mechano-chemical polishing in a suspension of 0.05 μm silica particles. The final thickness of tensile specimens was 180±5 μm.

140 MeV-C^{4+} ion beam was employed to irradiate the tensile specimens mounted on a sample stage equipped with a heating/cooling temperature-control system in the Cyclotron and Radioisotope Center, Tohoku University[11]. The temperature was continuously monitored and recorded by a thermocouple fixed in the vicinity of specimen throughout the irradiation. The irradiation temperature was carefully controlled at 573±10 K. Displacement damage was determined from the fraction of vacancies calculated by Kinchin-Pease option in SRIM code[12], with the displacement threshold energies of 40 MeV for Zr. Penetration depth of the 140 MeV-C^{4+} in Zr is ~180 μm, comparable to the thickness of tensile specimens. In order to create spatially homogeneous irradiation defects, a variable energy degrader was used. It is a rotating wheel system consisting of a set of Al foils with the thickness ranging from 0 to 284 μm, which enables to produce the roughly homogeneous distribution of irradiation defects throughout the specimen thickness. The beam current density was 3.4×10^{-3} A/m^2, Tensile specimens with displacement damages of roughly 0.2, 1.7, 3.1 and 5.3 dpa (displacement per atoms) were achieved in the present study. Additionally, the amount of implantation C atoms was estimated as 230 at. ppm for 3.1 dpa specimen.

Tensile tests were carried out at room temperature and the strain rate was set to 10^{-3} /s with a high-accuracy laser displacement measurer. Microstructure characterization was performed using 200 keV transmission electron microscopes (TEM). The TEM specimen was lifted out from the unstrained tensile specimens via a focused ion beam (FIB) technique.

The stress-strain (σ-ε) curves for unirradiated and irradiated specimens are shown in Fig. 1. The total elongation of unirradiated specimen was 25%, which was decreased evidently due to irradiation. Note that the uniform elongation was nearly zero for the highly irradiated specimens (3.1 and 5.3 dpa); this is probably an indication of the occurrence of the dislocation channeling. Both the yield strength (YS) and ultimate tensile strength (UTS) drastically increased at low doses below 1 dpa, and increased moderately beyond that point. The YS for the 3.1 and 5.3 dpa specimens was 137% and 145% of that of unirradiated specimen, whereas the uniform/total elongation for the 3.1 and 5.3 dpa specimens was less than a half of unirradiated specimen. A comparison of these two indicates that the rate of embrittlement is fairly faster than the rate of strengthening.

In the analysis of irradiation defect clusters, observation of the <c>-type loops were

performed from a direction close to the [11$\bar{0}$0] zone axis, where the <c>-type loops are in edge-on view parallel to the basal plane regardless of the Burgers vector. This aligned array of linear contract was typical feature of <c>-type loops observed in irradiated Zr and its alloys [7,13,14]. The diameter of the <c>-type loops was determined by the length of line segments visualized on TEM images. The diameter was in a range from 3 to 50 nm, and the mean diameter was 15.4±7.4 nm. The number density of <c>-type loops was 6.5×10^{20} /m^3. Observation of the <a>-type loops was performed near the [0001] zone axis. Seen from this direction, the <a>-type loops are in edge-on view parallel to the prismatic planes. The <c>-type loops are invisible in the case of b=1/2 ⟨0001⟩ but visible in the case of b=1/6 ⟨202$\bar{3}$⟩; however, those visible <c>-type loops are distinguishable from the <a>-type loops by shape on the TEM image. The diameter of <a>-type loops was in a range from ~3 to 30 nm, and the mean diameter was 7.2±3.6 nm. The number density of <a>-type loops was 1.2×10^{21} /m^3.

In conclusion, 140 MeV-C^{4+} irradiation at 573 K up to 5.3 dpa was successfully conducted on a Zr–1.8Nb alloy to evaluate its mechanical properties change. The yield strength and the total elongation of 3.1 dpa irradiated specimens were >137% and <50% of unirradiated specimen, indicating that the rate of embrittlement is fairly faster than the rate of strengthening. TEM observation on the 3.1 dpa specimen revealed that the size and number density of dislocation loops were 7.2 nm and 1.2×10^{21} /m^3 for the <a>-loops, 15.4 nm and 6.5×10^{20} /m^3 for the <c>-type loops, respectively.

This research was supported by JST Innovative Nuclear Research and Development Project.

References

1) Boyne A, Shen C, Najafabadi R, Wang Y, J. Nucl. Mater. **438** (2013) 209.
2) Byun T, Farrell K, J. Nucl. Mater. **326** (2004) 86.
3) Northwood D, Gilbert R, Bahen L, Kelly P, Blake R, Jostsons A, Madden P, Faulkner D, Bell W, Adamson R, J. Nucl. Mater. **79** (1979) 379.
4) Griffiths M, J. Nucl. Mater. **159** (1988) 190.
5) Yan C, Wang R, Wang Y, Wang X, Bai G, Nucl. Eng. Technol. **47** (2015) 323.
6) Jin H, Kim T, Ann. Nucl. Energy **75** (2015) 309.
7) Tournadre L, Onimus F, Béchade J, Gilbon D, Cloué J, Mardon J, Feaugas X, Toader O, Bachelet C, J. Nucl. Mater. **425** (2012) 76.
8) Woo O, Carpenter G, MacEwen S, J. Nucl. Mater. **87** (1979) 70.
9) Yamada S, Kameyama T, J. Nucl. Mater. **422** (2012) 167.
10) Hengstler-Eger R, Baldo P, Beck L, Dorner J, Ertl K, Hoffmann P, Hugenschmidt C, Kirk M, Petry W, Pikart P, Rempel A, J. Nucl. Mater. **423** (2012) 170.
11) Orihara H, Murakami T, Nucl. Instrum. Methods **188** (1981) 15.
12) Ziegler J, Manoyan J, Nucl. Instrum. Methods B **35** (1988) 215.
13) Yamada S, Kameyama T, J. Nucl. Mater. **422** (2012) 167.
14) Holt R, Gilbert R, J. Nucl. Mater. **137** (1986) 185.

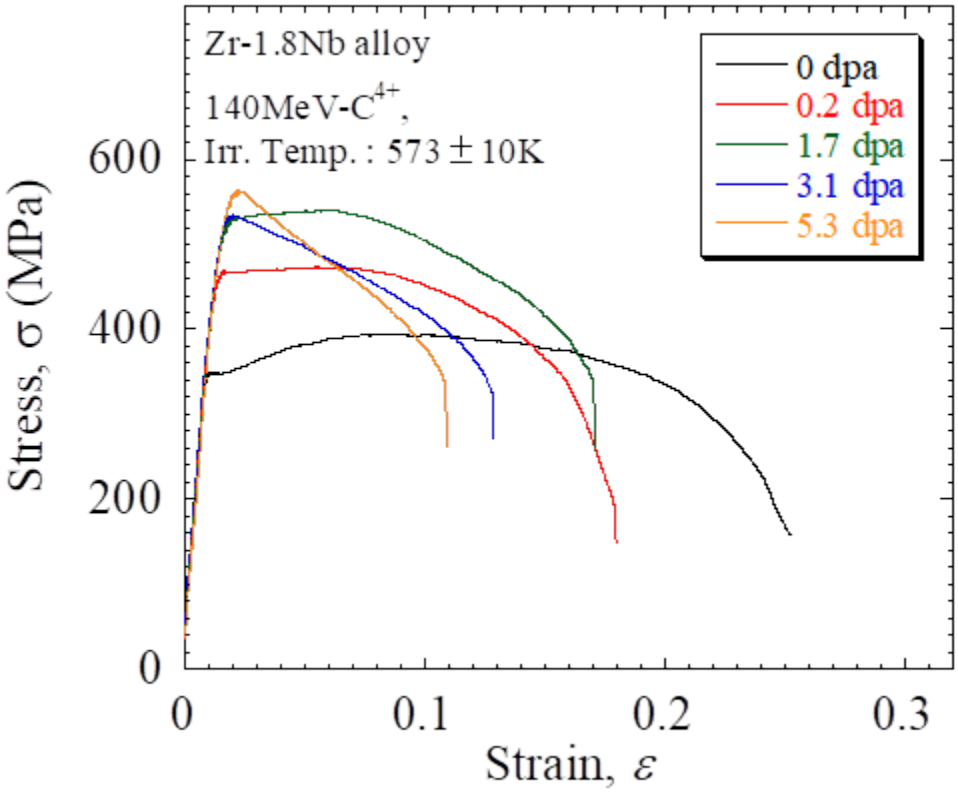

Figure 1. Stress-strain curves of irradiated and unirradiated Zr-1.8Nb alloy.

III. 3. Helium Implantation into Highly Microstructure-Controlled B_4C-based Ceramics

Maki R. S. S., Katabuchi T., and Yoshida K.*

Laboratory for Advanced Nuclear Energy, Institute of Innovative Research, Tokyo Institute of Technology

Introduction

B_4C pellets have been used as neutron absorbers in control rods of both boiling water reactors (BWR) and fast breeder reactors (FBR). Volume swelling occurs by accumulation of helium bubbles produced by the $^{10}B(n, \alpha)^7Li$ reaction[1-3], which results in failure of a cladding tube due to extensive mechanical interactions between B_4C pellets and cladding tubes[4]. To extend the lifetime of control rods and then improve safety performance of fast reactors, it is essential to develop the high-performance B_4C pellets to overcome the above problem. We have synthesized the highly microstructure-controlled B_4C-based ceramics for neutron absorbers by controlling the microstructure of B_4C pellet such as particle size, crystal-orientation, pore-diameter, pore-shape and pore-orientation. This highly controlled microstructure could release helium gas produced during neutron absorption without excessive accumulation of helium, and thereby suppress volume swelling. The purpose of this research is to mimic helium generation in a B_4C pellet by implanting helium ions, instead of neutron irradiation in a fast reactor, and evaluate accumulation and release of helium gas of highly microstructure-controlled B_4C-based ceramics.

Experimental procedure

The B_4C/ carbon nanotube (CNT) composite was used as target sample in this research. Commercial B_4C and CNT mixed with Al powder, sintering additive, were used as starting materials. Powder mixture with a composition of 85 vol% B_4C, 10 vol% CNT and 5 vol% Al was pressed into 22×35×1 mm rectangular plate. The fabrication of B_4C/CNT

**Present address: 2-12-1 O-okayama, Meguro-ku, Tokyo 152-8550 Japan. E-mail: maki.r.ab@m.titech.ac.jp*

composite was performed with a hot-press apparatus (FVPHP-R-5, Hi-Multi-5000, Fuji Dempa Kogyo Co., Ltd., Japan) at around a pressure of 60 MPa at 1950˚C for 1 hour under Ar gas flow (2 L/min). The ^{10}B isotopic composition of the B_4C sample was the natural abundance ratio (19.8%). In addition to the B_4C/CNT sample, a B_4C pellet, which had been irradiated with neutrons as a control rod CR0901 of the fast reactor, JOYO, was prepared for comparison. The burnup was estimated about 80×10^{20} captures/cc from calculation with the code HESTIA[5].

A fabricated B_4C/CNT sample was bombarded with He ions from a 930 AVF cyclotron of CYRIC. The implantation energy of helium ions was chosen to be 30 MeV. From calculation using the ion transport code SRIM[6], the implantation depth from the surface is 300 μm, deep enough that highly controlled microstructure well forms. A target holder was made for irradiation of a B_4C-based ceramics as shown in Fig. 1. The B_4C/CNT sample was set to the target station the course 1 of the first target room and irradiated with 30 MeV He^{2+} beam at an average beam current around 1 μA for 8 hours. The front surface of the sample was continually cooled with helium gas flow and the target holder was cooled with circulating water during implantation.

Helium gas release behavior of the He-implanted B_4C/CNT sample and the B_4C pellet (JOYO) was evaluated with a thermogravimetry mass spectrometer (TG-MS: JMS-Q1500GC, JEOL). Prior to the TG-MS analysis, these samples were pulverized using a B_4C mortar. In order to evaluate the dependence of the release behavior of helium gas on the grain size, two powder samples of the B_4C pellet (JOYO) with different grain sizes, about 50-400 and 1-10 μm, were prepared (Fig. 2).

Results and discussion

In the helium ion implantation, helium ions were implanted up to 1.1×10^{17} ion/cm^2, sufficient dose to evaluate the release behavior of helium gas. TG-MS analysis for the B_4C (JOYO) showed the dependence of the release behavior of helium gas on the grain size (Fig. 3). The helium gas was released promptly at lower temperature in fine powder than coarse powder. Thus, we prepared fine powder from He-implanted B_4C/CNT sample. Its release behavior of the helium gas had relatively good agreement with that of B_4C pellet (JOYO) as shown in Fig. 4, but the helium gas release was observed at higher temperature than B_4C pellet (JOYO).

Conclusion

In the present work, 30 MeV helium ions were implanted into B_4C-based ceramics using a He beam from a 930 AVF cyclotron at CYRIC. The release behavior of helium gas in the He-implanted B_4C-based ceramics was successfully evaluated with TG-MS analysis. It is found that helium gas release rate depends on the grain size, and He-implanted B_4C/CNT sample showed relatively similar behavior to a JOYO's B_4C pellet.

Acknowledgement

This work was supported by The Ministry of Education, Culture, Sports, Science and Technology (MEXT) under the framework of Innovative Nuclear Research and Development Program.

References

1) Jostsons A., Dubose C. K. H., Copeland G. L., Stiegler J. O., *J. Nucl. Mater.* **49** (1973/74) 136.
2) Hollenberg G. W., Basmajian J. A., *J. Am. Ceram. Soc.* **65** (1982) 179.
3) Maruyama T., Onose S., Kaito T., Horiuchi H., *J. Nucl. Sci. Tech.* **34** (1997) 1006.
4) Maruyama T., *J. Tech. Assoc. Refr.* **30** (2010) 80.
5) Ohkawachi Y., Maeda S., Sekine T., Nagasaki H., *Report JNC-TN9400-2002-070,* Japan Nuclear Cycle Development Institute (2003). (in Japanese)
6) Ziegler J. F., Ziegler M. D., Biersack J. P., *Nucl. Instrum. Methods B* **268** (2010) 1818.

Figure 1. A target holder for irradiation of a B_4C-based ceramics

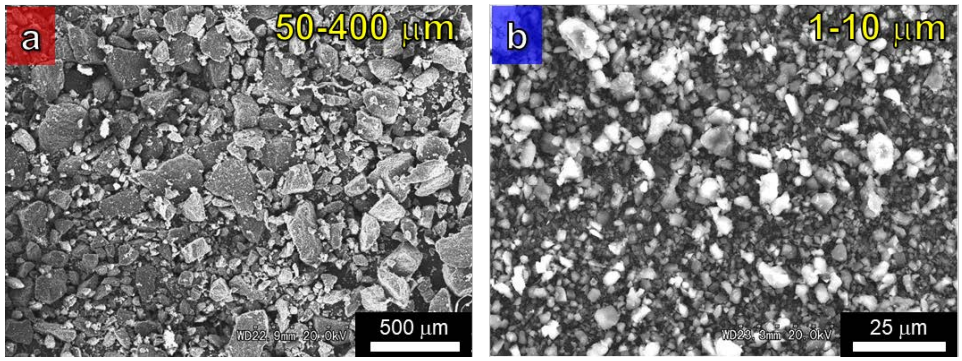

Figure 2. The pulverized B_4C pellet (JOYO) with different grain sizes; (a) coarse powder and (b) fine powder

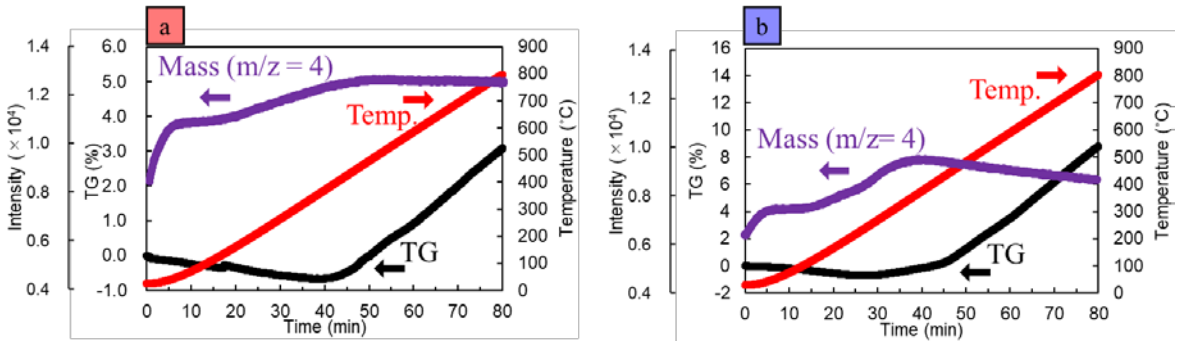

Figure 3. TGA curves and mass chromatograph of pulverized B_4C pellet (JOYO) with different grain sizes; (a) coarse powder and (b) fine powder

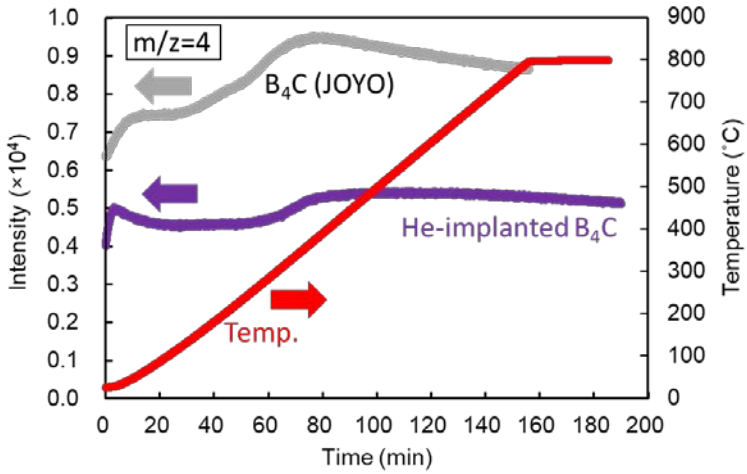

Figure 4. Mass chromatograph of pulverized B_4C pellet (JOYO) and He-implanted B_4C/CNT sample

III. 4. Neutron Spectrum Measurement for d-Li Neutrons Using Activation Method

Kwon S.[1], Ohta M.[1], Oyaidzu M.[1], Ochiai K.[1], Terakawa A.[2], Itoh M.[2], Ishibashi Y.[2], Yuki Y.[2], Sato S.[1], and Kasugai A.[1]

[1]National Institutes for Quantum and Radiological Science and Technology
[2]Cyclotron and Radioisotope Center, Tohoku University

We are carrying out a conceptual design activity of Advanced Fusion Neutron Source (A-FNS) facility, and are to perform radiation irradiation tests for fusion DEMO reactor materials in A-FNS[1)]. A-FNS produces a large number of neutrons via d-Li stripping reaction[2)] by bombarding a liquid lithium target with 40 MeV deuteron beam of 125 mA same as IFMIF[3)] projects. The enormous radiations should be measured and calculated precisely in A-FNS in order to evaluate the neutrons and photons indicate a DPA and ^{4}He production in the test specimen in the irradiation test module. As a candidate measurement method, we have proposed the neutron spectrum measurement system of A-FNS with neutron activation systems using water flow, and several activation monitors[4)]. Accurate dosimetry cross section data should be required for high precision measurement of the neutron spectrum using the activation method. However, the nuclear data libraries above 20 MeV neutrons are very limited. Although there are only two representative dosimetry cross section libraries, JENDL/D-99[5)] and IRDFF-1.05[6)], JENDL/D-99 is given in the neutron energy region below 20 MeV. Besides, an experimental data for a neutron-induced cross section in the high energy region above 20 MeV is also scarce. In order to verify the dosimetry cross sections and an applicability of the reactions as the neutron spectrum measurement above 20 MeV for A-FNS, we have performed an experiment of activation cross-section measurement on eight threshold dosimetry reactions with d-Li neutron source at CYRIC of Tohoku University.

Figure 1 shows a photograph of the experimental setup employed at the end of the 32-beam course of CYRIC. Along the beam line, the cylindrical solid lithium target of 25 mm in thickness and 20 mm in radius was set in a pure aluminum holder to prevent unnecessary long-lived activation products from the experimental apparatus. Several activation reactions were selected as the candidates based on its half-life, gamma intensity

and handleability[4]. The activation foils of Cobalt, Niobium, Gold and Bismuth were located at the positions of 0 cm, 5 cm, 10 cm distance from the aluminum holder, in order to measure the dosimetry reaction rates of the (n,p) and (n,xn) reactions. Table 1 shows the eight dosimetry reactions with the evaluable energy ranges in this experiment. In addition, two inclined panels with ± 30° were placed to measure the dosimetry reaction rates as a function of angle between the beam line and the foils, 6°, 22° and 38°, as shown in Fig. 2. The foils are in the form of pure metal with dimensions, 10.0 × 10.0 × 1.0 mm^3. The beam irradiation was performed for 5 hours with ~1.1 μA average beam current. After the irradiation, We measured the dosimetry reaction rates of $^{59}Co(n,p)^{59}Fe$, $^{59}Co(n,2n)^{58}Co$, $^{59}Co(n,3n)^{57}Co$, $^{93}Nb(n,2n)^{92m}Nb$, $^{197}Au(n,2n)^{196}Au$, $^{209}Bi(n,3n)^{207}Bi$, $^{209}Bi(n,4n)^{206}Bi$ and $^{209}Bi(n,5n)^{205}Bi$ reactions as functions of distances from the Li target holder, and angles between the beam line and foils to compare the calculation result of the reaction rate with the experiment ones due to differences of the neutron spectrum. The experimental analyses were performed using a Monte Carlo transport code, McDeLicious-11[7] that has been developed as the extension code of MCNP5[8] to simulate the d-Li neutron source. The latest fusion evaluated neutron data library, FENDL-3.1d[9], was used for the transport calculation. The reaction rates of the activation foils were calculated using the dosimetry cross-section data library, IRDFF-1.05. Several reactions data are not included in IRDFF-1.05, and we used the data in FENDL/A-3.0[10] for following reactions: $^{209}Bi(n,4n)^{206}Bi$ and $^{209}Bi(n,5n)^{205}Bi$.

Figures 3 and 4 show the typical results of the experiment. The Cal./Exp. is the ratios of the calculated reaction rates of the reactions to the experimental ones at 5 cm distance from the surface of the Li target and at 38° angle between the beam line and the foils, respectively. The calculated reaction rates of $^{59}Co(n,2n)^{58}Co$, $^{59}Co(n,3n)^{57}Co$, $^{93}Nb(n,2n)^{92m}Nb$, $^{197}Au(n,2n)^{196}Au$ and $^{209}Bi(n,3n)^{207}Bi$ reactions at 5 cm distance agree well the experimental one within 20%. The calculated reaction rates of $^{59}Co(n,p)^{59}Fe$, $^{59}Co(n,2n)^{58}Co$, $^{59}Co(n,3n)^{57}Co$, $^{93}Nb(n,2n)^{92m}Nb$, $^{197}Au(n,2n)^{196}Au$, $^{209}Bi(n,3n)^{207}Bi$ and $^{209}Bi(n,4n)^{206}Bi$ reactions at 38° angle agree well the experimental one within 20%. As the results, the reactions can be applied to the A-FNS neutron spectrum measurement system for the high neutron energy region. However, the calculated reaction rate of $^{209}Bi(n,5n)^{205}Bi$ reaction underestimates the experimental one at 5 cm distance and overestimates the experimental one at 38° angle, respectively. Further investigation for the accuracy of FENDL/A-3.0 is necessary. In this study, it is indicated that the present dosimetry cross-section data of $^{59}Co(n,3n)^{57}Co$, $^{197}Au(n,2n)^{196}Au$, $^{209}Bi(n,3n)^{206}Bi$, reactions in IRDFF-1.05 can be used for the A-FNS spectrum measurement system within ~20% of measurement accuracy. The

reactions can cover the neutron energy range from 10 MeV to 45 MeV.

References

1) Nishitani T. et al., *Fusion Sci. Technol.* **68** (2015) 326.
2) Serber R., *Phys. Rev.* **72** (1947) 1008.
3) Knaster J. et al., *Nat. Phys.* **12** (2016) 424.
4) Kwon S. et al., *Nucl. Mater. Energ.* **16** (2018) 207.
5) Kobayashi K. et al., JAERI 1344 (2002).
6) https://www-nds.iaea.org/IRDFF (current as of Aug. 2018).
7) Simakov S. P. et al., *Fusion Sci. Technol.* **62** (2012) 233.
8) X-5 Monte Carlo Team, LA-UR-03-1987 (2003).
9) https://www-nds.iaea.org/fendl (current as of Aug. 2018).

Table 1. Measured dosimetry reactions.

Foil nuclide	Reaction	Measured nuclide	Half-life	Measured γ-ray energy [keV]	Intensity [%]	Neutron sensitivity [MeV]	Measuring Time [sec]
^{59}Co	(n,p)	^{59}Fe	44.5 d	1099.24	56.5	8<E<25	~150,000
	(n,2n)	^{58}Co	70.9 d	810.76	99.45	13<E<27	~150,000
	(n,3n)	^{57}Co	271.7 d	122.06	85.6	25<E<45	~150,000
^{93}Nb	(n,2n)	^{92m}Nb	10.2 d	934.44	99.07	11<E<22	~1,050
^{197}Au	(n,2n)	^{196}Au	6.2 d	355.73	86.95	10<E<20	~1,000
^{209}Bi	(n,3n)	^{207}Bi	32.9 y	569.70	97.75	20<E<30	~250,000
	(n,4n)	^{206}Bi	6.2 d	803.10	99.00	30<E<40	~4,600
	(n,5n)	^{205}Bi	15.3 d	703.45	31.10	40<E<55	~250,000

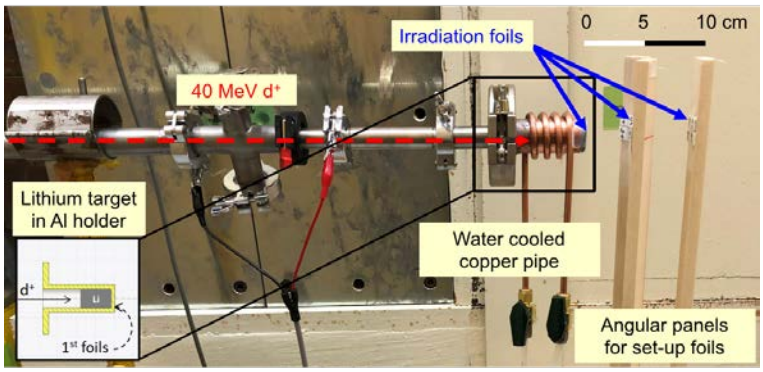

Figure 1. A photograph of the experimental setup.

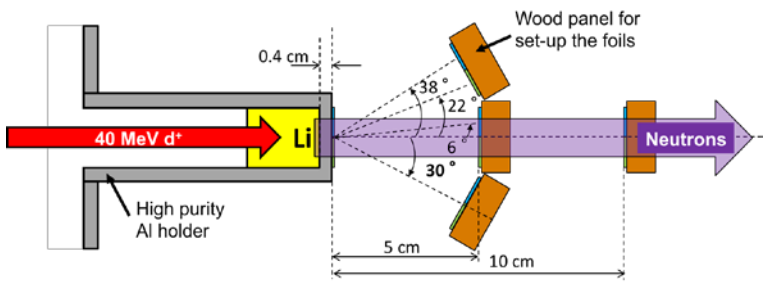

Figure 2. Cross sectional view of the experimental setup and irradiation foils position.

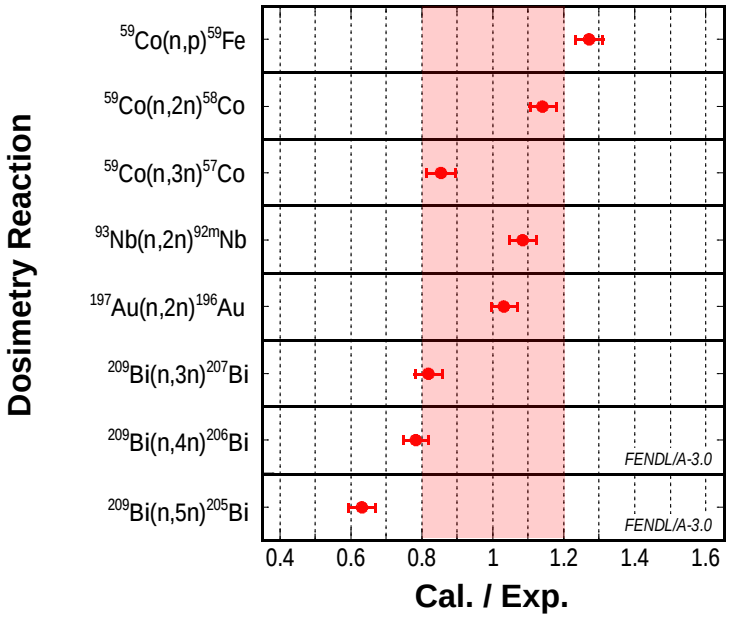

Figure 3. Cal./Exp. on the reaction rates of all reactions at 5 cm distance from the Li target holder.

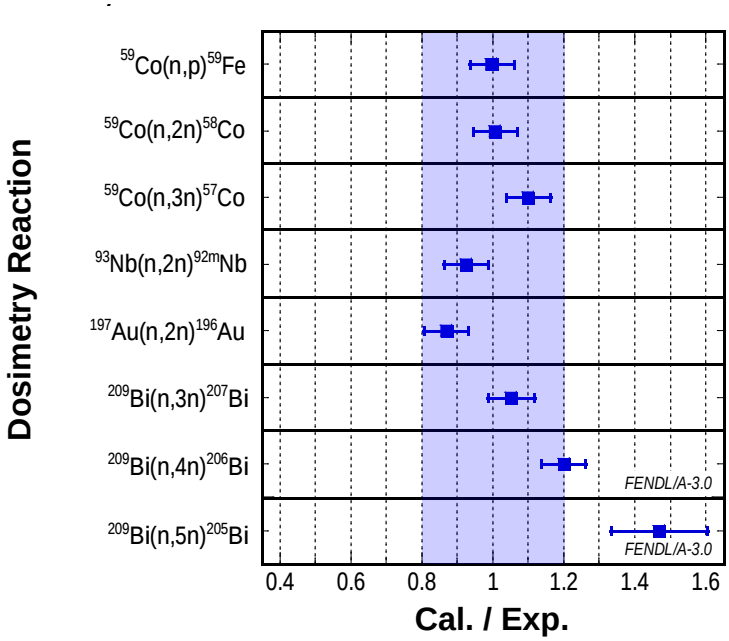

Figure 4. Cal./Exp. on the reaction rates of all reactions at 38° angle between the beam line and the foils.

III. 5. Radiation Hardness Assurance for Micro Lunar Rover Project: HAKUTO

Oikawa T.[1], Tanaka T.[2], and Yoshida K.[1]

[1]Department of Aerospace Engineering, Graduate School of Engineering, Tohoku University
[2]ispace inc.

Introduction

In the past 20 years, start-ups have emerged as the major drivers towards fueling another space race era, further advancing the space industry. One of the key players that assisted this movement is the Google Lunar XPRIZE (GLXP), which is an international competition of 16 teams around the globe. The challenge is to land on the Moon, to travel over 500 meters, and to send high definition video and images back to the Earth by the end of 2017. Among the competitors, team HAKUTO is the sole Japanese team, and we are at the final stage of rover development (as of the timing we had radiation test at Cyclotron Center)[1)]. Our rover needs to survive the extreme space environment, and the qualification of the avionics is required to confirm that the mission is feasible. Since the 1960s, space-grade electronics have been tailored based on military standards or the techniques nurtured during the space race[2)]. Owing to strict guidelines and testing protocols, customized parts were generally associated with a high development cost while the state-of-the-art technologies of that time were not implemented to reduce potential failure. With the selection being scarce, transitioning to readily available yet affordable commercial off-the-shelf (COTS) hardware was not a difficult choice. This trend enabled flexibility when choosing high performance power efficient platforms, replacing the obsolete devices for space applications. These products, however, still present challenges; many of the COTS components do not qualify for the successful operation under harsh space conditions. To verify their performance, intensive testing and inspection are conducted to ensure their reliability under such conditions. As a start of radiation assurance, the total ionization dose (TID) test is typically conducted using radioactive isotopes such as Co-60 or Cs-137 to determine whether the parts meet the desired confidence level for space operation[3)]. The

test enables the review of the COTS hardware degradation by accumulating a large amount of radiation in a short period of time, typically exposing it to a much higher dosage level beyond the mission requirement. Another aspect that needs to be considered is the single event effect (SEE) on the hardware to assess any probabilistic errors by high-energy bombardment[4]. Using these experiments for the preflight assessment review, COTS devices are certified as near flight-ready with an adequate reliability based on the terrestrial stage analysis. This test will focus on the SEE on an electronic device using a proton beam: a near representation of solar energetic particles.

Evaluation Methodology

During the testing phase, we defined several potential hazardous points the devices might experience during bombardment. Table 1 presents a list of potential failure modes during the experiment: SEU, single event functional interrupt (SEFI), and SEL. We represented the potential threat cases as a circle and not applicable as a cross, depending on the power mode of the electronics and the region of interest during the experiment. Furthermore, for each device, we investigated the functionalities that we would like to confirm (i.e., checking the serial outputs, read/write on RAM, analog-to-digital conversion (ADC) function, power consumption, communication status, and taking of images). In most cases, we monitored the device power supply current as a highest priority to determine the probability of SEL during equivalent mission dosages of radiation. Other potential breakdowns caused by the SEE, such as a single event gate rupture and a single event burnout, were not considered in this test as galactic energies are on the order of 1 GeV.

Results

The test results from the CYRIC radiation facility are shown in Table 2. Of the five tested electronics, the IC from the motor controller experienced SEL twice at 2350 and 3300 seconds. With the power reboot, the motor controller recovered back to its operational state both times without any increase in power consumption. Additionally, SEFI occurred once on the radio interface board at 1834 seconds, and the ADC value was not received via any serial output. Since the watchdog timer was not initiated, we concluded that the problem came from an abnormality in the serial function. We confirmed that the device could recover from the SEE by power reset, and an increase in power consumption was not observed. The other three devices did not experience any SEE throughout the test. Because of a high fluence rate at the CYRIC facility, the five tested devices were exposed beyond

the expected two days worth of the mission time frame on the Moon. In fact, all of them were irradiated enough for the rover to stay at least two lunar cycles. The few SEE instances justified the probability that a component malfunction by radiation is low, while each component is recoverable. Thus, we conclude that the device is radiation tolerable.

Conclusion

The COTS devices tested in this study demonstrated that the system can be recovered from the proton-induced SEE. Although one of the devices experienced an increase in power consumption due to SEFI, each powered hardware was able to recover using power rebooting. For future work, further SEE experiments on a fully integrated system should be conducted to verify any failures when several components are relaying on complex commands to various hardware. Moreover, we need to confirm the SEE occurrence based on the LET spectrum for the lunar surface conditions (by using heavy ions as radiation source). Future missions will most likely require the operation of the device for a longer time duration, and therefore, extensive testing will be required for further qualifications. This result has been published as journal paper[5].

Acknowledgments

We express our special thanks to the faculties and staff at Tohoku University and the CYRIC facility.

References

1) Walker, J., Britton N., Yoshida, K., Shimizu, T., Burtz, L. B., and Pala, A.: Field and Services Robotic, 13 (2016), pp. 313–330.
2) Hamiter, L.: The History of Space Quality EEE Parts in the United States, ESA Electronic Components Conference, 1991.
3) Avery, K., Finchel, J., and Mee, J.: Total Dose Test Results for Cube- Sat Electronics, 2011 IEEE Radiation Effects Data Workshop, 2011 pp.1–8.
4) Nicolaidis, M.: Soft Errors in Modern Electronic Systems, Springer Publishing Company, Incorporated, 2010, pp. 27–54.
5) Takuto OIKAWA, Toshiki TANAKA, Yuto SUEBE, Kentaro UNO, Hugo ZULIANI, Louis J. BURTZ, Kazuya YOSHIDA, The 31st ISTS Special Issue of Transaction of JSASS, Aerospace Technology Japan

Table 1. Potential Failure Mode Watch List for Each Device

Items	SEU	SEFI	SEL
CPU	○	○	○
TOF Camera[1]	×	○	○
ETH	×	○	○
IC #1	○	○	○
IC #2	○	○	○
IC #3	○	○	○
eMMC memory	○	×[2]	×
SPI NOR FLASH	○	×[2]	×

[1] For the ToF camera, image sensor degradation is also monitored in real time.
[2] SEFI is disregarded with these storage memory as the components are tested under non-powered mode.

Table 2. Radiation Test Results

Items	Fluence rate (counts/cm^2/s)	Fluence (counts/cm^2)	Duration (s)	Single Event Occurrence	Equivalent Exposure Time on the Moon (days)
Embedded IC #1	4.00E+05	1.50E+09	3.60E+03	None	174
Embedded IC #2	4.00E+05	1.50E+09	3.60E+03	Twice	174
Embedded IC #3	4.00E+05	0.67E+09	1.68E+03	Once	77
eMMC flash memory	4.00E+05	1.14E+09	2.85E+03	None	132
SPI NOR flash chip	4.00E+05	1.50E+09	3.60E+03	None	174

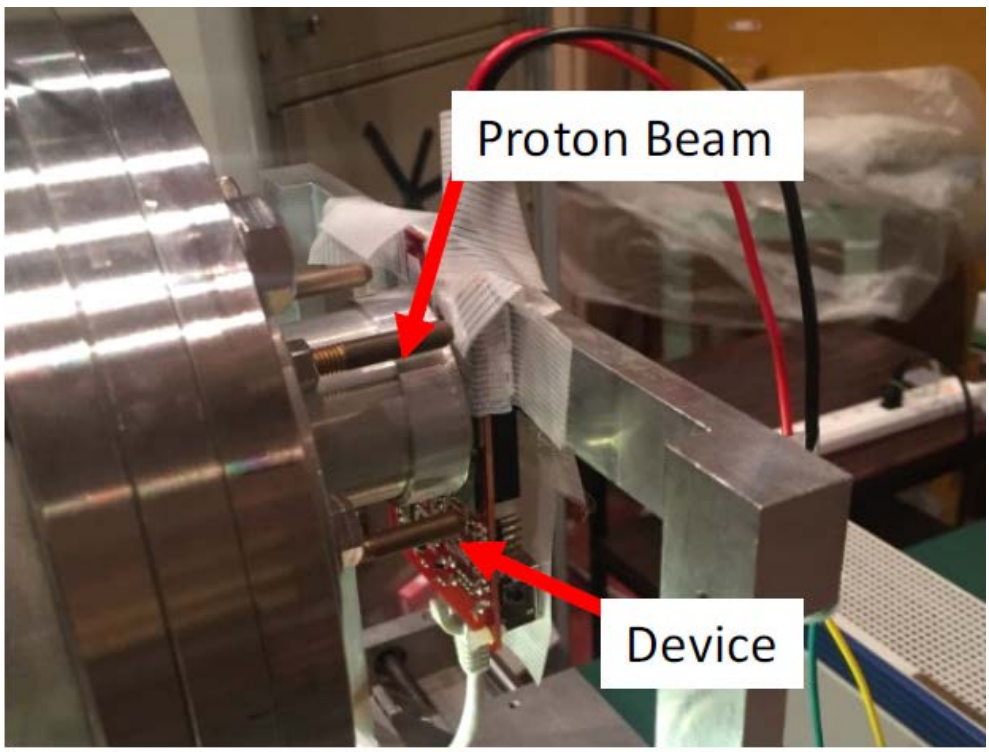

Figure 1. Test Configuration at Cyclotron Facility.

III. 6. Radiation Tolerance Tests of Electronic Components for Space-borne Dust and Debris Observations

Sakamoto Y.[1], Fujita S.[1], Ishimaru R.[2], Okudaira O.[2], Fujii M.[3], and Suzuki N.[4]

[1]Department of Aerospace Engineering, Tohoku University
[2]Planetary Exploration Research Center, Chiba Institute of Technology
[3]FAM Science
[4]Naito Densei Machida MFG, Co., Ltd.

Introduction

The Space Robotics Laboratory at Tohoku University is developing and operating 50-kg micro satellites and several-kg cubesats. The first satellite was launched on 2009, and now total 3 micro satellites and 2 cubesats were released to space under the collaboration with other organizations. S-CUBE satellite, 3U-size cubesat shown in Fig. 1, was developed by Planetary Exploration Research Center (PERC) at Chiba Institute of Technology, and Tohoku University collaborated in satellite bus system. The S-CUBE was released to space on 2015, and now the successive satellite is being developed by the same team.

In the bus system development of satellites, radiation tests for electrical components and non-metal mechanical materials are important works.

Each component can be exposed in severe radiation environment of space, and the satellite needs to work more than 3 years (micro satellite) or 10 years (large satellite).

Two types of radiation tests are generally tried, the one is total dose test using Cobalt 60 for the evaluation of long-term degradation of components. The radiation dose of test is much higher than real, and several-year radiation tolerance can be evaluated in only one-day test. Second one is single event upset/latch up test using protons or heavy ion, in which electrical circuits can have wrong behaviors because memorized data bit of RAM/ROM or output voltage of micro controller ports can be inverted. Hang-up of CPU program or serious damage in external connecting circuits are assumed.

In this paper, radiation tolerance of electrical circuits in new space-borne dust sensor designed for S-CUBE successive satellite was evaluated by proton irradiation test. The occurrence number of single events caused by high energy radiation in space were

evaluated. Electrical components are not space grade products but general industrial grades for low-cost development. Newly selected components which were not used in previous other satellites were tested.

A prototype of dust sensor is shown in Fig. 2. The detail film material and the method of multi-layer integration are now being considered. The detection of dust collision and damaged location by 8-piece piezoelectric sensors was tried in this prototype. The electrical signals from sensors are amped at first and only the frequency band with stronger signals are extracted by band pass filter. The signals are processed by A-D converter (ADC), and memorized in RAM or ROM by CPU/FPGA electrical board. This ADC chip and CPU/FPGA boards are evaluated in this test.

Methods

Electrical components of ADC and CPU/FPGA used in new dust sensor system are exposed in radiation beam of protons. Wrong behaviors of CPU/FPGA and occurrence rate of single events are evaluated. The beam energy is 80 MeV, which is general strength in single event tests for space-use components.

Single events are including a bit inverse of memorized data in RAM and inverted high/low signals at an output port of CPU/FPGA. The occurrence frequency of single events is once in 10^9 particles/cm^2 empirically. To obtain the statistically useful result, more than 100 times events are intentionally occurred by proton irradiation of 10^{11} particles/cm^2. From the report of ALOS satellite with 692-km height and sun-synchronous orbit, this beam strength was estimated as 435-year exposure in space (See Ref. 1).

Four types of test piece are prepared: a, b) two CPU evaluation boards (CPU 1 and CPU 2 are same products), c) AD converter board (ADC), d) FPGA evaluation board for Wide Earth Sensor (WES). Each piece was exposed exclusively to different strengths of radiation beam. Radiation time of each trial or each run is 1 hour in normal. After the calibration of radiation beam strength by facility operators, the conversion rate of proton numbers by using Faraday cup measurements at downstream. Diameter of beam is only 20 mm and the location of test board is adjusted for the IC chip to be centered in the beam circle.

Actual time schedule is shown in Table 1, and the appearance photos of test pieces are shown in Fig. 4.

Results of irradiated protons

Firstly, the values of SEM (second emittance monitor) and the conversion rate to proton numbers were obtained. By attaching a Faraday cup (FC) at the downstream of tube, the conversion rate [d), pC/counts] was determined by three measurements: FC at the upstream [a) U-FC, nA], FC at the downstream [b) D-FC, pC/100 sec], and SEM counts [c) SEM, counts/100s]. Then, by the irradiation area A and Coulomb per proton, the proton numbers per unit area and unit count [e) protons/cm^2.count] was determined. The results are shown in Table 2.

Beam strength and irradiation time of each trial are listed in Table.3. Run #11 to 24 are categorized to each test piece a-d). At the largest radiation run of each piece, the equivalent exposure years was estimated from the conversion rate of 10^{11} p/cm^2 = 435 years. This conversion rate is defined by the result of ALOS satellite, and this can be different in other orbits.

From the total number of protons, the equivalent total dose could be estimated. Total dose can damage or break an electrical component permanently. Our team is setting the target tolerance values of 10 krad for 3-year life satellites and 20 krad for 5-year life satellites. Mass stopping power of Silicon against 80 MeV proton is 6.885 MeV.cm^2/g. Total dose (rad) was calculated from this formula: total number of protons (protons/cm^2) x 6.885e+6 x 1.6e-19 (C/proton) x 1000 x 100. The results of each test piece are shown in Table 4. Total dose is including all the runs of each test piece, and it was total 220 krad in c) ADC, which was permanently broken in final.

Review of single events and radiation tolerance

In this review, brand and product names of each test piece is not specified. The a) CPU 1 and b) CPU 2 are same products and only the square CPU chip is exposed to radiation beam. The following 3 points were evaluated by 3 runs in each test piece.

1) Partial areas of 3 types RAM and 2 types ROM were surveyed and error rate was measured (final irradiation: 1.0e+11 [protons/cm^2])
2) Restoration of ECC RAM was counted (final irradiation: 8.2e+10 [protons/cm^2])
3) Difference of behaviors using external oscillator or on-chip oscillator (final irradiation: 8.4e+10 [protons/cm^2])

About 1), bit inversion errors in Main RAM and Standby RAM were often happening but ECC RAM had no errors. Both of ROMs had also no errors. About 2), restoration number was similar to the error number of Main RAM. The restoration rate was 0.33 times/sec in survey area of 262,144 bits. About 3), there was no difference behavior in

both of oscillators.

About 1), the detail results of error rate are shown as follows:

1-1) Main RAM, 5.1 bit/s, survey area = 4,194,304 bits

1-2) ECC RAM, 0.0 bit/s, survey area = 262,144 bits

1-3) Standby RAM, 0.08 bit/s, survey area = 16,384 bits

1-4) Code Flash ROM, 0.0 bit/s, survey area = 33,554,432 bits

1-5) Data Flash ROM, 0.0 bit/s, survey area = 524,288 bits

From these results, 2 ROMs integrated in CPU chip had strong tolerance for radiation. In some emergency situations, the program can be safely recovered to normal condition by resetting power supply. Also, ECC RAM had the similar strong tolerance by automatically restoration of bit errors. Mission data can be stored in here with higher reliability. Other RAM areas can have some bit errors and should be used for temporary measurement data or communication buffers. Main CPU program must be carried out in ROM or ECC RAM areas to avoid a trouble.

Error rate of Main RAM was 5.1 bits/s, and this equals to 1 bit error per 0.196 sec. For low-earth orbit satellite, total irradiation time of 10793 sec (Runs #11, #17, #18) can be equivalent to 1157-year operation, that is one bit error per 7.7 days in orbit. To accept this error rate, Main RAM area can be used to some extent.

About test piece of c) ADC, there was no trouble in Run #21, which equals to 2480-year radiation. But in the final Run #24, the chip was permanently broken. The consumption current of chip was abnormal value. As already described, the total dose could be 220 krad for ADC. This value can be required for Jupiter exploration spacecraft, but for low earth orbit satellites, 20 krad tolerance will be enough ability.

About test piece of d) WES, the commercial evaluation board was used which is including FPGA chip with CPU cores. In this test, CPU part was used in general manner, and the program was continuing RAM write and RAM check (read and compare with written bytes). The mismatch bytes were counted for total 512 MB RAM areas. Firstly, the program experienced high frequent hang up against originally planned minimum radiation. At Run #13, this was originally weakest radiation, but the program could not work more than a few seconds. Then, the new weaker x0.1 radiation was tried in Runs #14 and #16. In total 14 runs, the program could work for 81 seconds in average and total 4 errors of RAM write were monitored. At Run #15 with further half of strength, the program could run more than 5 minutes without any troubles. Total duration of Run #14 was 811 sec and 4.7e+9 p/cm^2. The hang up time of 81 sec equals to 4.7e+8 p/cm^2 or 2.04 year in space. The power

of WES sensor will be often turned on/off, then this kind of accident will be avoided in real operations. The RAM part of this chip was weaker tolerance compared to test pieces A) and B), and this shouldn't be used in important central part of satellite system.

Conclusions

The radiation test of single event latchup/upset was first experience to our satellite development team. Some reliable electrical parts already used in other satellites were candidates for our previous satellites, but new electrical parts can be tried for future satellites by the repeat of radiation tests. We could accumulate some skills about the test procedures and evaluation methods. As like in conventional established theories, normal RAM area had bit inversion errors frequently and ECC RAM had strong tolerance for long-term operations. Also, ROM was completely not affected by radiation. WES board using latest FPGA/CPU chip had much weaker tolerance in the test, but this can be used for sensor handling part although this will be not suitable for central computer. A combination chip of FPGA and CPU can be used conveniently for stable parallel processing of FPGA with fast numerical calculation of CPU. Through this test method, the radiation tolerance of each test piece was successfully evaluated quantitatively.

Acknowledgement

Although original test schedule was delayed in final, we could carry out the test successfully and obtain the significant results under the strong supports of CYRIC staffs. Our team really appreciate for them.

This work was supported by JSPS Grant-in-Aid for Scientific Research (C) Grant Number 16K06882.

References

1) Ohashi H, Sasaki S, Hirai T, Shibata H, Nogami K. Iwai T, "Development of a light weight, large area in-situ dust/debris detector," *Proceedings of the 4th Spacecraft Environment Symposium* (2008) JAXA-SP-07-030.

Table 1. Actual result of test schedule

Day 1	1 pm - : Lecture about the CYRIC facility 2:30 pm - : discussion of test configuration at test room 4:30 pm - 7pm: preparation of test pieces and measurement tools at restricted area
Day 2	8 am - : preparation (continue) 10 am - : start of proton radiators calibration by facility operators 1 pm - : measurement of proton particles conversion rate (Run #1 - #10) 2 pm - : start of proton radiation to test pieces (Run #11 - #24) <until 2:30 am of next day, total 12 h 30 m>
Day 3	2:30 am – 4 am : clean up of test pieces and measurement tools at restricted area

Table 2. Estimation of protons from measurements.

Case	a) U-FC (nA)	b) D-FC (pC/100s)	c) SEM (counts/100s)	d) pC/counts (= b/c)	e) protons/cm^2.count (= d/B.A)
1	0	37	90		
2	0.1	304	1821	0.167	330K
3	0.5	869	6041	0.144	290K
4	1	1596	11366	0.140	280K
5	4	6215	45391	0.137	270K
6	40	53427	433236	0.123	250K

A = 3.14 x 1cm^2
B = 1.6e-19 C / proton

Table 3. Radiation results of each test board and each trial, incl. the estimation of protons/cm^2 and equivalent exposed years.

Run#	a) CPU1
11	1nA, 3598s = 368K SEM = 1.0E+11 p/cm^2 = **(435 years)**

Run#	b) CPU2
17	1nA, 3598s = 293K SEM = 8.2E+10 p/cm^2
18	1nA, 3597s = 300K SEM = 8.4E+10 p/cm^2 = **(365 years)**

Run#	c) ADC
12	1nA, 3598s = 402K SEM = 1.1E+11 p/cm^2
19	1nA, 3598s = 279K SEM = 7.8E+10 p/cm^2
20	4nA, 3598s = 1535K SEM = 4.3E+11 p/cm^2
21	40nA, 599s = 2263K SEM = 5.7E+11 p/cm^2 = **(2480 years)**
22	10nA, 1540s = 1785K SEM = 4.8E+11 p/cm^2
24	10nA, 1199s = 1106K SEM = 3.0E+11 p/cm^2

Run#	d) WES
13	1nA, 561s = 62.4K SEM = 1.7E+10 p/cm^2 = **(74.0 years)**
14	0.1nA, 811s = 14.1K SEM = 4.7E+9 p/cm^2
15	0.05nA, 663s = 559 SEM = 1.8E+8 p/cm^2
16	0.1nA, 875s = 14.1K SEM = 4.7E+9 p/cm^2

SEM = counts/100s
p/cm^2 = protons/cm^2

equivalent exposed years:
10^11 p/cm^2 = 435 years

Table 4. Total dose estimation in each test board, and relationship with permanent damage

	a) CPU1	b) CPU2	c) ADC	d) WES
Run	#11	#17, #18	#12, #19-22, #24	#13-16
Total Doze	11 krad	18 krad	**220 krad**	3 krad
Permanent damage	none	none	**occurred**	none

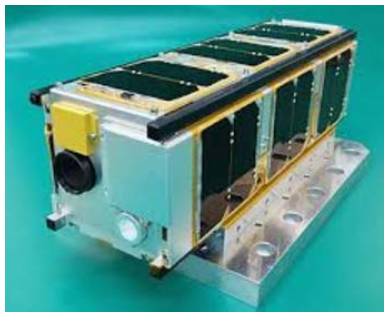

Figure 1. S-CUBE, 3-U cubesat for monitoring mission of shooting stars.

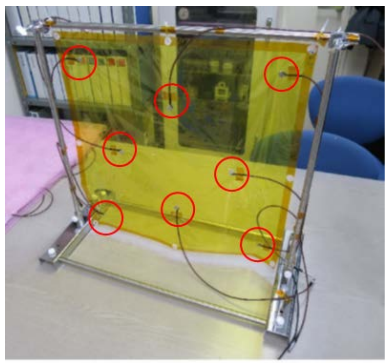

Figure 2. Dust sensor for 3-U cubesat, prototype for ground evaluation.

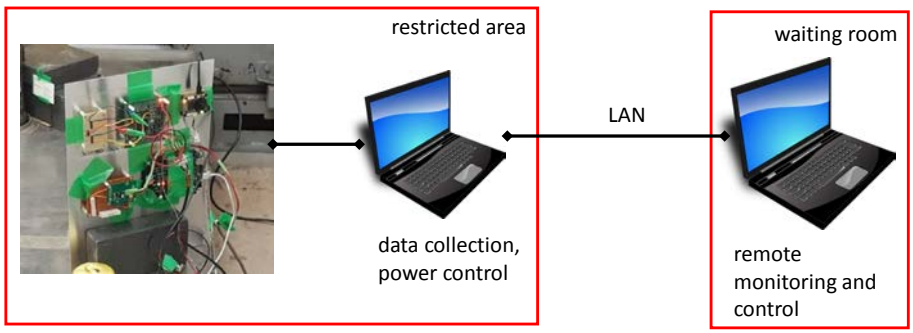

Figure 3. Test board for proton radiation and setup of signal measurements, including 4 types of IC evaluation boards

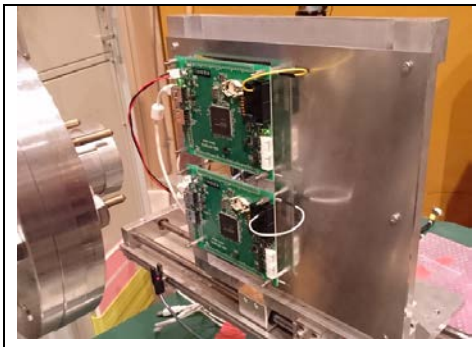

Setup of a) and b)

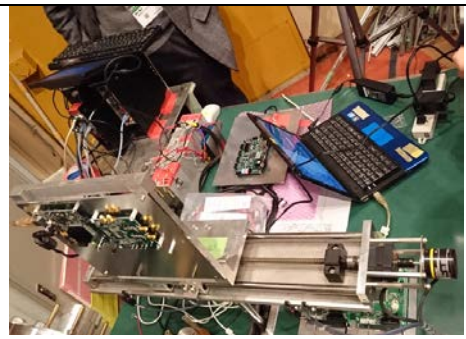

Setup of c)

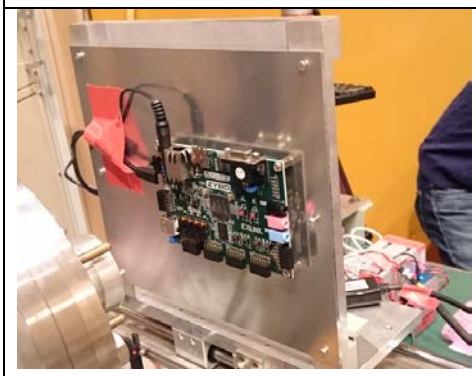

Setup of d)

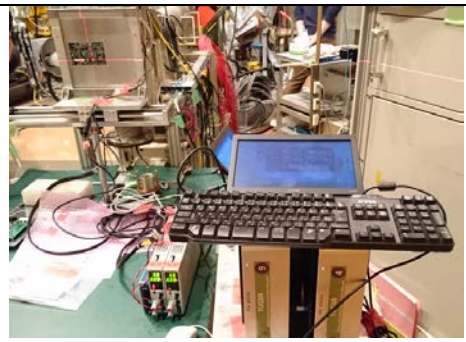

Setup of power control (automatic shutdown when over current, and remote ON/OFF control)

Figure 4. Appearance of test boards, incl. a) CPU 1, b) CPU 2, c) ADC, and d) WES

IV. NUCLEAR MEDICAL ENGINEERING

IV. 1. Water-equivalent Lengths Derived from Proton Computed Tomography

Terakawa A.[1], Hosokawa H.[1], Shigihara K.[1], Kajiyama A.[1], Nagao R.[1], Narumi K.[1], Hosokawa H.[1], Fujise Y.[1], Ushijima H.[1], Wakayama Y.[1], Fujiwara M.[2], Hitomi K.[2], Nagano Y.[2], and Nogami M.[2]

[1]Cyclotron and Radioisotope Center, Tohoku University
[2]Department of Quantum Science and Energy Engineering, Tohoku University

High-precise X-ray computed tomography (XCT) has commonly been used to obtain water-equivalent length (WEL) in ion-beam treatment planning because the effect of Compton scattering related to electron density is basically dominant in patients. However, the XCT-based treatment planning provides errors in depth-dose and range simulation due to the photoelectric effect and the beam-hardening effect. Yang et al. have reported that the XCT-based treatment planning causes uncertainties of 2.5 % for lung tissue and 5 % for born tissue in converting Hounsfield unit (HU) into relative stopping power (RSP) with respect to water[1)]. In order to reduce the errors in ion-beam treatment planning, proton computed-tomography (pCT) has recently received attention because pCT potentially provides more accurate RSP data than XCT. In this work, we aimed to derive WEPLs of typical phantoms (ethanol, water, a 40% aqueous solution of potassium dihydrogen phosphate) used in the HU-RSP conversion and various phantoms (resins and aqueous solutions of mineral salts of trace elements in human tissue) from pCT measurements. In addition, we aimed to evaluate and discuss range-simulation errors in proton treatment planning by comparing the WEPLs obtained from pCT with those of XCT.

The pCT measurements were performed using an 80-MeV proton beam and a beam-irradiation system for proton therapy studies[2),3)] at Cyclotron and Radioisotope Center, Tohoku University. Figure 1 shows the experimental setup for pCT. We used polymethyl methacrylate (PMMA) and polyethylene as resin phantoms, and $CaCl_2$, $MgCl_2$ and $FeCl_3$ as aqueous-solution phantoms other than the typical phantoms. Each phantom was a cylindrical one of 3 cm diameter. The proton beam was delivered to the phantom through collimators and a beam-intensity (BI) monitor. The size of the proton beam was

approximately 1 mm at the phantom. The residual energy of the proton beam after the phantom was measured with an energy detector in current mode operation while the effect of beam-intensity fluctuation on the energy measurement was corrected using the BI monitor. The BI monitor and energy detector were scintillator detector type using CsI(Tl) equipped with Si-PIN photodiodes. The pCT data were obtained by rotating the phantom at intervals of 3.6º

Figure 2 shows an axial reconstruction slice of the PMMA phantom based on pCT-based WEL values and a filtered-back-projection method. We have found that the deviation of the pCT-based WELs from the theoretical ones were within 3% for those phantoms whereas the deviations of the XCT-based WELs ranged from 1 to 11%. The results of this work have indicated that pCT significantly reduces the uncertainties in range simulation of the conventional ion-beam treatment planning using XCT, and has clinical benefits in taking full advantage of ion-beam therapy.

References

1) Yang Ming et al., Phys. Med. Boil. 57 (2012) 4095.
2) Terakawa A. et al., X-ray Spectrometry, 40 (2011), 198-201.
3) Terakawa A., et al., *Nucl. Instrm. and Meth. B 365 (2015) 606-610.*

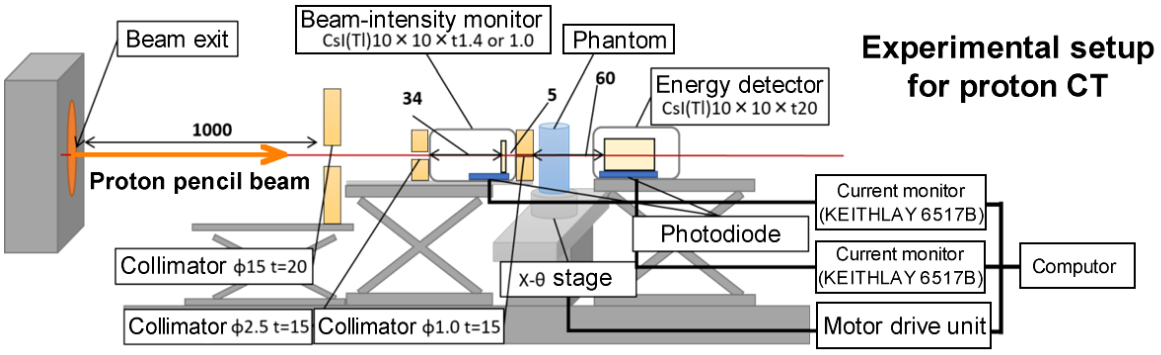

Figure 1. Experimental setup of the proton computed tomography.

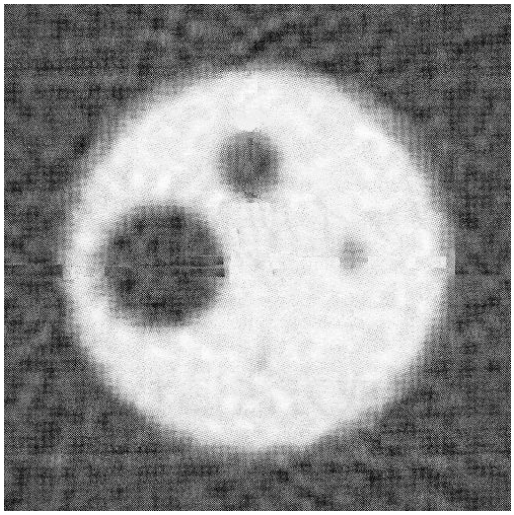

Figure 2. Axial reconstruction image of the PMMA phantom based on pCT-based WEL values and a filtered-back-projection method.

V. RADIOCHEMISRTY AND NUCLEAR CHEMISTRY

V. 1. Feasibility Study for Production of Medical Radioisotope ^{64}Cu with Accelerator-based Neutrons

Kin T.[1], Aoki K.[1], Araki N.[1], Yoshinami K.[1], Yamaguchi M.[2], Patwary M.K.A.[1], Watanabe Y.[1], and Itoh M.[3]

[1]Department of Advanced Energy Engineering Science, Kyushu University
[2]Department of Energy Science and Engineering, Faculty of Engineering, Kyushu University
[3]Cyclotoron and Radioisotope Center, Tohoku University

We have been developing a production method of medical radioisotopes (RI) by accelerator-based neutron[1)]. There are a few reactions to generate accelerator-based neutron e.g. DT or DD fusion reactions, (*p*,*n*) reaction, and (*d*,*n*) reaction[2)]. Among all, (*d*,*n*) reaction is especially promising reaction for the medical RI production. The reaction has two advantages. First, the generated neutron intensity is high, since the binding energy of deuteron is 2.2 MeV and it is weak enough to efficiently occur break-up reactions. Second, the neutron spectrum has a peak around the half of incident deuteron energy. In other words, the spectrum shape can be adjusted by changing the incident deuteron energy to produce RIs not to include large amounts of by-products.

In these two years, we have focused on the production method of ^{64}Cu which is one of a candidate of longer half-life PET nuclides compared with clinically used ones. A practically used production route is the ^{64}Ni(*p*,*n*) reaction. Accelerated protons bombard on the ^{64}Ni target directly in the method. However, because of the short range of proton in nickel, very small amount of the nickel target reacts with the protons. Therefore, highly enriched ^{64}Ni is required as a raw material to increase ^{64}Cu production amount, although the enrichment cost is very high because of the small natural abundance of ^{64}Ni (~1%). In contrast, we can use a large amount of raw material in the accelerator-based neutron method because of high transmission ability of neutrons. In addition, natural zinc can be used as raw material, since the neutron energy distribution can be adjusted to suppress the amount of by-products[3)]. Therefore, the accelerator-based neutron method can be an alternative of the existing production methods of ^{64}Cu.

For a feasibility study of the production method of ^{64}Cu by the accelerator-based

neutron, we have performed accelerator experiments at CYRIC with two purposes.

1) Systematic measurements of thick target neutron yield (TTNY) of the C(*d*,*n*) and Be(*d*,*n*) reactions to find the optimal deuteron energy for the ^{64}Cu production method.
2) Development of chemical separation method of ^{64}Cu from large amount of a raw material and investigation of its labeling efficiency to a typical ligand, DOTA by using actually produced ^{64}Cu by the accelerator-based neutron.

First, an example of the systematic measurement of TTNY of the C(*d*,*n*) reaction of 16-MeV deuteron is shown. The multiple foils activation method was adopted in the study, because the activation power of the neutron field can be directly measured by the method. Deuterons were accelerated to 16 MeV and bombarded on a neutron converter made of carbon. The multiple foils were irradiated by the accelerator-based neutron. After that, gamma rays emitted from the irradiated foils were measured by HP Ge detectors to derive the numbers of atom which are produced by the activation reactions. From these numbers of atom, the TTNY was derived by using unfolding code, GRAVEL[5)]. Figure 1 shows the result compared with theoretical TTNY prediction model, DEURACS[6)].

Next, preliminary results of chemical separation and labeling study are shown. Zinc oxide target was irradiated by the accelerator-based neutron generated by 25-MeV deuterons on the carbon neutron converter. After that, around 50 Bq/g/μC of ^{64}Cu was produced in the target. The target was divided into a few samples to investigate different chemical separation conditions. The solid-phase extraction method[4)] was adopted in the present study. In our investigation, we found that hydrochloride acid (HCl) density during the copper absorption to chelating column is very important for efficient separation. We have been investigating the optimal density. The extracted ^{64}Cu samples were labeled by DOTA with different temperature and labeling time. The labeling index is found to be dependent on the conditions. We have been also finding the most efficient labeling condition.

In future, we continue the systematic measurements of TTNY of the C(*d*,*n*) and Be(*d*,*n*) reactions to find the optimal incident deuteron energy to produce ^{64}Cu. In addition, some new RIs study not only of medical but also of agriculture and environment will be proposed.

References

1) T. Kin et al., Proceedings of International Symposium on Radiation Detectors and Their Uses (ISRD2018), JPS. Conf. Proc. (to be published).
2) Y. Nagai, et al., J. Phys. Soc. Jpn. **78**, (2009) 033201.

3) T. Kin, et al., J. Nucl. Sci. Technol. **54**, (2017) 1123.
4) M. Kawabata, et al., J. Radioanal. Nucl. Chem. **303**, (2015) 1205.
5) M. Matzke: Report PTB-N-19 (1994).
6) S. Nakayama, et al.: Phys. Rev. C **94**, (2016) 014618.

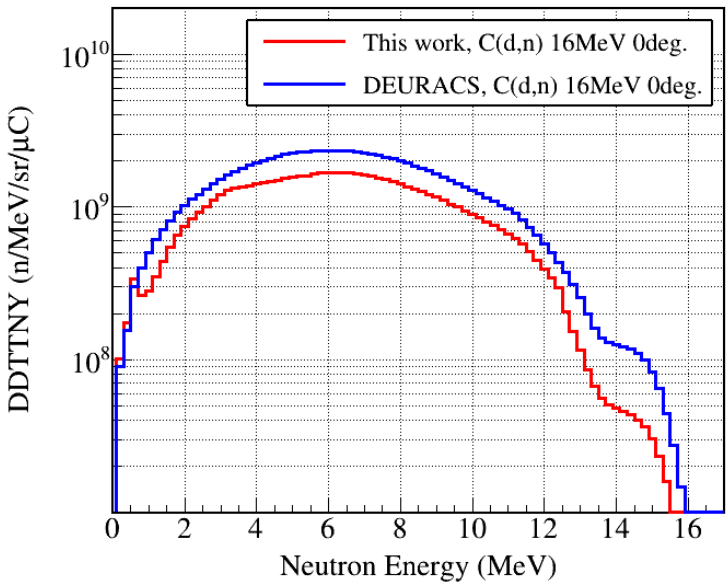

Figure 1. Resultant TTNY of the C(*d*,*n*) reaction at E_d = 16 MeV compared with TTNY derived by DEURACS.

V. 2. No-carrier-added Purification of ^{28}Mg Using Co-precipitation and Cation Exchange Method

Kikunaga H.[1], Haba H.[2], Komori Y.[2],Shibata S.[2], and Yano S.[2]

[1]Research Center for Electron Photon Science, Tohoku University
[2]RIKEN Nishina Center

The isotope ^{28}Mg is useful in biological sciences as a radioactive tracer[1,2]. Generally, ^{28}Mg is produced for each use in nuclear reactions because of its short half-life of 21.6 h[3]. The reaction ^{27}Al(α,3p)^{28}Mg is often chosen for the production of ^{28}Mg owing to its potential to produce no-carrier-added ^{28}Mg tracer with a convenient and low-cost target. Several groups have reported separation methods of ^{28}Mg from Al targets based on adsorption[4,5], co-precipitation[6], solvent extraction[7], and the cation exchange column method[8]. Although the cation exchange column method should yield a high purity tracer, it requires a large column and an eluant volume of a few hundred milliliters. In this work, we applied a co-precipitation method before the cation exchange column method to downsize the column volume. Downsizing chemistry leads to the reduction of waste and labor in separation procedures and the quality improvement of the tracer.

Magnesium-28 was produced in the ^{27}Al(α,3p)^{28}Mg reaction. An α-particle beam was delivered from either the AVF Cyclotron at CYRIC, Tohoku University or the RIKEN K70 AVF Cyclotron. The target stack of 7 Al foils (99.9% pure) with a thickness of 100 μm was irradiated with an α-particle beam with a beam energy of 50 MeV and a mean current of approximately 3 μA.

First, the conditions for the separation of ^{28}Mg from Na, which get mixed at the time of co-precipitation process, were searched for. After the irradiation, the Al targets were dissolved in 12 M (mol/dm^3) HCl diluted with water to 15 mL. The ^{28}Mg isotopes were co-precipitated with iron hydroxide by adding 2 mg of Fe(III) and 25 mL of 6 M NaOH and separated from $[Al(OH)_4]^-$ ions. After centrifugal separation, the precipitation of iron hydroxide was dissolved in 9 M HCl. The solution was passed through an anion exchange resin column (Dowex 1×8, 100-200 mesh, 1 mL), which adsorbs Fe(III) ions, and the resin

was washed with additional 9 M HCl. The eluate was heated to dryness and adjusted to 0.5 M oxalic acid. To investigate the behavior of the Na ions, approximately 300 Bq of ^{22}Na tracer was added to the solution. The solution was passed through a cation exchange resin column (Dowex 50W×8, 100-200 mesh, 1 mL) to adsorb ^{28}Mg isotopes. The resin was washed with 10 mL of 0.5 M oxalic acid to eliminate Al ions and then with 0.5 M HCl to eliminate Na ions. The elution curves of the cation exchange separation for Na and Mg are shown in Fig. 1. The Na ions are eluted completely within 10 mL of 0.5 M HCl whereas the Mg ions are retained onto the column. The ^{28}Mg isotopes were eluted from the column with 6 mL of 2 M HCl.

Next, the conditions for the separation of ^{28}Mg from ^{7}Be, which is produced in the side nuclear reactions, were searched for. The irradiated Al targets were dissolved in 12 M HCl. A portion of it, containing 0.1 mmol of Al and trace amounts of ^{7}Be, ^{24}Na, and ^{28}Mg, was heated to dryness and adjusted to 0.5 M oxalic acid. The solution was passed through a cation exchange column (Muromac 50W×8, 100-200 mesh, 1 mL), which adsorbs Al(III), ^{7}Be, ^{24}Na, and ^{28}Mg ions, following which the resin was washed with 7 mL of 0.5 M oxalic acid to eliminate Al(III) and 5 mL of 0.2 M HF. The elution curves of the cation-exchange separation is shown in Fig. 2. The ^{7}Be ions are eluted completely within 5 mL of 0.2 M HF, whereas the ^{24}Na and ^{28}Mg ions are retained onto the column.

The recommended chemical scheme for ^{28}Mg purification is shown in Fig. 3. The irradiated Al targets were dissolved in 9 M HCl and then diluted with water to 15 mL. The ^{28}Mg isotopes were co-precipitated with iron hydroxide by adding 2 mg of Fe(III) and 15 mL of 6 M NaOH and separated from Al, Na, and Be ions. The precipitation of iron hydroxide was dissolved in 9 M HCl. The solution was passed through an anion exchange resin column (Muromac 1×8, 100-200 mesh, 1 mL), which adsorbs Fe(III) ions, and the resin was washed with additional 9 M HCl. The eluate was heated to dryness and adjusted to 0.5 M oxalic acid. The solution was passed through a cation exchange resin column (Muromac 50W×8, 100-200 mesh, 1 mL) to adsorb ^{28}Mg isotopes. The resin was washed with 0.2 M HF for Be elimination, 0.5 M oxalic acid for Al elimination, and 0.5 M HCl for Na elimination. The ^{28}Mg isotopes were eluted from the column with 2 M HCl. The chemical yield of the separation procedure, determined by γ-spectrometry of ^{28}Mg, was approximately 85% and radioactivity other than ^{28}Mg was not detected in the Mg fraction.

References

1) Schimansky C., *J. Plant Nutr.* **8** (1985) 467.
2) Tanoi K. et al., *Plamt Soil* **384** (2014) 69.
3) Firestone R. B. and Shirley V. S., *Table of Isotopes, 8th ed.* (John Wiley and Sons, New York, 1996).
4) Hudis J., *J. Inorg. Nucl. Chem.* **4** (1957) 237.
5) Nozaki T., *Int. J. Appl. Radiat. Isot.* **26** (1975) 17.
6) Lundqvist H. and Malmborg P., *Int. J. Appl. Radiat. Isot.* **30** (1979) 33.
7) Mukhopadhyay K. and Lahiri S., Radiochim. Acta **90** (2002) 65.
8) Iwata R. et al., *J. Radioanal. Nucl. Chem.* **159** (1992) 233.

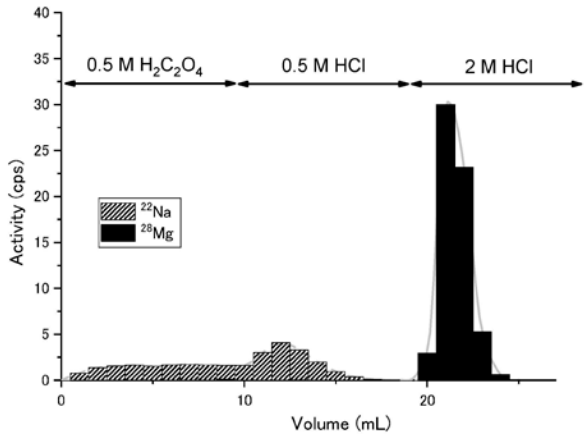

Figure 1. Elution curves for the cation exchange separation for Na and Mg.

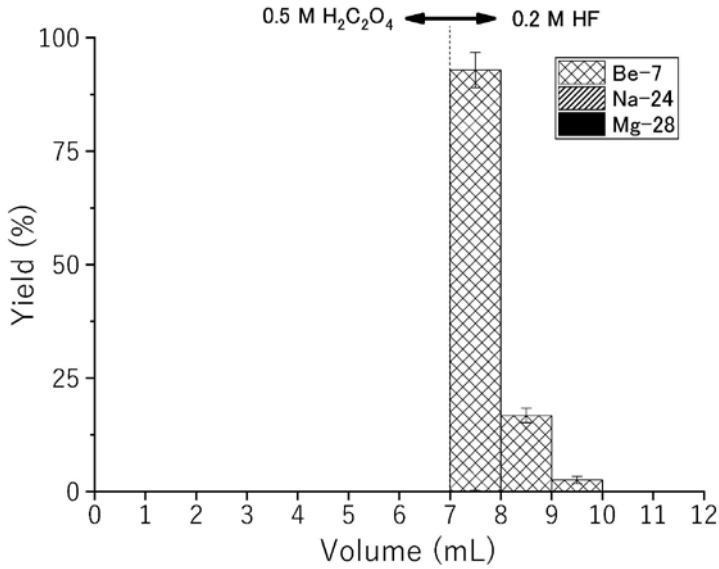

Figure 2. Elution curves for the cation exchange separation of Be, Na, and Mg.

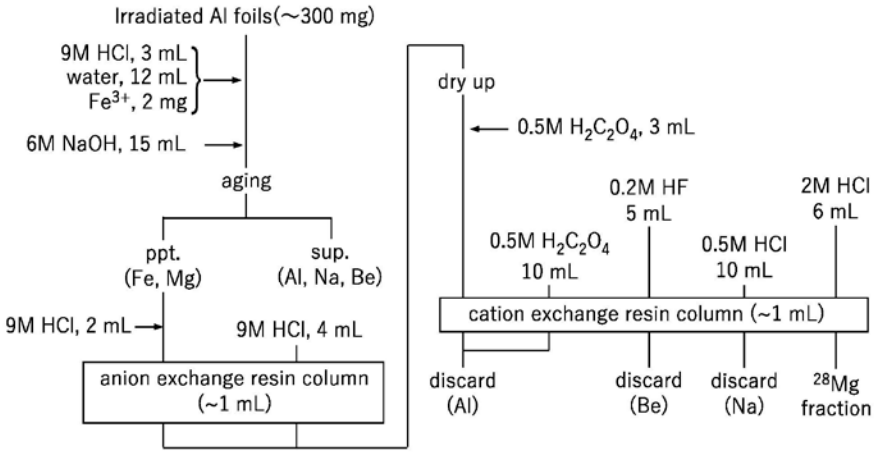

Figure 2. Chemical procedure for the preparation of no-carrier-added ^{28}Mg tracer.

V. 3. Development of Separation for Carrier-free Astatine Using Column Chromatography

Ikeda H.[1,2,3], Kikunaga H.[2,3], Yano S.[3], Komori Y.[3], Yokokita T.[3], Haba H.[3], and Watabe H.[1]

[1]Cyclotron and Radioisotope Center, Tohoku University
[2]Research Center for Electron Photon Science, Tohoku University
[3]Nishina-Center for Accelerator-Based Science, RIKEN

Astatine-211 (^{211}At) is a nuclide expected to be applied to targeted alpha therapy (TAT). In order to apply ^{211}At for TAT, production of carrier-free astatine is required to prevent unexpected reactions. The main production method of ^{211}At is ^{209}Bi(α, 2n)^{211}At reaction, which used natural bismuth (Bi) for the target. The irradiated targets are purified by dry distillation in many facilities[1)]. Depending on the conditions during vaporization of ^{211}At, however, the yield of ^{211}At can reduce greatly. Although solvent extraction, one of the other separation methods of ^{211}At, is simple method, aqueous solution is contaminated with the organic solvent after back extraction. Thus, the separation method has to further improve or to develop other approach (for example, ^{211}Rn/^{211}At generator system[2,3)]). In this study, we chose column chromatography as a separation method of astatine. This method can be expected high yield of ^{211}At with simple operation.

We produced ^{210}At at Cyclotron and Radioisotope Center (CYRIC), or ^{211}At at Nishina-Center for Accelerator-Based Science, RIKEN. Bismuth oxide (Bi_2O_3) pellet was used for target (~180 mg). The target was irradiated with 50-MeV α particles (100 particle nA) at CYRIC, and 29-MeV α particles (250 particle nA) at RIKEN AVF cyclotron. Quantification of ^{210}At and ^{211}At was all performed using γ-spectroscopy. The activity of ^{210}At and ^{211}At were determined from peaks of 245-keV and 687-keV γ-rays, respectively. The irradiated Bi_2O_3 target was dissolved in 2 mL of 4 mol/L hydrochloric acid (HCl) containing 1 mol/L sodium hydrogen sulfite ($NaHSO_3$). This solution was added a 6 mL of 0.84 mol/L EDTA·2Na aqueous solution (stock solution).

We tried column chromatography experiments using strong anion exchange resin (Muromac© 1X8 100-200 mesh, Muromachi Chemical Co., Ltd.), activated carbon (CNovel®

MH-00, Toyo Tanso Co., Ltd.), and weak anion exchange resin (3-aminopropylsilica gel, Tokyo Chemical Industry Co., Ltd.). In the cases of strong anion exchange resin and activated carbon, almost all At was trapped on the columns. Trapped At was not eluted by concentrated HCl. However, At on the activated carbon column was eluted by 10 M NaOH solution. Therefore, based on Scheme 1, we drawn an elution curve of At in activated carbon. In the case of weak anion exchange resin, almost of all At was not trapped on the column (Scheme 2 and Fig. 2).

$NaHSO_3$ was added as a reducing agent in the stock solution, which was pH 1. Iodine, one of the homologous of astatine, becomes iodide ion (I^-) if there are enough HSO_3^- [4]. Under the condition of pH 1, the chemical form of astatine can be At^-, At^+, or AtO^+.[5, 6] It is known that most of the HSO_3^- ions at pH 1 are SO_3^{2-}. The redox potential of At^- and SO_3^{2-} are +0.35 V and –0.07 V, respectively[7,8]. From the above, it can be inferred that chemical species of astatine was At^- in the stock solution.

As the result of activated carbon column chromatography, the 85% of charged At^- was eluted by 10 column volumes of 10 M NaOH solution. It is suggested that At is oxidized to AtO(OH) at pH 14 which is the condition of the eluent.[5] This result suggested that AtO(OH) do not adsorbed on activated carbon. We found a simple method to separate At in high yield (~86%). However, the solution of At was a strong alkaline. Therefore, using this solution is impossible for biological research. In the case of weak anion exchange column chromatography, Cl^- in the stock solution may have inhibited At trapping. In the absence of any anions, almost all of I^- adsorb on weak anion exchange column.[9] It is necessary to dissolve the irradiated Bi target under conditions not including anions which may inhibit adsorption of astatine to the resin.

In the future, we will consider other dissolution methods and column chromatography of other adsorbents.

References

1) S. Lindegren, T. Bäck, H.J. Jensen, Appl. Radiat. Isot., 55 (2001) 157.
2) J.R. Crawford, P. Kunz, H. Yang, P. Schaffer, T.J. Ruth, Appl. Radiat. Isot., 122 (2017) 222.
3) E. Maeda, A. Yokoyama, T. Taniguchi, et al., J. Radioanal. Nucl. Chem, 303 (2015) 1465.
4) V. Gáspár, K. Showalter, J. Am. Chem. Soc., 109 (1987) 4869.
5) D.C. Sergentu, D. Teze, A. Sabatié‐Gogova, et al., Chem. Eur. J., 22 (2016) 2964.
6) J. Champion, C. Alliot, S. Huclier, et al., Inorg. Chim. Acta, 362 (2009) 2654.
7) G.W.M. Visser, Radiochim. Acta, 47 (1989) 97.
8) W.G. McMillan, J.D. Roberts, C.D. Coryell, J. Am. Chem. Soc., 64 (1942) 398.
9) M. Miyashita, S. Yamashita, Bunseki Kagaku, 46 (1997) 143.

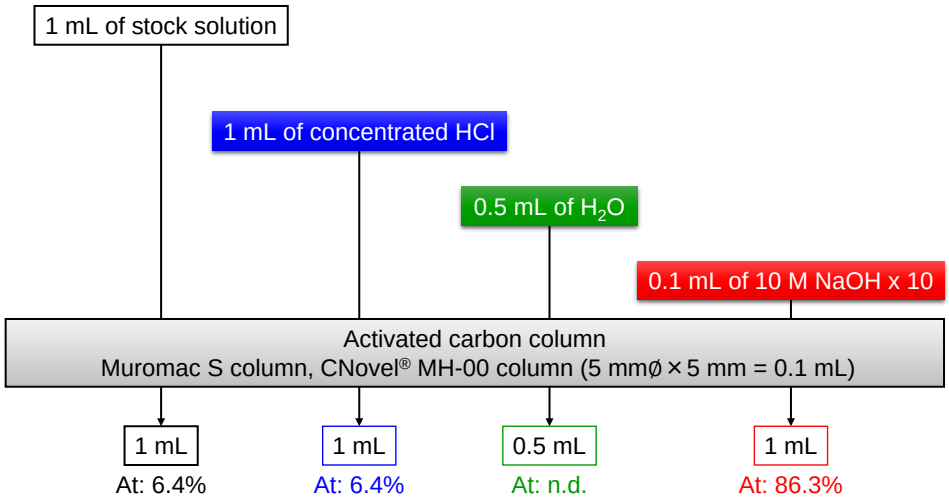

Scheme 1. Separation method of At using column chromatography (adsorbent: activated carbon)

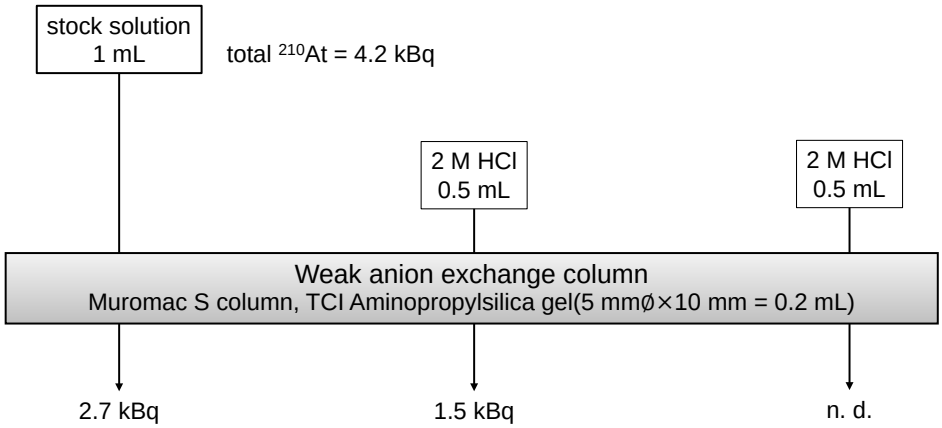

Scheme 2. Separation method of At using column chromatography (adsorbent: weak anion exchange resin)

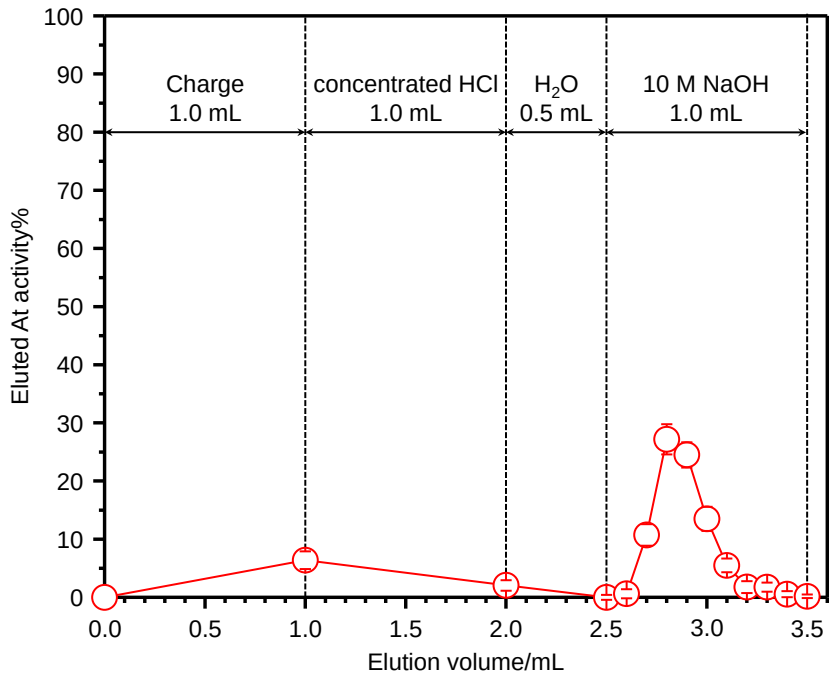

Figure 1. Elution curve of At from activated carbon column

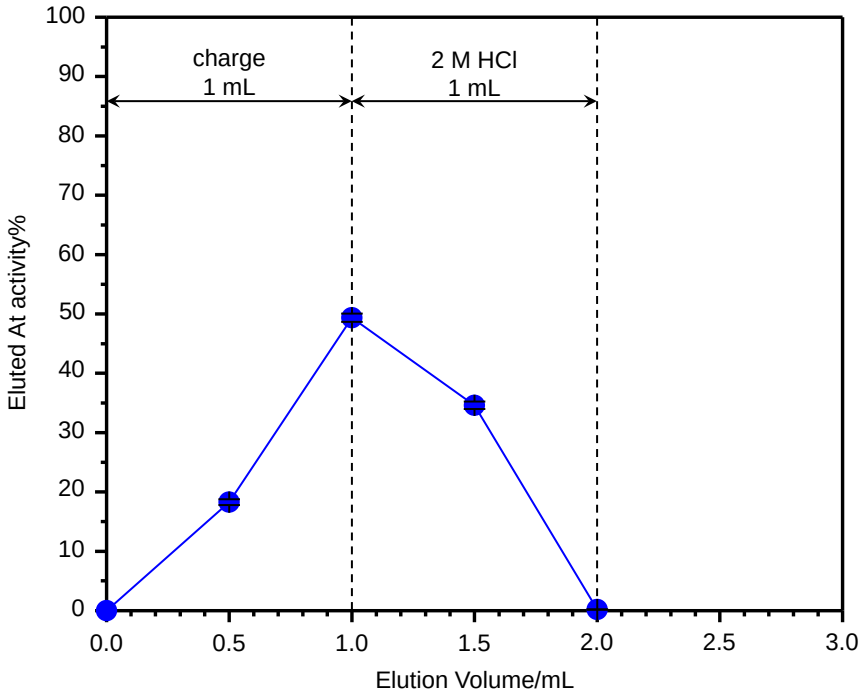

Figure 2. Elution curve of At from weak anion exchange column

VI. RADIOPHARMACEUTICAL CHEMISTRY AND BIOLOGY

VI. 1. Using Short Half-life Nuclide ^{107}Cd for Real-time Imaging and Analysis of Cadmium Dynamics in Cd-Hyperaccumulator *Arabidopsis halleri* ssp. *gemmifera* by PETIS System

Huang Y- Kohda T.[1], Qian ZJ.[1], Chien MF.[1], Ikeda H.[2,3], Yin Y.-G.[4], Kawachi N.[4], Sugawara K.[5], Kitajima N.[6], Suzui N.[4], Watabe H.[2], and Inoue C.[1]

[1]*Graduate School of Environmental Studies, Tohoku University*
[2]*Cyclotron and Radioisotope Center, Tohoku University*
[3]*Research Center for Electron Photon Science, Tohoku University*
[4]*National Institutes for Quantum and Radiological Science and Technology*
[5]*Faculty of Science and Technology, Seikei University*
[6]*Technology Development Division, Fujita Corporation*

Introduction

Positron-emitting tracer imaging system (PETIS), one of the most advanced radiotracer-based imaging methods available today can provide serial time-course images (i.e. animation) of the two-dimensional distribution of a radiotracer within a living organism without contact. Its principle is the same as that of positron emission tomography (PET), which has been widely used for medical diagnosis, but PETIS was specially designed for studying plants and this system enables monitoring of the real-time movement of the tracer in living plants as a video, and also quantitative analysis of the movement of substances by freely selecting a region of interest (ROI) on the image data obtained[1,2].

Cadmium (Cd) hyperaccumulator *Arabidopsis halleri* ssp. *gemmifera* is a perennial weed that spreads widely in Central Europe and East Asia[3]. *A. halleri* ssp. *gemmifera* has a remarkable capacity to uptake Cd. In hydroponic conditions, *A. halleri* ssp. *gemmifera* has been reported to accumulate Cd 2700 mg/kg in shoots without growth inhibition[4]. Also *A. halleri* ssp. *gemmifera* was proved that it had the high accumulation capacity of cadmium in the soil field experiment[5]. For the further phytoremediation application to Cd contamination, Cd uptake and translocation mechanism in *A. halleri* ssp. *gemmifera* need to be clear. The present work aims to visualize the Cd uptake and translocation dynamics in *A. halleri* ssp.*gemmifera* using PETIS and positron-emitting ^{107}Cd tracer.

Methods

Plant cultivation

Seeds of the *A. halleri* ssp. *gemmifera* were germinated and then hydroponically grown in a 250 mL synthetic pot with 1/5 modified Hoagland solution in a growth chamber with the following conditions: 72.9 μmol m^{-2} s^{-1} photon flux density supplied by cool white fluorescent lamps, 60-70% humidity, at 22 °C during a 16:8-h light and dark photoperiod. The culture solution was renewed every week. Approximately 2-month-old plant was used in the whole plant cadmium imaging experiment.

^{107}Cd tracer and PETIS Imaging

^{107}Cd radioisotope was produced as follows[1)]: A natural, 1-mm-thick silver foil was bombarded for 120 min with a 17-MeV proton beam at a current of 3 μA delivered from a cyclotron at Cyclotron and Radioisotope Center, Tohoku University. The irradiated target was dissolved in 4 mL of concentrated nitric acid and 2 mL of water in a glass beaker on a heater. After adding 20 mL of warm water, hydrochloric acid with gradually increasing concentrations from 0 to 2 M was added slowly to the solution to precipitate the silver gently but completely. This gradient was made by adding 10 mL of 2 M hydrochloric acid to 30 mL of water little by little. The supernatant was filtered with a 0.22-mm filter and dried out by heating in a new glass beaker. ^{107}Cd on the bottom of the beaker was dissolved in an appropriate volume of the culture solution containing a designed concentration of nonradioactive Cd.

For *Arabidopsis halleri* ssp. *gemmifera* imaging, the roots of an intact *A. halleri* ssp. *gemmifera* plants were inserted in a 5 mL plastic disposable open root cell (KGS 1509-F01-07,Kumikouki Co., Gunma, Japan), and the shoots were fixed to an acrylic board. The acrylic board was placed in the field of view of the PETIS (PPIS-4800; Hamamatsu Photonics, Hamamatsu, Japan). Open root cell was supplied with 5 mL of 1/5 Hoagland solution containing concentrations 10 μM of $CdSO_4$ labeled with 30 MBq (1.68 pmol) ^{107}Cd. The movement of ^{107}Cd in the plants, including the roots and shoots, was monitored by the PETIS every 10 min for 36 h. The solution was continuously stirred with gentle aeration in order to maintain a uniform composition in each compartment of the root cell. All imaging experiments were conducted in a growth chamber with continuous light at a density of 72.9 μmol m^{-2} s^{-1}. The time course data of the Cd amount (mol) in the regions of interest in the images were calculated by the values of the signal intensity (cps) extracted

using the NIH Image J 1.50 software (http://rsb.info.nih.gov/ij/), counting efficiency of the system (cps Bq^{-1}) and molar activity (Bq mol^{-1}).

Quantitative Determination and Decay Correction

In the feeding experiments, the indicated amounts of nonradioactive Cd were mixed with measured activities of pure ^{107}Cd at a certain time before feeding to the plants. Therefore, the amount of total Cd (i.e. sum of radioactive and nonradioactive Cd) corresponding to the radioactivity of ^{107}Cd at a given time can be easily determined. The graphs shown in this paper indicate the relative amounts of total Cd (%), not just the intensities of ^{107}Cd signal.

Results and Discussions

The tracer solution containing ^{107}Cd was administered to *A. halleri* ssp. *gemmifera* plant and the dynamics of ^{107}Cd in intact whole plant was monitored by PETIS (Figs. 1a and 2a). As a result, obvious clear serial images of ^{107}Cd distributions from the roots to the shoots were successfully obtained for 36 h (Fig. 1b). Because the amount of non-radioactive cadmium labeled with ^{107}Cd was calculated by ^{107}Cd radioactivity, Fig. 2b represents the time course of cadmium. The amount of cadmium in the hydroponic solution decreased rapidly for the first 2 h and slowly after 3 h. The amount of cadmium in the roots increased rapidly for the first 6 h and reached a plateau of approximately at 12 h after feeding. The time-course curves of Cd in shoots showed opposite trends to solution values. It was estimated that at the end of the PETIS experiment 50% of Cd absorbed by the roots from solution was transported into the shoots in plants. This is the first reported study to visualize Cd movement non-invasively in an intact Cd hyperaccumulator, *A. halleri* ssp. *gemmifera*. In comparison with the previous studys[1, 2], the imaging data from this study also can be applied for quantitative analysis of the dynamics and kinetics of Cd uptake and transport in *A. halleri* ssp. *gemmifera*. The further research is required to investigate the Cd dynamics and kinetics in *A. halleri* ssp. *gemmifera* with different Cd conditions.

Acknowledgement

This work was supported by Supply Platform of Short-lived Radioisotopes for Fundamental Research.

References

1) Fujimaki S, Suzui N, Ishioka N, Kawachi N, Ito S, et al., *Plant Physiol* **152** (2010) 1796.
2) Fontanili L, Lancilli C, Suzui N, Dendena B, Yin Y-G., et al., *Rice* **9** (2016) 16.
3) Claire-Lise M, Nathalie V, *New Biotechnol* **30** (2012) 9.
4) Kupper H, Lombi E, Zhao FJ, McGrath SP, *Planta* **212** (2000)75.
5) Zhang Z, Wen X, Huang Y- Kohda T, Inoue C, Liang Y, *Plant Soil* **418** (2017) 165.

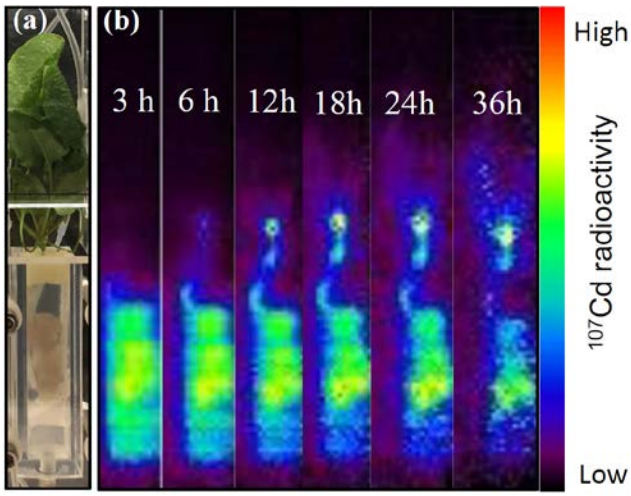

Figure 1. Serial images of ^{107}Cd movement in *A. halleri* ssp. *gemmifera* plant. **(a)** Photograph of test plant in the experimental apparatus. **(b)** Serial images of the whole plant (0–36 h). Each frame was created from the integration of 18 (b) original images collected every 10 min.

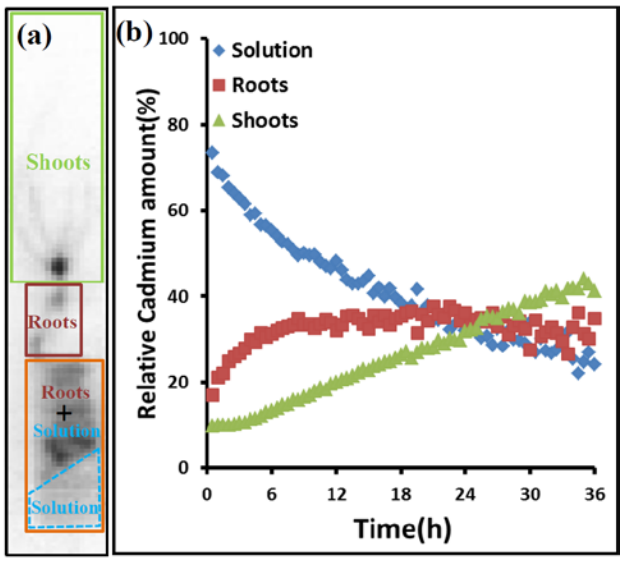

Figure 2. Time course of Cd amount in *A. halleri* ssp. *gemmifera* plant. **(a)** Examined regions of the plant. The blue dotted rectangle indicates the region of the solution, the orange solid rectangle that of the solution and the root, the red solid rectangle that of the root above the solution and the green solid rectangle that of the shoots. **(b)** Time course of the relative cadmium amount in the solution, roots and shoots.

VI. 2. Minimization of the Amount of Kryptofix 2.2.2/$KHCO_3$ for Microscale Radiosynthesis of ^{18}F-Labeled Probes

Iwata R.[1], Pascali C.[2], Terasaki K.[3], Ishikawa Y.[1], Furumoto S.[1], and Yanai K.[4]

[1]Cyclotron and Radioisotope Center, Tohoku University
[2]Fondazione IRCCS Istituto Nazionale dei Tumori, Italy
[3]Cyclotron Research Center, Iwate Medical University
[4]Graduate School of Medicine, Tohoku University

Nowadays the $^{18}O(p,n)^{18}F$ reaction on enriched [^{18}O]water is widely used for the production of no-carrier-added [^{18}F]fluoride ([^{18}F]F^-). The labeling use of this [^{18}F]F^- requires a rapid and efficient separation and recovery from the target water mostly by the combined use of a disposable anion exchange cartridge Sep-Pak QMA (HCO_3^-) and a Kryptofix 2.2.2-$KHCO_3$ complex (K.222/$KHCO_3$) dissolved in a mixture of water and acetonitrile (MeCN). Since the presence of water spoils the subsequent reaction of [^{18}F]F^- in an aprotic solvent such as MeCN and DMSO, the eluate from the cartridge is usually evaporated to dryness by repeated azeotropic distillation. To avoid this laborious procedure two alternative methods were reported: an electrochemical concentration method[1)] and a minimalist approach[2)]. The former method is based on trapping [^{18}F]F^- on the surface of a carbon electrode and releasing it into a small amount of dry MeCN or DMSO containing K.222/$KHCO_3$. The [^{18}F]F^- ready for reaction is prepared in <100 μL within 6 min but the recovery yield of reactive [^{18}F]F^- is unsatisfactorily low (<60%). On the other hand, the minimalist approach, which avoids repeated evaporations by applying a precursor in an “onium” form dissolved in dry methanol (MeOH) to the elution of [^{18}F]F^- from the QMA cartridge, yields a recovery higher than 95%. MeOH can be then rapidly evaporated and a suitable aprotic solvent added to the residue for subsequent ^{18}F-substitution. Weak point of this approach is the limited applicability since only few precursors are are available in an “onium” form. Thus, based on this minimalist approach, we developed a more general method starting from the K.222/K[^{18}F]F that can be applied to the radiosynthesis of various ^{18}F-labeled probes while minimizing also the amount of K.222/$KHCO_3$ for microscale radiosynthesis (see next report).

A 1-1.5 mL portion of the diluted $[^{18}F]F^-$, which was produced in $[^{18}O]H_2O$ (98 atom%-enrichment, Taiyo Nippon Sanso) with the Cypris HM-12 cyclotron at CYRIC, was passed through either a silica-based anion exchange cartridge of Sep-Pak Plus Light QMA (HCO_3^-, 46 mg, Waters) or a polymer-based anion exchange cartridge of Oasis MAX (HCO_3^-, 10 mg, Waters). The cartridge was washed with dry MeCN or MeOH (2-3 mL) to remove water and the $[^{18}F]F^-$ was then eluted with K.222/$KHCO_3$ in MeCN or MeOH (5-40 mM, 50-300 µL) followed by further rinse with MeOH (70 µL). Figure 1a clearly indicates that dry MeOH was a much better solvent than MeCN for eluting $[^{18}F]F^-$ from the cartridge with K.222/$KHCO_3$. As expected, higher concentrations of K.222/$KHCO_3$ allowed for better elutions of $[^{18}F]F^-$ and Fig. 1b also shows that the relatively larger ion exchange capacity of QMA lowered the recovery yields than that of Oasis MAX. As expected, this difference in performance becomes even more critical at low concentrations or volumes. The minimum amount of K.222/$KHCO_3$-MeOH still affording a high recovery yield was determined as 40 mM-200 µL for QMA and 10 mM-200 µL for MAX (Fig. 1b).

Even such a small content of K.222/$KHCO_3$ in 200 µL MeOH increases its concentration by >10 times up when the MeOH volume is reduced down to <20 µL. This high concentration may affect unfavorably the reaction as demonstrated in the synthesis of protected $[^{18}F]$FDG (Fig. 2)[3], where no relevant effect on the yield was observed between 10-80 mM whereas a rapid drop was registered at volumes leading to concentrations above 80 mM. For this reason, a practical method for efficient removal of K.222/$KHCO_3$ had to be developed for microscale radiosynthesis of ^{18}F-labeled probes. Three commercially available cartridges of OASIS MCX (H^+, 10mg), OASIS MCX (H^+, 30 mg) and Sep-Pak Plus Light CM (H^+, 130 mg) were examined to remove/decrease the K.222/K^+ present in the MAX cartridge eluate. A cation exchange cartridge was connected to the MAX cartridge and the target content was passed through the two cartridges. After rinsing with MeOH (2 mL), $[^{18}F]F^-$ was eluted with a 20 mM K.222/$KHCO_3$-MeOH solution (200 µL) followed by MeOH (100 µL). Concentration of K.222/K^+ in the eluate was semi-quantitatively estimated by color spot test and the intensity of its spot was compared with those of 10 standard solutions of known concentrations (0-20 mM) of K.222/$KHCO_3$ in MeOH. As shown in Fig. 3, best results were obtained with Oasis MCX (30 mg; 30 µeq of cation exchange capacity). It retained the majority of K.222/$KHCO_3$, with less than 0.2 mM eluting into a reaction vial. The concentration of K.222/$KHCO_3$ in the reaction solvent could be readjusted by adding an appropriate amount of a 20 mM K.222/$KHCO_3$–MeOH

solution to the eluate before MeOH evaporation.

In conclusion, the amount of K.222/$KHCO_3$ was successfully minimized for efficient recovery of [^{18}F]F^- from the target water and readjusted for microscale radiosynthesis using the combined use of Oasis MAX and MCX disposable cartridges. The present results were published in Applied Radiation & Isotopes[3] and in part presented at 22nd International Symposium on Radiopharmaceutical Sciences, May 14-19, 2017 in Dresden (Germany).

Acknowledgement—The present study was supported by JSPS KAKENHI Grant Number 16H05383.

References

1) Saiki H, Iwata R, Nakanishi H, et al., *Appl Radiat isot* **68** (2010) 1703.
2) Richarz R, Krapf P, Zarrad F, et al., *Org Biomol Chem* **12** (2014) 8094.
3) Iwata R, Pascali C, Terasaki K, et al., *Appl Radiat Isot* **125** (2017) 113.

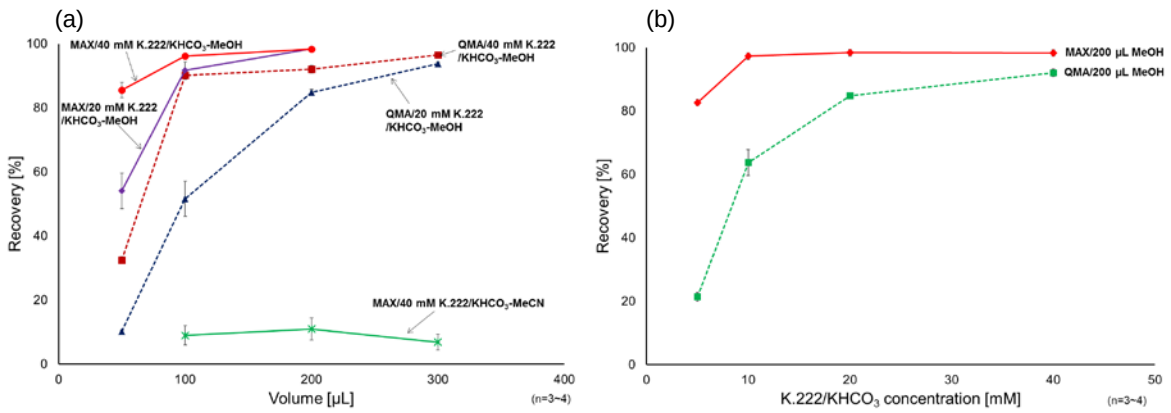

Figure 1. (a) [^{18}F]Fluoride recovery yield from QMA and MAX cartridges vs a volume of K.222/$KHCO_3$-MeOH or K.222/$KHCO_3$-MeCN and (b) [^{18}F]fluoride recovery yield from QMA and MAX cartridges vs a K.222/$KHCO_3$ concentration in MeOH.

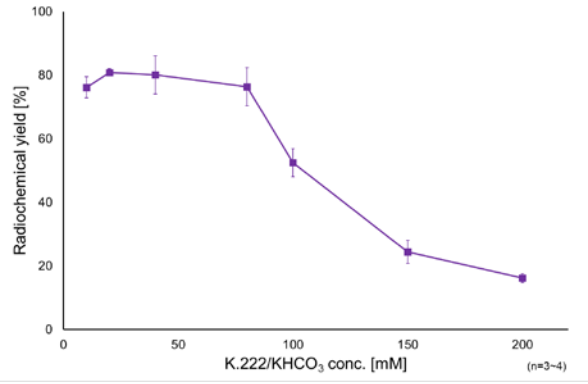

Figure 2. Radiochemical yield of protected [^{18}F]FDG as a function of MeCN volume with 10-80 mM K.222/$KHCO_3$.

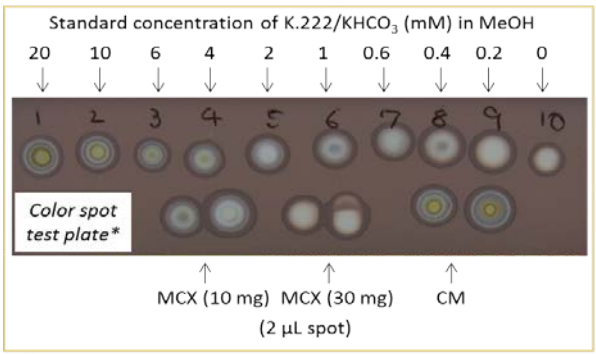

*Obtained from JFE Incorp.

Initial K.222/$KHCO_3$	:	20 mM	20 mM	20 mM
[^{18}F]F^- trapped by MAX	:	100%	100%	100%
		↓	↓	↓
Cation exchange cartridge	:	*Oasis MCX (10 mg)*	*Oasis MCX (30 mg)*	*CM Light (130 mg)*
		↓	↓	↓
Leaked K.222	:	2-4 mM	<0.2 mM	>10 mM
Recovered [^{18}F]F^-	:	94±2% (n=9)	93±1% (n=12)	32±7% (n=13)

Figure 3. Semi-quantitative analysis of K.222 by color spot test and removal of K.222/K^+ from a methanolic solution of K.222/$KHCO_3$/K[^{18}F]F by Sep-Pak CM and Oasis MCX cartridges.

VI. 3. Microscale One-pot Radiosynthesis of ^{18}F-Labeled Probes

Iwata R.[1], Pascali C.[2], Terasaki K.[3], Ishikawa Y.[1], Furumoto S.[1], and Yanai K.[4]

[1]Cyclotron and Radioisotope Center, Tohoku University
[2]Fondazione IRCCS Istituto Nazionale dei Tumori
[3]Cyclotron Research Center, Iwate Medical University
[4]Graduate School of Medicine, Tohoku University

Radiochemistry of no-carrier-added [^{18}F]fluoride (nca [^{18}F]F^-) with high molar activity (specific activity) is essentially microchemistry defined as “chemistry with minute quantities of material”. For instance, the carrier amount of 10 GBq [^{18}F]F^- having a molar activity of 100 GBq/μmol is only 0.1 μmol. Therefore, to better exploit this feature the idea of microreactors was introduced for the radiosynthesis of ^{18}F-labeled probes as an advanced tool allowing the reduction in quantities of reagents as well as rapid and efficient reactions. This concept has been partly exploited in microfluidics, where reactions take place in microchannels filled with flowing reagents However, because of this continuous flow, the overall solvent volume often exceeds several hundred μL, i.e. a volume comparable to that is the same level with a conventional automated radiosyntheses carried out in a glass vessel. Consequently, in such cases the scale reduction advantages associated to microreactors is clearly lost.

One-pot radiosynthesis is a batchwise method for carrying out two consecutive procedures of labeling and deprotection in one reaction vessel. We thought the use of a microreactor to be better suitable to this way of operating and to lead to several advantages over conventional scale radiosynthesis, such as reduction in amount of precious/toxic reagents; increase in precursor concentrations (and thus in radiochemical yields); easier and faster purification. For this purpose we successfully minimized the amount of K.222/$KHCO_3$ needed for an efficient recovery of [^{18}F]F^-. In this report we describe a new microscale method for the one-pot radiosynthesis of two widely used ^{18}F-labeled probes: [^{18}F]fallypride, a dopamine D2/D3 radioligand and *O*-(2-[^{18}F]fluoroethyl)-L- tyrosine ([^{18}F]FET), a positron emitting tyrosine analog for tumor imaging.

[^{18}F]Fallypride and [^{18}F]FET were prepared according to the synthesis schemes shown in Fig. 1. Their precursors, tosyl-fallypride (2 mg) and TET (12 mg), were obtained from ABX and dissolved in 1 mL of either DMSO or MeCN. Using the 20 mM K.222/$KHCO_3$-MeOH containing K.222/K[^{18}F]F (Solution A), which was prepared by eluting [^{18}F]F^- retained by an Oasis MAX cartridge with 20 mM K.222/$KHCO_3$-MeOH (see the present CYRIC Annual Report for details), the following 3 methods were performed to develop microscale one-pot radiosynthesis.

- Method 1: a 5-50 μL portion of the 20 mM K.222/$KHCO_3$-MeOH containing K.222/K[^{18}F]F (Solution A) was put in a small glass vial (300 μL) and evaporated to dryness at 85°C with He (200 mL/min). To the residue was added the same volume as Solution A of precursor solution (DMSO for [^{18}F]fallypride or MeCN for [^{18}F]FET) and then heated for the reaction.
- Method 2: a 5-50 μL portion of Solution A in a glass vial was brought to 300 μL with MeOH and evaporated to dryness at 85°C with He (200 mL/min). The same volume of precursor solution (DMSO for [^{18}F]fallypride or MeCN for [^{18}F]FET) was added to the residue and then heated for the reaction.
- Method 3: a 5-50 μL portion of Solution A in a glass vial was brought to 300 μL with MeOH followed by addition of 5-50 μL of DMSO. The MeOH was carefully evaporated and to the remaining DMSO was added the same volume of a MeCN solution of precursor. MeCN was quickly removed by evaporation and the vial was capped and heating was continued.

For [^{18}F]FET 2 M HCl was added to the reaction solution and the mixture was heated at 120°C for 10 min. The reaction solution was cooled in an ice bath and then diluted with KF (1 M). RCYs were determined by HPLC analysis of the crude solution (column: InertSustain C18, 4.7 x 150 mm; Solvent: MeCN/20 mM NaH_2PO_4/MeCN 40:60, 2.0 mL/min for [^{18}F]fallypride, MeCN/10 mM H_3PO_4 10:90, 2.0 mL/min for [^{18}F]FET). These analytical conditions were also applied to the purification of the crude product.

The radiochemical yields (RCYs) obtained for both probes with the three methods were compared. Method 1 was not practical because only a part of the total volume of the MeOH eluate was used but an ideal procedure to provide the highest RCYs at a given solvent volume, whereas Method 2 was a simulation of a practical procedure which started from the same volume of the MeOH with that eluted from the MAX cartridge (300 μL).

Figure 2 indicates that RCYs for the two probes in Method 1 gradually decreased by decreasing the solvent volume down to 20 μL, with a drastic drop beyond this point. On the other hand, RCYs in Method 2 were more markedly affected by the volume reduction, suggesting that this straightforward approach could not be adopted to practical microscale radiosynthesis due to its low RCYs. The decrease in the RCYs for Method 2 might be caused mainly by deposition of K.222/K[^{18}F]F on the vessel walls that could not be reached by the reaction solvent. In Method 3 addition of DMSO, which was expected to catch and concentrate K.222/K[^{18}F]F during MeOH evaporation, considerably improved the RCYs of both [^{18}F]fallypride and [^{18}F]FET. Although RCYs did not exceed those obtained by Method 1, Method 3 seems to be promising for further improvement in developing practical microscale radiosynthesis.

Figure 3 demonstrates that HPLC purification of the crude products obtained by microscale radiosynthesis was conveniently performed with an analytical column. The purifications were finished within 5 min for [^{18}F]fallypride and 4 min for [^{18}F]FET.

In conclusion, addition of DMSO to the MeOH eluate prior to its evaporation provided an efficiently concentrated solution of [^{18}F]F^- for microscale radiosynthesis of [^{18}F]fallypride and [^{18}F]FET. The present results were presented at International Symposium on 22nd Radiopharmaceutical Sciences, May 14-19, 2017 in Dresden (Germany).

Acknowledgement—The present study was supported by JSPS KAKENHI Grant Number 16H05383.

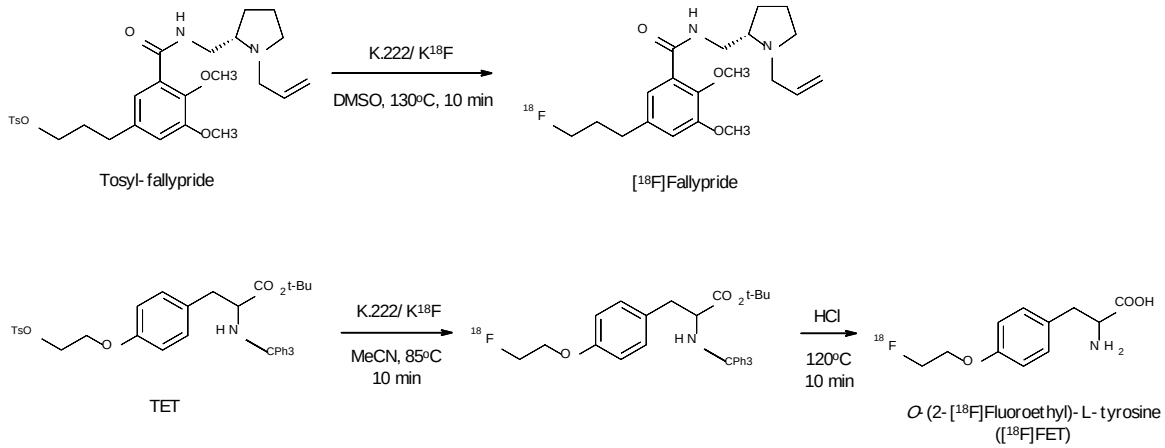

Figure 1. Synthesis schemes of [^{18}F]fallypride and [^{18}F]FET

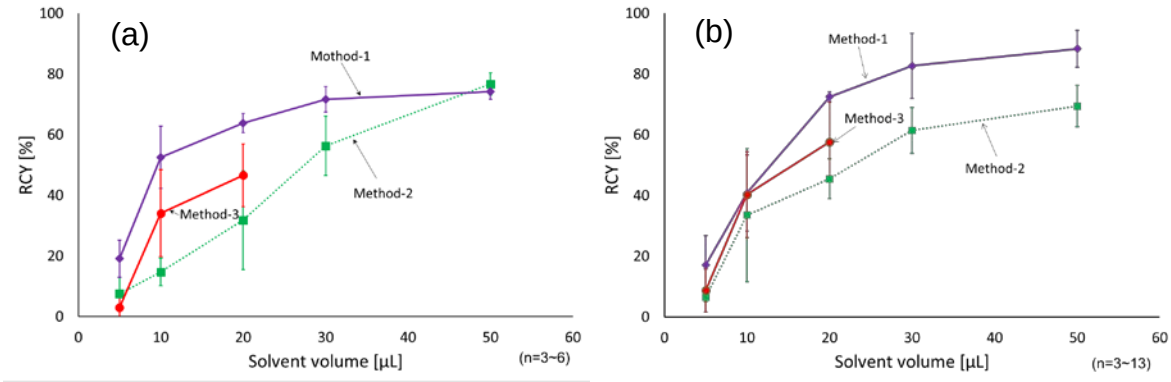

Figure 2. Dependence of RCY on solvent volume in the radiosynthesis of (a) [^{18}F]fallypride and (b) [^{18}F]FET.

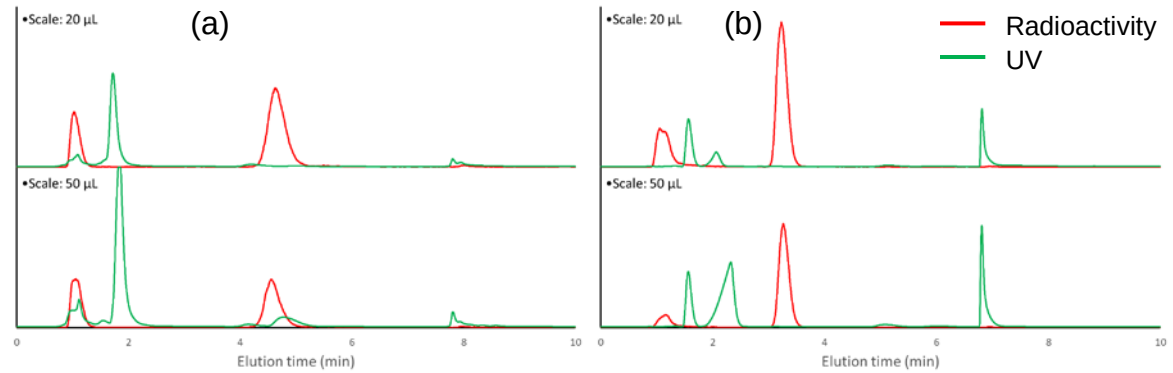

Figure 3. HPLC purification of (a) [^{18}F]fallypride and (b) [^{18}F]FET prepared in 20 and 50 μL scales.

HPLC conditions for [^{18}F]fallypride
- Column: InertSustain C18 (4.6x150 mm)
- Solvent: EtOH/20 mM NaH_2PO_4 (25/75)
- Flow rate: 2.0 mL/min
- UV: 254 nm

HPLC conditions for [^{18}F]FET
- Column: InertSustain C18 (4.6x150 mm)
- Solvent: EtOH/50 mM AcOH (10/90)
- Flow rate: 2.0 mL/min
- UV: 280 nm

VI. 4. Development of ^{18}F-Labeled Phosphonium Compounds for Imaging Mitochondria-rich Cells by Positron Emission Tomography

Tominaga T., Ishikawa Y., Iwata R., and Furumoto S.

Cyclotron and Radioisotope Center, Tohoku University

Introduction

Mitochondria, which is one of eukaryotic organelles, plays an important role in the production of ATP to supply energy required for various activities of cells. Cells of the heart and brown adipose tissue (BAT) contain many mitochondria and consume large amounts of energy. In vivo measurement of the mitochondrial activity could be valuable for diagnosis of diseases caused by mitochondrial dysfunction. ^{18}F-FBnTP is a fluorine-18 labeled triarylphosphonium (TAP) compound which accumulates in mitochondria depending on mitochondria membrane potential (MMP) (1). Although ^{18}F-FBnTP has been often used for imaging and assessing mitochondrial function of the heart and BAT in basic research, the complicated reaction procedures and sever reaction conditions for the radiosynthesis have hampered the clinical application of the tracer. To overcome this difficulty, we have been tried to develop new ^{18}F-labeled TAP derivatives (2). In this study, we have established a novel convenient method for synthesizing ^{18}F-labeled TAP compounds.

Methods

As the new radiosynthesis strategy different from conventional one, we devised a method to synthesize a ^{18}F-labeled phosphonium compound by synthesizing a ^{18}F-labeled triarylphosphine as an intermediate and then reacting it with an appropriate electrophile. Firstly, the reaction conditions of solvent and temperature for preparation of the phosphonium scaffold from ^{18}F-labeled phosphine intermediate and benzyl bromide (electrophile) were examined. Then, we tested several derivatives of benzyl bromide for synthesizing the ^{18}F-labeled phosphonium derivatives (^{18}F-TP-001~006) under the optimized reaction conditions.

Next, we biologically assessed the usefulness of ^{18}F-TP-001~006 as a mitochondrial

imaging tracer. Each tracer was injected into the mouse or rat tail vein and evaluated the tissue uptake rate of the tracer by biodistribution study and small animal PET imaging. Cellular uptake mechanism of the tracer was also examined by using a JC-10 probe for MMP measurement.

Results and Discussion

A ^{18}F-labeled triarylphosphine was prepared from the corresponding tosylate precursor by conventional radiofluorination method using ^{18}F-KF/K222, and then reacted with benzyl bromide. As the results of the examination of the second reaction conditions, the solvent, temperature, and time were optimized as acetonitrile, 100ºC, and 10 min, respectively. Under the conditions, ^{18}F-TP-001 was radiosynthesized in good radiochemical yields of 43±18% (Fig. 1). The other ^{18}F-TP derivatives were also prepared in moderate-to-good radiochemical yields under the same conditions. This method is a simple one-pot procedure and requires no corrosive reagents and sever reaction conditions, suggesting the feasibility of automated radiosynthesis of ^{18}F-TP.

Biodistribution study revealed that most of the derivatives showed high heart uptakes at 60 min post-injection. Especially, ^{18}F-TP-003 indicated higher accumulation in myocardium compared to other compounds with a large heart-to-liver uptake ratio (9.2). Cellular accumulation rate of ^{18}F-TP-003 was correlated well with a JC-10 uptake among three different cell lines, indicating that cellular accumulation of ^{18}F-TP-003 depends on MMP. Rat heart was clearly visualized by PET with ^{18}F-TP-003 (Fig. 2).

Conclusion

We developed a novel method for a synthesis of ^{18}F-labeled TP derivative by one-pot procedure. This method would increase the flexibility in drug design of ^{18}F-TP and be useful in the study on structure-activity relationship. ^{18}F-TP-003, one of the ^{18}F-TP derivatives, could be a potential candidate for a mitochondria imaging tracer.

References

1) I. Madar, H. T. Ravert, Y. Du, J. Hilton, L. Volokh, R. F. Dannals, J. J. Frost, J. M. Hare, *J. Nucl. Med. 2006, 47, 1359-1366*.
2) T. Tominaga, H. Ito, Y. Ishikawa, R. Iwata, K. Ishiwata, S. Furumoto, *J Label Compd Radiopharm. 2016, 59, 117–123*.

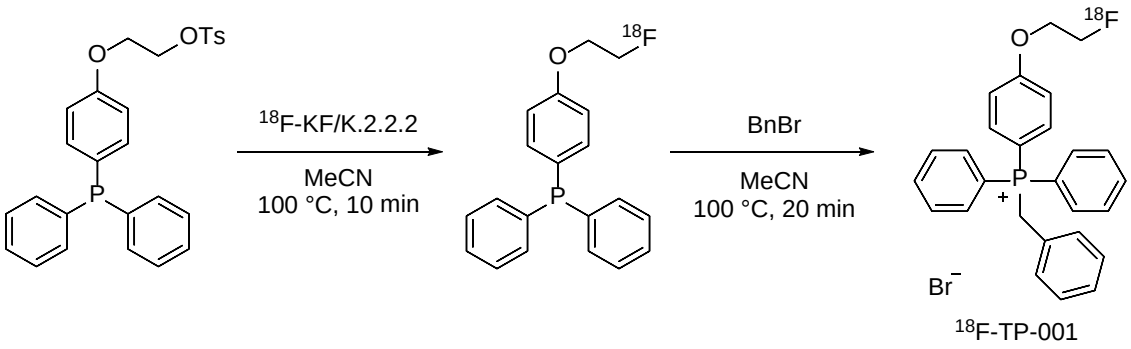

Figure 1. Radiosynthesis scheme of ^{18}F-TP-001.

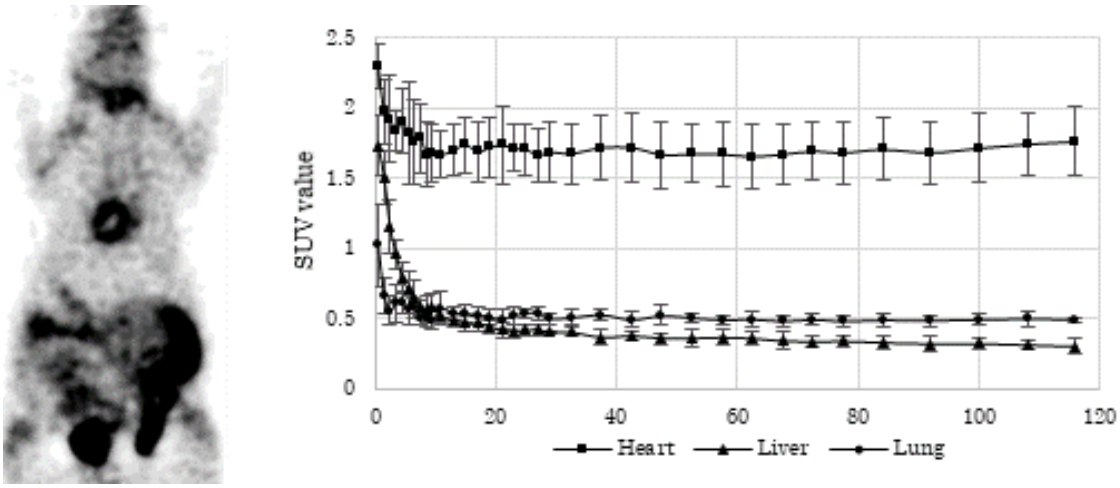

Figure 2. A rat PET image of ^{18}F-TP-003 (left) and time activity curves of the heart, liver, and lung (right).

VI. 5. Radiosynthesis of ^{11}C-Labeled Single Chain Antibody to HER2 by Cell-free Protein Synthesis System

Abe Y.[1], Ishikawa Y.[1], Iwata R.[1], Higuchi K.[2], Kigawa T.[2], Yokoyama J.[3], and Furumoto S.[1]

[1]Cyclotron and Radioisotope Center, Tohoku University
[2]RIKEN Innovation Center, [3]Taiyo Nippon Sanso

Introduction

Recent advances in genetic engineering has made it possible to prepare large amounts of antibodies, to humanize them, and to make their size small. Since molecular biology of cancer rapidly progressed, cancer treatment is shifting to molecular targeted therapy with an antibody specific for antigen of cancer cells. As a result, development of a molecular imaging technique of the therapeutic target has become important. For example, an antibody type diagnostic probe can be used for monitoring in the course of treatment by the immunotherapy with an antibody. Therefore, we have tried to develop a novel method for preparation of positron-emitter labeled antibody by using cell-free protein synthesis (CFPS) system (1). The method is to synthesize an antibody in vitro by using enzymes, several factors, template mRNA, natural amino acids, and a positron-emitter labeled amino acid (Fig. 1). In this study, we prepared and biologically evaluated a ^{11}C-labeled single chain antibody (scFv) to HER2 which is a transmembrane protein receptor with tyrosine kinase activity and overexpressed in breast and stomach cancers. HER2 is used as a prognostic factor for breast cancer diagnosis and a predictor of therapeutic effect. That is, HER2 positive breast cancer has poor prognosis and anti-HER2 therapy responds well. HER2-PET would be applicable to imaging biomarkers for diagnosis and therapy monitoring of breast cancer.

Methods

In this study, a single chain antibody of trastuzumab (tra-scFv) which bind strongly to HER2 was prepared by using CFPS system (Musaibo-Kun®) and ^{11}C-methionine as a part of amino acid sources for protein synthesis. To the kit solution of CFPS system, template DNA (plasmid) and ^{11}C-methionine (ca 1400 MBq/mL in saline) were added and incubated at 37℃.

After the incubation, ^{11}C-tra-scFv was purified by immune-affinity chromatography. Radiochemical yields was determined by SDS-PAGE and autoradiography (ARG). Binding affinity of ^{11}C-tra-scFv to HER2 was assessed by cell-biding assay using SK-OV-3 (human ovarian cancer cells with high expression of HER2) and MCF7 (human breast cancer cells with low expression of HER2). The tissue uptake of the tracer was evaluated by biodistribution study and small animal PET imaging.

Results and Discussion

Decay-corrected radiochemical yields of ^{11}C-tra-scFv were 8.6~13%. The binding rates (%ID/10^6 cells) of ^{11}C-tra-scFv were 15.8 ± 0.6 %ID/10^6 cells and 2.2 ± 0.2 %ID/10^6 cells for SK-OV-3 and MCF7, respectively (Fig. 2). The binding to SK-OV-3 was strongly inhibited by addition of trastuzumab, suggesting the specific binding of ^{11}C-tra-scFv to HER2 molecule. Biodistribution study in normal mice (ICR mice) demonstrated that ^{11}C-tra-scFv accumulated mainly in the kidney at 30 min and 60 min post-injection (Fig. 3). This biodistribution was also confirmed by PET imaging. These data indicate that the injected ^{11}C-tra-scFv shows smooth clearance from the body through kidney. This feature is necessary to obtain PET images of the thoracic region with low radioactivity background. Actually, when ^{11}C-tra-scFv was injected into a tumor bearing mouse made by implantation of SK-OV-3 cells to flank, the tumor was clearly visualized by PET (Fig. 4). Moreover, ^{11}C-tra-scFv showed high binding to the tumor tissue sections of SK-OV-3 in vitro, and the binding was completely blocked by addition of trastuzumab. These findings indicate that ^{11}C-tra-scFv can specifically bind to HER2 molecule expressed in the tumor tissue.

Conclusion

Using cell-free protein synthesis system and ^{11}C-methionin, we succeeded to prepare ^{11}C-labeled a single chain antibody which shows high binding to the antigen molecule. This study demonstrated that ^{11}C-tra-scFv synthesized by this method could be useful as a PET tracer for HER2 positive tumor imaging.

References

1) Matsuda T, Furumoto S, Higuchi K, Yokoyama J, Zhang MR, Yanai K, Iwata R, Kigawa T., *Bioorg. Med. Chem. 2012, 20, 6579-6582*.

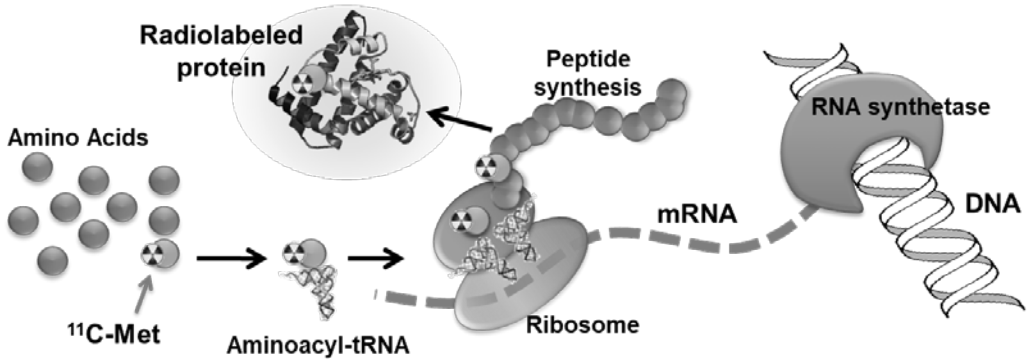

Figure 1. Radiosynthesis scheme of ^{11}C-labeled protein by cell-free protein synthesis system and ^{11}C-methionin (^{11}C-Met).

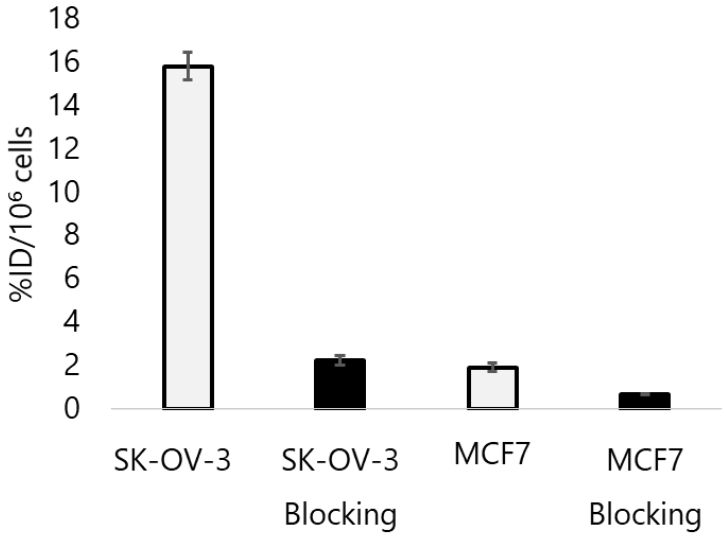

Figure 2. Cell binding assay for evaluation of binding of ^{11}C-tra-scFv to HER2 using SK-OV-3 (human ovarian cancer cells with high expression of HER2) and MCF7 (human breast cancer cells with low expression of HER2).

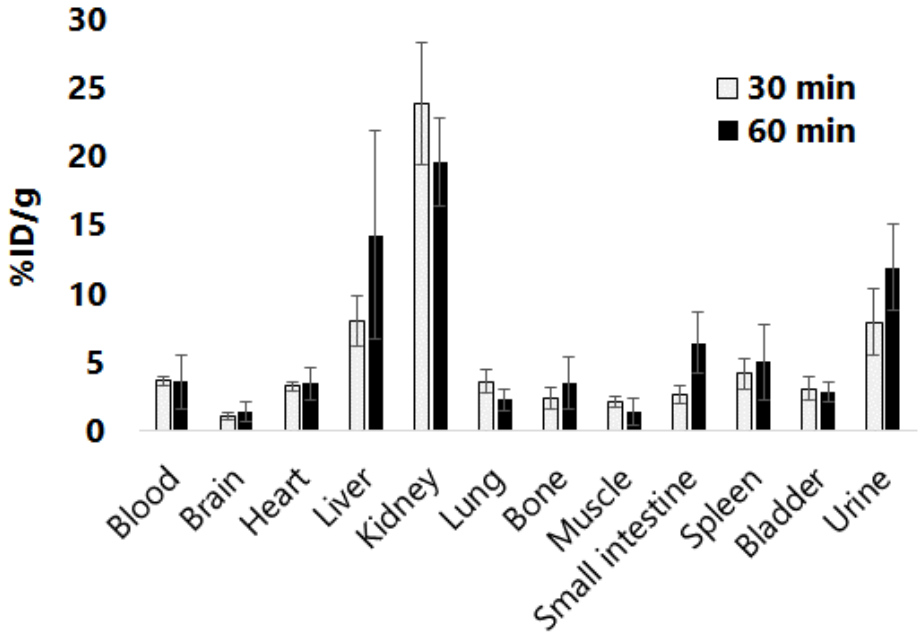

Figure 3. Biodistribution of ^{11}C-tra-scFv in ICR mice.

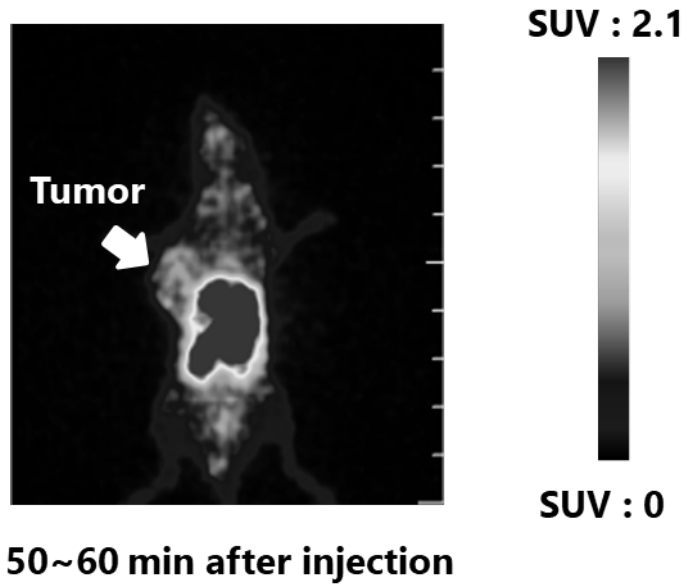

Figure 4. Tumor imaging by PET with ^{11}C-tra-scFv.

VI. 6. Monoamine Oxidase-B: Alternative Target of [^{18}F]THK-5351

Harada R.[1,2], Ishiki A.[2], Furumoto S.[3], Kudo Y.[2], Arai H.[2], Okamura N.[4], and Yanai K.[1]

[1]Tohoku University Graduate School of Medicine
[2]Institute of Development, Aging and Cancer, Tohoku University
[3]Cyclotoron and Radioisotope Center, Tohoku University
[4]Faculty of Medicine, Tohoku Medical and Pharmaceutical University

Introduction

[^{18}F]THK-5351 was one of first generation tau PET tracers that was designed originally to detect tau aggregates in the form of paired helical filaments found in brains of patients with Alzheimer's disease (AD). Previous in vitro autoradiography of [^{18}F]THK-5351 exhibited the selective binding in a laminar fashion in the cortex of formalin fixed brain sections from AD, which corresponded to tau immunohistochemistry[1,2]. Clinical PET studies of [^{18}F]THK-5351 demonstrated that elevated tracer retention in sites susceptible to tau deposition in various tauopathies including AD, progressive non-fluent aphasias (PNFA), progressive supranuclear palsy (PSP), and corticobasal syndrome (CBS)[2-4]. However, there was high binding of [^{18}F]THK-5351 in the subcortical regions such as the basal ganglia and thalamus even in control subjects whose brains are not expected to harbor tau aggregates. In addition, the tracer binding in these regions was correlated with age. To understand the binding nature of [^{18}F]THK-5351 and identify its targets, we investigated the binding property of [^{18}F]THK-5351 using fresh frozen human brain tissues including an autopsy-confirmed case of AD who underwent [^{18}F]THK-5351 PET scan before death.

Methods

Experiments were performed under the regulations of the Ethics Committee of the Tohoku University Graduate School of Medicine. Postmortem brain tissues from control subjects and patients with AD were acquired from Tohoku University Brain Bank and Tissue Solutions Ltd (Glasgow, UK). Twelve-micron thick brain slices were generated with a cryostat (Microm HM560; Thermo Scientific, Waltham, MA) using a -20°C chamber temperature and -15°C object temperature. Sections were transferred to MAS-coated glass

slides (Matsunami Glass Ind., Ltd, Osaka, Japan). After drying, the sections were stored at -80°C. Brain sections were dried and dipped in PBS for a total of 25 min, and then pre-incubated in PBS containing 1% bovine serum albumin (BSA). Brain sections were then incubated for 30 min at room temperature with 3 nM [^{3}H]THK-5351 (molar activity, 2.96 TBq/mmol; radiochemical purity, 98.9%, Sekisui Medical Inc., Tokyo, Japan). After incubation, sections were washed sequentially with PBS containing 1% bovine serum albumin (BSA) for 5 min, followed by PBS for 5 min twice. Dried sections were exposed to an imaging plate for tritium (BAS IP TR 2025 E, GE Healthcare, UK) for 3 days. The autoradiographic images were obtained from Typhoon FLA-7000 (GE Healthcare). *In vitro* competitive autoradiography was performed in the presence of 3 μM unlabeled ligands or inhibitors, which were obtained from Sigma-Aldrich and Tocris Bioscience (Bristol, UK).

Results

Displaceable binding of [^{3}H]THK-5351 was observed in the basal ganglia of normal subjects containing no amyloid plaques and tau tangles (Fig. 1). Competitive autoradiography was performed using various ligands whose targets have been reported in human basal ganglia. Lazabemide and rasagiline, which are known as reversible and irreversible monoamine oxidase-B (MAO-B) inhibitors, respectively, displaced [^{3}H]THK-5351 binding completely. However, no remarkable competition was observed with the other tested ligands, including a dopamine transporter inhibitor (GBR12935), μ-opioid receptor agonist (DAMGO), MAO-A inhibitor (clorygyline), and I_2 imidazoline receptor ligand (idazoxan) (Fig. 1).

In vitro autoradiography of [^{3}H]THK-5351 in various regions from an autopsy-confirmed AD case who underwent [^{18}F]THK-5351 PET scan before death demonstrated [^{3}H]THK-5351 binding was substantially reduced in the presence of MAO-B inhibitor, Lazabemide, whereas [^{3}H]THK-5351 binding remained detectable , albeit the binding in the basal ganglia was completely displaced (Fig. 2).

Discussions

This study demonstrated that tau PET tracer [^{18}F]THK-5351 bound to MAO-B as well as tau aggregates in fresh frozen human brain tissues. A recent human blocking study using selective irreversible MAO-B inhibitor, selegiline, confirmed this finding in vivo[5]. Recent imaging-autopsy correlations demonstrated that in vivo [^{18}F]THK-5351 binding was correlated with the density of tau aggregates and MAO-B in a patient with AD and PSP[6,7].

Previously, we observed selective binding to tau aggregates in paraffin-embedded fixed brain sections[1,2]. However, the fixation of tissues may affect the tracer binding because formalin produces cross-linkage of proteins and may result in diminishing the natural binding sites such as MAO-B enzymes or yielding the artificial binding sites. In fact, [^{18}F]THK-5351 binding in the basal ganglia disappeared after fixation (data not shown). These results highlighted the importance of appropriate experimental procedure in the evaluation of tracer binding.

Conclusions

MAO-B is an alternative binding target of [^{18}F]THK-5351. MAO-B is an attractive target for in vivo assessment of neuroinflammation such as astrogliosis. Therefore, [^{18}F]THK-5351 PET might be useful imaging biomarker for astrocytosis in neurodegenerative diseases.

References

1) Tago T, Furumoto S, Okamura N, et al., *J Nucl Med* **57 (**2016) 608.
2) Harada R, Okamura N, Furumoto S, et al., *J Nucl Med* **57 (**2016) 208.
3) Kikuchi A, Okamura N, Hasegawa T, et al., Neurology **87 (**2016) 2309.
4) Ishiki A, Harada R, Okamura N, Tomita N, Rowe CC, Vilemagne VL, Yanai K, Kudo Y, Arai H. Eur J Neurol **24 (**2017) 130.
5) Ng KP, Pascol TA, Mathotaarachchi S, et al. Alzheimers Res Ther **9 (**2017) 130.
6) Harada R, Ishiki A, Kai H, et al. J Nucl Med **59 (**2018) 671.
7) Ishiki A, Harada R, Kai H, et al. Acta Neuropathol Commun. **6 (**2018) 53.

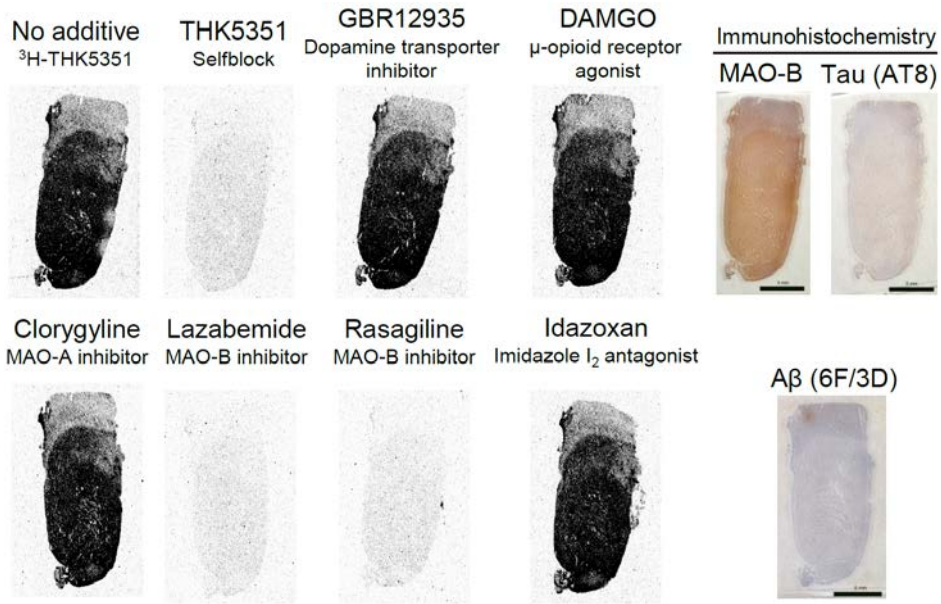

Figure 1. *In vitro* autoradiograms of [^{3}H]THK-5351 in basal ganglia brain sections from a normal control subject (83-year-old male) in the absence (no additive) and presence of unlabeled THK5351 and various inhibitors/ligands, namely GBR12935 (dopamine transporter inhibitor), DAMGO (μ-opioid receptor agonist), clorygyline (MAO-A inhibitor), lazabemide (MAO-B inhibitor), rasagiline (MAO-B inhibitor) and idazoxan (imidazoline I_2 antagonist). Immunohistochemistry images of tau (AT8), Aβ (6F/3D), and MAO-B are also shown.

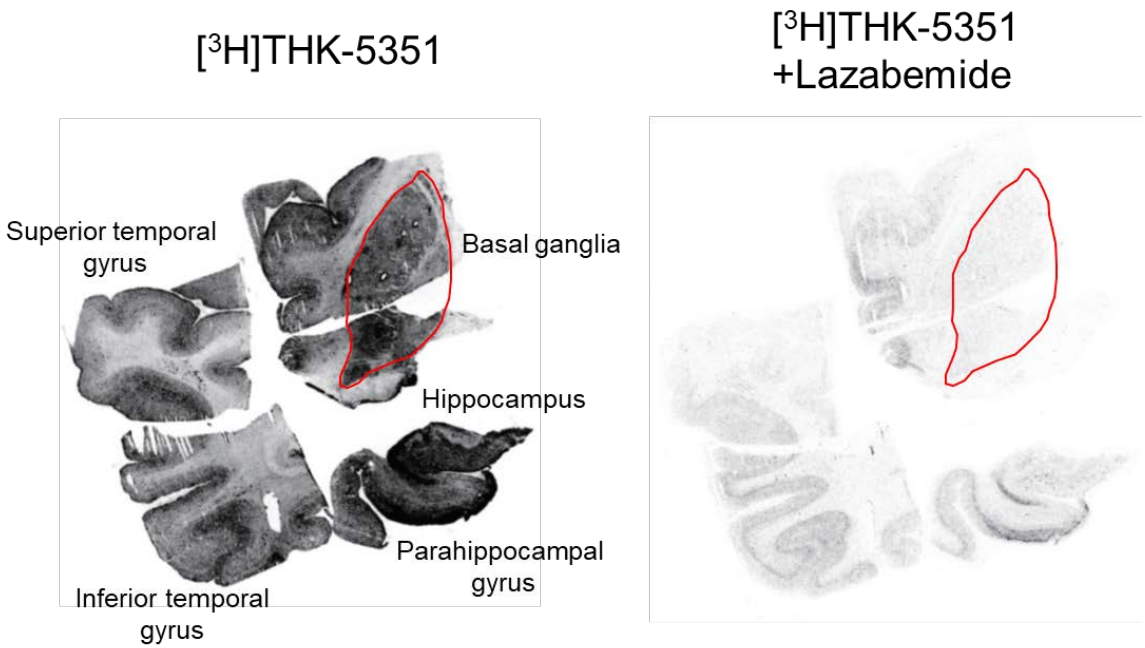

Figure 2. In vitro autoradiography of [^{3}H]THK-5351 in brain sections from an autopsy-confirmed AD case (81-y-old male) who underwent [^{18}F]THK-5351 PET scan before death in absence and presence of selective reversible MAO-B inhibitor, Lazabemide. Red notes the basal ganglia.

VII. NUCLEAR MEDICINE

VII. 1. Neuroimaging with [^{18}F]THK-5351 PET in Progressive Supranuclear Palsy

Ishiki A.[1], Harada R.[2], Tomita N.[1], Watanuki S.[3], Hiraoka K.[3], Tashiro M.[3], Kudo Y.[4], Furukawa K.[5], Okamura N.[5], and Arai H.[1,4]

[1]Tohoku University Hospital
[2]Tohoku University Graduate School of Medicine
[3]Cyclotron and Radioisotope Center, Tohoku University
[4]Aging and Cancer, Tohoku University
[5]Tohoku Medical and Pharmaceutical University

Introduction

Tau positron emission tomography (PET) would be useful for the diagnosis of Alzheimer's disease (AD) and non-AD tauopathies, such as progressive supranuclear palsy (PSP), corticobasal degeneration (CBD), and some variants of frontotemporal lobar degeneration (FTLD). [^{18}F]THK-5351 was one of the first-generation tau PET radiotracers that was designed originally to detect tau aggregates in the form of PHF-tau in AD[1)]. Clinical PET studies in PSP and CBS patients have demonstrated prominent [^{18}F]THK-5351 retention in the midbrain and basal ganglia where tau pathology was observed frequently at autopsy[2,3)]. However, recent studies have suggested the existence of off-target binding to monoamine oxidase-B (MAO-B). Selegiline, a selective irreversible MAO-B inhibitor, substantially reduced [^{18}F]THK-5351 binding in the brain of patients with PSP as well as AD[4)]. In an autopsy case of AD, [^{18}F]THK-5351 PET signal reflects the combination of tau pathology and reactive astrocytes in the AD brain[5)]. However, what an [^{18}F]THK-5351 PET signal reflects in the PSP brain remains unclear. We examined imaging-pathology correlation in two autopsy-confirmed PSP patients who showed prominent tracer retention on an antemortem [^{18}F]THK-5351 PET scan.

Materials and methods

PET images were acquired using an Eminence STARGATE PET scanner. After intravenous injection of [^{18}F]THK-5351 (185 MBq) or [^{11}C]PiB (296 MBq), dynamic PET

images were obtained for 60 ([^{18}F]THK-5351) or 70 ([^{11}C]PiB) min. T1-weighted magnetic resonance images (MRI) were obtained using a SIGNA 1.5-Tesla machine. Standardized uptake value (SUV) images of [^{18}F]THK-5351 (40–60 min after injection) and [^{11}C]PiB (50–70 min after injection) were obtained. The regional SUV-to-cerebellar cortex SUV ratio (SUVR) was used as an index of tracer retention. SPM12 software and PMOD Ver. 3.7 software were used for image analysis.

The left hemisphere of the brain was immersed in 10% formalin for histology. The brain portions were frozen for biochemical analyses and unfixed tissue-based assays. Tissue sections of paraffin-embedded blocks were stained with Luixol fast blue and hematoxylin-eosin. Selected sections were stained with anti-tau AT8, anti-β-amyloid 4G8, anti-α-synuclein P-syn/81A, anti-TDP43 pS409/410–1, and anti-GFAP 6F2 antibodies.

Quantification of tau and glial fibrillary acidic protein (GFAP) immunoreactivity, in vitro autoradiography of [^{18}F]THK-5351 and [^{3}H]THK-5351, semiquantification of PHF-tau by immunoblotting, and quantification of MAO-B and GFAP by enzyme-linked immunosorbent assay (ELISA) were performed (previously reported[6]).

Results

Subject 1

An 84-year-old male presented with memory disturbance and disorientation. One year later, standing and gait became unstable with progression of extrapyramidal signs and PSP was diagnosed clinically. PET scans were performed 2 years after the diagnosis of PSP. At the time of the PET scan, he was bedridden and the Mini-Mental State Examination (MMSE) score was 1 of 30. The PSP rating scale score was 82. A brain MRI showed a typical "hummingbird sign". He died of aspiration pneumonia 295 days after the PET scan.

Subject 2

A 73-year-old male presented with memory disturbance. Mild cognitive impairment was diagnosed clinically 3 years after the first symptoms appeared. He gradually presented with speech impairment, stereotypical behavior, and change of food preference, and progressive nonfluent aphasia (PNFA) was diagnosed. One year later, he presented with unstable gait and was prone to falls. At the PET scan, he was bedridden and the MMSE score was 1 of 30. An MRI showed diffuse brain atrophy prominent in the right anterior temporal, hippocampus, amygdala, and caudate nuclei. He died of aspiration pneumonia 79 days after PET scan.

[^{18}F]THK-5351 and [^{11}C]PiB PET scans

Figure 1 shows the [^{18}F]THK-5351 PET images from the two subjects. Images from a cognitively normal individual are shown for comparison at the bottom. Subject 1 showed significant [^{18}F]THK-5351 retention in the globus pallidus and midbrain. Mild tracer retention was observed also in the other cortices, including parahippocampal and inferior temporal gyri. Subject 2 showed prominent [^{18}F]THK-5351 retention in the parahippocampal and inferior temporal gyri, as well as the globus pallidus and midbrain. No remarkable retention of [^{11}C]PiB was observed in the neocortex in both of the subjects.

Neuropathological examination

Brain weight in subject 1 was 1580 g. Autopsy revealed severe atrophy in the midbrain tegmetum, pons, subthalamic nucleus, and relatively mild atrophy in the frontal cortex, but not in the basal ganglia. Neuropathological examination revealed tau pathology in neuronal and glial cells consistent with PSP. Globose tangles were observed in the midbrain, pons, medulla, subthalamic nucleus, and nucleus basalis of Meynert. Moderate numbers of tufted astrocytes were observed also in the amygdala, motor cortex, and superior frontal gyrus. Neurofibrillary tangles were observed in the area which corresponded to age-related Braak stage II. The tau immunoreactivity density appeared greatest in the medial temporal regions, followed by the basal ganglia and frontal cortex. Gliosis and neuronal loss were observed also in the substantia nigra. However, amyloid-β, α-synuclein, and TDP-43 pathology were absent in this case.

Brain weight in subject 2 was 920 g. Autopsy revealed atrophy in the temporal lobes, midbrain, pons, globus pallidus, hypothalamic nucleus, and cerebellar dentate nucleus. There was neuronal loss in the pigmented neurons of the substantia nigra and locus coeruleus. AT8 immunostaining revealed abundant tau burden, including neurofibrillary tangles, globose tangles, tufted astrocytes, coiled bodies, and neuropil threads in the temporal, cingulate, frontal, striatum, globus pallidus, and subthalamic nucleus. In addition, thorn-shaped astrocytes, typical in aging-related tau astrogliopathy, were observed in the temporal lobe gray and white matter. Sparse amyloid plaques were observed. Both α-synuclein and TDP-43 pathology were absent in this case. Gliosis was severe in the bilateral hippocampus and amygdala. Astrocytosis with neuronal loss was prominent in the temporal cortex, followed by the frontal and cingulate cortices. These tau lesions were composed of 4-repeat tau. These

results were consistent with atypical PSP, which was diagnosed as PSP-FTD.

In vivo–in vitro correlation analyses

Biochemical analysis revealed the presence of 4-repeat tau in both cases. In subject 1, sarkosyl-insoluble tau was high in the parahippocampal gyrus and hippocampus, moderate in the globus pallidus and putamen, and low in other areas. The parahippocampal gyrus contained 3- and 4-repeat tau, suggesting that they are age-related tau. AT8 immunohistochemistry was positive in the brain sections from the same tissue. In subject 1, in vivo [^{18}F]THK-5351 binding was correlated significantly with sarkosyl-insoluble tau levels determined by Western blot analysis ($r = 0.67$, $P = 0.039$). In addition, we found strong correlations between in vivo [^{18}F]THK-5351 binding and MAO-B levels ($r = 0.78$, $P = 0.0096$), between in vivo [^{18}F]THK-5351 binding and GFAP level ($r = 0.67$, $P = 0.039$). In vitro [^{3}H]THK-5351 binding assay using brain homogenates also demonstrated a strong correlation between in vivo [^{18}F]THK-5351 retention and in vitro tracer binding in subject 1 ($r = 0.92$, $P = 0.005$). Tau and GFAP immunoreactivities in the brain sections were measured quantitatively for correlation analysis between in vivo tracer retention and histopathology. We observed positive correlation trends between in vivo [^{18}F]THK-5351 retention and tau loads ($r = 0.48$, $P = 0.06$), and between in vivo [^{18}F]THK-5351 retention and GFAP immunoreactivity ($r = 0.49$, $P = 0.05$). In subject 2, in vivo [^{18}F]THK-5351 binding was correlated significantly with tau-immunohistochemistry using AT8 antibody ($r = 0.48$, $P = 0.037$). Furthermore, in vivo [^{18}F]THK-5351 retention was correlated positively with the density of GFAP immunoreactive astrocytes ($r = 0.64$, $P = 0.0033$).

In vitro autoradiography

In vitro autoradiography of [^{18}F]THK-5351 in frozen sections demonstrated high tracer binding in the globus pallidus as well as putamen in subject 1 and in the frontal cortex in subject 2, which was consistent with in vivo PET results. These bindings were displaced completely after treatment with MAO-B inhibitor, Lazabemide. The spatial pattern of [^{18}F]THK-5351 binding was similar to that of MAO-B immunostaining, suggesting that the target of [^{18}F]THK-5351 binding was MAO-B positive astrogliosis rather than the tau aggregates in the PSP brain.

Discussion

Tremendous efforts have been made to develop tau-selective PET radiopharmaceuticals. The first-generation tau PET tracers, such as [^{11}C]PBB3, [^{18}F]AV1451, and [^{18}F]THK-5351, showed nonnegligible off-target binding. In this study, we expanded the imaging-pathology correlation analysis to autopsy-confirmed PSP cases showing two different clinical phenotypes, Richardson syndrome (PSP-RS) and PNFA.

A patient with PSP-RS showed the spatial distribution of [^{18}F]THK-5351 retention which was similar to cases of classic PSP-RS. Postmortem examination of this patient confirmed the existence of 4-repeat tau aggregates in these regions. However, imaging-pathology correlation analysis indicated a significant correlation between in vivo [^{18}F]THK-5351 retention and MAO-B level. Furthermore, in vitro autoradiography demonstrated that [^{18}F]THK-5351 binding in the globus pallidus was displaced by the MAO-B inhibitor, suggesting that [^{18}F]THK-5351 mainly binds to the MAO-B rather than the 4-repeat tau aggregates. In our previous study using paraffin-embedded fixed brain sections, we observed specific binding of [^{18}F]THK-5351 to tufted astrocytes and neurofibrillary tangles in the PSP brain[2]. However, the fixation of tissues and use of alcohol in the differentiation process may affect the tracer binding in in vitro autoradiography experiments. In this study, we performed in vitro autoradiographs of fresh-frozen sections without using alcohol and found a substantial amount of tracer binding to MAO-B. Fresh-frozen section results showed good agreement with antemortem [^{18}F]THK-5351 PET analysis. These results highlighted the importance of appropriate experimental procedures in the validation of PET radiopharmaceuticals.

We observed a significant correlation between tau pathology and GFAP in both of our subjects. A postmortem study reported that the density of GFAP correlated with that of neurofibrillary tangles, but not with tufted astrocytes in PSP, suggesting the greater contribution of neurofibrillary tangles to astrogliosis in PSP[7]. MAO-B is expressed dominantly in the mitochondrial outer membrane of astrocytes. Since elevation of MAO-B levels in the brain has been implicated in several neurodegenerative diseases, MAO-B is an attractive target as a molecular imaging marker of astrogliosis. Our study strongly supported that [^{18}F]THK-5351 PET dominantly reflected the binding to MAO-B in patients with PSP. Therefore, [^{18}F]THK-5351 PET would be useful for in vivo assessment of astrogliosis in PSP. Future research should proceed with development of PET tracers for selective detection of astrogliosis and sensitive detection of 4-repeat tau in the human brain.

References

1. Harada R, Okamura N, Furumoto S, et al., J Nucl Med 57(2016) 208.
2. Ishiki A, Harada R, Okamura N, et al. Eur J Neurol 24(2017) 130.
3. Kikuchi A, Okamura N, Hasegawa T, et al., Neurology 87(2016) 2309.
4. Ng KP, Pascoal TA, Mathotaarachchi S, et al., Alzheimers Res Ther 9(2017) 25
5. Harada R, Ishiki A, Kai H, et al., J Nucl Med 59(2017) 671
6. Ishiki A, Harada R, Kai H, et al., Acta Neuropathol Commun. 6(2018) 53
7. Togo T, Dickson DW. Acta Neuropathol 104(2012) 398

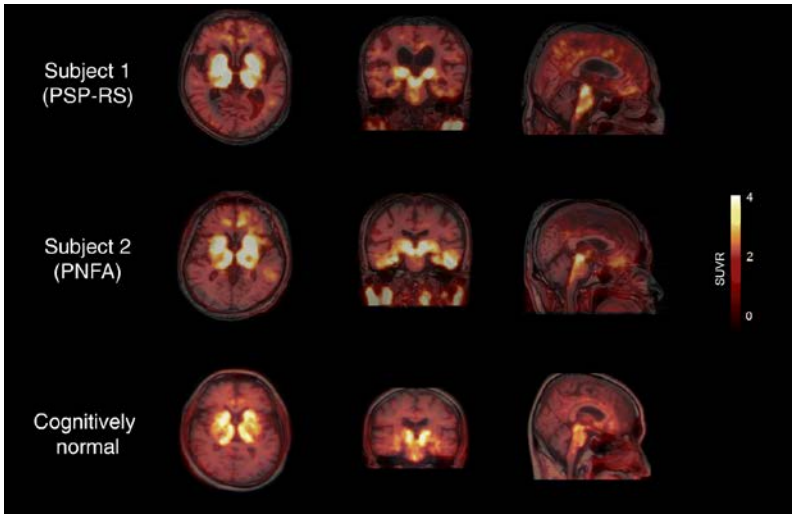

Figure 1. [^{18}F]THK-5351 PET images from two study subjects and a cognitively normal subject.

VII. 2. *In vivo* Visualization of Tau Deposits in Corticobasal Syndrome by ^{18}F-THK5351 PET

Kikuchi A.[1], Okamura N.[2], Hasegawa T.[1], Harada R.[2], Watanuki S.[3], Funaki Y.[3], Hiraoka K.[3], Baba T.[1], Sugeno N.[1], Oshima R.[1], Yoshida S.[1], Kobayashi J.[1], Ezura M.[1], Kobayashi M.[4], Tano O.[5], Mugikura S.[6], Iwata R.[3], Ishiki A.[7], Furukawa K.[7], Arai H.[7], Furumoto S.[3], Tashiro M.[3], Yanai K.[2], Kudo Y.[7], Takeda A.[8], and Aoki M.[1]

[1]*Department of Neurology, Tohoku University Graduate School of Medicine*
[2]*Department of Pharmacology, Tohoku University Graduate School of Medicine*
[3]*Cyclotron and Radioisotope Center, Tohoku University*[3]
[4]*Department of Neurology, Tohoku Pharmaceutical University Hospital*
[5]*Department of Neurology, Sendai Medical Center*
[6]*Department of Diagnostic Radiology, Tohoku University Graduate School of Medicine*
[7]*Institute of Development, Aging and Cancer, Tohoku University*
[8]*Department of Neurology, National Hospital Organization, Sendai Nishitaga Hospital*

CBS is an asymmetric higher cortical dysfunction with parkinsonism, dystonia, and myoclonus[1-4]. ^{18}F-THK5351 is a novel radiotracer with a binding affinity for tau protein deposits[5]. We did not know whether ^{18}F-THK5351 radiotracers detect tau deposits *in vivo* in patients with CBS. We evaluated whether ^{18}F-THK5351 PET can bind to tau pathology in living patients with CBS.

Five patients with CBS and eight age-matched normal controls (NCs) underwent ^{18}F-THK5351 PET scans. Probable CBS was diagnosed based on the modified Cambridge criteria[6]. All patients were right-handed. The NC group was comprised of volunteers with no cognitive or motor function impairments, who did not have any observable cerebrovascular lesions as indicated by MRI scans. This study protocol was approved by the Ethics Committee of the Tohoku University Hospital. Written informed consent was obtained from each patient or his/her guardian(s) after they were given a complete description of the study. We performed image analysis using the PNEURO module in PMOD software (version 3.6). In statistical analysis, we used a repeated measures analysis of variance (ANOVA) followed by Holm-Sidak's multiple comparisons test to compare regional ^{18}F-THK5351 retention in normal controls versus patients with CBS. The analyses were performed using GraphPad Prism6 software.

^{18}F-THK5351 PET images in a patient with CBS (70-year-old female, MMSE score 13) and a NC (61-year-old female, MMSE score 30) are shown in figure 1. We observed high ^{18}F-THK5351 retention in the precentral and postcentral gyri, and basal ganglia in the patient with CBS. ^{18}F-THK5351 retention for the bilateral precentral, postcentral, superior frontal, and superior parietal gyri and globus pallidus and left posterior cingulate gyrus was significantly higher in patients with CBS than in NCs ($p<0.005$). In all patients with CBS, a higher uptake of ^{18}F-THK5351 was seen in the regions contralateral to the symptom-predominant side.

Higher accumulation of ^{18}F-THK5351 was seen in the precentral and postcentral gyri, and globus pallidus in patients with CBS than in NCs. The spatial patterns of ^{18}F-THK5351 binding were compatible with tau deposit distributions observed in brain autopsies of patients with CBS[7-9]. These results suggest that ^{18}F-THK5351 PET is able to visualize tau deposits in patients with CBS. One limitation in this study was the relatively small sample size. We therefore could not examine the association between ^{18}F-THK5351 retention and clinical severity in CBS.

^{18}F-THK5351 PET demonstrated high tracer signals in sites susceptible to tau deposition in patients with CBS. ^{18}F-THK5351 should be considered as a clinical tool in the assessment of tau burden in CBS. Future clinical studies should clarify whether the radiotracer is a suitable biomarker for the early diagnosis and monitoring of disease progression in CBS[1].

References

1) Kikuchi A., Okamura N., Hasegawa T., Harada R., Watanuki S., Funaki Y., Hiraoka K., Baba T., Sugeno N., Oshima R., Yoshida S., Kobayashi J., Ezura M., Kobayashi M., Tano O., Mugikura S., Iwata R., Ishiki A., Furukawa K., Arai H., Furumoto S., Tashiro M., Yanai K., Kudo Y., Takeda A. and Aoki M., Neurology. **87** (2016) 2309.
2) Rebeiz J.J., Kolodny E.H. and Richardson E.P., Jr., Arch. Neurol. **18** (1968) 20.
3) Gibb W.R., Luthert P.J. and Marsden C.D., Brain. **112** (1989) 1171.
4) Boeve B.F. Lang A.E. and Litvan I., Ann. Neurol. **54** (2003) S15.
5) Harada R., Okamura N., Furumoto S., Furukawa K., Ishiki A., Tomita N., Tago T., Hiraoka K., Watanuki S., Shidahara M., Miyake M., Ishikawa Y., Matsuda R., Inami A., Yoshikawa T., Funaki Y., Iwata R., Tashiro M., Yanai K., Arai H. and Kudo Y., J. Nucl. Med. **57** (2016) 208.
6) Mathew R., Bak T.H. and Hodges J.R., J. Neurol. Neurosurg. Psychiatry. **83** (2012) 405.
7) Kouri N., Murray M.E., Hassan A., Rademakers R., Uitti R.J., Boeve B.F., Graff-Radford N.R., Wszolek Z.K., Litvan I., Josephs K.A. and Dickson D.W., Brain. **134** (2011) 3264.
8) Tsuboi Y., Josephs K.A., Boeve B.F., Litvan I., Caselli R.J., Caviness J.N., Uitti R.J., Bott A.D. and Dickson D.W., Mov. Disord. **20** (2005) 982.
9) Okazaki K., Fu Y.J., Nishihira Y., Endo M., Fukushima T., Ikeuchi T., Okamoto K., Onodera O., Nishizawa M. and Takahashi H., Neuropathology. **30** (2010) 140.

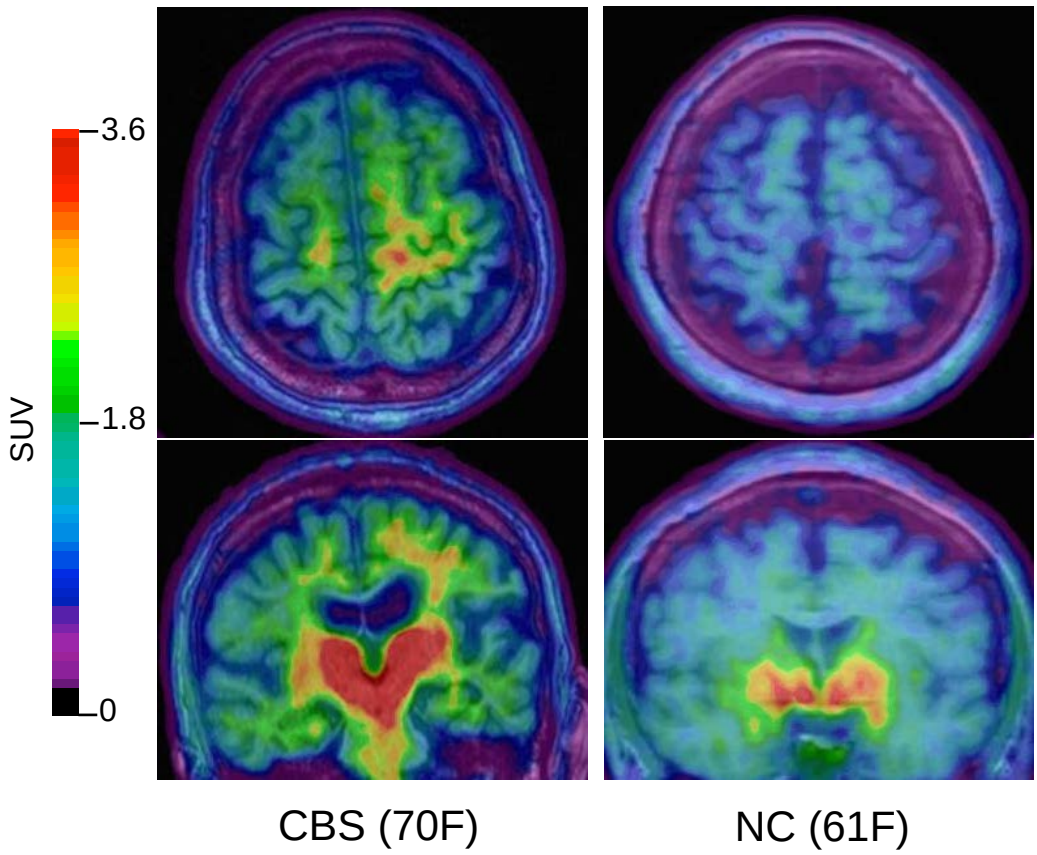

Figure 1. ^{18}F-THK5351 PET images overlaid on MRI data in a patient with corticobasal syndrome (CBS) and in a normal control (NC) subject.
^{18}F-THK5351 retention in the precentral and postcentral gyri, globus pallidus, and putamen was more evident in the patient with CBS than in the NC.

VII. 3. Brain Metabolic Changes of Cervical Dystonia with Spinocerebellar Ataxia Type 1 after Botulinum Toxin Therapy

Kikuchi A.[1], Takeda A.[1,2], Sugeno N.[1], Miura E.[1], Kato K.[1], Hasegawa T.[1], Baba T.[1], Konno M.[1], Oshima R.[1], Watanuki S.[3], Hiraoka K.[3], Tashiro M.[3], and Aoki M.[1]

[1]Department of Neurology, Tohoku University Graduate School of Medicine
[2]Department of Neurology, National Hospital Organization Sendai-Nishitaga Hospital
[3]Cyclotron and Radioisotope Centre, Tohoku University

Cervical dystonia is characterized by involuntary abnormal movements and postures of the head and neck. We often experience long-term remission of cervical dystonia after several botulinum toxin treatments [1)]. To confirm whether botulinum toxin acts on the central level[2-5)] as well as neuromuscular junctions, we study the changes of brain metabolism in a cervical dystonia patient with spinocerebellar ataxia type 1 (SCA1) before and after botulinum toxin A (BTX-A) therapy using ^{18}F-fluorodeoxyglucose (FDG) positron emission tomography (PET)[1)].

A 33-year-old man was hospitalized with severe fixed retrocollis, very mild cerebellar ataxia and pyramidal tract sign. Sensory trick, stereotype, and task specificity were observed. Brain MRI showed mild atrophy in the cerebellum and pons. Genetic analysis revealed expanded 49 CAG repeats in the SCA1 gene. An initial FDG-PET study was performed one month after the initial BTX-A treatment. His retrocollis exhibited dramatic and sustained improvement after several BTX-A treatments and was still improved 9 months after the last BTX-A treatment. A second FDG-PET study was then performed. The time difference between the first and second scans was 20 months. The types and doses of drugs were the same in the two FDG-PET studies.

We compared the FDG PET findings of this patient before or after BTX-A therapy to those of 18 age-matched normal controls. Two-sample t-tests were used for comparisons between the normal controls and the patient before and after BTX-A therapy using SPM5 software. The statistical threshold was set at family-wise error (FWE) $p<0.001$. The study protocol was approved by the Ethical Committee of Tohoku University Graduate School of

Medicine and a written informed consent was obtained from each subject after a complete description of the study. In the initial FDG-PET study, this patient showed hypermetabolism in the bilateral putamen and primary sensorimotor cortex compared to the 18 normal subjects. After the BTX-A therapy, most of the hypermetabolism in the bilateral putamen and primary sensorimotor cortex disappeared in this patient compared to in the normal group.

Because the frequency of dystonia in SCA1 patients is about 0 to 15%[6-8], cervical dystonia may be a presenting symptom in some patients with SCA1. Cervical dystonia showed a significant hypermetabolism in the lentiform nucleus[9] or the putamen[10] compared to normal controls using FDG PET. The cervical dystonia in this patient could be dramatically improved by the depression of hypermetabolism in the bilateral putamen and primary sensorimotor cortex after several BTX-A treatments. Therefore, the overactivities of bilateral putamen and primary sensorimotor cortex may be one of the most important factors for the pathogenesis of cervical dystonia with SCA1.

Cervical dystonia in this patient was improved in the long-term after several BTX-A treatments. BTX-A may act on the central nervous system (CNS) through afferent pathways from the injected site[2]. This patient is the first report to demonstrate that hypermetabolism in the bilateral putamen and primary sensorimotor cortex in cervical dystonia returns to normal after BTX-A therapy. We suggest that BTX-A has some effects on the CNS level to cause normalization in basal ganglia circuits and prolonged improvement[1].

References

1) Kikuchi A., Takeda A., Sugeno N., Miura E., Kato K., Hasegawa T., Baba T., Konno M., Oshima R., Watanuki S., Hiraoka K., Tashiro M. and Aoki M., Intern. Med. **55** (2016) 1919.
2) Giladi N., J. Neurol. Sci. **152** (1997) 132.
3) Kanovsky P., Streitova H., Dufek J., Znojil V., Daniel P. and Rektor I., Mov. Disord. **13** (1998) 108.
4) Ceballos-Baumann A.O., Sheean G., Passingham R.E., Marsden C.D. and Brooks D.J., Brain. **120** (1997) 571.
5) Etgen T., Muhlau M., Gaser C. and Sander D., J. Neurol. Neurosurg. Psychiatry. **77** (2006) 1017.
6) Lee W.Y., Jin D.K., Oh M.R., Lee J.E., Song S.M., Lee E.A., Kim G.M., Chung J.S. and Lee K.H., Arch. Neurol. **60** (2003) 858.
7) Pareyson D., Gellera C., Castellotti B., Antonelli A., Riggio M.C., Mazzucchelli F., Girotti F., Pietrini V., Mariotti C. and Di Donato S., J. Neurol. **246** (1999) 389.
8) Sasaki H., Fukazawa T., Yanagihara T., Hamada T., Shima K., Matsumoto A., Hashimoto K., Ito N., Wakisaka A. and Tashiro K., Acta. Neurol. Scand. **93** (1996) 64.
9) Magyar-Lehmann S., Antonini A., Roelcke U., Maguire R.P., Missimer J., Meyer M. and Leenders K.L., Mov. Disord. **12** (1997) 704.
10) Galardi G., Perani D., Grassi F., Bressi S., Amadio S., Antoni M., Comi G.C., Canal N. and Fazio F., Acta. Neurol. Scand. **94** (1996) 172.

VII. 4. Partial Volume Corrections for Tau and Amyloid PET Imaging with [^{18}F]THK5351 and [^{11}C]PiB

Shidahara M.[1,2], Thomas A.B.[3], Okamura N.[4], Ibaraki M.[5], Matsubara K.[5], Oyama S.[2], Ishikawa Y.[2], Watanuki S.[2], Iwata R.[2], Furumoto S.[2], Yanai K.[6], Watabe H.[2], and Tashiro M.[2]

[1]*Department of Quantum Science and Energy Engineering, Tohoku University*
[2]*Cyclotron Radioisotope Center, Tohoku University*
[3]*Institute of Nuclear Medicine, University College London*
[4]*Tohoku Medical and Pharmaceutical University*
[5]*Research Institute for Brain and Blood Vessels-Akita*
[6]*Department of Pharmacology, Tohoku University School of Medicine*

Introduction

Brain Positron Emission Tomography (PET) imaging of neurofibrillary tangle (tau) and amyloid β peptide (amyloid) has been recognized as having an important role in the diagnosis of Alzheimer's disease (AD)[1)]. However, due to the spatial resolution of PET system, the PET image suffers from partial volume effect (PVE), where regional uptake of radiotracer is blurred and its quantification is degraded[2)]. In order to compensate PVE on observed brain PET images, many partial volume correction (PVC) methods, which utilize both the spatial resolution and individual structural images (e.g. MRI), have been proposed. The classical and popular PVC methods are Müller-Gärtner (MG)[3)] and the geometric transfer matrix (GTM) methods[4)].

There have been several reports which state that applying PVC improved image quality of tau and amyloid PET and improved the accuracy and precision of the quantification of tracer uptake[5-14)]. However, in many cases, the applied PVC method were limited to MG or GTM. Furthermore, Greve et al. reported that different PVC methods (MG, GTM, and Meltzer) result in different conclusions in a FDG cross-sectional aging study of elderly subjects[15)]. There is a need to perform a comparison study of the popular PVC methods for tau and amyloid PET studies and to explore the possibility of other techniques. In this study, we report 4 PVC methods for tau and amyloid PET images: traditional MG, GTM, and other Regional voxel-based (RBV)[16)] and Iterative Yang (IY)[17)] methods.

Material and Methods

PET and MR images of 1 HC (81 y.o., Female) and 1 AD (80 y.o., Male) subjects, who had both a [^{11}C]PiB and [^{18}F]THK5351 PET scan, were used in this study. The PET studies were performed using Eminence STARGATE (Shimadzu Inc., Kyoto, Japan). After a 10-min ^{131}Cs transmission scan, 60- and 70-min dynamic scanning was started immediately after the intravenous administration of 304.9-347.4 MBq [^{11}C]PiB and 176.1-178.0 MBq [^{18}F]THK5351, respectively. All emission data were reconstructed using 3D-DRAMA (1 iteration, 128 filter cycle, 30 relaxation factor)[18] with attenuation and scatter corrections[19] and post filter of three dimensional Gaussian (3 mm FWHM). SUV images with 40-60 min time frame images were obtained. This study was approved by the Ethics Committee on Clinical Investigations of Tohoku University School of Medicine, and was performed in accordance with the Declaration of Helsinki. Written informed consent was obtained from all subjects after a complete description of the study had been made.

Brief explanations of 4 PVC methods were described below by using abbreviations as shown in Table 1. The MG[3] is voxel-based method for gray matter regions with the assumption of uniform-tracer uptake in white matter.

$$f_{c,gray}(x) = \frac{f(x) - A_{white,f(x)} \cdot p_{white}(x) \otimes PSF}{p_{gray}(x) \otimes PSF}, \tag{1}$$

The GTM method[4, 20] is ROI-based method and $C_{i,f(x)}$ is calculated as follows,

$$\begin{bmatrix} C_{1,f(x)} \\ \vdots \\ C_{i,f(x)} \\ \vdots \\ C_{N,f(x)} \end{bmatrix} = \mathbf{T}^{-1} \begin{bmatrix} A_{1,f(x)} \\ \vdots \\ A_{i,f(x)} \\ \vdots \\ A_{N,f(x)} \end{bmatrix}, \tag{2}$$

where **T** is the geometric transfer matrix of t_{ij}, which represents the contribution of spill-over from D_i into D_j. The RBV is an extension of the GTM and the voxel-wise correction of Yang et al.[21]. This process is given below:

$$\begin{aligned} f_c(x) &= f(x) \cdot \left[\frac{f_s(x)}{f_s(x) \otimes PSF} \right] \\ f_s(x) &= \sum_{i=1}^{N} \left[C_{i,f(x)} \cdot p_i(x) \right] \end{aligned} . \tag{4}$$

The Iterative Yang (IY) is a further adaptation of the Yang method[21]. This process is iterated several times with iteration number k is given below:

$$
\begin{aligned}
f_c^{\,0}(x) &= f(x) \\
f_c^{\,k+1}(x) &= f(x)\cdot\left[\frac{f_s^{\,k}(x)}{f_s^{\,k}(x)\otimes PSF}\right] \\
f_s^{\,k}(x) &= \sum_{i=1}^{N}\left[A_{i,f_c^{\,k}(x)}\cdot p_i(x)\right]
\end{aligned}
\tag{5}
$$

Automated parcellation of individual MR image was implemented by the FreeSurfer neuroimage analysis software package with version 5.1. The assignment of the parcellation map into 50 regions is shown in previous our report[22]. PVC processes were implemented using the PETPVC toolbox (https://github.com/UCL/PETPVC) and were applied assuming a resolution of 5 mm FWHM. Both uncorrected and PVC images with [^{18}F]THK5351 and [^{11}C]PiB were normalized with averaged ROI value in cerebellar grey matter to generate SUVR images.

Results and discussion

Figure 1 shows SUVR values of uncorrected PET images, 3 voxel-based and 1 ROI-based PVC results of the HC and AD subjects, for both tracers. The amount of recovery by RBV and IY were almost the same, similar with that of GTM, but different from those of MG (e.g., hippocampus of AD in [^{18}F]THK5351 and frontal of AD in [^{11}C]PiB). For HC subject, MG showed small increase of tracer uptake compared with other methods.

In the present study, we compared 4 partial volume correction methods for tau and amyloid PET imaging. Subjects undergoing tau and amyloid PET imaging are often expected to have brain atrophy, with or without physiological change in the region. It is difficult to accurately quantify tracer uptake in atrophic regions due to PVE. PVC for tau and amyloid PET imaging is expected to compensate PVE for more accurate quantification of tracer uptake, and is therefore essential for these applications[8].

However, the presented results suggest that most PVC techniques can produce different amounts of recovery in each region, subject condition, and tracer, even though RBV and IY showed the same results. In particular, MG showed different amount of recovery between subject conditions. In a previous study by Thomas et al., after PVC of MG, overestimation of [^{11}C]PiB uptake in the hippocampal region of an AD phantom was observed, even though that of a HC phantom was not[16]. We also observed a similar tendency with this correction technique. This indicates that tracer uptake in the hippocampal region after MG PVC may lead to a misinterpretation of pathological change.

Conclusion

PVC is essential processing when studying populations that are likely to have atrophy. However, in regions of high uptake of [^{18}F]THK5351 and [^{11}C]PiB, different PVCs demonstrated different SUVRs. The degree of difference between PVE uncorrected and corrected data depends on not only PVC algorithm but also subject conditions. Traditional PVC methods are straight-forward to implement but careful interpretation of the results is necessary.

References

1) Okamura N, Harada R, et al. *Ageing Res Rev*. (2016) 107-13.
2) Soret M, Bacharach SL, et al. *J Nucl Med*. **48** (2007) 932-45.
3) Muller-Gartner HW, Links JM, et al. *J Cereb Blood Flow Metab*. **12** (1992) 571-83.
4) Rousset OG, Ma Y, et al. *Journal of nuclear medicine*. **39** (1998) 904-11.
5) Adamczuk K, De Weer AS, et al. *Neuroimage Clin*. **2** (2013) 512-20.
6) Brendel M, Hogenauer M, et al. *Neuroimage*. **108** (2015) 450-9.
7) Forster S, Yousefi BH, et al. *Eur J Nucl Med Mol Imaging*. **39** (2012) 1927-36.
8) Ito H, Shinotoh H, et al. *Eur J Nucl Med Mol Imaging*. **41** (2014) 745-54.
9) Matsubara K, Ibaraki M, et al. *Neuroimage*. **143** (2016) 316-24.
10) Mori T, Shimada H, et al. *J Neurol Neurosurg Psychiatry*. **85** (2014) 449-55.
11) Rullmann M, Dukart J, et al. *J Nucl Med*. **57** (2016) 198-203.
12) Scholl M, Lockhart SN, et al. *Neuron*. **89** (2016) 971-82.
13) Su Y, Blazey TM, et al. *Neuroimage*. **107** (2015) 55-64.
14) Villemagne VL, Furumoto S, et al. *Eur J Nucl Med Mol Imaging*. **41** (2014) 816-26.
15) Greve DN, Salat DH, et al. *Neuroimage*. **132** (2016) 334-43.
16) Thomas BA, Erlandsson K, et al. *Eur J Nucl Med Mol Imaging*. **38** (2011) 1104-19.
17) Erlandsson K, Buvat I, et al. *Phys Med Biol*. **57** (2012) R119-59.
18) Tanaka E, Kudo H. *Phys Med Biol*. **55** (2010) 2917-39.
19) Ibaraki M, Matsubara K, et al. *Ann Nucl Med*. **30** (2016) 690-8.
20) Rousset OG, Collins DL, et al. *Journal of nuclear medicine*. **49** (2008) 1097-106.
21) Yang C, Huanf C, et al. *IEEE Trans Nucl Sci*. **43** (1996) 3322-7.
22) Shidahara M, Thomas BA, et al. *Ann Nucl Med*. **31** (2017) 563-9.

Table 1. Definitions and abbreviations for PVC processing

Abbreviation	Description
$f(x)$	uncorrected PET image
$f_c(x)$	PVE corrected PET image
$f_s(x)$	synthetic PET image
$p_i(x)$	anatomical probability of *i*-th region at location x
N	the total number of regions
$A_{i,\,f(x)}$	Averaged value of $f(x)$ at i-th region
$C_{i,\,f(x)}$	PVE corrected value for $f(x)$ at i-th region
D_i	Volume of i-th region
PSF	Point spread function
$\otimes$	Operation of three-dimensional convolution integral.

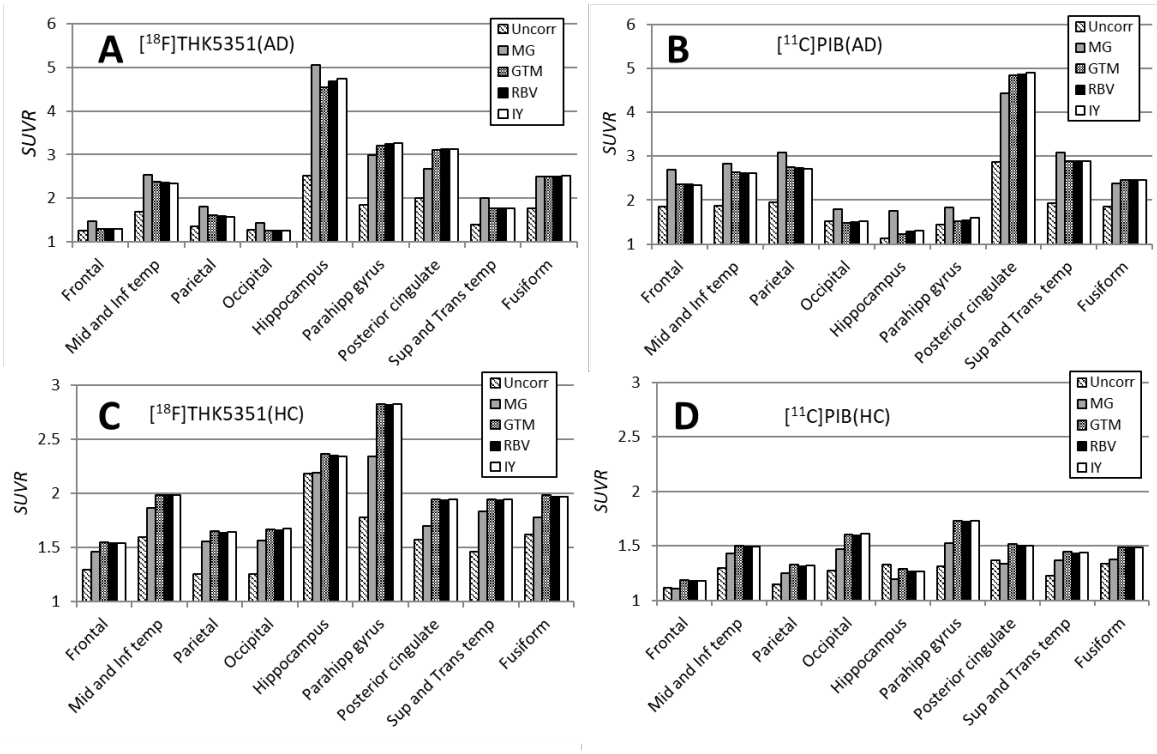

Figure 1. ROI comparisons of uncorrected and PVC SUVRs for a HC and AD subject with [^{18}F]THK5351 and [^{11}C]PiB

VII. 5. Biomathematical Modeling Approach to Predict Clinical SUVRs for Amyloid PET Imaging

Shidahara M.[1,2], Seki C.[3], Nai YH.[2], Okamura N.[4], Furumoto S.[2], Yanai K.[5], Watabe H.[2], and Tashiro M.[2]

[1]Department of Quantum Science and Energy Engineering, Tohoku University
[2]Cyclotron Radioisotope Center, Tohoku University
[3]National Institutes for Quantum and Radiological Science and Technology
[4]Faculty of Medicine, Tohoku Medical and Pharmaceutical University
[5]Department of Pharmacology, Tohoku University School of Medicine

Introduction

The aggregation of amyloid β peptide is one of the pathological observations in the brains of individuals with Alzheimer's disease (AD). Amyloid imaging using positron emission tomography (PET) has been recognized as having an important role in the diagnosis of AD[1)]. In the last decade, many PET radioligands for amyloid imaging have been developed; some of them have successfully been applied in human PET studies.

In general, the discovery and development of radioligands for clinical application requires complicated and sometimes empirical procedures in terms of chemical (e.g., stability of labeling and lipophilicity) or biological (e.g., affinity, metabolites and density of the target) factors[2,3)]. Even though these factors have been well-investigated in the case of candidate radioligands, several factors obtained in *in vitro* or *in vivo* animal studies may not be applicable to human studies; it is not easy to develop successful radioligands and satisfy clinical demands[4)]. We need to know not only the micro parameters of the candidate radioligands but also overall macroscopic performance.

Recently, there has been growing interest concerning more efficient development of successful radioligands in clinical studies using systematic evaluation of their overall performance (e.g., outcome measures)[3)]. It is obvious that the use of *in vivo* PET scans in experimental animals or humans is the fastest and easiest approach for the evaluation of the overall performance of the candidate radioligand. However, the development of a labelling protocol for positron emitter isotopes and the synthesis of a radioligand for PET studies are

labor intensive and also take considerable time. Therefore, in order to contribute on the radioligand development, we proposed a new method to predict standardized uptake value (*SUVR*) of amyloid PET radioligands using biomathematical modeling and *in silico* parameters (Fig. 1)[5]. The methodology includes empirical formula of lipophilosity (logP), free fraction of radioligand in blood (f_p) and free fraction of radioligand in tissue (f_{ND}). In this study, we investigated the influence of empirical formulae based on 3 datasets of f_p and f_{ND} reported by Guo et al.[3], Summerfield et al.[6], and Wan&Mauer[7,8] on the outcome, predicted SUVRs, of [^{11}C]PiB, [^{11}C]BF-227, [^{11}C]AZD2184, [^{11}C]SB-13, [^{18}F]FACT, [^{18}F]florbetapir, [^{18}F]florbetaben, [^{18}F]flutemetamol, [^{18}F]FDDNP and [^{18}F]AZD4694.

Material and Methods

We assumed that the radioligand for amyloid imaging obeyed the simplified one-tissue compartment model (1TCM) (Fig. 1). The kinetic parameters (K_1, k_2 and BP_{ND}) for each radioligand in the human brain were mathematically modelled, where K_1, k_2 and BP_{ND} are the influx and efflux rate constants between arterial plasma and brain tissue, and the binding potential, respectively. The time–activity curves (TACs), with or without specific binding of the radioligand in brain tissue, were calculated as follows:

$$\begin{aligned} C_{target}(t) &= K_1 \cdot C_p(t) \otimes \exp\left[-\left(\frac{k_2}{1+BP_{ND}}\right)t\right] \\ C_{reference}(t) &= K_1 \cdot C_p(t) \otimes \exp(-k_2 t) \end{aligned} \quad (1)$$

where C_{target} is the TAC of the target region, where the radioligand specifically binds to the target protein. $C_{reference}$ is the TAC of the reference region without the target protein. C_p is the arterial plasma input function. The influx rate constant from plasma to brain tissue, K_1 [mL/cm^3/min] was formulated using the Renkin–Crone model as follows:

$$K_1 = f \cdot \left[1 - e^{(-PS/f)}\right] \quad (2)$$

where P, f and S are capillary permeability [cm/min], perfusion [mL/cm^3/min] and capillary surface area [cm^2/cm^3 of brain], respectively. f and S were set to 0.6 [mL/cm^3/min] and 150 [cm^2/cm^3 of brain], respectively. Permeability P in **Eq. (2)** was empirically formulated as follows [3]:

$$P = 10^{\left\{-0.121(c\log D - 2.298)^2 - 2.544\log\left(V_x^{1/3}\right) - 2.525\right\}} \quad (3)$$

where *clogD* and V_x are lipophilicity and the McGowan volume [cm^3/mol/100], respectively. The efflux rate constant from brain tissue to plasma, k_2 [1/min], was expressed using the following equation, assuming equilibrium in the radioligand

concentrations between plasma and brain tissue.

$$k_2 = \frac{V_{aq\_P} \cdot K_1}{V_{aq\_T}} \cdot \frac{f_{ND}}{f_P} \tag{4}$$

where V_{aq_p} and V_{aq_T} are the apparent aqueous volume in plasma, the apparent aqueous volume in tissue and these were set to 0.98 [solvent/mL of plasma] and 0.9 [solvent/mL of tissue], respectively[3]. Both f_P and f_{ND} were estimated from empirical formulae, which were established from f_P and f_{ND} measured from *in vitro* binding experiments using mouse brain and plasma, and *in silico* lipophilicity. Here in this study, we tested 3 data sets of f_P and f_{ND} reported by Guo et al.[3], Summerfield et al.[6], and Wan&Mauer[7,8]. The radioligand binding capacity at the target site, BP_{ND}, was modelled[5] as follows:

$$BP_{ND} = f_{ND}\left\{\frac{B_{avail-42}}{K_{D-42}} + \frac{B_{avail-40}}{K_{D-40}}\right\} = f_{ND}\left\{\frac{a}{K_{D-42}} + \frac{(1-a)}{K_{D-40}}\right\}B_{avail} \tag{5}$$
$$B_{avail} = B_{avail-42} + B_{avail-40}$$

where a, $K_{D\text{-}42}$ and $K_{D\text{-}40}$ are the fractions of $A\beta_{1\text{-}42}$, the dissociation constant for $A\beta_{1\text{-}42}$ and $A\beta_{1\text{-}40}$, respectively. $B_{avail\text{-}42}$, $B_{avail\text{-}40}$ and B_{avail} were available binding sites of $A\beta_{1\text{-}42}$ and $A\beta_{1\text{-}40}$, ($A\beta_{1\text{-}42}$ + $A\beta_{1\text{-}40}$), respectively. a was assumed to have a value of 0.7, which is biochemically derived from fractions of extra-cellular insoluble $A\beta_{1\text{-}42}$ in both AD and HC brains [9]. The TACs of the target and reference regions were calculated using K_1, k_2 and BP_{ND} and fixed arterial input function C_p using Eq. (1). The parameter of interest, *SUVR*, was then estimated from the predicted TACs. Finally, for each data sets of f_p and f_{ND}, the predicted *SUVR* were compared with their clinical counterparts, *SUVR*[5].

Results and discussion

Figure 2A shows the relationships between *in silico* lipophilicity and *in vitro* $f_{ND,}$ and Fig. 2B shows the relationships between *in vitro* f_{ND} and f_P using the datasets of Guo's, Summerfield's and Wan&Maurer's, respectively. For each dataset, correlations between lipophilicity and f_{ND} and between f_{ND} and f_P were observed. Figure 3 shows the relationship between predicted SUVR and clinically observed SUVRs, these results were obtained by applying empirical formulae in Fig. 2 into the prediction scheme of SUVR of the 10 amyloid radioligands. In this study, we calculated Moriguchi logP as the lipophilicity[5]. Even though there was inconsistent use of lipophilicity between the 3 datasets (clogD and clogP by different softwares) and ours (*MlogP*) for the estimation of f_p and f_{ND}, positive

correlations between predicted and clinically observed SUVRs were observed (Fig. 3). These results supported the fact that our approach (*MlogP*) without the use of *in vitro* experiments for f_p and f_{ND} estimation can be applied to other amyloid radioligands, even though the data-sets selected for estimation of f_p and f_{ND} resulted in different values of the predicted SUVRs.

Conclusion

For all 3 data sets of f_p and f_{ND}, predicted *SUVR* showed good correlation with clinically observed *SUVR* for the 10 clinically applied amyloid tracers, however, the values of predicted SUVR were different from each datasets. These results will be contributed on the future improvement of the methodology.

References

1) Okamura N, Harada R, et al. *Ageing Res Rev*. (2016) 107-13.
2) Innis RB, Cunningham VJ, et al. *J Cereb Blood Flow Metab*. **27** (2007) 1533-9.
3) Guo Q, Brady M, et al. *J Nucl Med*. **50** (2009) 1715-23.
4) Laruelle M, Slifstein M, et al. *Mol Imaging Biol*. **5** (2003) 363-75.
5) Arakawa Y, Nai Y, et al. *J Nucl Med*. **58** (2017) 1285-92.
6) Summerfield SG, Read K, et al. *J Pharmacol Exp Ther*. **322** (2007) 205-13.
7) Maurer TS, Debartolo DB, et al. *Drug metabolism and disposition: the biological fate of chemicals*. **33** (2005) 175-81.
8) Wan H, Rehngren M, et al. *J Med Chem*. **50** (2007) 4606-15.
9) Steinerman JR, Irizarry M, et al. *Arch Neurol*. **65** (2008) 906-12.

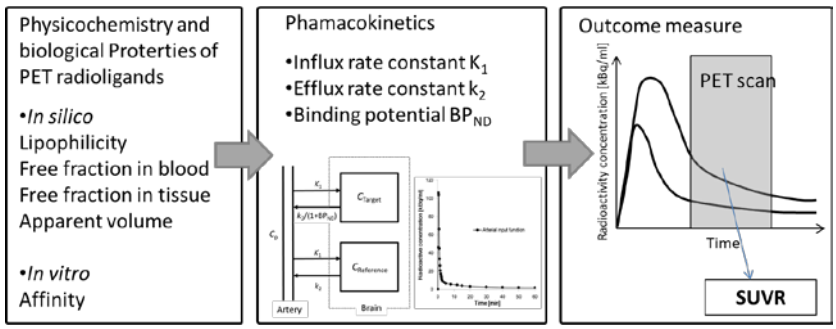

Figure 1. Overview of our biomathematical model: From physicochemical/biological properties of PET radioligand, pharmacokinetic parameters (K_1, k_2 and BP_{ND}) are estimated, then outcome measure (SUVR) is predicted through time activity curves of simplified 1 tissue model for both target and reference regions.

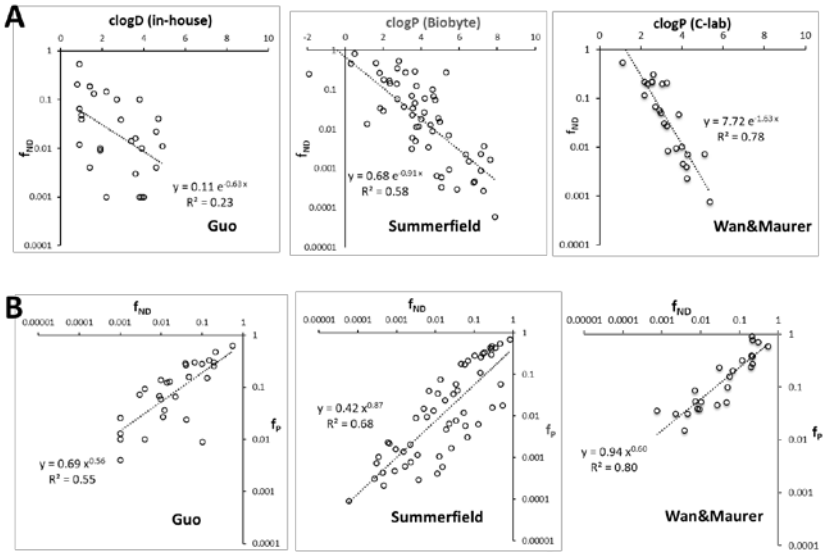

Figure 2 Relationship between in silico lippophilisity and f_p (A) and between f_p and f_{ND} (B) for 3 databases of Guo's, Summerfield's and Wan&Maurer's.

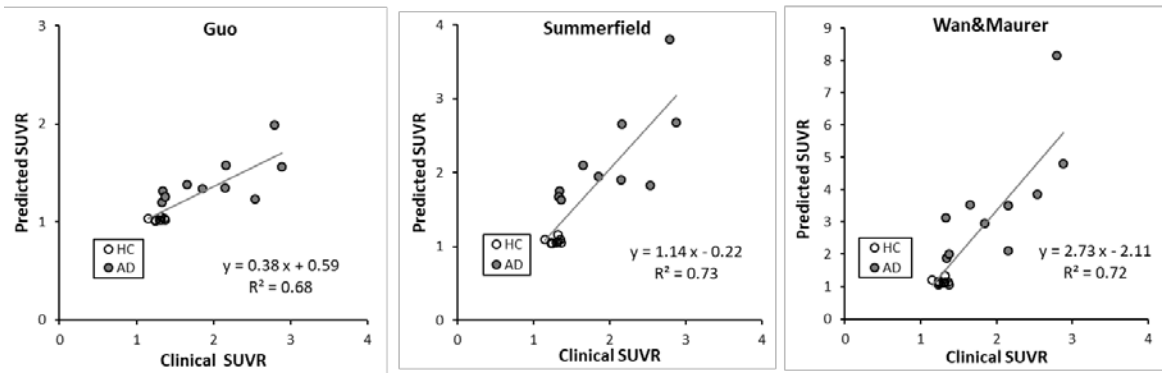

Figure 3 Relationship between clinically observed SUVR and predicted SUVR by our model based on 3 databases, Guo's (A), Summerfield's (B) and Wan&Maurer's (C).

VII. 6. Differential Activation in Amygdala and Plasma Noradrenaline during Colorectal Distention by Administration of Corticotropin-reporteleasing Hormone between Healthy Individuals and Patients with Irritable Bowel Syndrome

Tanaka Y.[1,2], Kanazawa M.[2], Kano M.[2,3], Morishita J.[2], Hamaguchi T.[2], Van Oudenhove L.[4], Ly H. G.[4], Dupont P.[5], Tack J.[4], Yamaguchi T.[6], Yanai Y.[7,8], Tashiro M.[8], and Fukudo S.[2]

[1]*Department of Integrative Genomics, Tohoku Medical Megabank Organization, Tohoku University*
[2]*Department of Behavioral Medicine, Tohoku University Graduate School of Medicine*
[3]*Department of Frontier Research Institute for Interdisciplinary Sciences, Tohoku University Graduate School of Medicine*
[4]*Translational Research Center for Gastrointestinal Disorders (TARGID), Department of Clinical & Experimental Medicine, KU Leuven, Belgium*
[5]*Laboratory for Cognitive Neurology, Department of Neurosciences, KU Leuven, Belgium*
[6]*Departments of Biostatistics, Tohoku University Graduate School of Medicine*
[7]*Departments of Pharmacology, Tohoku University Graduate School of Medicine*
[8]*Cyclotron and Radioisotope Center, Tohoku University*

Corticotropin-releasing hormone (CRH) is a major mediator of stress responses in the brain-gut axis. Hypothalamic CRH secretion results in secretion of adrenocorticotropic hormone (ACTH) from the pituitary, which stimulates the adrenal gland to release cortisol. CRH receptors are widely distributed in the intestine as well as throughout the central nervous system[1)]. Functional brain imaging studies with positron emission tomography (PET) and functional magnetic resonance imaging (fMRI) during visceral stimulation in IBS patients[2)] showed more activation in the insula, cingulate cortex, prefrontal cortices, amygdala, and hippocampus[3)] compared to healthy controls. In this study, we investigated the influence of CRH on HPA-axis and brain responses to visceral stimuli in IBS patients and healthy controls. Here, we hypothesized that exogenous administration of CRH in IBS patients is associated with increased responses in both the “visceral pain matrix”, especially the emotional-arousal network, and the ACTH-cortisol axes compared to healthy controls.

We enrolled 16 male IBS patients and 16 male healthy subjects, and randomly divided them between CRH and saline injection groups. All of the IBS patients were diagnosed based on the Rome lll criteria[4)]. The State-Trait Anxiety Inventory and

Self-Rating Depression Scale were used to assess their anxiety and depression levels and showed no significant differences between IBS and HC groups. This study was approved by the Ethics Committee of the Tohoku University Graduate School of Medicine, Japan. We used the barostat protocol. A bag was inserted into the colorectum. The catheter was then connected to computerized barostat equipment (Synectics Visceral Stimulator; Medtronics Synectics; Shoreview, MN). The patients randomly underwent no (0 mmHg), mild (20 mmHg), or strong (40 mmHg) colorectal distension. CRH (2 μg/kg) or saline was then administered via injection, and the distention protocol was repeated. Blood samples were obtained from an intravenous cannula after each period, and subjective symptoms were evaluated using an ordinate scale[2)]. rCBF in each subject was measured using a PET scanner in three-dimension sampling mode (HEADTOME V SET-2400W; Shimadzu, Kyoto, Japan). The scanner produced 63 transaxial slices with a thickness of 3.125 mm, an axial field of view of 200 mm, an in-plane resolution of 5.9 mm, full width at half maximum (FWHM), and an axial resolution of 3.9 mm FWHM. For each scan, 30 seconds after receiving injection of approximately 185 MBq of $H_2{}^{15}O$ intravenously through the right cubital vein, colorectal bag inflation was started. Data acquisition (70 s) began after barostat bag inflation. Plasma noradrenaline, adrenaline, ACTH, and cortisol levels were measured at the time of each distention. Data were analyzed using SPM8. ROIs were defined using the Wake Forest University (Winston-Salem, North Carolina) PickAtlas toolbox in SPM8 as follows: amygdala, hippocampus, insula, secondary/primary somatosensory cortex, anterior cingulate cortex, midcingulate cortex, thalamus, posterior cingulate cortex, medial prefrontal cortex, ventrolateral prefrontal cortex, dorsolateral prefrontal cortex, midbrain and pons. Active voxels for each ROI were considered statistically significant at a threshold of Family-Wise Error (FWE) corrected $P < .05$. An overall generalized estimating equation (GEE) analysis (SPSS 21.0, IBM Corp.) was performed during the random distention.

The comparison between IBS patients and controls at baseline after CRH injection showed significantly higher activity in the right amygdala in IBS patients compared to controls in a regions of interest (ROI) analysis ($t = 3.63$, cluster [k] = 42, ROI PFWE-corr = .017; local maximum—x: 34, y: 2, z: -22) (Figure). There was no significant difference between IBS patients and controls for the contrast baseline after saline injection – baseline before saline injection. The controls receiving CRH injection showed significantly stronger activation in the amygdala, hippocampus and middle cingulate cortex at intense distention

compared to baseline compared to those receiving saline injection in a ROI analysis (Fig. 1). However, there were no differences in brain responses between IBS patients receiving CRH injection compared to patients receiving saline injection.

The neuroendocrine changes after CRH or saline injection during random distention was analyzed using GEE. Plasma ACTH showed a significant drug effect ($P < .001$) and drug × distention interaction ($P = .027$) (Fig. 1). However, there was no significant difference between the two groups (IBS, controls). Serum cortisol levels showed a significant drug effect ($P < .001$), drug × distention interaction ($P < .001$) and drug × distention × group interaction ($P = .001$) (Fig. 1).

During random distention after drug injection, ordinate scale showed a significant group effect in the abdominal pain scale ($P < .001$). All ordinate scales showed significant distention effects.

We showed that exogenous administration of CRH modulates the increases in colorectal distention-induced activation of visceral sensation-related brain regions and neuroendocrine changes in both IBS patients and healthy controls. IBS patients had higher baseline activities in the amygdala, a key emotional-arousal area within the visceral pain networks, after CRH injection than controls. Rather, CRH increases colorectal distention-induced activity in the amygdala in healthy subjects but not IBS patients. Our findings suggest a ceiling response in the amygdala during CRH administration and colorectal distention in IBS patients and its synergetic activation of neuroendocrine function may be an important factor to trigger gastrointestinal symptoms in IBS patients[5)].

References

1) Fukudo S. *Physiology of the gastronintestinal tract*. Oxford: Academic Press (2012) 791-816.
2) Hamaguchi T, Kano M, Rikimaru H, Kanazawa M, Itoh M, Yanai K, Fukudo S. *Neurogastroenterol Motil*. **16** (2004) 299.
3) Mayer EA, Berman S, Suyenobu B, Labus J, Mandelkern MA, Naliboff BD, Chang L. *Pain*. **115** (2005) 398.
4) Longstreth GF, Thompson WG, Chey WD, Houghton LA, Mearin F, Spiller RC. *Gastroenterology* **130** (2006) 1480.
5) Tanaka T., Kanazawa M., et al., PLoS One. 11 (2016) e0157347.

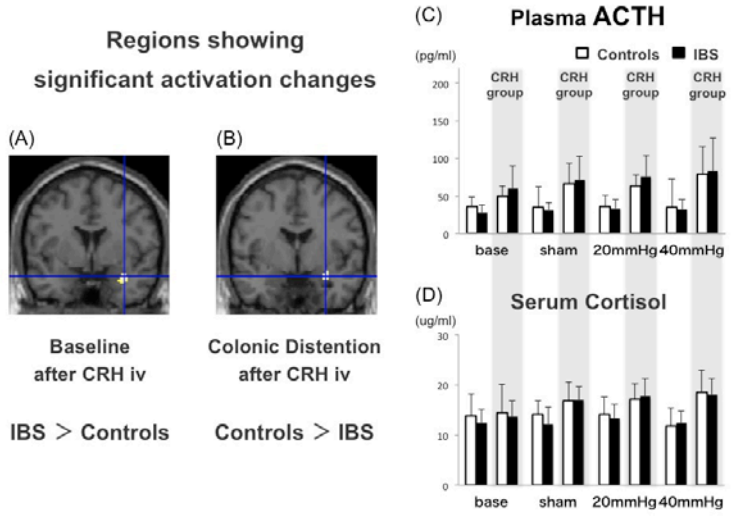

Figure 1. Regional brain and neuroendocrine responses. (A) IBS patients showed significantly more activity than controls in the right amygdala at baseline after CRH injection compared with that at baseline before CRH injection. (B) Controls showed significantly greater activation than IBS patients in the right amygdala at intense distention after CRH injection compared with saline injection than IBS patients. (C) A significant drug effect and drug × distention interaction in plasma ACTH (pg/ml) and (D) a significant drug effect, drug × distention interaction and drug × distention × group interaction in serum cortisol during random distention after drug injection was noted between controls with saline (n = 8), IBS patients with saline (n= 8), controls with CRH (n = 8) and IBS patients with CRH (n = 8), analyzed by GEE.

VII. 7. Relationship between Sympathoadrenal and Hypothalamic-pituitary-adrenal Response during Colorectal Distention in Patients with Irritable Bowel Syndrome and Healthy Controls

Tanaka T.[1], Kanazawa M.[1], Michiko Kano M.[1,2], Tashiro M.[3], and Fukudo S.[1]

[1]Department of Behavioral Medicine, Tohoku University Graduate School of Medicin
[2]Department of Frontier Research Institute for Interdisciplinary Sciences, Tohoku University Graduate School of Medicine
[3]Cyclotron RI Center, Tohoku University

Corticotropin-releasing hormone (CRH) mediates stress responses in the brain-gut axis. Administration of CRH modulates brain activation and the autonomic nervous system in response to colorectal distention. Increased hypothalamic-pituitary-adrenal (HPA) responses to stress stimulation alter the balance between afferent and efferent neural pathways. We have found that activity in brain regions implicated in CRH secretion, such as amygdala and hippocampus, are suppressed during visceral stimulation in men with IBS[1)]. The noradrenaline system hub is found in the locus coeruleus (LC), which sends neural projections to the amygdala and hypothalamus, which in turn contain numerous CRH receptors. The LC also sends major projections to the frontal cortex, which is able to regulate the amygdala[2)]. Male IBS patients likely exhibit a similar pattern both in the amygdala and in plasma noradrenaline levels following CRH injection during stimulation[1] in our previous report. These findings implicate parallel modifications in the HPA and catecholamine pathways. The catalytic activity of phenylethanolamine N-methyltransferase (PNMT), which is the enzyme that synthesizes adrenaline from noradrenaline, is regulated by cortisol, and stress induces adrenal PNMT activity[3)]. Nociceptive stressors induce a strong correlation between ACTH levels and catecholamine levels[4)]. Nevertheless, how the HPA-catecholamine network is modulated during visceral stress in IBS patients remains unknown. Sex differences in central nervous system responses to visceral stress, perception, and motility have also been reported in patients with IBS. Here, we hypothesized the relationship between sympathoadrenal and hypothalamic-pituitary-adrenal (HPA) responses to colorectal

distention in patients with irritable bowel syndrome (IBS).

We enrolled 32 patients with IBS (16 women and 16 men) and 32 healthy subjects (16 women and 16 men), and randomly divided them between CRH and saline injection groups. All of the patients with IBS were diagnosed based on the Rome lll criteria[5]. The State-Trait Anxiety Inventory and Self-Rating Depression Scale were used to assess their anxiety and depression levels and showed no significant differences between IBS and HC groups. This study was approved by the Ethics Committee of the Tohoku University Graduate School of Medicine, Japan. We used the barostat protocol. A bag was inserted into the colorectum. The catheter was then connected to computerized barostat equipment (Synectics Visceral Stimulator; Medtronics Synectics; Shoreview, MN). The patients randomly underwent no (0 mmHg), mild (20 mmHg), or strong (40 mmHg) colorectal distension. CRH (2 μg/kg) or saline was then administered via injection, and the distention protocol was repeated. Blood samples were obtained from an intravenous cannula after each period, and subjective symptoms were evaluated using an ordinate scale[1]. The heart rate (HR) and HR variability (HRV; calculated as the low [LF, 0.04–0.15 Hz] to high frequency [HF, 0.15–0.4 Hz] peak ratio, LF/HF) were analyzed using electrocardiography (SCM 6000; Fukuda Denshi; Tokyo, Japan). R-R intervals during the distention were calculated using computer software (R-R Interval Analyzing Program, HPS-RRA; Fukuda Denshi). Plasma noradrenaline, adrenaline, adrenocorticotropic hormone (ACTH), and cortisol levels were measured at the time of each distention. Data were analyzed using SPSS 21.0 (IBM Corporation; Armonk, NY, USA). An overall generalized estimating equation (GEE) analysis (SPSS 21.0, IBM Corp.) was performed during the random distention. Network analyses within the neuroendocrine system were conducted using structural equation modeling in Amos 22.0 (IBM Corp.). A satisfactory model usually has a comparative fit index ≥ 0.95 and a root mean square error of approximation < 0.05.

We found sex-based differences in plasma noradrenaline levels, but not in plasma ACTH, serum cortisol, or plasma adrenaline. As a result, the following analyses were performed on data from each subgroup in the IBS and HC groups, including both men and women. In HCs receiving a placebo injection, plasma ACTH and noradrenaline levels were negatively correlated (rho = –.609, P = .012) during 40 mmHg distention, but were unrelated to plasma adrenaline levels. ACTH levels in IBS patients receiving a placebo injection were positively correlated with cortisol levels (40 mmHg distention: rho = .818, P < .001). ACTH levels were also significantly correlated with adrenaline levels during 40 mmHg distention

(rho = .605, P = .013). ACTH and plasma adrenaline levels were not significantly correlated in these participants in the 40mmHg distention condition.

Structural equation modeling was used to analyze the relationship between ACTH-cortisol and noradrenaline-adrenaline, assess network differences between IBS and HC groups, and examine the effect of CRH on these relationships. (Figure 1) The model fit was tested together for the CRH and saline groups in both the IBS and HC groups (χ 2(4) = 1.706, P = .790, comparative fix index = 1.000, root mean square error of approximation = .000, 95% CI = 0.000–0.126). Higher plasma ACTH levels in patients with IBS were associated with higher levels of serum cortisol (β = .94, P < .001); we found a similar association with plasma adrenaline levels (β = .972, P < .001) during 40mmHg distention in IBS patients were administered saline, and plasma ACTH levels in IBS patients who were administered CRH (cortisol: β = .711, P < .001; adrenaline: β = .496, P < .001). In contrast, in HCs, plasma ACTH levels were significantly associated with serum cortisol levels in the placebo group (β = .744, P < .001).

GEE analysis showed a significant distention × group × drug interaction (P = .016) for HF power, but not HR or LF/HF ratio (HR, P = .939; LF/HF ratio, P = .408). There were no significant distention × group × drug × sex interactions with any of the HRV parameters (HR, P = .295; HF, P = .197; LF/HF ratio, P = .110). Spearman's correlation analysis showed significant correlations between plasma adrenaline levels and HR, as well as HF power, for all levels of distention, in HCs who were administered CRH. (Table 1) In addition, there was a significant correlation between the LF/HF ratio and plasma adrenaline levels in these participants during the 40mmHg distention. The plasma adrenaline levels and HRV were not correlated in patients with IBS, but there was a significant correlation between HR and plasma ACTH levels, as well as serum cortisol levels, during the 40mmHg distention in the IBS placebo group.

The relationship between HPA-sympathoadrenal responses and CRH levels during colorectal distention differs between IBS patients and controls. The threshold for ACTH-induced adrenaline release was enhanced only during strong distention in HCs. In contrast, there was a correlation in the IBS group, even in the absence of distention. We have provided evidence for sex-based differences in plasma noradrenaline levels, but not in plasma ACTH, serum cortisol, or plasma adrenaline levels. Interpretation of the results herein must therefore account for the influence of the mensuration cycle in women. In conclusion, modulation of

adrenal gland activity in response to ACTH stimulation may contribute to the brain-gut pathophysiology characteristic of IBS.[6)]

References

1) Tanaka Y, Kanazawa M, Kano M, Morishita J, Hamaguchi T, Van Oudenhove L, et al. *PLoS One* **11** (2016) e0157347.
2) Sara SJ. *Nat Rev Neurosci* **10** (2009) 211.
3) Wurtman RJ. *Metabolism* **51** (2002) 11.
4) Goldstein DS, Kopin IJ. *Endocr Regul* **42** (2008) 111.
5) Longstreth GF, Thompson WG, Chey WD, Houghton LA, Mearin F, Spiller RC. *Gastroenterology* **130** (2006) 1480.
6) Tanaka Y, Kanazawa M, Kano M, Tashiro M, Fukudo S. *PLoS One* **13** (2018) e0199698.

Table 1. Features of HRV during 40 mmHg distention and correlation between HRV and neuroendocrine variables. Data are shown as rho scores of the Spearman rank correlation coefficient. Data for %HF or LF/HF were used to assess the correlations with plasma ACTH, serum cortisol, plasma adrenaline, and noradrenaline levels. *P < 0.05, **P < 0.01. HR, heart rate; HF, high frequency; LF, low frequency; Ad, adrenaline; NA, noradrenaline; ACTH, adrenocorticotropic hormone; SD, standard deviation.

Variable	Mean	SD	ACTH	Cortisol	Ad	NA
HC with placebo injection (n = 16)						
HR	77.23	9.89	0.04	-0.28	0.45	-0.12
HF power	437.89	338.40	-0.11	0.21	-0.39	-0.04
LF/HF	2.48	1.55	-0.37	-0.02	-0.31	0.42
HC with CRH injection (n = 16)						
HR	83.73	19.08	0.25	0.44	0.77 **	0.37
HF power	658.02	993.43	-0.41	-0.51 *	-0.72 **	-0.29
LF/HF	4.38	2.92	0.10	0.20	0.66 **	0.38
IBS with placebo injection (n = 16)						
HR	73.48	12.30	0.58 *	0.54 *	0.22	0.17
HF power	931.64	1725.64	-0.22	-0.05	0.10	-0.28
LF/HF	3.18	2.79	-0.13	-0.38	-0.24	0.25
IBS with CRH injection (n = 16)						
HR	80.27	11.96	0.21	0.21	0.44	-0.12
HF power	197.78	167.70	0.18	-0.07	-0.27	0.04
LF/HF	4.70	2.59	0.04	0.28	0.41	0.01

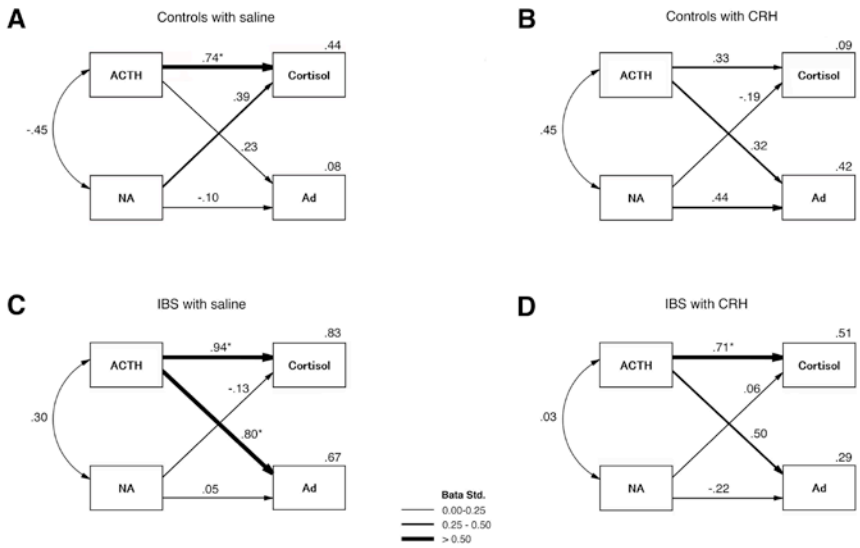

Figure 1. Neuroendocrine response models during 40 mmHg distention (A) HCs injected with saline (n= 16), (B) HCs injected with CRH (n = 16), (C) patients with IBS injected with saline (n = 16), and (D) patients with IBS injected with CRH (n = 16). *P < .0125 indicate significant paths. The squared multiple correlations (R2) of the variables are reported in the top right corner. There were no significant factor correlations between ACTH and NA. ACTH, plasma ACTH; cortisol, serum cortisol; HCs, healthy controls; NA, plasma noradrenaline; Ad, plasma adrenaline; ACTH, adrenocorticotropic hormone; IBS, irritable bowel syndrome; CRH, corticotropin-releasing hormone.

VII. 8. Effects of Levocetirizine and Diphenhydramine on Regional Cerebral Glucose Metabolism and Hemodynamic Responses during Cognitive Tasks

Kikuchi A.[1], Inami A.[1], Nasir F.B.M.[1], Mohsen A.[1,2,3], Watanuki S.[1], Miyake M.[1], Matsuda R.[1], Koike D.[1], Ito T.[1], Sasakawa J.[1], Takeda K.[1], Hiraoka K.[1], Yanai Y.[1,2], Watabe H.[1], and Tashiro M.[1]

[1]Cyclotron and Radioisotope Center, Tohoku University
[2]Tohoku University Graduate School of Medicine
[3]National Institute of Biomedical Innovation, Health, and Nutrition

Introduction

Histamine plays important roles in various brain functions, such as arousal, attention, and cognition[1,2)]. On the other hand, antihistamines often have sedative side effects. The adverse effects are mainly due to the ability of antihistamines to penetrate the blood–brain barrier, blocking neuronal transmission in the histaminergic nervous system in the brain. We have studied brain functional changes because of sedative effect of antihistamines. This time, we investigated the regional brain activity during cognitive tasks after administration of sedative and non-sedative antihistamines in terms of cerebral glucose metabolic changes and examined its relationship with regional hemodynamic response.

Materials and Methods

Eighteen healthy young volunteer (21.7 ± 0.8 years) participated in the study. This study used a double-blind, placebo-controlled, three-way, crossover design. Single doses of levocetirizine 5 mg, diphenhydramine 50 mg, and placebo (lactobacillus tablets) were administered orally with 100 mL water. Treatment periods were separated by a washout period of at least 6 days. The first PET scan (PET1) was performed in the resting state before oral administration (baseline) and the second PET scan (PET2) was done at 120 min post-administration (Fig. 1). The cognitive testing battery consisted of the word fluency test (Task1), two-back test (Task2), and Stroop test (Task3), all of which were prepared to activate the prefrontal cortex. Each of the three tasks took 60 s and each task was separated by 20-s-

long pre-task and post-task resting phases. A session including the three tasks was repeated six times, taking 30 min in total (Fig. 1). Also, assessment of subjective sleepiness was performed with the Stanford Sleepiness Scale (SSS) and the line analog rating scale (LARS); (Fig. 1).

We investigated cerebral glucose metabolic changes using positron emission tomography (PET). Brain scans were performed by the Eminence STARGATE PET scanner (Shimadzu Corp., Kyoto, Japan). Subjects were first scanned in the "resting" control condition (PET1) and later in the "task" condition (PET2) to compare the regional brain metabolic changes due to antihistamines (Fig. 1). PET brain images were transformed into those reflecting standardized uptake values (SUVs), normalized by body weight and by injected radioactivity of FDG. These SUV images were analyzed to identify regional changes in glucose consumption using a software package, Statistical Parametric Mapping (SPM8; Functional Imaging Laboratory, London, UK)[3], which performed voxel-by-voxel analysis.
During the cognitive tasks, hemodynamic responses were recorded as changes in oxygenated hemoglobin concentrations (Δoxy-Hb) in the frontal cortex using the OMM-3000 System (Shimadzu Corp., Kyoto, Japan). In the present study protocol, the first cognitive task (word fluency task: Task1) was initiated after the pre-task resting period and lasted for 60 s; this was followed by other post-task and pre-task resting periods and then the second task (20 s each). Then, the second (two-back task: Task2) and the third (Stroop task: Task3) tasks were assigned in a similar manner. Thus, the set of three cognitive tests was repeated six times (Fig. 1). The cerebral hemodynamic response pattern was examined for each task and for each drug treatment condition. For NIRS data analysis in the present study, we focused on the increase of oxy-Hb concentration which is considered as an estimate of regional brain activation. The oxy-Hb data were also corrected baseline offset (zero) to the task-starting time (t= 0) and were transformed into Δoxy-Hb data, and were averaged to demonstrate hemodynamic responses in bilateral prefrontal areas during tasks for the three drug treatment conditions. ΔOxy-Hb waveforms values were averaged throughout the task phase (0 to 60 s) for statistical examination.

For statistical analyses, we used SPSS 22.0 (Japanese version). For the subjective sedation, SSS and LARS scores were both examined by applying non-parametric examinations such as the Friedman test and Wilcoxon signed rank test (two-tailed; $p \leq .05$). All results of cognitive tests, including word counts in word fluency tests and accuracy and reaction time in two-back and Stroop tests, were also examined between drug treatments using non-parametric methods such as the Friedman test and Wilcoxon signed rank test (two-

tailed; $p \leq .05$). For the statistical analyses of PET images, the repeated ANOVA option of the SPM8 software package was applied because normal distribution and equal variance were confirmed. Significant findings were additionally examined by post hoc multiple pairwise treatment comparisons using a Bonferroni test (two-tailed; $p \leq .05$). For the statistical analyses of NIRS data, non-parametric examinations such as the Friedman test and Wilcoxon signed rank test (two-tailed; $p \leq .05$) were applied because normal distribution and equal variance were not confirmed. Significant findings were additionally examined by post hoc multiple pairwise treatment comparisons using the Wilcoxon signed rank test (two-tailed; $p \leq .05$). Details are described in our published paper[4].

The ethics committee of the University Graduate School of Medicine approved the study protocol.

Results and Discussion

Subjective feelings were no significant differences between placebo and treatment conditions. Performance in Stroop test (accuracy) was significantly impaired after treatment with the sedative antihistamine compared with both the placebo ($p = .008$) and levocetirizine treatment ($p = .001$).

FDG-PET analysis using SPM8 revealed significant regional brain changes in glucose consumption during cognitive tasks (PET2) compared with the pre-treatment resting images (PET1) for each drug treatment condition (Fig. 2). Notably, the activation in Broca's area (Brodmann area: BA44/45), BA9, and BA10 was observed in all treatment conditions. Regional energy consumption was more prominent and more extensive with antihistamine treatments than with placebo in the following order: diphenhydramine > levocetirizine > placebo.

Hemodynamic responses were examined in the prefrontal regions that showed significant activation in FDG-PET (BA9, -10, and -44/45). Prefrontal activation (ΔOxy-Hb) was much more prominent during Task1 than during the other tasks. Thus, activation during Task2 and Task3 was much less prominent. In terms of temporal analysis, cortical activation patterns during Task1 in BA9, -10, and -44/45 were compared in both hemispheres (Fig. 3). Basically, there was no clear difference in shape of Δoxy-Hb waveforms between drug treatments (Fig. 3). In the all treatment conditions, there was an initial small peak (at 5 s after task onset) and the highest peak (at 60 to 70 s after task onset) in hemodynamic responses. There were some significant differences between hemispheres and between treatment conditions, with the general trend for higher activation following placebo treatment than

following antihistamine treatment (Fig. 3). So, hemodynamic responses during the word fluency task seemed to be suppressed by antihistamine treatment compared with placebo (Fig. 3), as previously demonstrated by Tsujii and colleagues[5].

FDG-PET results and NIRS results seem to be contradictory based on the “coupling” theory (linear correlation between the regional energy consumption and perfusion), where slight increased consumptions of oxygen and glucose due to regional brain activation are followed by a rapid and considerable surge in oxygen and glucose concentrations due to rapid capillary dilations in the activated brain regions. Thus, in principle, brain activation should be accompanied by a marked increase in oxy-Hb concentration. Antihistamines might possibly suppress the permeability of brain capillaries, dulling the prompt hemodynamic responses. However, such suppression might complicate continuous hemodynamic responses (up to 30 min, as in the present study).

Conclusion

Under sedative condition of administrating antihistamine, physiological “coupling” between metabolism and perfusion in the healthy human brain may not be maintained. This uncoupling may be caused by a combination of increased energy demands in the prefrontal regions and suppression of vascular permeability in brain capillaries after antihistamine treatment. Further research is needed to elucidate this mechanism.

Acknowledgements

M. Tashiro, K. Yanai, H. Watabe, and K. Hiraoka have potential conflicts of interest regarding the present study. The present study was supported by a collaboration research grant from GlaxoSmithKline (to M. Tashiro). We thank Mr. Yuma Arakawa for his support of PET scanning. We thank Mrs. Chiyuki Onose for her contribution as a clinical research coordinator. We also thank Mr. Akihiro Ishikawa of Shimadzu Corp., Kyoto, Japan for his technical support and encouragement.

References

1) Haas, H., & Panula, P., *Nat Rev Neurosci, 4(2)* (2003) 121–30.
2) Theunissen, E.L., Vermeeren, A., van Oers, A.C., et al., *Clin Exp Allergy, 34(2)* (2004) 250–8.
3) Friston, K.J., Frith, C.D., Liddle, P.F., et al., *vol.11, no. 4,* (1991) 690-699.
4) Kikuchi, A, Fairuz, B.M.N., Inami, A, et al., *Hum Psychopharmacol Clin Exp*. (2018) e2655.
5) Tsujii, T., Yamamoto, E., Ohira, T., Takahashi, T., et al., *Neurosci Res 67(1),* (2010) 80-5.

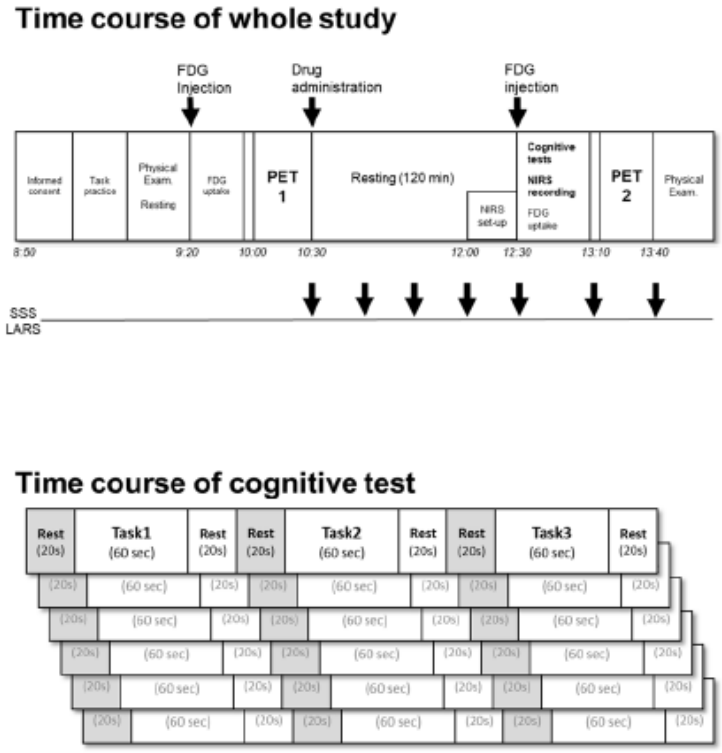

Figure 1. Schematic diagrams of the entire study protocol (top) and of the cognitive test protocol. FDG, [^{18}F]fluorodeoxyglucose; LARS, line analog rating scale; NIRS, near-infrared spectroscopy; PET, positron emission tomography; SSS, Stanford Sleepiness Scale (Reproduced from Ref.4).

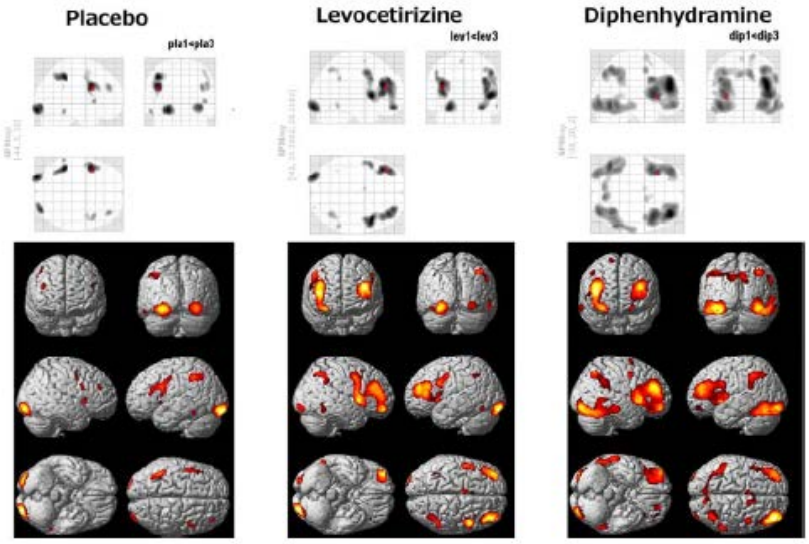

Figure 2. Results of voxel-by- voxel statistical parametric analysis of positron emission tomography [^{18}F]fluorodeoxyglucose images. Statistically significant voxels are presented in the transparent standard brain space (glass brain, top) and superimposed onto the standard magnetic resonance imaging brain template images (bottom). The metabolic results of a voxel-by- voxel comparison of regional cerebral glucose metabolic images using statistical parametric mapping (SPM8; height threshold, $p < .05$, corresponding to z value >3.1; extent threshold 10 voxel minimum, with correction for multiple comparisons). L, left hemisphere; R, right hemisphere (Reproduced from Ref.4)

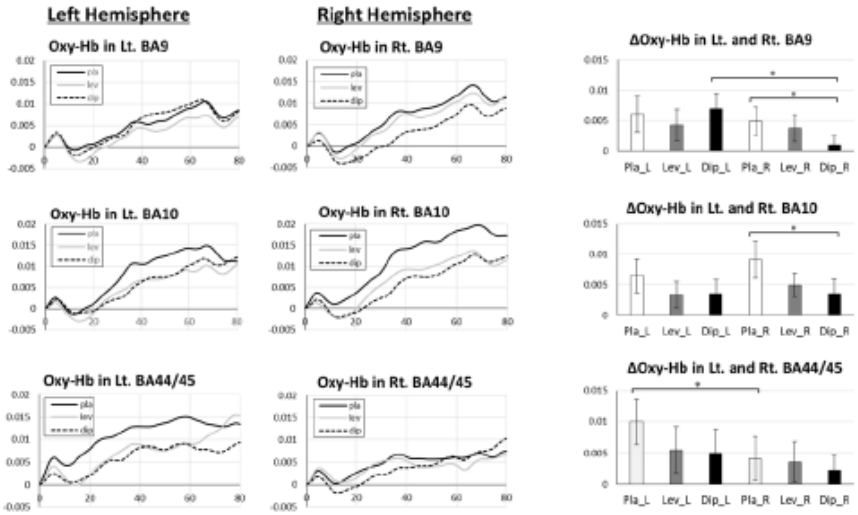

Figure 3. Changes in oxygenated hemoglobin (Δoxy-Hb) waveforms showing cortical activation patterns during word fluency task (Task1) in BA9, BA10, and BA44/BA45 in the left and right hemispheres measured with near-infrared spectroscopy (left and middle columns). Results of statistical examination regarding the quantitative analysis of activation (right column). *p < .05, **p < .001 for the post hoc Wilcoxon signed rank test. BA, Brodmann area; Lt., left; Rt., right; Pla, placebo; Lev, levocetirizine; Dip, diphenhydramine; oxy-Hb, oxygenated haemoglobin (Reproduced from Ref.4).

VII. 9. A Positron Emission Tomographic (PET) Study to Consider the Working Mechanism of an Alternative Therapy on Neck Pain Patients.

Inami A.[1], Ogura T.[1,2], Watanuki S.[1], Masud M.[3], Shibuya K.[4], Miyake M.[1], Matsuda R.[1], Hiraoka K.[1], Itoh M.[4], Fuhr AW.[3,5], Yanai K.[1,6], and Tashiro M.[1]

[1]Cyclotron and Radioisotope Center, Tohoku University
[2]Japan Chiropractic Doctor College
[3]Department of Nuclear Medicine, United Hospital
[4]Sendai Medical Imaging Clinic
[5]Activator Methods International, Ltd
[6]Department of Pharmacology, Graduate School of Medicine, Tohoku University

Chiropractic Spinal Manipulation (CSM), an alternative medicine technique, has been considered as one of the main treatment techniques for neuro-muscular-skeletal problems. And main complaints of the patients are often neck pain, back pain and low-back pain[1-4]. However, the mechanism by which CSM leads to pain relief has not been fully understood yet. In addition, it has been also suggested that the pain in chronic low-back pain is associated with reduction of local brain activity. Our strategy was to explore the regional brain activity changes after CSM by using positron emission tomography (PET), which enables the measurement of the regional brain activity and muscle metabolic activity simultaneously in human at whole-body. The aim of the present study is to investigate brain and skeletal muscles activity changes after CSM by using [^{18}F]fluorodeoxyglucose ([^{18}F]FDG) and PET [5].

We recruited 21 male subjects (mean age +/- SD: 26.4 +/- 5.9 years) with cervical pain and shoulder stiffness. PET scanning was performed twice on each participant, at resting (control condition) and after CSM intervention (treatment condition). Questionnaires were also used for evaluation of subjective sensation of their pain intensities. A subjective pain intensity was evaluated by using a visual analogue scale (VAS), rated by each participant before and after CSM intervention, and muscle tone and salivary amylase were also measured. The protocol is shown in Figure 1. Brain PET images were analyzed using the voxel-wise statistical analysis software package Statistical Parametric Mapping 8 (SPM8) in order to identify regional glucose metabolic changes. PET images of the neck

and shoulder regions were coregistered to the MR images of the same subject; regions of interest (ROIs) for cervical muscles were then manually drawn on the PET images using Dr. View software, using MR images as references. ROIs were drawn on major muscles of the neck shoulder (trapezius muscle at C7-T1 levels bilaterally, splenius, semispinalis, elevator scapular muscles at C6-C7 levels bilaterally). We performed statistical analysis using standardized uptake value (SUV) for analysis the differences of muscle glucose uptake. [5)]

The results of the statistical analysis found regional brain activity that increased or decreased after CSM intervention (Figure 2). As for regional brain metabolic changes after CSM intervention, the regional activation (increased metabolism) was detected in the dorsal anterior cingulate cortex (dACC) (Brodmann area [BA] 32), cerebellar vermis (CV), and somatosensory association cortex. And the regional deactivation (decreased metabolism) was detected in regions including the prefrontal cortex (PFC) and temporal sites. On the other hand, certain cervical muscles showed a tendency toward decreased glucose metabolism after CSM, although the difference was not statistically significant. As for subjective pain, a significantly lower visual analogue scale (VAS) score was noted after CSM. Cervical muscle tone and salivary amylase measures were significantly decreased after CSM[5)].

In summary, the present study demonstrated sympathetic relaxation and corresponding regional brain metabolic changes, as well as reduced muscle glucose uptake, muscle tone and decreased pain intensity following a CSM. We were able to get one of the useful information to elucidate the underlying mechanism of clinical effects of the CSM by using [^{18}F]FDG-PET[5)].

References

1) World Health Organization. WHO Guidelines on basic training and safety in chiropractic. 2006.
2) Budgell BS. *J Manipulative Physiol Ther*., **23** (2000) 104-106.
3) Crawford JP, Hickson GS, Wiles MR. *J Manipulative Physiol Ther*., **9** (1986) 27-32.
4) Sung PS, Kang YM, Pickar JG. *Spine*, **30** (2005) 115-122.
5) Inami A, et al. *Evid Based Complement Alternat Med.*, **2017** (2017) 4345703.

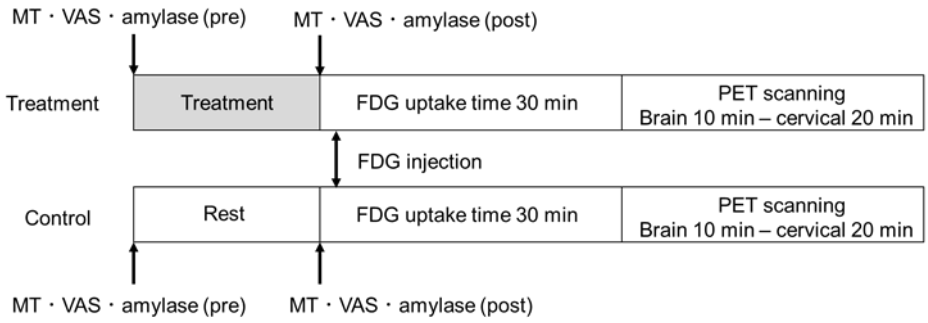

Figure 1. Schematic diagram of the study protocol (reproduced from Ref. 5)

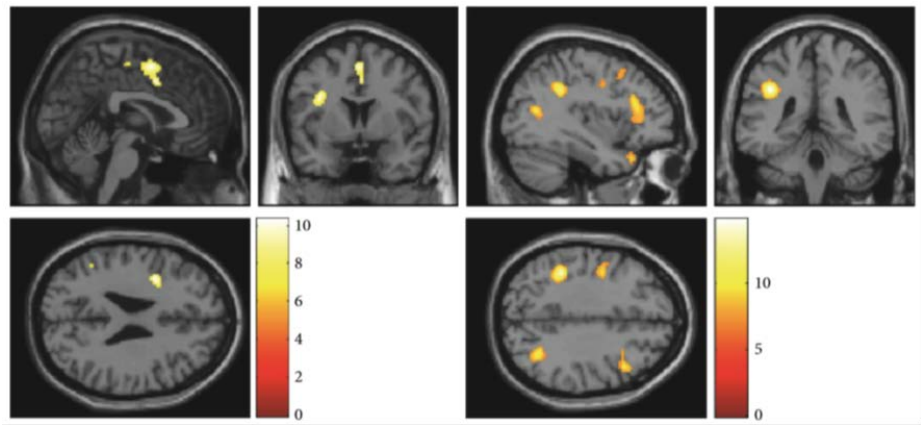

Figure2. Regional activation (left) and deactivation (right) after spinal manipulation therapy (SMT) using an activator adjusting instrument. Glucose metabolism is increased in regions including the anterior cingulate cortex and cerebellar vermis but is relatively reduced in many sites, including the prefrontal cortex, after SMT. The voxel height threshold is $p < 0.05$, corrected for multiple comparisons; the extent threshold is10 voxels minimum. (reproduced from Ref. 5).

VIII. RADIATION PROTECTION AND TRAINING OF SAFETY HANDLING

VIII. 1. Beginners Training for Safe Handling of Radiation and Radioisotopes at Tohoku University

Watabe H., Abe S., Mayama F., Nagakura Y., Miyake Y., and Yuki H.

Cyclotron and Radioisotope Center, Tohoku University

This report summarizes the beginners training for safe handling of radiation and radioisotopes at Tohoku University from 2016 to 2017. Twice a year (in May and in November), we organize two lecture courses, namely 1) Radiation and Isotopes, 2) X-ray Machines and Electron Microscope and practices. Since November 2002, we have also organized lectures in English for students or researchers who are not familiar with Japanese language. Persons who have intension to work in synchrotron radiation facilities used to participate Synchrotron Radiation (SOR) course which was begun since 1995. From 2016, we stopped to offer SOR course, and those persons take the lecture of 1) Radiation and Isotopes, instead. The training is held under the help for lectures and practice from various departments and research institutes of the university.

The training for "Radiation and Radioisotopes" is for persons who use unshielded radioisotopes and accelerators, and has been conducted from 1977. The contents of lectures and practices are shown in Table 1. The departments or institutes to which trainees belong and the distributions of trainees are shown in Table 2 and Table 3.

The training for "X-ray machines and electron microscopes" started at the end of 1983. The training is scheduled at the same time as that for "Radiation and Radioisotopes". In this course, only lectures are given with no practice. The contents of lectures are shown in Table 4. The departments or institutes to which trainees belong and the distributions of trainees are shown in Table 5 and Table 6.

Table 1. Contents of the lectures and practices for "Radiation and Radioisotopes" in 2016 and 2017.

Lectures (one day)	Hours
Introduction to radiation	0.5
Effects of radiation on human	1.0
Radiation physics and measurements	1.0
Chemistry of radioisotopes	1.0
Radiological protection ordinance including video	1.5
Safe handling of radioisotopes	1.5

Practices (one day)	Hours
Treatment of unsealed radioactive solution	4.0
Measurement of surface contamination and decontamination	1.0
Measurement of gamma-rays and beta-rays	2.0

Table 2. Distribution of trainees for “Radiation and Radioisotopes” in 2016.

Department	Staff	Student	Total	English class
CYRIC	4	6	10	0
Medicine	8	30	38	3
Dentistry	3	6	9	2
Pharmacy	1	41	42	0
Science	3	88	91	9
Engineering	10	150	160	19
Agriculture	2	35	37	0
Research Institutes	33	81	114	20
The others	0	0	0	0
Total	64	437	501	53

Table 3. Distribution of trainees for “Radiation and Radioisotopes” in 2017.

Department	Staff	Student	Total	English class
CYRIC	0	5	5	2
Medicine	8	35	43	0
Dentistry	2	3	5	1
Pharmacy	0	32	32	0
Science	2	101	103	7
Engineering	6	164	170	16
Agriculture	0	37	37	0
Research Institutes	20	115	135	25
The others	0	0	0	0
Total	38	492	530	51

Table 4. Contents of the lectures for “X-ray machines and Electron microscopes” in 2016 and 2017.

Lectures (one day)	Hours
Safe handling of X-ray machines	1.5
Radiological protection ordinance	0.5
Video for safe handling of radiation and radioisotopes	0.5

Table 5. Distribution of trainees for “X-ray machines and Electron microscopes” in 2016.

Department	Staff	Student	Total	English class
CYRIC	0	0	0	0
Medicine	12	0	12	1
Dentistry	4	7	11	0
Pharmacy	2	3	5	0
Science	0	34	34	2
Engineering	8	204	212	10
Agriculture	1	2	3	0
Research Institutes	13	83	96	24
The others	0	0	0	0
Total	40	333	373	37

Table 6. Distribution of trainees for “X-ray machines and Electron microscopes” in 2017.

Department	Staff	Student	Total	English class
CYRIC	0	0	0	0
Medicine	0	4	4	1
Dentistry	9	13	22	0
Pharmacy	1	1	2	0
Science	0	16	16	2
Engineering	9	201	210	19
Agriculture	0	2	2	0
Research Institutes	15	73	88	14
The others	0	0	0	0
Total	34	310	344	36

VIII. 2. Radiation Protection and Management

Yuki H.[1], Abe S.[1],Ohtomo K.[1], Watabe H.[1], and Nakae H.[2]

[1]Cyclotron and Radioisotope Center, Tohoku University
[2]Japan Environment Research Co., Ltd.

(1) Overview

During the fiscal year of 2016 and 2017, research and education in the center were conducted as active as usual.

(2) Unsealed radionuclides used in CYRIC

The species and amounts of the four most used unsealed radionuclides during the fiscal year of 2016 and 2017 are listed in Table 1. The table includes the isotopes produced by the cyclotron as well as those purchased from the Japan Radioisotope Association or taken over from other radioisotope institutes.

(3) Radiation exposure dose of individual worker

The exposure doses of the workers in CYRIC during 2016 and 2017 are given in Table 2. The doses were sufficiently lower than the legal dose limits.

(4) Radiation monitoring of the workplace

Radiation dose rates inside and outside of the controlled areas in CYRIC were monitored periodically and occasionally when needed. They were generally below the legal dose limits although there are several “hot spots” in mSv/hr range like slits or beam stopper of the 930 cyclotron and so on. Surface contamination levels of the floors inside the controlled areas were also measured with a smear method and a survey meter method. They were under the legal regulation levels.

(5) Wastes management

The radioactive wastes were delivered to the Japan Radioisotope Association in the

fiscal year of 2016 and 2017.

The concentration of radioisotopes in the air released from the stack after filtration was monitored with stack gas monitors. The values of concentration were well below the legal regulation levels. The radioactive water was stocked in the tanks at least for 3 days and then released to the sewerage after confirming that the concentration was lower than the legal regulation levels.

Table 1. The four most used unsealed radioisotopes used in CYRIC during the fiscal year of 2016 and 2017.

	2016	2017
C-11	639.02 GBq	396.54 GBq
O-15	9.1887 GBq	5.7750 GBq
F-18	1.5421 TBq	1.5734 TBq
P-32	1.1193 GBq	1.8759 GBq

Table 2. Occupational radiation exposures in CYRIC during the fiscal year of 2016 and 2017.

Dose range (mSv)	Number of individuals	
	2016	2017
0.0 - 5.0	329	319
5.0 - 10.0	1	0
10.0 - 15.0	0	0
15.0 - 20.0	0	0
20.0 - 25.0	0	0
25.0 - 50.0	0	0
50.0 -	0	0
Total number of persons monitored	330	319

IX. PUBLICATIONS

IX. PUBLICATIONS

[1003] Are there nuclear structure effects on the isoscalar giant monopole resonance and nuclear incompressibility near $A \sim 90$?
Gupta Y.K., Garg U., Howard K.B., Matta J.T., Senyigit M., Itoh M., Ando S., Aoki T., Uchiyama A., Adachi S., Fujiwara M., Iwamoto C., Tamii A., Akimune H., Kadono C., Matsuda Y., Nakahara T., Furuno T., Kawabata T., Tsumura M., Harakeh M.N., Kalantar-Nayestanaki N.
Phys. Lett. B **760** (2016) 482-485.
http://dx.doi.org/10.1016/j.physletb.2016.07.021

[1004] Effect of ground-state deformation on isoscalar giant resonances in ^{28}Si.
Peach T., Garg U., Gupta Y.K., Hoffman J., Matta J.T., Patel D.,1, Madhusudhana Rao P.V., Yoshida K., Itoh M., Fujiwara M., Hara K., Hashimoto H., Nakanishi K., Yosoi M., Sakaguchi H., Terashima S., Kishi S., Murakami T. Uchida M., Yasuda Y., Akimune H., Kawabata T.,9, Harakeh M.H., Colo` G.
Phys. Rev. C **93** (2016) 064325.
https://doi.org/10.1103/PhysRevC.93.064325

[1005] Deformation effects on isoscalar giant resonances in ^{24}Mg.
Gupta Y. K., Garg U., Hoffman J., Matta J., Madhusudhana Rao P.V., Patel D., Peach T., Yoshida K., Itoh M., Fujiwara M., Hara K., Hashimoto H., Nakanishi K., Yosoi M., Sakaguchi H., Terashima S., Kishi S., Murakami T., Uchida M., Yasuda Y., Akimune H., Kawabata T., Harakeh M.N.
Phys. Rev. C **93** (2016) 044324.
https://doi.org/10.1103/PhysRevC.93.044324

[1006] Candidate Resonant Tetraneutron State Populated by the ^{4}He (^{8}He, ^{8}Be) Reaction.
Kisamori K., Shimoura S., Miya H., Michimasa S., Ota S., Assie M., Baba H., Baba T., Beaumel D., Dozono M., Fujii T., Fukuda N., Go S., Hammache F., Ideguchi E., Inabe N., Itoh M., Kameda D., Kawase S., Kawabata T., Kobayashi M., Kondo Y., Kubo T., Kubota T., Kurata-Nishimura M., Lee C.S., Maeda Y., Matsubara H., Miki K., Nishi T., Noji S., Sakaguchi S., Sakai H., Sasamoto Y., Sasano M., Sato H., Shimizu Y., Stolz A., Suzuki H., Takaki M., Takeda H., Takeuchi S., Tamii A., Tang L., Tokieda H. Tsumura M., Uesaka T., Yako K., Yanagisawa Y., Yokoyama R., Yoshida K.
Phys. Rev. Lett. **116** (2016) 052501.
https://doi.org/10.1103/PhysRevLett.116.052501

[1007] Inverse kinematics (*p*, *n*) reactions studies using the WINDS slow neutron detector and the SAMURAI spectrometer.
Yasuda J., Sasano M., Zegers R.G.T., Baba H., Chao W., Dozono M., Fukuda N., Inabe N., Isobe T., Jhang G., Kameda D., Kubo T., Kurata-Nishimura M., Milman E., Motobayashi T., Otsu H., Panin V., Powell W., Sakai H., Sako M., Sato H., Shimizu Y., Stuhl L., Suzuki H., Tangwancharoen S., Takeda H., Uesaka T., Yoneda K., Zenihiro J., Kobayashi T., Sumikama T., Tako T., Nakamura T., Kondo Y., Togano Y., Shikata M., Tsubota J., Yako K., Shimoura

S., Ota S., Kawase S., Kubota Y., Takaki M., Michimasa S., Kisamori K., Lee C.S., Tokieda H., Kobayashi M., Koyama S., Kobayashi N., Wakasa T., Sakaguchi S., Krasznahorkay A., Murakami T., Nakatsuka T., Kaneko M., Matsuda Y., Mucher D., Reichert S., Bazin D., Lee J.W.
Nucl. Instr. Meth. B **376** (2016) 393-396.
https://doi.org/10.1016/j.nimb.2016.02.007

[1008] Magic and tune-out wavelengths for atomic francium
Dammalapati U., Harada K., Sakemi Y.
Phys. Rev. A 93, 043407 (2016)
https://doi.org/10.1103/PhysRevA.93.043407

[1009] Laser frequency locking with 46 GHz offset using an electro-optic modulator for magneto-optical trapping of francium atoms
Harada K., Aoki T., Ezure S., Kato K., Hayamizu T., Kawamura H., Inoue T., Arikawa H., Ishikawa T., Aoki T., Uchiyama A., Sakamoto K., Ito S., Itoh M., Ando S., Hatakeyama A., Hatanaka K., Imai K., Murakami T., Nataraj H. S., Shimizu Y., Sato T., Wakasa T., Yoshida H. P., Sakemi Y.
Appl. Opt. 55, 1164 (2016)
https://doi.org/10.1364/AO.55.001164

[1010] Transportation of a radioactive ion beam for precise laser-trapping experiments
Kawamura H., Ando S., Aoki T., Arikawa H., Harada K., Hayamizu T., Inoue T., Ishikawa T., Itoh M., Kato K., Köhler L., Sakamoto K., Uchiyama A., Sakemi Y.
Review of Scientific Instruments 87, 02B921 (2016)
https://doi.org/10.1063/1.4935013

[1011] [^{18}F]THK-5351: a novel PET radiotracer for imaging neurofibrillary pathology in Alzheimer disease.
Harada R., Okamura N., Furumoto S., Furukawa K., Ishiki A., Tomita N., Tago T., Hiraoka K., Watanuki S., Shidahara M., Miyake M., Ishikawa Y., Matsuda R., Inami A., Yoshikawa T., Funaki Y., Iwata R., Tashiro M., Yanai K., Arai H., Kudo Y.
J. Nucl. Med. Mol. Imag. **57** (2016) 208-214.
https://dx.doi.org/10.2967/jnumed.115.164848

[1012] Synthesis and characterization of ^{18}F-interleukin-8 using a cell-free translation system and 4-^{18}F-fluoro-L-proline.
Harada R., Furumoto S., Yoshikawa T., Ishikawa Y., Shibuya K., Okamura N., Ishiwata K., Iwata R., Yanai K.
J. Nucl. Med. Mol. Imag. **57** (2016) 634-639.
https://dx.doi.org/10.2967/jnumed.115.162602

[1013] Structure-activity relationship of 2-arylquinolines as PET imaging tracers for tau pathology in Alzheimer's disease.
Tago T., Furumoto S., Okamura N., Harada R., Adachi Hajime., Ishikawa Y., Yanai K., Iwata R., Kudo Y.
J. Nucl. Med. Mol. Imag. **57** (2016) 608-614.
https://dx.doi.org/10.2967/jnumed.115.166652

[1014] Radiosynthesis and preliminary biological evaluation of a new ^{18}F-labeled triethylene

glycol derivative of triphenylphosphonium.
Tominaga T., Ito H., Ishikawa Y., Iwata R., Ishikawa K., Furumoto S.
J. Label. Compd. Radiopharm. **59** (2016) 117-123.
https://dx.doi.org/10.1002/jlcr.3379

[1015] Characterization of the radiolabeled metabolite of tau PET tracer ^{18}F-THK5351.
Harada R., Furumoto S., Tago T., Katsutoshi F., Ishiki A., Tomita N., Iwata R., Tashiro M., Arai H., Yanai K., Kudo Y., Okamura N.
Eur. J. Nucl. Med. Mol. Imag. **43** (2016) 2211-2218.
https://dx.doi.org/10.2967/jnumed.115.164848

[1016] Continuous-flow synthesis of *N*-succinimidyl 4-[^{18}F]fluorobenzoate using a single microfluidic chip.
Kimura H., Tomatsu K., Saiki H., Arimitsu K., Ono M., Kawashima H., Iwata R., Nakanishi H., Ozeki E., Kuge Y., Saji H.
Plos One **11** (2016) e0159303.
https://dx.doi.org/10.1371/journal.pone.0159303

[1017] Visualization of mineral elements Na, Mg, P, S, K, Ca, Mn, and Cs and the dynamics of photosynthates derived from $^{14}CO_2$ in Arabidopsis by a newly developed real-time radioisotope imaging system (RRIS).
Sugita R., Kobayashi N.I., Hirose A., Saito T., Iwata R., Tanoi M., I Nakanishi T.M.
Plant Cell Physiol. **57** (2016) 743-753.
https://dx.doi.org/10.1093/pcp/pcw056

[1018] In vivo visualization of tau deposits in corticobasal syndrome by ^{18}F-THK5351 PET.
Kikuchi A, Okamura N, Hasegawa T, Harada R, Watanuki S, Funaki Y, Hiraoka K, Baba T, Sugeno N, Oshima R, Yoshida S, Kobayashi J, Ezura M, Kobayashi M, Tano O, Mugikura S, Iwata R., Ishiki A., Furukawa K., Arai H., Furumoto S., Tashiro M., Yanai K., Kudo Y., Takeda A., Aoki M.
Neurology **87** (2016) 2309-2316.
https://dx.doi.org/10.1212/wnl.0000000000003375

[1019] Anti-EGFR scFv tetramer (tetrabody) with a stable monodisperse structure, strong anticancer effect, and a long in vivo half-life.
Asano R., Koyama N., Hagiwara Y., Masakari Y., Orimo R., Arai K., Ogata H., Furumoto S., Umetsu M., Kumagai I.
FEBS Open Bio. **6** (2016) 594-602.
https://dx.doi.org/10.1002/2211-5463.12073

[1020] Dynamic PET Measures of Tau Accumulation in Cognitively Normal Older Adults and Alzheimer's Disease Patients Measured Using [^{18}F] THK-5351.
Lockhart S.N., Baker S.L., Okamura N., Furukawa K., Ishiki A., Furumoto S., Tashiro M., Yanai K., Arai H., Kudo Y., Harada R., Tomita N., Hiraoka K., Watanuki S., Jagust W.J.
Plos One **11** (2016) e0158460.
https://dx.doi.org/10.1371/journal.pone.0158460

[1021] Performance evaluation of the small-animal PET scanner ClairvivoPET using NEMA NU 4-2008 Standards.
Sato K., Shidahara M., Watabe H., Watanuki S., Ishikawa Y., Arakawa Y., Nai Y.H.,

Furumoto S., Tashiro M., Shoji T.
Phys. Med. Biol. **61** (2016) 696-711.
https://dx.doi.org/10.1088/0031-9155/61/2/696

[1022] Differential Activation in Amygdala and Plasma Noradrenaline during Colorectal Distention by Administration of Corticotropin-Releasing Hormone between Healthy Individuals and Patients with Irritable Bowel Syndrome.
Tanaka Y., Kanazawa M., Kano M., Morishita J., Hamaguchi T., Van Oudenhove L., Ly HG., Dupont P., Tack J., Yamaguchi T., Yanai K., Tashiro M., Fukudo S.
PLoS One **11** (2016) e0157347.
https://dx.doi.org/10.1371/journal.pone.0157347

[1023] Brain Metabolic Changes of Cervical Dystonia with Spinocerebellar Ataxia Type 1 after Botulinum Toxin Therapy.
Kikuchi A., Takeda A., Sugeno N., Miura E., Kato K., Hasegawa T., Baba T., Konno M., Oshima R., Watanuki S., Hiraoka K., Tashiro M., Aoki M.
Intern Med. **55** (2016) 1919-22.
https://dx.doi.org/10.2169/internalmedicine.55.5843

[1024] A simulated car-driving study on the effects of acute administration of levocetirizine, fexofenadine, and diphenhydramine in healthy Japanese volunteers.
Inami A., Matsuda R., Grobosch T., Komamura H., Takeda K., Yamada Y., Miyake M., Hiraoka K., Maurer M., Yanai K., Tashiro M.
Hum Psychopharmacol. **31** (2016) 167-77.
https://dx.doi.org/10.1002/hup.2524

[1025] Regional Volume Decreases in the Brain of Pax6 Heterozygous Mutant Rats: MRI Deformation-Based Morphometry.
Hiraoka K., Sumiyoshi A., Nonaka H., Kikkawa T., Kawashima R., Osumi N.
PLoS One **11** (2016) e0158153.
https://doi.org/10.1371/journal.pone.0158153

[1026] A History of Biological Illustrators in Japan.
Ariga K., Tashiro M.
J. Natural Sci. Illustration **48** (2016) 3-8.

[1027] Gd-EOB-DTPA-enhanced-MR imaging in the inflammation stage of nonalcoholic steatohepatitis (NASH) in mice. Yamada T, Obata A, Kashiwagi Y, Rokugawa T, Matsushima S., Hamada T., Watabe H., Abe K.
Magnetic Resonance Iimaging **34** (2016) 724-729.
https://dx.doi.org/10.1016/j.mri.2016.03.009

[1028] Imaging of radiocesium uptake dynamics in a plant body by using a newly developed high-resolution gamma camera.
Kawachi N., Yin Y., Suzui N., Ishii S., Yoshihara T., Watabe H., Yamamoto S., Fujimaki S. *J. Environmental Radioactivity* **151** (2016) 461-467.
https://dx.doi.org/10.1016/j.jenvrad.2015.04.009

[1029] Development of ultrahigh resolution Si-PM-based PET system using 0.32mm pixel scintillators.

Yamamoto S., Watabe H., Watabe T., Ikeda H., Kanai Y., Ogata Y., Kato K., Hatazawa J.
Nucl. Instrum. Meth. Phys. Res. Section A **836** (2016) 7-12.
https://dx.doi.org/10.1016/j.nima.2016.08.045

[1030] Prevalence and prognosis of prodromal Alzheimer's disease as assessed by magnetic resonance imaging and 18F-fluorodeoxyglucose–positron emission tomography in a community: Reanalysis from the Osaki-Tajiri Project.
Meguro K., Akanuma K. Meguro M., Yamaguchi S., Ishii H., Tashiro M.
Psychogeriatrics **16** (2016) 116-120.
https://doi.org/10.1111/psyg.12131

[1031] Early symptoms of Alzheimer's disease in Japan and Taiwan.
Yang Y.H., Hsu C.L., Chou M.C., Kasai M., Meguro K., Kiu C.K.
Geriatr. Gerontol. Int. **16** (2016) 797-803.
https://doi.org/10.1111/ggi.12557

[1032] Necker cube copying may not be appropriate as an examination of dementia: reanalysis from the Tajiri Project.
Oonuma J., Kasai M., Meguro K., Akanuma K, Yamaguchi S., Meguro M.
Psychogeriatrics **16** (2016) 298-304.
https://doi.org/10.1111/psyg.12161

[1033] Alzheimer's disease with cerebrovascular disease: Current status in the Asia Pacific region.
Chen C., Homma A., Mok V.C., Krishnamoorthy E., Alladi S., Meguro K., Abe K., Dominguez J., Marasigan S., Kandiah N., Kim S.Y., Lee D.Y., De Silva H.A., Yang Y.H., Pai M.C., Senanarong V., Dash A.
J. Intern. Med. **280** (2016) 359-374.
https://doi.org/10.1111/joim.12498

[1034] Impaired attention function based on the Montréal Cognitive Assessment in vascular dementia patients with frontal hypoperfusion: The Osaki-Tajiri Project.
Akanuma K., Meguro K., Kato Y., Takahashi Y., Nakamura K., Yamaguchi S.
J. Clin. Neurosci. **28** (2016) 128-132.
https://doi.org/ 10.1016/j.jocn.2015.08.047.

[1035] The group reminiscence approach can increase self-awareness of memory deficits and evoke a life review in people with mild cognitive impairment: The Kurihara Project data.
Nakamura K., Kasai M., Nakai M., Nakatsuka M., Meguro K.
JAMDA **17** (2016) 501-507.
https://doi.org/10.1016/j.jamda.2015.11.009

[1036] Improved diagnostic accuracy of SPECT through statistical analysis and the detection of a "sensorimotor hotspot" sign for the diagnosis of Alzheimer's disease in a community-based study: "The Osaki-Tajiri Project."
Kaneta T., Nakatsuka M., Nakamura K., Seki T., Yamaguchi S., Tsuboi M., Meguro K.
Clin. Nucl. Med. **41** (2016) e1-6.

[1037] Neuroepidemiologic and neurobehavioral characteristics of motoric cognitive risk in an old-old population: The Kurihara Project.

Kumai K., Meguro K., Kasai M., Nakamura K., Nakatsuka M.
Dement. Geriatr. Cogn. Dis. Extra. **6** (2016) 176-182.
https://doi.org/ 10.1159/000445539

[1038] Decreased physical activity associated with executive dysfunction correlates with cognitive impairment among older adults in the community: A retrospective analysis from the kurihara project.
Kobayashi Y., Takahashi Y., Seki T., Kaneta T., Amarume K., Kasai M., Meguro K.
Dement. Geriatr. Cogn. Dis. Extra. **6** (2016) 350-360.
https://doi.org/ 10.1159/000448027

[1039] Qualitative assessment of instrumental activities of daily living in older persons with very mild dementia: The Kurihara Project.
Ouchi Y., Kasai M., Nakamura K., Nakatsuka M., Meguro K.
Dement. Geriatr. Cogn. Dis. Extra. **6** (2016) 374-381.
https://doi.org/ 10.1159/000446769

[1040] Impaired Picture Arrangement subscores (WAIS-III) associated with decreased place orientation and frontal/occipital blood flow in Alzheimer's disease: Implications for social judgment dysfunction. The Osaki-Tajiri Project.
Kato Y., Meguro K., Nakatsuka M., Nakamura K., Tsuboi M., Yamaguchi S.
Psychiatry Res. Neuroimaging **256** (2016) 65-69.
https://doi.org/ 10.1016/j.pscychresns.2016.04.012

[1041] Impact of Alzheimer's disease in nine Asian countries.
Yang Y.H., Meguro K., Kim S.Y., Shim Y.S., Yu X., Chen C.L.H., Wang H., Lam L., Senanarong V., Dominguez J., Lu P., Lin Y.T., Hu C.J., Chiu P.Y., Fuh J.L., Wang W.F., Yu B.C., Li T., Wang M.W., Situmeang R.F.V., Jang J.W., Zhang J., Chan W.C., Zhou Y.Y., Lou H., Zhang L., Ye M., Chen X.
Gerontology **62** (2016) 425-433.
https://doi.org/10.1159/000443525

[1042] Handling of household flammables by elderly dwelling in the community: General survey on actual status. The Kurihara Project.
Takada J., Meguro K., Ishikawa H., Ouchi Y., Nakatsuka M., The Kurihara Project Members.
J. Community Med. Health Educ. **6** (2016) 463.
https://doi.org/10.4172/2161-0711.1000463

[1043] Handling of household flammables by elderly dwelling in the community: Executive function and judgment involved in handling errors. The Kurihara Project.
Ishikawa H., Takada J., Meguro K., Ouchi Y., Nakatsuka M., The Kurihara Project Members.
J. Community Med. Health Educ. **6** (2016) 464.
https://doi.org/10.4172/2161-0711.1000464

[1044] Measurement of the 3-α decay from the Hoyle and the broad 10 MeV state in ^{12}C.
Itoh M., Ando S., Aoki T., Arikawa H., Ezure S., Harada K., Hayamizu T., Inoue T., Ishikawa T., Kato K., Kawamura H., Sakemi Y., Uchiyama A.
J. Phys. Conf. Seri. **863** (2017) 012019
https://doi.org/10.1088/1742-6596/863/1/012019

[1045] Search for the rare γ-decay mode in ^{12}C.
Tsumura M., Kawabata T., Furuno T., Koshikawa A., Murata M., Morimoto T., Adachi S., Tamii A., Hatanaka K., Ito T., Zenihiro J., Kubono S., Itoh M., Matsuda Y., Maeda Y., Sakaguchi S., Akimune H., Fujimura H., Ou I., Hashimoto T., Iwamoto C.
J. Phys. Conf. Seri. **863** (2017) 012075
http://doi.org/10.1088/1742-6596/863/1/012075

[1046] Production of ^{92}Y via the $^{92}Zr(n,p)$ reaction using the C(*d*,*n*) accelerator neutron source.
Kin T., Sanzen Y., Kamida M., Watanabe Y., Itoh M.
EPJ. Web of Conf. **146** (2017) 08009
https://doi.org/10.1051/epjconf/201714608009

[1047] Measurement of Muonium Hyperfine Structure at J-PARC.
Tanaka K.S., Aoki M., Fukao Y., Higashi Y., Higuchi T., Iinuma H., Ikedo Y., Ishida K., Ito T.U., Iwasaki M., Kadono R., Kamigaito O., Kanda S., Kawall D., Kawamura N., Koda A., Kojima K.M., Kubo M.K., Matsuda Y., Matsudate T., Mibe T., Miyake Y., Mizutani T., Nagamine K., Nishimura S., Nishiyama K., Ogitsu T., Okubo R., Saito N., Sasaki K. , Seo S., Shimomura K., Strasser P., Sugano M., Tajima M., Tanaka T., Tomono D., Torii H.A., Torikai E., Toyoda A., Ueno K., Ueno Y., Yagi D., Yamamoto A., Yoshida M.
JPS Conf. Proc. **18** (2017) 011022.
https://doi.org/10.7566/JPSCP.18.011022

[1048] Frequency Measurement of Tellurium Lines Near Calcium.
Dammalapati U., Harada K., Inoue T., Ito S., Kawamura H., Sakamoto K., Tanaka S. K., Uchiyama A., Yoshioka R., Sakemi Y.
J. Phys.Soc. Jpn. **86** (2017) 124301.
https://dx.doi.org/10.7566/JPSJ.86.124301

[1049] Light shifts induced by nuclear spin-dependent parity-nonconserving transitions of ultracold Fr for the detection of nuclear anapole moment
Aoki, T., Torii Y., Sahoo B., Pratap D. B., & Harada K., Hayamizu, T., Sakamoto K., Kawamura H., Inoue T., Uchiyama A., Ito S., Yoshioka R., Tanaka S. K., Itoh, M., Hatakeyama, A., Sakemi Y.
Asian J. Phys. **25** (2017) 1247.

[1050] Parity-nonconserving interaction-induced light shifts in the 7S1/2 – 6D3/2 transition of the ultracold 210Fr atoms to probe new physics beyond the standard model
Aoki, T., Torii, Y., Sahoo, B. K., Das, B. P., Harada, K., Hayamizu, T., Sakamoto, K., Kawamura, H., Inoue, T., Uchiyama, A., Ito, S., Yoshioka, R., Tanaka, K. S., Itoh, M., Hatakeyama, A., Sakemi, Y.
Appl. Phys. B **123** (2017) 120.
https://doi.org/10.1007/s00340-017-6673-3

[1051] Minimization of the amount of Kryptofix 222-$KHCO_3$ for applications to microscale ^{18}F-radiolabeling.
Iwata R., Pascali C., Terasaki K., Ishikawa Y., Furumoto S., Yanai K.
Appl. Radiat. Isot. **125** (2017) 113-118.
https://dx.doi.org/10.1016/j.apradiso.2017.04.021

[1052] A comparison of five partial volume correction methods for Tau and Amyloid PET imaging with [^{18}F]THK5351 and [^{11}C]PiB.
Shidahara M., Thomas B.A., Okamura N., Ibaraki M., Matsubara K., Oyama S., Ishikawa Y., Watanuki S., Iwata R., Furumoto S., Tashiro M., Yanai K., Gonda K., Watabe H.
Ann. Nucl. Med. **31** (2017) 563-569.
https://dx.doi.org/10.1007/s12149-017-1185-0

[1053] Tau imaging with [^{18}F]THK‐5351 in progressive supranuclear palsy.
Ishiki A., Harada R., Okamura N., Tomita N., Rowe C.C., Villemagne V.L., Yanai K., Kudo Y., Arai H., Furumoto S., Tashiro M., Furukawa K.
Euro. J. Neurol. **24** (2017) 130-136.
https://dx.doi.org/10.1111/ene.13164

[1054] In Vivo Comparison of Tau Radioligands ^{18}F-THK-5351 and ^{18}F-THK-5317.
Betthauser T.J., Lao P.J., Murali D., Barnhart T.E., Furumoto S., Okamura N., Stone C.K., Johnson S.C., Christian B.T.
J. Nucl. Med. **58** (2017) 996-1002.
https://dx.doi.org/10.2967/jnumed.116.182980

[1055] Prediction of the Clinical SUV Ratio in Amyloid PET Imaging Using a Biomathematic Modeling Approach Toward the Efficient Development of a Radioligand.
Arakawa Y., Nai Y.H., Shidahara M., Furumoto S., Seki C., Okamura N., Tashiro M., Kudo Y., Yanai K., Gonda K., Watabe H.
J. Nucl. Med. **58** (2017) 1285-1292.
https://dx.doi.org/10.2967/jnumed.116.183566

[1056] A report of the automated radiosynthesis of the tau positron emission tomography radiopharmaceutical, [^{18}F]-THK-5351.
Neelamegam R., Yokell D.L., Rice P.A., Furumoto S., Kudo Y., Okamura N., El Fakhri G.
J. Label. Compd. Radiopharm. **60** (2017) 140-146.
https://dx.doi.org/10.1002/jlcr.3482

[1057] Development of [^{11}C]/[^{3}H]THK-5351 – A potential novel carbon-11 tau imaging PET radioligand.
Stepanov V., Svedberg M., Jia Z., Krasikova R., Lemoine L., Okamura N., Furumoto S., Mitsios N., Mulder J., Långström B., Nordberg A., Halldin C.
Nucl. Med. Biol. **46** (2017) 50-53.
https://dx.doi.org/10.1016/j.nucmedbio.2016.12.004

[1058] Regional tau deposition and subregion atrophy of medial temporal structures in early Alzheimer's disease: A combined positron emission tomography/magnetic resonance imaging study.
Sone D., Imabayashi E., Maikusa N., Okamura N., Furumoto S., Kudo Y., Ogawa M., Takano H., Yokoi Y., Sakata M., Tsukamoto T., Kato K., Matsuda H.
Alzheimers Dement. (Amst.) **9** (2017) 35–40.
https://dx.doi.org/10.1016/j.dadm.2017.07.001

[1059] The clinical pharmacology of non-sedating antihistamines.
Yanai K., Yoshikawa T., Yanai A., Nakamura T., Iida T., Leurs R., Tashiro M.
Pharmacol. Ther. **178** (2017) 148-156.

https://dx.doi.org/10.1016/j.pharmthera.2017.04.004

[1060] Glucose Metabolic Changes in the Brain and Muscles of Patients with Nonspecific Neck Pain Treated by Spinal Manipulation Therapy: A [(18)F]FDG PET Study.
Inami A., Ogura T., Watanuki S., Masud MM., Shibuya K., Miyake M., Matsuda R., Hiraoka K., Itoh M., Fuhr AW., Yanai K., Tashiro M.
Evid. Based Complement. Alternat. Med. **2017** (2017) 4345703
https://doi.org/10.1155/2017/4345703

[1061] SR-B1 Is a Silica Receptor that Mediates Canonical Inflammasome Activation.
Tsugita M., Morimoto N., Tashiro M., Kinoshita K., Nakayama M.
Cell Rep. **18** (2017) 1298-1311.
https://dx.doi.org/10.1016/j.celrep.2017.01.004

[1062] Biomathematical screening of amyloid radiotracers with clinical usefulness index.
Nai Y., Shidahara M., Seki C., Watabe H.
Alzheimer's & Dementia **3** (2017) 542-552.
https://dx.doi.org/10.1016/j.trci.2017.08.006

[1063] Development of a cherenkov light imaging system for studying the dynamics of radiocesium in plants.
Kurita K., Suzui N., Yin Y., Ishii S., Watabe H., Yamamoto S., Kawachi N.
J. Nucl. Sci. Technol. **54** (2017) 662-667.
https://dx.doi.org/10.1080/00223131.2017.1299051

[1064] ^{137}Cs transmission imaging and segmented attenuation corrections in a small animal PET scanner.
Nai Y., Ose T., Shidahara M., Watabe H.
Radiol. Phys. Technol. **10** (2017) 321-330.
https://dx.doi.org/10.1007/s12194-017-0407-4

[1065] Association of coronary perivascular adipose tissue inflammation and drug-eluting stent-induced coronary hyperconstricting responses in pigs.
Ohyama K., Matsumoto Y., Amamizu H., Uzuka H., Nishimiya K., Morosawa S., Hirano M., Watabe H., Funaki Y., Miyata S., Takahashi J., Ito K., Shimokawa H.
Arteriosclerosis, Thrombosis, and Vascular Biology **37** (2017) 1757-1764.
https://dx.doi.org/10.1161/ATVBAHA.117.309843

[1066] Three-dimensional dose distribution of proton beams derived from luminescence images of water.
Yamamoto S., Watabe H., Toshito T., Komori M.
J. Instrument. **12** (2017) 05019-05019.
https://dx.doi.org/10.1088/1748-0221/12/05/P05019

[1067] Depression and dementia in old-old population: history of depression may be associated with dementia onset. The Tome Project.
Liu Y.C., Meguro K., Nakamura K., Akanuma K., Nakatsuka M., Seki T., Nakaaki S., Mimura M., Kawakami N.
Fron.t Aging Neurosci. **9** (2017) 335.
https://doi.org/10.3389/fnagi.2017.00335

[1068] Language background in early life may be related to neuropsychiatry symptoms in patients with Alzheimer disease.
Liu Y.C., Hsu J.L., Wang S.J., Yip P.K., Meguro K., Fuh J.L.
BMC Geriatr. **17** (2017) 50.
https://doi.org/10.1186/s12877-017-0435-2

[1069] Improved learning of sequential behavior during cane gait training or stair climbing after femoral neck fracture: an implication for donepezil for very mild Alzheimer's disease.
Kumai K., Nakamura K., Meguro K.
Psychogeriatrics **17** (2017) 144-145.
https://doi.org/10.1111/psyg.12204

[1070] Speaking one more language in early life has only minor effects on cognition in Taiwanese with low education level: the Taishan Project.
Liu Y.C., Liu Y.Y., Yip P.K., Meguro M., Meguro K.
Psychogeriatrics **17** (2017) 256- 261.
https://doi.org/10.1111/psyg.12230

[1071] Gender's effects to the early symptoms of Alzheimer’s disease in 5 Asian Countries.
Yang Y.H., Meguro K., Dominguez J., Chen C.L., Wang H., Ong P.A.
Am. J. Alzheimers Dis. Other Demen. **32** (2017) 194-199.
https://doi.org/10.1177/1533317517698796

[1072] Cholinesterase inhibitors are compatible with psychosocial intervention for Alzheimer disease patients suggested by neuroimaging findings.
Meguro K.
Psychiatry Res. Neuroimaging **259** (2017) 29-33.
https://doi.org/10.1016/j.pscychresns.2016.09.009

[1073] Fear of falling and cognitive impairments in elderly people with hip fractures.
Kasai M., Meguro K., Ozawa H., Kumai K., Imaizumi H., Minegishi H., Oi H., Oizumi A., Yamashiro M., Matsuda M., Tanaka M., Itoi E.
Dement. Geriatr. Cogn. Dis. Extra. **7** (2017) 386-394.
https://doi.org/10.1159/000480497

[1074] Current healthcare system for community residents with dementia: A questionnaire survey for dispensing pharmacies, home care support offices, and visiting care support offices.
Takahashi K., Aoki H., Sato Y., Chiba Y., Meguro K.
J. Community Med. Health Educ. **7** (2017) 565.
https://doi.org/10.4172/2161-0711.1000565

X. MEMBERS OF COMMITTEES

X. MEMBERS OF COMMITTEES (as of Jan. 1, 2018)

General

(Chairman)	Kazuhiko	Yanai	(Graduate School of Medicine)
	Sadayoshi	Ito	(Executive Vice President)
	Masayuki	Imai	(Graduate School of Science)
	Kimiko	Sekiguchi	(Graduate School of Science)
	Yoshio	Hosoi	(Graduate School of Medicine)
	Keiichi	Sasaki	(Graduate School of Dentistry)
	Noriyasu	Hirasawa	(Graduate School of Pharmaceutical Sciences)
	Akira	Hasegawa	(Graduate School of Engineering)
	Keiichi	Konoki	(Graduate School of Agricultural Science)
	Kazuhiko	Nishitani	(Graduate School of Life Sciences)
	Atsuki	Terakawa	(Graduate School of Biomedical Engineering)
	Asao	Yamamura	(Institute for Materials Research)
	Yasuhisa	Matsui	(Institute of Development, Aging and Cancer)
	Nobuaki	Sato	(Institute of Multidisciplinary Research for Advanced Materials)
	Keiichi	Jingu	(University Hospital)
	Toshimi	Suda	(Research Center for Electron Photon Science)
	Manabu	Tashiro	(CYRIC)
	Hiroshi	Watabe	(CYRIC)
	Shozo	Furumoto	(CYRIC)
	Masatoshi	Itoh	(CYRIC)
	Hirokazu	Tamura	(Graduate School of Science)
	Shin	Fukudo	(Graduate School of Medicine)
	Yoshitaka	Kinouchi	(Institute for Excellence in Higher Education)
	Yasuyuki	Taki	(Institute of Development, Aging and Cancer)

Cyclotron

(Chairman)	Masatoshi	Itoh	(CYRIC)
	Toshio	Kobayashi	(Graduate School of Science)
	Hirokazu	Tamura	(Graduate School of Science)
	Satoshi	Nakamura	(Graduate School of Science)
	Masayuki	Imai	(Graduate School of Science)
	Kimiko	Sekiguchi	(Graduate School of Science)
	Yasushi	Kino	(Graduate School of Science)
	Akira	Hasegawa	(Graduate School of Engineering)
	Atsuki	Terakawa	(Graduate School of Engineering)
	Yoshikawa	Akira	(Institute for Materials Research)
	Nobuaki	Sato	(Institute of Multidisciplinary Research)
	Toshimi	Suda	(Research Center for Electron Photon Science)
	Manabu	Tashiro	(CYRIC)
	Hiroshi	Watabe	(CYRIC)
	Shozo	Furumoto	(CYRIC)

Radiation Protection and Training of Safe Handling

(Chairman)	Hiroshi	Watabe	(CYRIC)
	Naohito	Iwasa	(Graduate School of Science)
	Takeo	Yoshikawa	(Graduate School of Medicine)
	Noriyasu	Hirasawa	(Graduate School of Pharmaceutical Sciences)
	Atsuki	Terakawa	(Graduate School of Engineering)
	Keietsu	Abe	(Graduate School of Agricultural Science)
	Kazumasa	Ohashi	(Graduate School of Life Sciences)
	Yasuyoshi	Nagai	(Institute for Materials Research)
	Motoaki	Sugiura	(Institute of Development, Aging and Cancer)
	Kentaro	Takanami	(University Hospital)
	Kazuhiko	Yanai	(Graduate School of Medicine)
Manabu	Tashiro	(CYRIC)	
	Shozo	Furumoto	(CYRIC)
(Observer)	Hideyuki	Yuki	(CYRIC)

Life Science

(Chairman)	Manabu	Tashiro	(CYRIC)
	Kazuhiko	Yanai	(Graduate School of Medicine)
	Haruo	Saito	(Graduate School of Medicine)
	Yoshio	Hosoi	(Graduate School of Medicine)
	Kei	Takase	(Graduate School of Medicine)
	Mikiko	Suzuki	(Graduate School of Medicine)
	Keiichi	Sasaki	(Graduate School of Dentistry)
	Masahiro	Hiratsuka	(Graduate School of Pharmaceutical Sciences)
	Atsuki	Terakawa	(Graduate School of Engineering)
	Kensaku	Mizuno	(Graduate School of Life Sciences)
	Kozo	Tanaka	(Institute of Development, Aging and Cancer)
	Nariyasu	Mano	(University Hospital)
	Hiroshi	Watabe	(CYRIC)
	Shozo	Furumoto	(CYRIC)
	Yoshihito	Funaki	(CYRIC)
	Kotaro	Hiraoka	(CYRIC)

Prevention of Radiation Hazards

(Chairman)	Hiroshi	Watabe	(CYRIC)
	Naohito	Iwasa	(Graduate School of Science)
	Yasushi	Kino	(Graduate School of Science)
	Manabu	Tashiro	(CYRIC)
	Shozo	Furumoto	(CYRIC)
	Masatoshi	Itoh	(CYRIC)
	Hideyuki	Yuki	(CYRIC)
	Katsuo	Aizawa	(CYRIC)

Research Program

(Chairman)	Masatoshi	Itoh	(CYRIC)
	Hirokazu	Tamura	(Graduate School of Science)

	Toshio	Kobayashi	(Graduate School of Science)
	Kimiko	Sekiguchi	(Graduate School of Science)
	Kazuhiko	Yanai	(Graduate School of Medicine)
	Shin	Fukudo	(Graduate School of Medicine)
	Kohsuke	Gonda	(Graduate School of Medicine)
	Masahiro	Kozuki	(Graduate School of Medicine)
	Akira	Hasegawa	(Graduate School of Engineering)
	Atsuki	Terakawa	(Graduate School of Engineering)
	Yuki	Satoh	(Institute for Materials Research)
	Hiroyuki	Arai	(Institute of Development, Aging and Cancer)
	Yasuyuki	Taki	(Institute of Development, Aging and Cancer)
	Keiichi	Jingu	(University Hospital)
	Toshimi	Suda	(Research Center for Electron Photon Science)
	Hidetoshi	Kikunaga	(Research Center for Electron Photon Science)
	Tsutomu	Sekine	(Institute Excellence in Higher Education)
	Manabu	Tashiro	(CYRIC)
	Hiroshi	Watabe	(CYRIC)
	Shozo	Furumoto	(CYRIC)
(Observer)	Yohei	Matuda	(CYRIC)
(Observer)	Kazuo	Tanaka	(CYRIC)
(Observer)	Hideyuki	Yuki	(CYRIC)

XI. STAFF AND STUDENTS

XI. STAFF AND STUDENTS (as of January 1, 2018)

Director Kazuhiko Yanai

Division of Accelerator

Masatoshi Itoh
Yohei Matsuda
Yoko Ishibashi
Tsutomu Shinozuka[1)]
Yoshihiro Shimbara[2)]
Yasuaki Ohmiya[3)]
Naoto Takahashi[3)]
Junya Suzuki[3)]
Ken Takahashi[3)]
Takayuki Honma[3)]
Yuki Akashige[3)]

Division of Instrumentations

Hirokazu Tamura[4)]
Atsuki Terakawa[5)]
Kenichi Harada
Kazuo Tanaka
Takeshi Inoue[6)]
Hirokazu Kawamura[6)]
Hikonojo Orihara[1)]
Yasuhiro Sakemi[1)]

Division of Radiopharmaceutical Chemistry

Shozo Furumoto
Yoshihito Funaki
Yoichi Ishikawa
Ren Iwata[1,7)]

Kazuko	Takeda
Kiichi	Ishiwata[1)]
Koichi	Kato[1)]
Yukitsuka	Kudo[1)]

Division of Cyclotron Nuclear Medicine

Manabu	Tashiro
Shin	Fukudo[8)]
Miho	Shidahara[8)]
Kotaro	Hiraoka
Shoichi	Watanuki
Keiichiro	Yamaguchi[1)]
Kazuo	Kubota[1)]
Hiroshi	Fukuda[1)]
Ikuo	Odano[1)]
Katsutoshi	Furukawa[1)]
Nobuyuki	Okamura[1)]
Takashi	Seki[1)]
Toshihiko	Sato[1)]
Soichi	Ando[1)]
Takeshi	Ogura[2)]
Tomoyuki	Narashima[2)]
Jo	Morishita[2)]
Kyokuto	Dan[2)]
Akie	Inami[2)]

Division of Radiation Protection and Safety Control

Hiroshi	Watabe
Shigeo	Matsuyama[5)]
Hayato	Ikeda
Masayasu	Miyake
Hideyuki	Yuki
Shinsuke	Abe
Takashi	Nakamura[1)]

Mamoru	Baba[1)]
Etsushu	Kuraoka[1)]
Iwao	Kanno[1)]
Keizo	Ishii[1)]
Kazuhiro	Ohtomo
Hirokazu	Nakae[9)]

Division of Geriatric Behavioral Neurology

Kenichi	Meguro
Nakatsuka	Masahiro
Kei	Nakamura
Atsuko	Imagawa
Mari	Kasai[1)]
Hideki	Yamazaki[1)]
Shutaro	Nakaaki[1)]
Yoritoshi	Kobayashi[2)]
Mizuho	Yoshida[2)]
Eisei	Furuya[2)]
Keiichi	Kumai
Yuriko	Kato
Junko	Takada
Konomi	Takahashi

Undergraduates and Graduate Students

Aiko	Uchiyama	(Graduate School of Science)
Jun	Okamoto	(Graduate School of Science)
Saki	Ito	(Graduate School of Science)
Kohei	Karasudani	(Graduate School of Science)
Risa	Yoshioka	(Graduate School of Science)
Shunya	Ishida	(Faculty of Science)
Koki	Kasamatsu	(Faculty of Science)
Takahiro	Tominaga	(Graduate School of Pharmaceutical Sciences)
Kazumi	Mikado	(Graduate School of Pharmaceutical Sciences)
Ryo	Akita	(Graduate School of Pharmaceutical Sciences)

Yoshimi	Hayakawa	(Graduate School of Pharmaceutical Sciences)
Kosuke	Emura	(Graduate School of Pharmaceutical Sciences)
Rei	Takeuchi	(Graduate School of Pharmaceutical Sciences)
Yuka	Ito	(Graduate School of Pharmaceutical Sciences)
Yoshihiro	Ando	(Faculty of Pharmaceutical Sciences)
Teruyuki	Tanaka	(Faculty of Pharmaceutical Sciences)
Asuka	Kikuchi	(Graduate School of Medicine)
Senri	Oyama	(Graduate School of Medicine)
Ying Hwey	Nai	(Graduate School of Medical Engineering)
Fairuz Binti	Mohd Nasir	(Graduate School of Medical Engineering)
Md. Shahidul	Islam	(Graduate School of Medical Engineering)
Mahabubur	Rahman	(Graduate School of Medical Engineering)
Yuto	Nagao	(Graduate School of Medical Engineering)
Takayuki	Ose	(Graduate School of Medical Engineering)

Office Staff

Toshimitsu	Muraoka
Katsuo	Aizawa
Shinichi	Suenaga
Genki	Fukaya
Kyoko	Fujisawa
Kei	Ito
Nayoko	Aota
Ryoko	Ito
Fumiko	Mayama
Ikuko	Tojo
Aya	Sugawara

1) Research professor
2) Research fellow
3) SHI Accelerator Service Ltd.
4) Graduate School of Science
5) Graduate School of Engineering
6) Frontier Research Institute for Interdisciplinary Sciences
7) JSPS researcher
8) Graduate School of Medicine
9) Japan Radiation Protection Co., Ltd.

Edited by *Ren IWATA*
Tomoe Nagakura

Published by *CYRIC PR Committee*